Grabs and Cohesive Bulk Solids

Virtual prototyping using a validated co-simulation

Mohajeri, M.

DOI
10.4233/uuid:b232e542-4881-4b02-8677-a7b1dd37b6b0

Publication date
2021

Document Version
Final published version

Citation (APA)
Mohajeri, M. (2021). *Grabs and Cohesive Bulk Solids: Virtual prototyping using a validated co-simulation*. [Dissertation (TU Delft), Delft University of Technology]. https://doi.org/10.4233/uuid:b232e542-4881-4b02-8677-a7b1dd37b6b0

Important note
To cite this publication, please use the final published version (if applicable).
Please check the document version above.

Grabs and Cohesive Bulk Solids

Virtual prototyping using a validated co-simulation

M. Javad Mohajeri

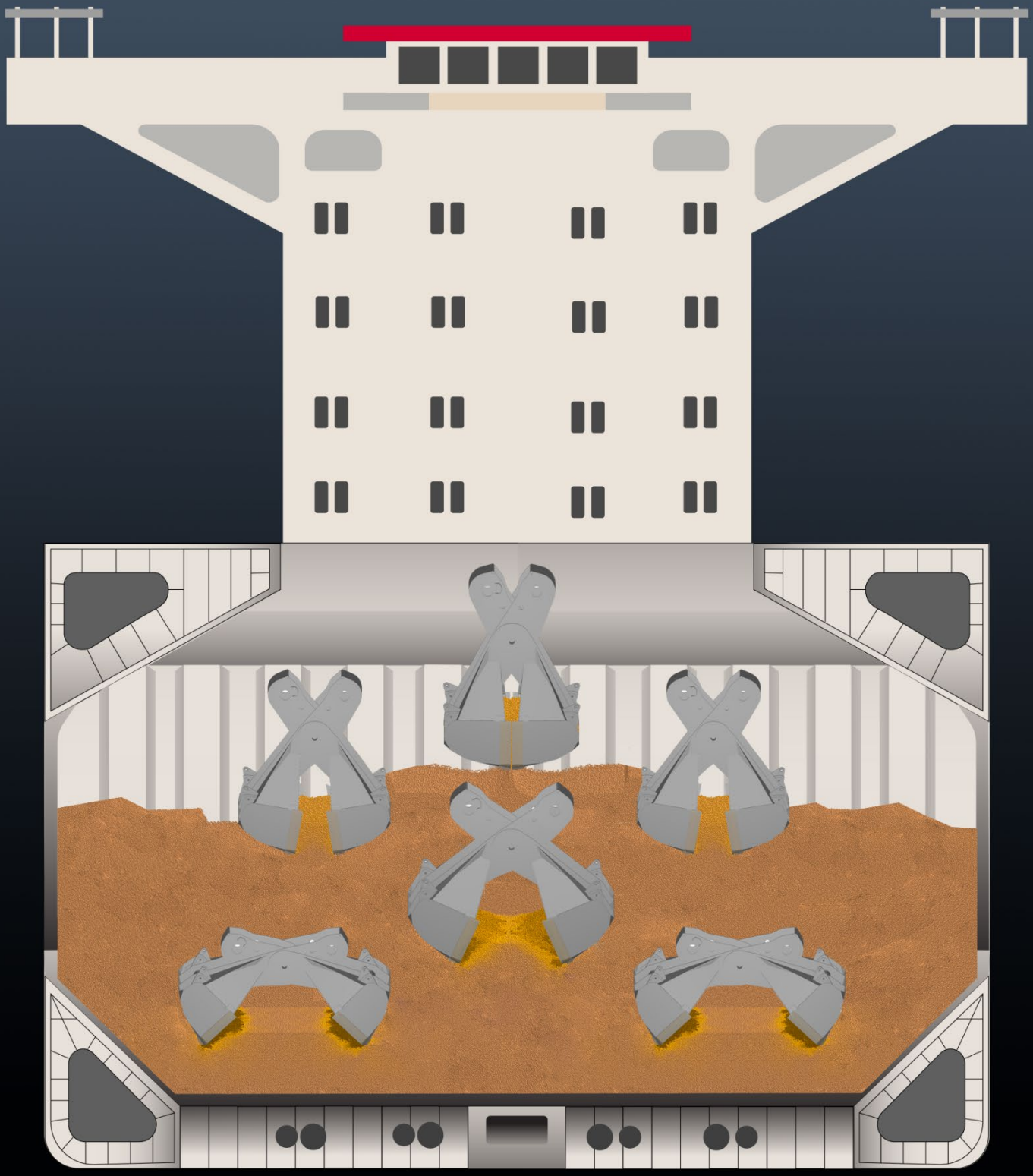

Propositions

Accompanying the dissertation

Grabs and Cohesive Bulk Solids

Virtual prototyping using a validated co-simulation

by M. Javad Mohajeri

1. A validated full-scale simulation of the grabbing process of bulk solid cargo is a reliable platform for virtual prototyping in realistic operational conditions. (This thesis.)
2. An accurate simulation of equipment as it interacts with bulk solids is possible using a proper contact model and the simplest particle shape, the sphere, with no negative effect on the computation time and complexity of simulation. (This thesis.)
3. Applying multi-objective optimisation methods systematically to the simulation of bulk handling equipment is the key step towards robust designs. (This thesis.)
4. In a system driven by competitiveness and the free market, the trait of being ambitious is a potential risk for the exploitation of human and natural resources.
5. In the economic crisis caused by a pandemic, those giant companies making massive profits must share the majority of their gains with the people who have been hit by the same crisis.
6. In theory, capitalism is supposed to encourage free market for competition, but in practice a capitalistic system does its best to suppress competition.
7. Someone who is afraid of failure will not have a story to tell.
8. The culture of “work hard and party hard” overwhelms many employees with stress in long-term, so “work normal and party normal” should be promoted as a healthy culture.
9. The COVID-19 virus knows no borders, neither should humanity.
10. Unhappy the land that needs heroes. - Bertolt Brecht

These propositions are regarded as opposable and defendable, and have been approved as such by the promotors Dr. ir. D. L. Schott and Prof. dr. ir. C. van Rhee.

Grabs and Cohesive Bulk Solids

Virtual prototyping using a validated co-simulation

Proefschrift

Ter verkrijging van de graad van doctor

aan de Technische Universiteit Delft,

op gezag van de Rector Magnificus Prof.dr.ir. T.H.J.J. van der Hagen,

voorzitter van het College voor Promoties,

in het openbaar te verdedigen op woensdag 21 april 2021 om 10:00 uur

door

Mohammadjavad MOHAJERI

Master of Science in Civil Engineering, Tarbiat Modares University, Iran

geboren te Gonbadekavous, Iran

Dit proefschrift is goedgekeurd door de:

Promotors: Dr.ir. D.L. Schott, en Prof.dr.ir. C. van Rhee

Samenstelling van de promotiecommissie:

Rector magnificus	voorzitter
Dr.ir. D.L. Schott	Technische Universiteit Delft, promotor
Prof.dr.ir. C. van Rhee	Technische Universiteit Delft, promotor

Onafhankelijke leden:

Prof.dr. K.G. Gavin	Technische Universiteit Delft
Prof.dr.ir. P. Breedveld	Technische Universiteit Delft
Prof.dr.-Ing. A. Katterfeld	Otto von Guericke Universiteit Magdeburg, Duitsland
Prof.dr. C. Coetzee	Stellenbosch Universiteit, Zuid-Afrika
Dr. M.W.N. Buxton	Technische Universiteit Delft

The research described in this dissertation is supported by NEMAG B.V.

Keywords: grab, discrete element method, cohesive bulk material, iron ore, virtual prototype optimization

Printed by: Ipskamp printing

ISBN: 978-94-6421-324-9

An electronic version of this dissertation is available at

http://repository.tudelft.nl

Summary

Due to the high demand of iron ore products in the steel industry, they have the largest share in dry bulk trading per year, above coal and grains. Approximately 9000 Cape-size bulk carriers with capacities up to 400 000 tonnes (DWT) transport the annual demand of iron ore to destination ports. Grabs are employed extensively to unload iron ore from ship holds. A fast and reliable unloading process is required to maintain a minimized cost for port operators and to deliver iron ore products to customers on time. In practice, many factors, such as moisture, varying material properties over the cargo depth and grab's dynamics, contribute in creating challenges for achieving the desired performance during the unloading process. A solution for improving the unloading process is to enhance the design of grabs by using simulation-based methods. This enables a higher mass of iron ore to be collected per grab cycle, thus minimizing the total unloading time of a bulk carrier.

Virtual prototyping of grabs is a novel simulation-based method that allows for evaluating the design performance in an affordable way. The virtual prototype of a grab as it interacts with bulk material are co-simulated at full-scale by coupling two different solvers: Discrete Element Method (DEM) and MultiBody Dynamics (MBD). The co-simulation requires virtual crane operator, CAD model of grab connected to a crane, and calibrated DEM material model as inputs. Over the past decade, reliable DEM calibration procedures have been developed to model free-flowing bulk solids, such as iron ore pellets, sand and gravel. However, due to moisture content the majority of iron ore products show cohesive and stress-history dependent behaviours, which should be considered in the calibration procedure. Additionally, considering particle size and shape of such fine iron ore products, the extreme computation time of DEM simulations is a challenge to be solved. Furthermore, a grab is often used to handle a broad variety of iron ore cargoes that are different in their properties, such as moisture content, shear strength and bulk density. The variability of bulk solid properties influences the grabbing process considerably, and thus, the grab's efficiency.

The primary objective of this dissertation is to develop an accurate co-simulation of grab and cohesive iron ore, and utilizing it for optimizing virtual prototypes. Once properties of an iron ore product in interaction with equipment are characterized, a reliable multi-variable calibration procedure needs to be employed to set various input parameters of a DEM material model, including continuous and categorical variables. Furthermore, once proper scaling rules are applied on the DEM simulation, a full scale grab-material co-simulation can be set up to be validated. Next, by determining the optimal settings of design variables the effect of bulk cargo variation on

the grab's efficiency can be minimized. This is the fundamental strategy of robust grab design. Bulk terminal operators value grabs that are optimized for multiple objectives, including a maximized efficiency with a minimized deviation.

A consolidation-penetration test method is developed to investigate whether the stress-history dependent behaviour of iron ore is significant for the grab application. This laboratory test method replicates the pre-consolidation stress expected in a cargo pile during the grabbing process. Next, grab relevant bulk properties of a range of iron ore products are characterized using laboratory test methods, such as consolidation-penetration, ring shear, wall friction and ledge angle of repose tests. The obtained data are used for calibrating a realistic material model. Coefficient of static friction, surface energy, and particle shear modulus are found to be the most significant continuous variables for the simulated processes, and the rolling friction treatment is found to be a significant categorical variable. Next, the DEM material model of a cohesive iron ore is created by using a reliable multi-variable multi-objective calibration procedure. The calibrated DEM parameter set and its definiteness are verified using 20 different bulk response values.

Once the material model is calibrated, scaling rules for the selected contact model are applied to minimize the computation time of the co-simulation. The scaling rules are verified for a range of particle sizes, geometry dimensions, test devices, and cohesive forces. Geometry dimensions should be scaled separately from the particle size to maintain the constant bulk mass and volume quantities. The co-simulation of grab and cohesive iron ore is set up using up-scaled particles with a mean diameter of 55 mm. The scaling rules resulted in a reduction from 10^3 hours of computation time for around 8 million particles, to just under 4 hours for around 600 000 particles.

The simulated grabbing process is validated by conducted full-scale grabbing experiments in the cargo hold. This allowed the process to be recorded in realistic operational conditions. The co-simulation is validated by comparing its predictions to experimental data from various aspects, such as grab's kinematics and dynamics. The predictions of the co-simulation compared well to experimental data in all aspects, including force in cables, torque in winches, kinematics of geometry, payload, collected volume and average porosity of bulk solid. The validated co-simulation proves that the stress-dependent behaviour of cohesive cargo as it interacts with the grab were captured successfully.

Finally, a multi-objective optimization framework is established to incorporate the bulk cargo variation in the design procedure. Two objectives are included in the optimization framework: a maximized grab performance in average, and a minimized deviation from the average performance. To map the relationships between geometric design parameters and the mentioned objectives, different virtual prototypes of grabs are simulated for a broad range of iron ore cargoes. Next by applying a surrogate modelling-based optimizer, an optimal grab design is created. The optimal grab design is then tested using the co-simulation, assessing to what extent the predictions of the surrogate model match with the simulated responses. The established optimization framework offers straight forward steps to design grabs for varying bulk cargo properties.

The entire chain of a bulk handling system, especially for cohesive materials, can be simulated accurately at full-scale, aiming at maximizing the performance of the entire system. To achieve that, the approach presented in this work can be implemented for other bulk solids as well as for bulk handling equipment other than grabs. Moreover, the validated co-simulation of grab and cohesive iron ore paves the way for innovating design and operation concepts, thereby further minimizing the required time and energy for unloading iron ore carriers.

Table of content

1

Introduction on co-simulation of grabs and cohesive bulk solids

Iron ore products are transported from origin mines to customers, which are mainly steel manufacturers. Due to the high demand of iron ore products in the steel industry, they have the largest dry bulk trading per year, above coal and grains [1]. Global production of iron ore in 2009 amounted to 1552 million ton, which has been raised to 2494 ton in 2018 [2]. The two main exporting countries of iron ore are Australia and Brazil, sharing around 75% of the global market [3]. The top 5 importing countries are located in Asia and Europe, which results in intercontinental shipping of iron ore products. In 2018, a total of 3210 million ton of dry bulk solids have been shipped; of which 46% was iron ore [1]. More than 90% of the yearly tonnage transport of iron ore is shipped by Cape-size bulk carriers [4]. Approximately 9000 Cape-size carriers with capacities up to 400 000 tonnes (DWT) transport the annual demand of iron ore to destination ports.

To unload iron ore cargoes from bulk carriers at destination, grabs are employed. Figure 1-1 displays a grab unloading a bulk carrier. The mooring time of bulk carriers needs to be as short as possible, thus, minimizing costs of terminal operators and other stakeholders. Therefore, a time-efficient and reliable unloading process is required at destination ports. Considering the increasing

global demand for iron ore, the unloading process can be improved in terms of productivity to use available facilities, such as cranes, in a sustainable way. A promising solution for improving the unloading process is to enhance design of grabs.

Figure 1-1. Unloading bulk carriers at destination using grabs

1.1. The Grabbing Process

During unloading of a bulk carrier, grabs collect the material from the cargo hold to transfer toward the next handling element, which is usually a hopper-conveyor system. A cycle of unloading the cargo using grabs consists of the following phases:

- Grabbing bulk solids from the cargo hold,
- Transferring the grab from the cargo hold toward next handling equipment,
- Releasing the collected material (e.g. on a hopper-conveyor system), and
- Transferring the empty grab to the cargo hold.

The grab's efficiency, η_{grab}, depends mainly on the first part, the grabbing process, which determines the amount of bulk solid collected, M_{DWT}. Therefore, investigating the grabbing process is the main focus of this dissertation. The grab's efficiency in an unloading cycle, η_{grab}, can be calculated using Eq. (1.1).

$$\eta_{grab} = \frac{M_{DWT}}{M_{DWT} + M_e} \tag{1.1}$$

where M_{DWT} is the weight of collected bulk solids using the grab, and M_e is the grab's weight when it is empty. The grab's efficiency for iron ore cargoes is typically in the range of 0.5 to 0.75. To improve the grab's efficiency for a specific crane capacity, M_e should be minimized while M_{DWT} is maximized. The general model of the grabbing process (i.e. of an iron ore cargo) is schematically shown in Figure 1-2. In addition to the grab design itself, dimensions of ship's hold, properties of bulk cargo, crane operator, crane specifications are main contributing elements in the grabbing process. Thus, predicting performance of new design concepts is still a challenge, as it requires considering interactions between multiple contributing elements.

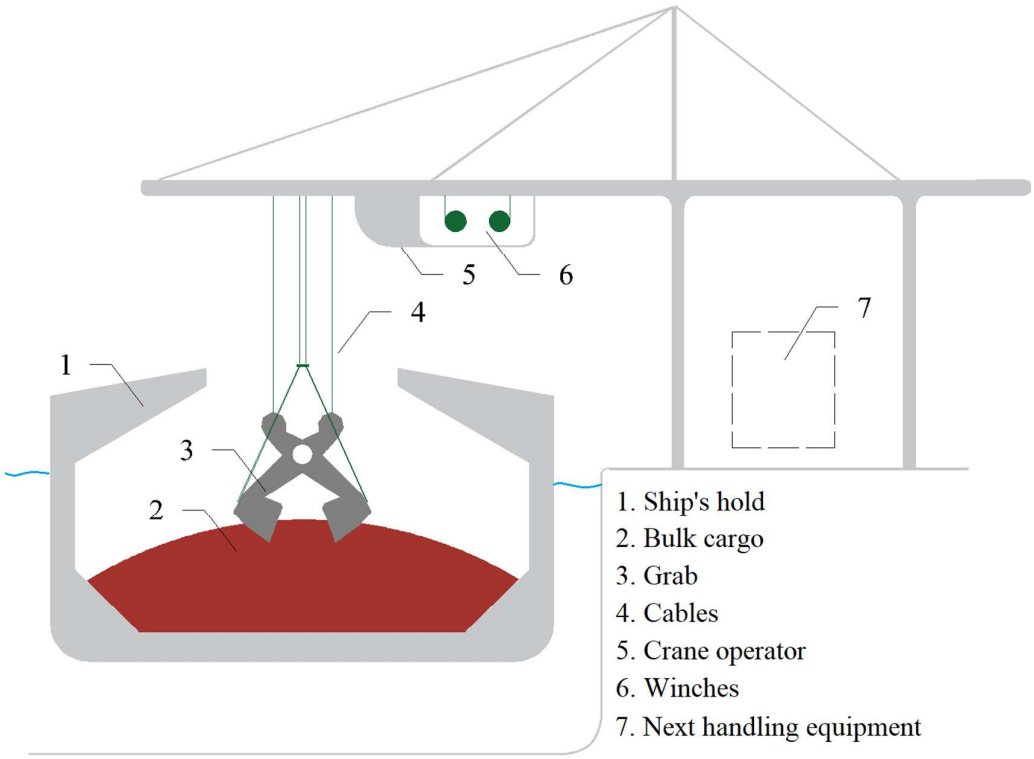

Figure 1-2. General model of grabbing process (i.e. of iron ore) during unloading bulk carriers

Furthermore, a grab is often used to handle a broad variety of iron ore cargoes that are different in their properties, such as moisture content, shear strength and bulk density. The variability of bulk solid properties influences the grabbing process considerably, and thus, the grab's efficiency [5]. The consistency in grab's efficiency needs to be maintained for designing a robust product. However, bulk cargo variability has not explicitly been incorporated in the design process of grabs and other equipment.

To design and develop a new grab, its performance needs to be evaluated in a range of operational conditions. For example, quantifying the payload, M_{DWT}, allows to decide whether the new grab design meets expectations. This can be evaluated either by physical or virtual prototyping of new design concepts.

1.2. Physical Prototyping of Grabs

Physical prototyping is a traditional approach to enhance the grabbing process by fabricating new design concepts for testing. Manufacturers create new design concepts using their engineering knowledge and in-house experience. In the physical prototyping approach, once a new design concept is developed, a real-scale grab is manufactured.

The real-scale grab prototype is tested at a bulk terminal to evaluate its performance during the grabbing process. For example, Figure 1-3 shows a real-scale prototype that was built to be tested at a bulk terminal in 1968. This prototype aimed at improving the grabbing process at the final stage of unloading a ship's hold, where the bulk cargo is trimmed. The product was finalized after manufacturing multiple real-scale prototypes with incremental improvements, and it is currently being used at bulk terminals (shown in Figure 1-1). It is known that physical prototyping is a time- and cost-intensive design approach, requiring multiple grabs to be manufactured.

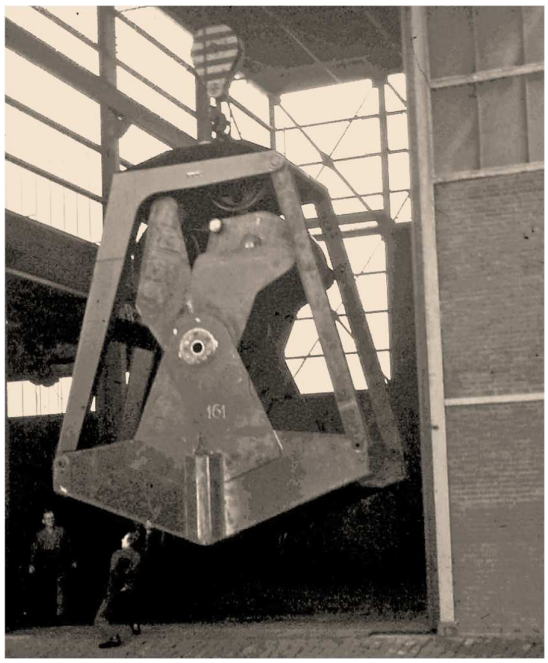

Figure 1-3. A real-scale physical prototype is built to be tested at bulk terminal (1968, Rotterdam). Courtesy of Nemag B.V.

1.3. Virtual Prototyping of Grabs in Interaction with Bulk Solids

The virtual prototyping of grabs [6–10] is a novel design technology. The virtual prototyping offers a time- and cost-efficient way to replicate the grabbing process of bulk solids in a simulation environment. To model grabs in interaction with bulk solids, a co-simulation framework is used that couples a Discrete Element Method (DEM) solver with a MultiBody Dynamic solver. Figure 1-4 presents the co-simulation framework, which requires virtual crane operator, CAD model of grab connected to a crane, and calibrated material model as inputs. A coupling server communicates between two solvers at each time interval; the geometry motion is calculated using the MBD solver, and the reaction forces on the geometry is calculated using the DEM solver.

To set up the DEM simulation, a material model needs to be included. A material model replicates the behavior of an actual bulk solid in interaction with equipment. Calibration and verification of DEM input parameters is the common approach to ensure that the material model simulates the behavior of corresponding bulk solid properly [11].

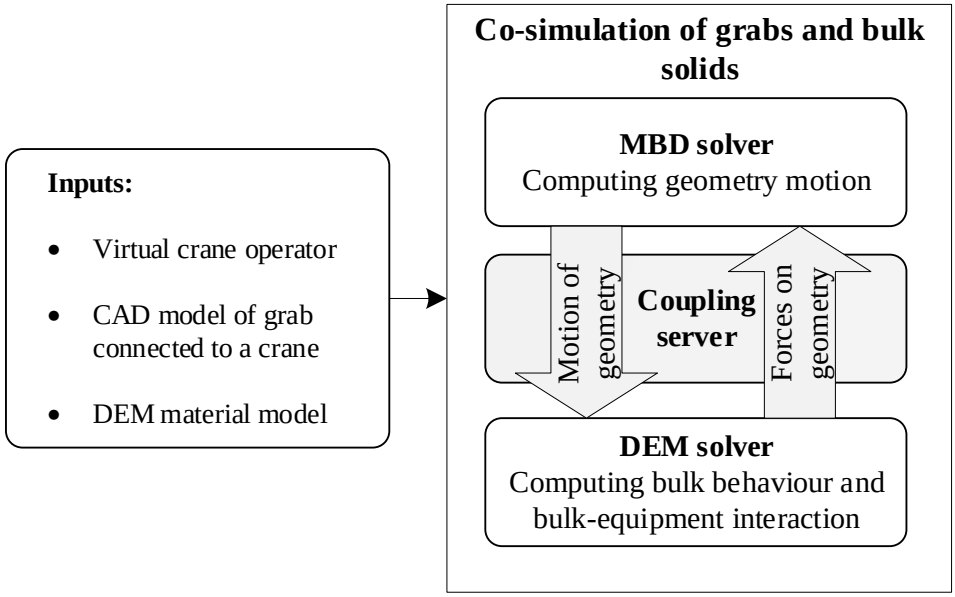

Figure 1-4. Co-simulation framework between MBD and DEM solvers to simulate the grabbing process

Figure 1-5 displays a generic DEM calibration procedure, including main components. In general, input variables of DEM, such as particle density, friction coefficients, and particle shape, are varied until the mismatch between simulated and actual bulk response is minimized. Over the past decade, reliable DEM calibration procedures have been developed to model free-flowing bulk solids, such as iron ore pellets [9], glass beads [12], sinter ore [13], sand [14,15], and gravel [16,17]. By setting multiple targets for the DEM calibration, more than a single bulk response can

be considered. This prevents the “ambiguous parameter combinations” problem in the DEM calibration procedure, which is discussed in detail in [17]. For example, to calibrate DEM input variables for simulating iron pellets in interaction with ship unloader grabs, Lommen [8] considered at least three different calibration targets. The static angle of repose was replicated using the ledge and free-cone methods; the penetration resistance of iron pellets was also replicated, using a wedge penetration test setup. The calibrated material model was used to simulate the grabbing process of iron ore pellets in a real-scale co-simulation. The co-simulation was validated by comparing its outcome to real-scale experiments on the grabbing process.

In contrast to such a free-flowing material, the majority of iron ore products and other bulk cargoes (e.g. coal) show cohesive and stress-history dependent behaviours, which cannot be captured using the current DEM material model. Additionally, considering particle size and shape of such fine iron ore products, the extreme computation time of DEM simulation is another challenge to be solved. Scaling techniques can offer a promising solution to minimize the computation time.

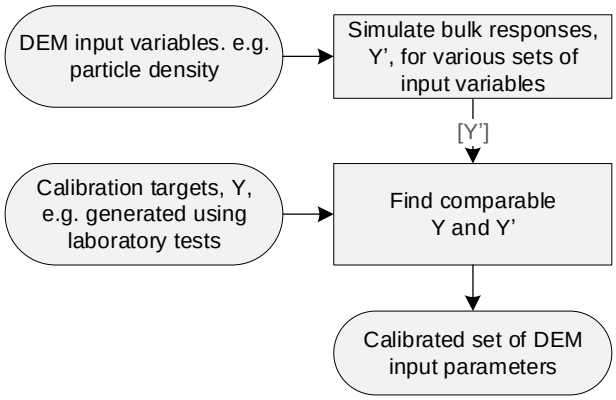

Figure 1-5. Main components of a generic DEM calibration procedure.

In general, iron ore products are produced in different particle size ranges, such as lump, pellet, sinter feed and pellet feed. Lump ore products have particle size between 6.3 and 40 mm [18]. Particle size range of pellets is between 8 and 14 mm; because of size and characteristics of particles in iron ore pellets, the variations of moisture content or consolidation state does not play a role on their bulk properties [8]. Therefore, pellet as well as lump size iron ore products are considered as free-flowing materials. Figure 1-6 displays three different iron ore samples, pellets, sinter feed and pellet feed categories, indicating the difference in their particle size distribution. Sinter feed and pellet feed products have a particle size usually less than 11 mm [19,20]. Cohesive

forces between particles are created due to the liquid bridge, and hence the amount of moisture present influence material behaviour and its interaction with equipment.

Figure 1-6. Various size range in iron ore products; pellets, sinter feed and pellet feed [21]

Furthermore, piles of iron ore in bulk carriers can be up to 20 m deep [19]. Due to the self-weight of bulk solid, a considerable vertical pressure (stress) is created over the pile depth. This vertical pressure probably densifies moist iron ore cargoes over the pile depth. It is unclear whether the densification of iron ore cargoes influences the grabbing process upon unloading of bulk carriers.

Therefore, the current co-simulation framework [8] needs to be extended to include a realistic DEM material model of iron ore fines, such as sinter feed type, in interaction with grabs. Figure 1-7 schematically illustrates a DEM contact spring-damper system between two particles, *a* and *b*. Here, three main modules are identified: contact force in the normal direction is denoted by f_N, while f_T and τ_R represent force in the tangential direction and rotational torque respectively. Without choosing a proper combination of contact modules, calibrating a realistic DEM material model is infeasible.

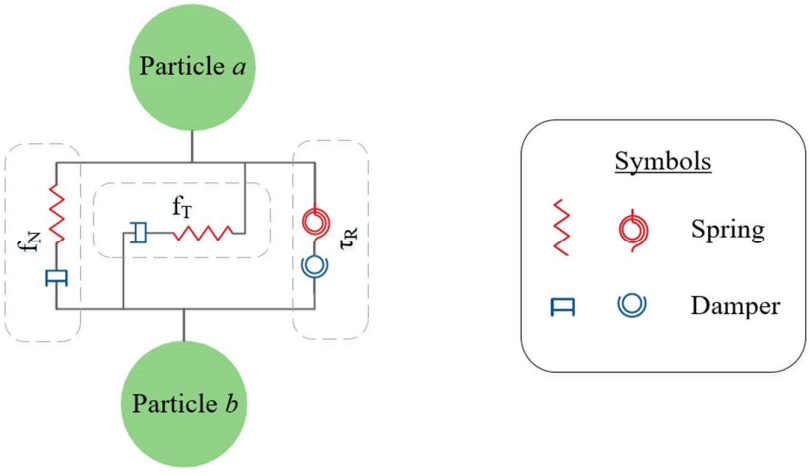

Figure 1-7. A contact spring-damper system between two particles, including normal, tangential, and rotational directions

The current co-simulation framework uses an elastic contact model, which is not able to capture cohesive and stress-history dependent behaviours [22]. Including the plastic overlap in a contact spring enables the possibility of capturing the stress-history dependent behaviour [23]. Elasto-plastic adhesive contact springs are promising options to calibrate material behaviour of iron ore fine products that are moist [24]. Figure 1-8 shows a schematic model of an elasto-plastic adhesive contact spring, which consists of three parts: (I) loading, (II) unloading/reloading, and (III) adhesive parts. By introducing cohesive forces as well as elasto-plastic stiffness into the DEM calibration procedure, the number of DEM input variables and the number of required bulk responses increase [23,25–27]. Therefore, a reliable calibration procedure is required to calibrate DEM material models that are based on elasto-plastic adhesive springs.

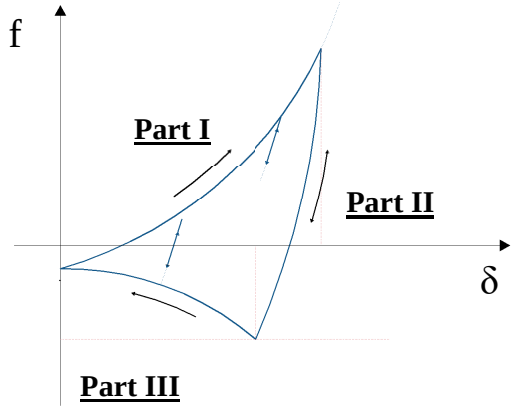

Figure 1-8. A non-linear elasto-plastic adhesive contact spring.

1.4. Research Objectives

The primary objective of this dissertation is to simulate the grabbing process of cohesive iron ore cargoes accurately. This can be achieved by establishing a reliable DEM calibration procedure as well as a scaling approach for elasto-plastic adhesive contact springs. The common approach to create DEM calibration targets is to determine bulk responses using experiments at laboratory, such as penetration [28], angle of repose [26], shear cell [29] test setups. Once the DEM material model is calibrated, a real-scale co-simulation needs to be set up that has a practical computation time. Up-scaling of DEM particles can offer a solution to minimize the computation time [30]. Next, validating the accuracy of the simulated grabbing process is required.

Furthermore, by including the material model of iron ore fines in the existing co-simulation framework, a systematic design framework can be established to enhance the grab's efficiency. It is important to determine the optimal settings of design variables in order to minimize the effects

of bulk cargo variation on the grab's efficiency. Such an approach is the fundamental strategy of robust design [31]. Bulk terminal operators value grabs that are optimized to satisfy multiple objectives, including a consistent, and simultaneously, a maximized efficiency. Therefore, a multi-objective optimization framework is developed to incorporate the bulk cargo variation in the design procedure of grabs.

The following research questions are addressed in this dissertation:

1 How can the effect of stress-history dependency of cohesive iron ore on the grabbing process be evaluated using a laboratory experimental setup?
2 What are variability and interdependency of iron ore properties and their interactions with equipment in realistic transport and storage conditions?
3 How to minimize the computation cost for a large scale co-simulation of grabs and cohesive bulk solids?
4 What is a reliable calibration procedure to develop a realistic material model of cohesive iron ore for the grabbing process?
5 What is the accuracy of the MBD-DEM co-simulation of grabs and cohesive iron in replicating the actual process?
6 How can bulk cargo variation be included in the design procedure of grabs?

1.5. Outline of This Dissertation

The outline of this dissertation is illustrated in Figure 1-9 and a brief description of the content of each chapter is outlined below.

Chapter 2 presents a consolidation-penetration test method to investigate whether the stress-history dependent behaviour of iron ore is significant. Such a laboratory test method replicates the consolidation stress expected in a cargo pile during the grabbing process.

Chapter 3 studies the material characteristics of iron ore fine samples further, in conditions similar to unloading conditions in the cargo hold of the vessel. Various characteristics are quantified, such as shear strength, wall fiction, ledge angle of repose and penetration resistance.

In Chapter 4, first an appropriate DEM contact model is selected for modelling cohesive and stress-dependent behaviours of iron ore products. Next, to overcome the extreme computation time of DEM simulations, a hybrid particle-geometric scaling approach is established.

In Chapter 5, a material model is calibrated to simulate the cohesive iron ore sample including its stress-history dependency behaviour. A reliable multi-step optimization framework is established to consider feasibility and definiteness in the calibration procedure.

Chapter 6 compares the simulated grabbing process of cohesive iron ore to reality, therefore establishing a validated model. To achieve this, bulk cargo properties in interaction with a Scissors grab are determined at a bulk terminal.

Chapter 7 demonstrates a multi-objective optimization framework to incorporate the bulk cargo variation in the design procedure. Virtual prototypes of grabs are tested in handling a broad range of iron ore cargoes, resulting in an optimal grab design.

Chapter 8 concludes the adequacy of the research approach and provides recommendations for further research on enhancing the grabbing process and other similar applications.

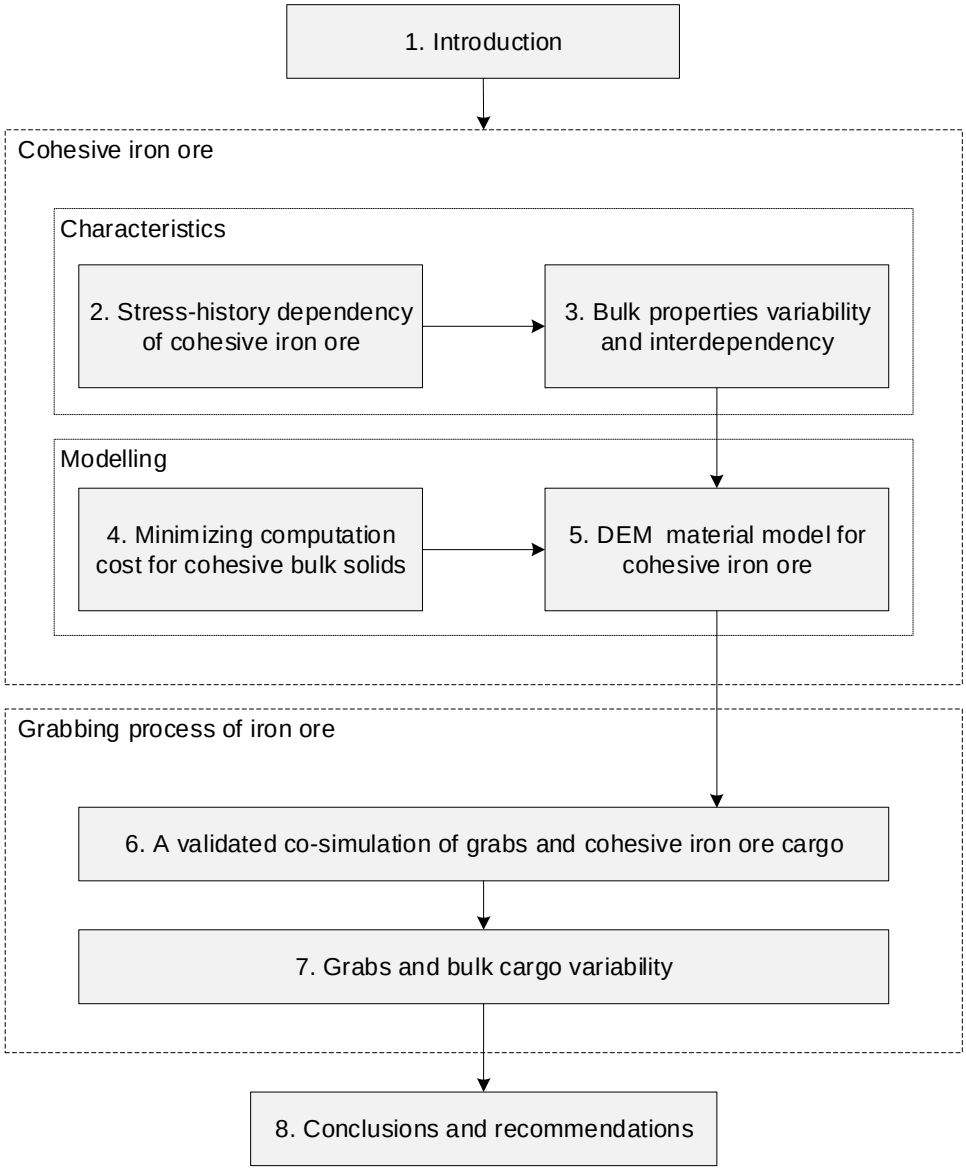

Figure 1-9. Visual outline of this dissertation

2

Stress-history dependency of cohesive iron ore*

The grabbing process starts with cutting the free surface of the bulk iron ore. The initial penetration depth of the grabs' knives into the material is an important success factor in their filling ratio. The resistance to penetration is influenced by the consolidation process of the cargo, which occurs during loading and sailing. When bulk carriers arrive at the port of destination, the iron ore cargo is often in a partially consolidated form in the cargo hold. In this chapter, a test method is developed to mimic the penetration process of the grabs' knives into material, and to determine whether the penetration resistance of iron ore fine is sensitive to the pre-consolidation. The relationship between pre-consolidation and bulk density is investigated as well.

Section 2.1 describes the material properties of an iron ore fine cargo. Furthermore, the test method is described including the experimental hardware and procedure. Next, levels of pre-consolidation are selected to create an experimental plan. Section 2.2 presents results of the

---

* This chapter corresponds to the reference: M. Mohajeri, F.M. Sickler, C. van Rhee, D.L. Schott, "A consolidation-penetration test for wedge-shaped penetration tools". Journal of FME Transactions, Volume 46, Issue 3, 2018, 392-399. DOI: 10.5937/fmet1803392M.

experiment, including the influence of pre-consolidation on the penetration resistance and the bulk density. Section 2.3 presents conclusion on the link between the pre-consolidation and the penetration resistance for the grabbing process.

2.1. Material Properties and a Consolidation-Penetration Test Method

As the unloading of a ship's hold starts and proceeds, the grab collects bulk material that is stored at greater depths. Consequently, when the grab's knives touch the bulk surface that is an over-consolidated condition. Over-consolidation means that the current existing vertical stress is less than the historical maximum stress. The historical maximum, which is referred as the pre-consolidation stress, is the maximum vertical overburden stress that a particular sample has sustained in the past [32]. Since the grabs' performance is influenced by the initial penetration depth of their buckets into bulk materials, it is expected that a higher pre-consolidation stress results in a lower grab payload by reducing its initial penetration depth.

The exact state of the iron ore cargo remains unknown, as many factors are involved in its production, loading and transportation. For instance, the varying forces that acted upon the cargo during loading and sailing can lead to different states of compaction [4]. The state of compaction or the relative density compares the current packing with both the densest and the loosest packing conditions.

In [8], a penetration test was used to calibrate the Discrete Element parameters of iron ore pellets in interaction with grabs. Due to the low sensitivity of pellets to consolidation, no significant influence on the penetration resistance could be identified. However, the majority of the iron ore products are iron ore fines (IOFs), which are expected to have a higher penetration resistance in the over-consolidated condition.

The influence of pre-consolidation on the penetration resistance of soil material has been investigated by a number of researchers; some examples are [33], [34] and [35]. However, the influence of pre-consolidation on the penetration resistance of IOFs has not been investigated yet.

2.1.1. Cargo (IOF) characteristics

Iron ore products are produced in three different particle size ranges: pellets, sinter feed and pellet feed. The first ore, pellets, are marble-sized, heat-hardened balls of iron and have a particle size between 8 and 18 mm [8]. The other two groups have a particle size usually smaller than 6.3 mm

[36]. Figure 2-1 displays three samples, one of each iron ore category, indicating the difference in their particle size range.

Pellets are out of the scope of the current investigation, since consolidation does not play a role in their resistance against grabs knives' penetration [8]. Therefore, a pellet feed type of iron ore is selected for this experiment. Table 2-1 shows the particle size and density characteristics of the iron ore sample. 50% of the sample weight consists of particles smaller than 0.88 mm, and 80% of the particles have a diameter between 0.001 and 6.3 mm, indicating a wide particle size distribution.

Pellets Sinter feed Pellet feed

Figure 2-1. Iron ore products with different particles sizes

Table 2-1. Characteristics of the iron ore sample [37]

Particle size distribution (mm)	d_{10}	0.001
	d_{50}	0.088
	d_{90}	6.3
Particle density (kg/m^3)	4182	

IOF cargoes are often transported in a wet state, and their bulk properties, such as bulk density and compressibility, are different in wet and dry states [38]. To create this wet state, first the iron ore sample was dried in an oven device according to the procedure described in [39], and then water was added to the dry sample.

Since cargo moisture should be always low enough to prevent any hazardous cargo liquefaction [40], the sample was prepared with only 5% dry-based moisture content. Dry-based moisture content is the portion of a representative sample consisting of water, expressed as a percentage of the total dry mass of that sample [32]. This parameter can be expressed as follows:

$$MC = 100\,\frac{\rho_b - \rho_d}{\rho_d} \qquad (2.1)$$

where ρ_b and ρ_d are the bulk density in wet and dry states respectively.

A mixing machine was used to combine the water with the dry iron ore to create a homogeneous moisture distribution. Figure 2-2, which shows the iron ore before and after the mixing, indicates that prior to mixing there are several relatively large agglomerated particles present in the material. Most of these agglomerates are created during the drying process of the IOF sample in the oven. During mixing, these pieces are broken down into smaller pieces.

Next, to create an over-consolidated sample, representing the cargo's in-hold situation, an estimation of this cargo condition is required. This is a challenging job, since a combination of both deterministic and non-deterministic forces act upon the cargo, such as the weight of the cargo itself, the drop height during the cargo loading and the waves' impact during sailing. Additionally, it is nearly impossible to identify which of these forces are more influential on the grabs' performance during the unloading of cargo.

Therefore, the design guideline for bulk carriers [41], as well as [42], is used to estimate a range of consolidation stresses required to replicate the IOF cargo condition in a laboratory environment. Based on the design guideline, the maximum height of the IOF pile inside the hold of a typical Cape-size bulk carrier should be limited to 15 m; this complies with the measurement data of [20]. However, based on [42], the height of an IOF cargo pile can be up to 20 m in practice. Therefore, the maximum height of an IOF cargo is assumed to be 20 m, to cover the whole range.

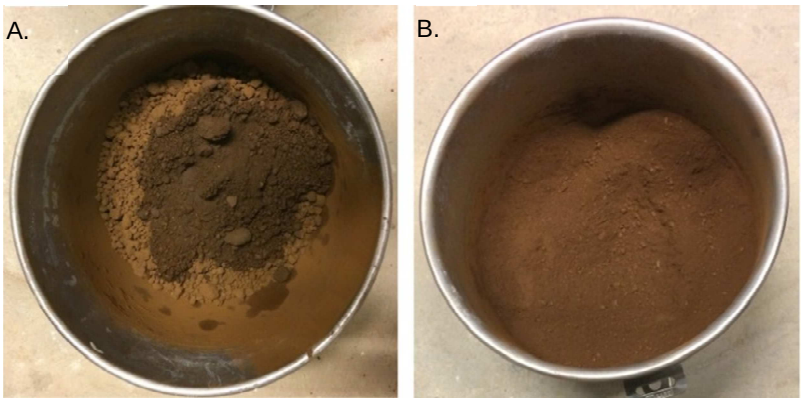

Figure 2-2. The iron ore sample before (A) and after (B) mixing with the mixer machine [37]

Since the aim of the current chapter is to investigate the relationship between vertical consolidating pressure and penetration resistance of the cargo, a range of pre-consolidation stresses are determined to replicate the confining pressure acting on IOF cargoes at different

layers. Figure 2-3 displays a 3D view of an IOF cargo pile in the ship's hold. The geometrical profile suggests different levels of vertical pressure along the pile depth.

Figure 2-3. Laser scan of a ship's hold containing cargo of iron ore fine [20]

2.1.2. Experimental hardware

A column of iron ore with the height of 20 m and the area of 1 m^2 approximately weighs 55 tons, corresponding to vertical confining pressure of 540 kPa at the bottom of the column. In order to replicate this pressure, a hydraulic servo-controlled test frame is selected with a maximum force of 200 kN.

Figure 2-4 displays the schematic cross section of the penetration tool selected for this study. This is the same tool that [8] used to study the penetration of a grab into the iron ore pellets. Using the same tool aids in producing comparable results, which will be used for the grab design application.

A wedge-shaped penetration tool is chosen, as plane stress is required to resemble the penetration of a grab in iron ore. The tool is chosen to be symmetric to minimize the bending stress in the experimental apparatus. The 40 mm width of the penetration tool is based on manufacturing requirements; this specify a minimum of 30 mm and a maximum of 50 mm as the characteristics of a real grab. The tool angle was chosen to be 30º as this is the standard angle used by other researchers such as [43] and [44], as well as in the existing industrial scale grabs. The wedge length is 200 mm.

The ideal penetration tool tip shape for minimizing penetration resistance is a sharp one. However, due to the abrasive nature of iron ore, in practice a sharp tip wears off quickly; therefore, a blunt tip is often used.

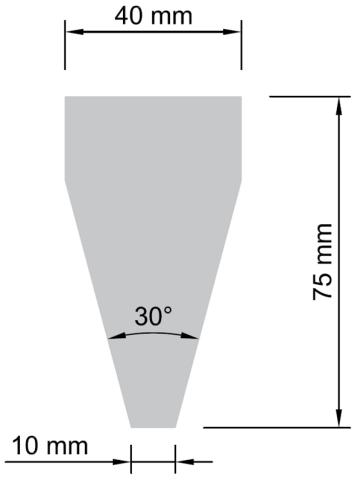

Figure 2-4. Cross section of the wedge penetration tool [8]

Figure 2-5 displays details of the test container. The dimensions of the container are limited by the apparatus to be used for the penetration test. The penetration tool has a depth of 75 mm. Care has to be taken that the tests are unaffected by the adjacent sides or bottom wall of the container [45]. To avoid this wall effect, the depth of the container should be at least 75 mm multiplied by 2, which results in 150 mm. The length of the container is of importance because as the material is penetrated the material will displace to the sides. For the cone penetration into sand, the ratio used of the nearest wall to the cone diameter is larger than 2 [46]. To ensure that enough space on both sides of the wedge is available, at least 80 mm of space on each side of the penetration tool is required, resulting in a total container width of 80 + 80 + 40 = 200 mm. These dimensions result in a container with a volume of 15 liters. 24 kg of the iron ore sample is used to fill the container.

Before starting the consolidation phase, the sample of the iron ore is loosened to ensure that almost no consolidation remains from mixing or transportation. Then the iron ore is loaded in the designed container, and the bulk surface is leveled out manually.

In order to create a homogeneous sample, the state of compaction should be uniform along the depth. One of the factors that could affect the state of compaction is the layer thickness [47] or “under-compaction” effect that is investigated in [48]. To study the influence of this factor on the test results, consolidating in one layer and three layers are considered in the test procedure. In both cases, each layer is consolidated using the same compressive force. A rigid top plate (1, in

Figure 2-5) is placed between the hydraulic jack and the bulk surface to distribute pressure uniformly on the sample.

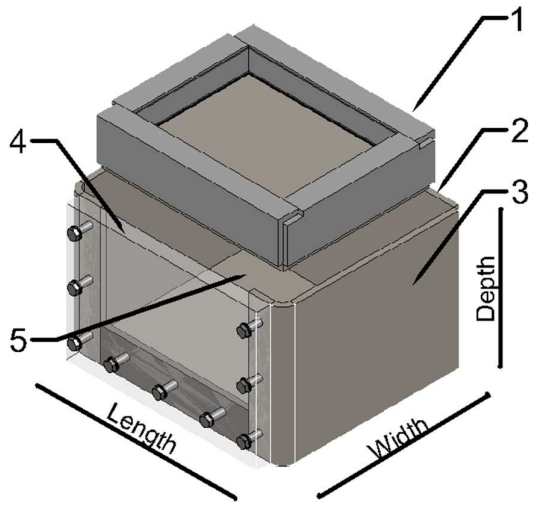

Item No.	Quantity	Title	Material	Function
1	1	Top plate	-	Consolidation
2	1	Back plate	S355 J2+N	N.A (fixed)
3	2	Side plate	S55 J2+N	N.A. (fixed)
4	1	Transparent plate	Plexiglas	Capture flow
6	1	Bottom plate	S355 JR	N.A (fixed)

Figure 2-5. Details of the test container

For the experiment of consolidating in one layer, 24 kg of the iron ore sample is poured into the container using a small shovel. After creating a levelled-out surface, the sample is consolidated by applying the predetermined force of 5 kN on the top plate, equivalent to 66.7 kPa consolidating pressure on the sample. Next, in a separate experiment, the sample is consolidated in three layers of 8 kg each by applying the same consolidating pressure.

In the next phase, the penetration phase, the reaction force on the wedge tool during penetration into the iron ore sample is measured. Since previous research, [8] and [43], have stated that the penetration velocity has little to no influence on the penetration resistance, a constant velocity of 6 mm/s is used.

Figure 2-6 displays the consolidation phase, as well as the material condition before starting the penetration phase. After the penetration phase, the wedge is moved upward to the initial position with the same velocity (6 mm/s). After each experiment, the container is emptied and the sample is loosened.

Figure 2-6. Consolidating the iron ore sample; Left) consolidating iron ore with the top plate, Right) Starting point of the penetration phase

To calculate the bulk density, the material depth is determined by using the elevation where the wedge tool touches the bulk surface, and a force of 0.1 kN is measured.

Figure 2-7 shows the schematic set-up for determining the vertical displacement of the wedge tool relative to the material depth. Since the test apparatus does not record the displacement data relative to the material depth, the sample surface is adjusted with +10 mm. Therefore, the penetration resistance can be compared in a consistent manner.

2.1.3. Experimental plan

The two dependent variables measured in this experiment are, I) the recorded reaction force on the wedge during penetration into the sample, the so-called penetration resistance, and II) the bulk density of the sample after the consolidation phase. The effect of three independent variables on them are measured: I) number of consolidated layers, II) applied consolidation stress and III) number of repetitions.

In the first experiment, the sensitivity of the penetration resistance to the number of consolidated layers is investigated. The experiment determines whether consolidating the iron ore sample in one layer or in three layers influences the penetration resistance significantly.

For the second experiment, the effect of increasing consolidation stress on the penetration resistance is investigated. Table 2-2 shows the range of forces and the corresponding consolidation stress to be applied on the iron ore sample. As explained in 2.1.1, several levels of

consolidation stress are determined to represent a range of possible vertical confining pressure in ships' holds, at different depths in the iron ore cargo.

Each test is repeated at least three times. This makes it possible to measure the penetration resistance and the bulk density in at least three test repetitions, and to plot the confidence interval of the results.

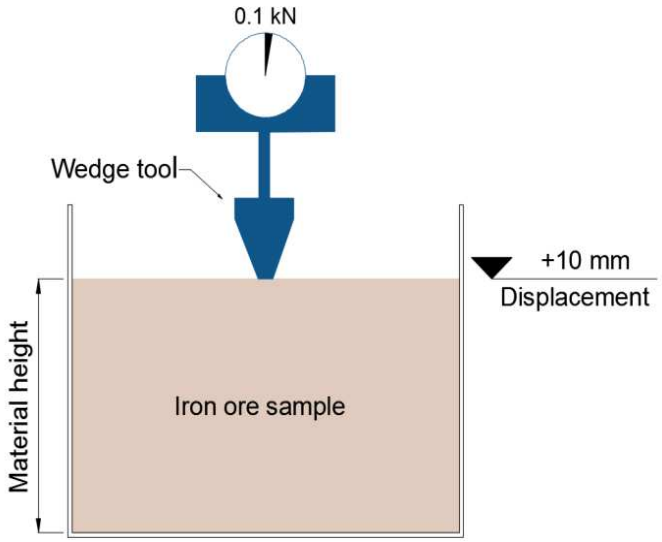

Figure 2-7. Schematic view of the set-up for measuring the displacement of the wedge tool over material depth

Table 2-2. Levels of applied consolidation stress

Applied force [kN]	0	1	5	10	20	40
Equivalent consolidation stress [kPa]	0	13.3	66.7	133.3	266.7	533.3

2.2. Test Results

Figure 2-8 illustrates the effect of the consolidation strategy, one layer versus three layers, on the penetration resistance. For a stress level of 66.7 kPa, the average penetration resistance, as well as the 95% confidence intervals (CI 95%), are shown for both cases. Even though at the initial depths, with the displacement smaller than 40 mm, the recorded reaction forces in both cases are similar, they start to diverge as the tool penetrates deeper. The difference is quantified by calculating the ratio of the average penetration resistance at the 100 mm wedge displacement in the case of consolidating in one layer over the other case; this ratio is 0.91.

The difference at the greater depths is likely to be caused by applying more consolidating energy to the second and third layers; this results in a slightly stiffer bulk material, and thus more

resistance to penetration. Comparing the bulk density supports this idea; in the case of consolidating in three layers, the bulk density (average) is 11 kg/m^3 higher than the other case. However, considering the similarity in the trend of the penetration resistance in both cases, the overlapping confidence intervals, and the small difference in the bulk density, the second set of experiments are conducted by consolidating the sample in one layer.

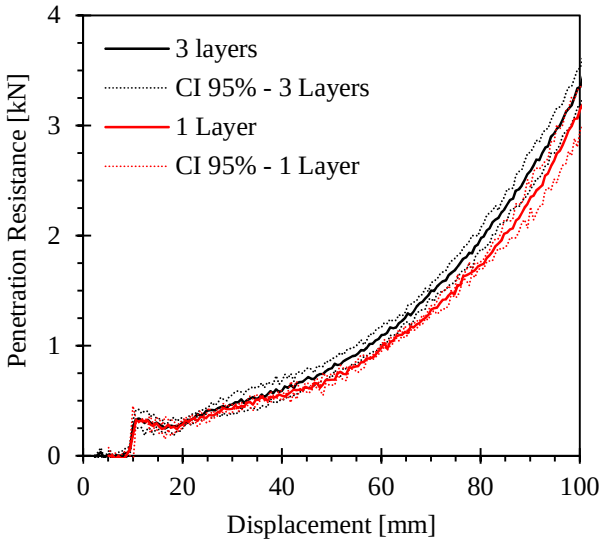

Figure 2-8. The effect of number of consolidation layers on the penetration resistance; consolidation stress: 66.7 kPa

A major objective of this chapter is to determine the relationship between penetration resistance and consolidation stress. Their relationship is illustrated in Figure 2-9, which presents the penetration resistance at 100 mm of the wedge displacement for all the applied levels of consolidation stress. The circles indicate the average of the measurement, and the 95% confidence interval for each consolidation level is displayed using vertical error bars. The variations in the measured penetration resistance can be explained by the manual operation of the consolidation phase.

As expected, with increasing consolidation stress, the penetration resistance increases as well. However, the rate of increasing the penetration resistance decreases when the consolidation stress increases. For instance, applying the first level of consolidation (13.3 kPa) increases the penetration resistance by 67% compared to the loose condition. At the other end of the diagram, increasing the applied consolidation stress by 100% (266.7 kPa), resulted in only a 22% increase in the penetration resistance.

To quantify this non-linear behavior, a quadratic regression (dashed line in Figure 2-9) with $R^2 = 0.9976$ is fitted on the data. R^2, the coefficient of determination, is commonly interpreted as

the proportion of total variance explained by the independent variable [49]. When $R^2 = 1$, all the variance is explained by the regression model. A linear regression can only fit the data with $R^2 = 0.9038$. Therefore, the quadratic regression model with a R^2 of 0.9976 demonstrates the accuracy of the fitted non-linear model.

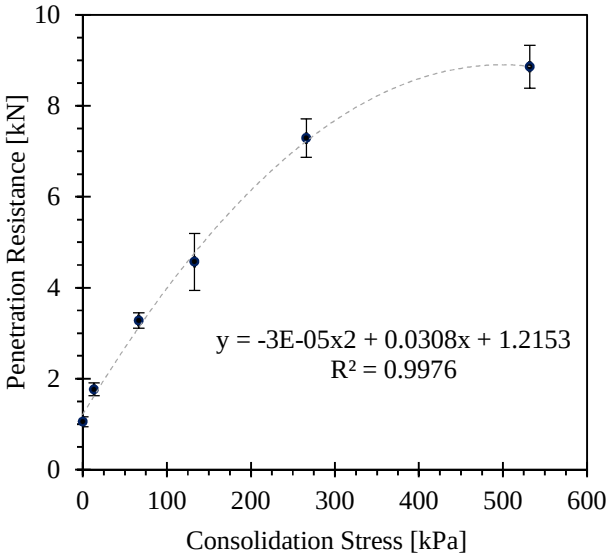

Figure 2-9. The penetration resistance at 100 mm wedge displacement for each compaction level (as stated in Table 2-2); included is a non-linear regression line (dashed) equation and its R^2 value

Figure 2-10 displays another non-linear behavior; a sudden increase in the penetration resistance at initial depths of consolidated material is observed. After this, the measured penetration resistance decreases again. With an increasing consolidation stress, this peak increases in magnitude and repetition over depth, which can be explained due to the shear failure mechanism of the bulk material. Schulze [19] explained that if a consolidated specimen is sheared under normal stress it will start to flow (fail) when a sufficiently large shear force is applied. For instance, comparing the initial peak for different levels of consolidation indicates that a higher state of compaction requires a higher (shear) force to initiate particle flow.

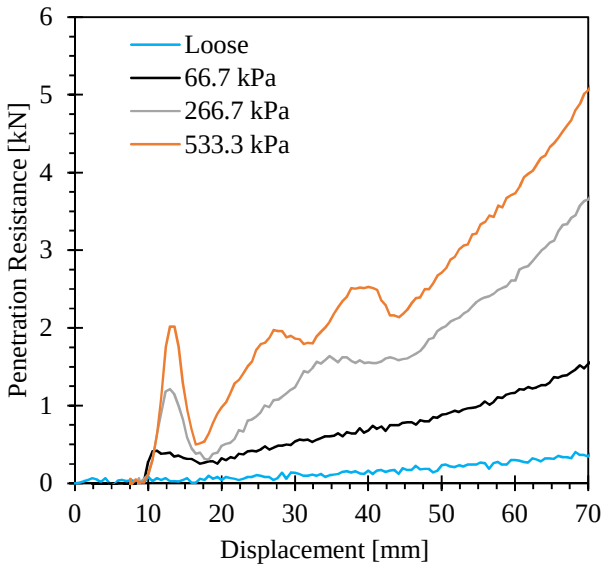

Figure 2-10. Effect of consolidation stress on the failure pattern

One of the major bulk material factors affecting penetration resistance is bulk density [51]. A higher relative bulk density often results in a higher penetration resistance. In what follows, first, the relationship between bulk density and consolidation stress is described; next, the relationship between penetration resistance and bulk density is illustrated.

Figure 2-11 displays the relationship between the applied consolidation stress and the measured bulk density. The approach used to measure the bulk density (Figure 2-7), might have introduced some level of error into the result. For instance, the average bulk density of the sample in the loose condition is higher than that of the next consolidation level (13.3 kPa), which is not as expected. In addition, the confidence interval of the average bulk density in the loose condition is larger, than that of other consolidation levels. This is probably caused by leveling out the bulk surface manually; it is difficult to create a repeatable and perfectly flat surface in this way.

A clear trend is that the higher the consolidation stress, the higher the resulting bulk density. For example, the average bulk density in the loose condition is 2109 kg/m^3, and this increasing to 2275 kg/m^3 at the highest consolidation stress (533.3 kPa). This relation was expected, since applying consolidating stress reduces the voids in the sample, and thus, makes it denser. To quantify the relationship between the bulk density and the consolidation stress, a non-linear regression model is fitted, with a $R^2 = 0.9614$.

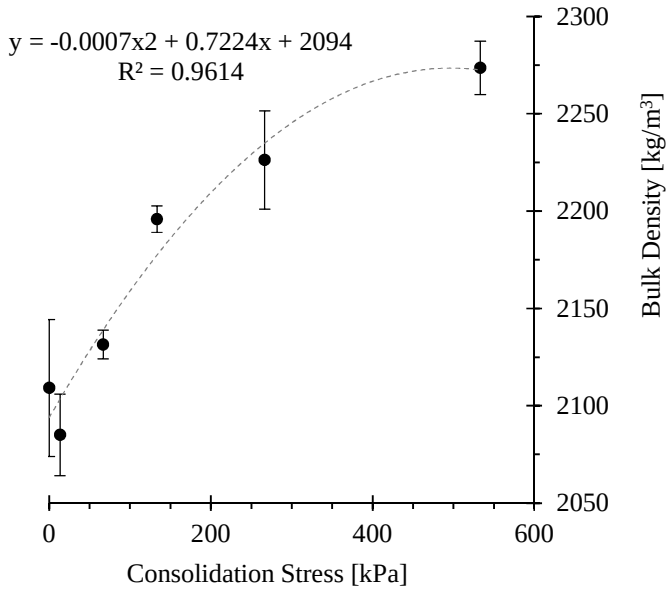

Figure 2-11. Average bulk density at different levels of consolidation; Included is a non-linear regression line (dashed) equation and its R^2 value

The bulk density result can be used to link the test results to the iron ore condition in the ship's holds during the unloading. For example, by measuring the relative bulk density of the cargo, the required energy for the initial penetration of the grab's knives can be estimated. This value is useful for finding a design that requires the least amount of energy, allowing the grab a greater initial penetration.

By integrating the resulting force (in *N*) over the depth (in *m*), the penetration resistance in Joules is obtained. Figure 2-12 displays the relationship between the penetration resistance at 100 mm wedge displacement and bulk density. The circles indicate the average of the measurement done at different levels of consolidation stress. The 95% confidence of interval of the penetration resistance and bulk density are displayed using vertical and horizontal error bars respectively.

As was expected, a higher energy is required for cutting a denser sample. However, this is with exception of the test results in the loose condition, in which the recorded bulk density is higher than the next level of consolidation stress. The result can be fitted using a linear regression model with a $R^2 = 0.9211$, suggesting a linear relationship between the penetration resistance and bulk density. However, since there are overlaps between the 95% confidence intervals of the bulk density data, caution in interpreting the relationship is advised.

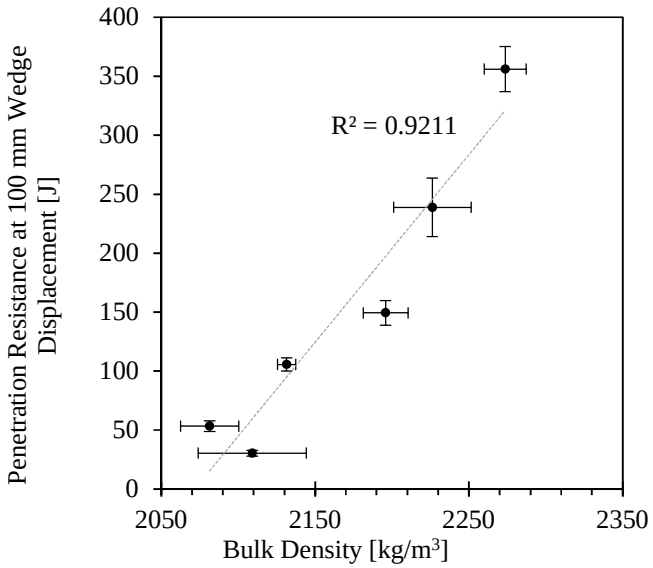

Figure 2-12. Relationship between bulk density and penetration resistance; included is a linear regression line (dashed) equation and its R^2 value

2.3. Conclusion

The test method developed in this chapter has been successfully used to investigate the effect of consolidation stress on the penetration resistance. A wedge-shaped tool was penetrated into a moist sample of iron ore fine that replicates the interaction between a grab's knives and bulk material.

- An increasing non-linear relationship between the pre-consolidation and the penetration resistance was found. Therefore, there is a strong link between the stress-history dependency of cohesive iron ore and the grabbing process.
- Regarding the experimental procedure, a one-layer strategy was adequate for creating a consolidated sample of iron ore fine. The results are repeatable, with only one exception, the results of bulk density in the loose condition.

In the next chapter, the created test method in combination with other test methods will be used to characterize bulk properties of iron ore fines that are likely to be sensitive to consolidation, such as the sinter feed type of iron ore. Next chapter will also focus on moisture content as a variable, which is known to affect the penetration resistance and compressibility of fine granular materials. Including the moisture content, allows for investigating the interdependency of bulk properties in a quantitative way.

3

Variability and interdependency of bulk properties of cohesive iron ore*

Bulk properties of iron ore such as bulk density and compressibility depend on various factors, such as particle properties [8] and moisture content [52]. Therefore, in addition to identifying properties of an iron ore product, variability of the product needs to be also considered in the design and operation of handling equipment. An ideal unit of bulk transport or storage equipment is able to handle cohesive iron ore with consistent productivity. In practice, however, uncontrollable bulk property variations affect the productivity. Therefore, this chapter quantifies variability and interdependency of bulk property of a range of cohesive iron ore products that originate from Brazil.

Grab relevant bulk properties of iron ore products are divided into two groups. Possible influencing bulk properties on the grabbing are identified in Section 3.1. Also, this section presents a list of bulk properties that are dependent to the influencing ones. Three different laboratory test

---

* This chapter corresponds to the reference: M.J. Mohajeri, M.J. van den Bos, C. van Rhee, D.L. Schott, “Bulk properties variability and interdependency determination for cohesive iron ore”. Powder Technology, Volume 367, 2020, 539-557. DOI: 10.1016/j.powtec.2020.04.018.

methods relevant to the grabbing process are employed, which are introduced in Section 3.2. Section 3.3 describes the experimental design diagram, including selected levels for influencing bulk properties and experimental plan. Using a multi-variate experimental plan, three influencing characteristics of iron ore – type, moisture content and consolidation state – are included. Experimental results are presented in Section 3.4. Furthermore, correlations between influencing and dependent bulk properties are analyzed in Section 3.5. A stress-history dependent behavior is captured in both the shear and penetration tests, with the results being highly dependent on the pre-consolidation stress. Section 3.6 presents the conclusion on determined variability and interdependency for the iron ore samples, as well as further recommendations.

3.1. Influencing and Dependent Bulk Properties of Iron Ore Products

The uncontrollable variations of independent variables can be responsible for product performance inconsistency [53]. Thus, it is important to determine the optimal settings of controllable factors in order to minimize the effects of uncontrollable variations on the process. This is the fundamental strategy of robust design [31]. A number of examples on minimizing the effects of uncontrollable variations on the process can be found in [54–58]. However, in practice the distribution of uncontrollable variables and their link to the process is often unknown. As a practical solution, one can assume a range of possible variations of the uncontrollable variables to use in the design optimization process [55]. However, assuming an unrealistic distribution may end to biased optimization outcome with inadequate performance [57].

Figure 3-1 illustrates how the variability of iron ore properties plays a role in the handling process. The process input is a specific type of equipment (i.e. grab). A rope grab that is lowered on an iron ore cargo is displayed in Figure 3-2.

In the flowchart, key performance indicators (KPIs) of equipment assess product performance, such as grab's payload and energy consumption. In the handling process, bulk materials are stored and transported; for instance once ships reach the destination, using grabs cargoes are excavated to be transported to quay side. The first group of input variables is design and operation parameters, which can be controlled, such as bucket dimensions and operating speed. The second group, bulk properties variability, is the uncontrollable variation of bulk properties, which are difficult or nearly impossible to be controlled by designers or operators. For example, the inherent properties related to the material origin, effects of mining aspects condition (e.g. water table height), the mine excavation process and the preprocessing before sending to

destinations (e.g. grinding). The bulk properties variability are divided into two groups in this chapter, influencing and dependent bulk properties. In general, influencing bulk properties are responsible for the variations of dependent bulk properties.

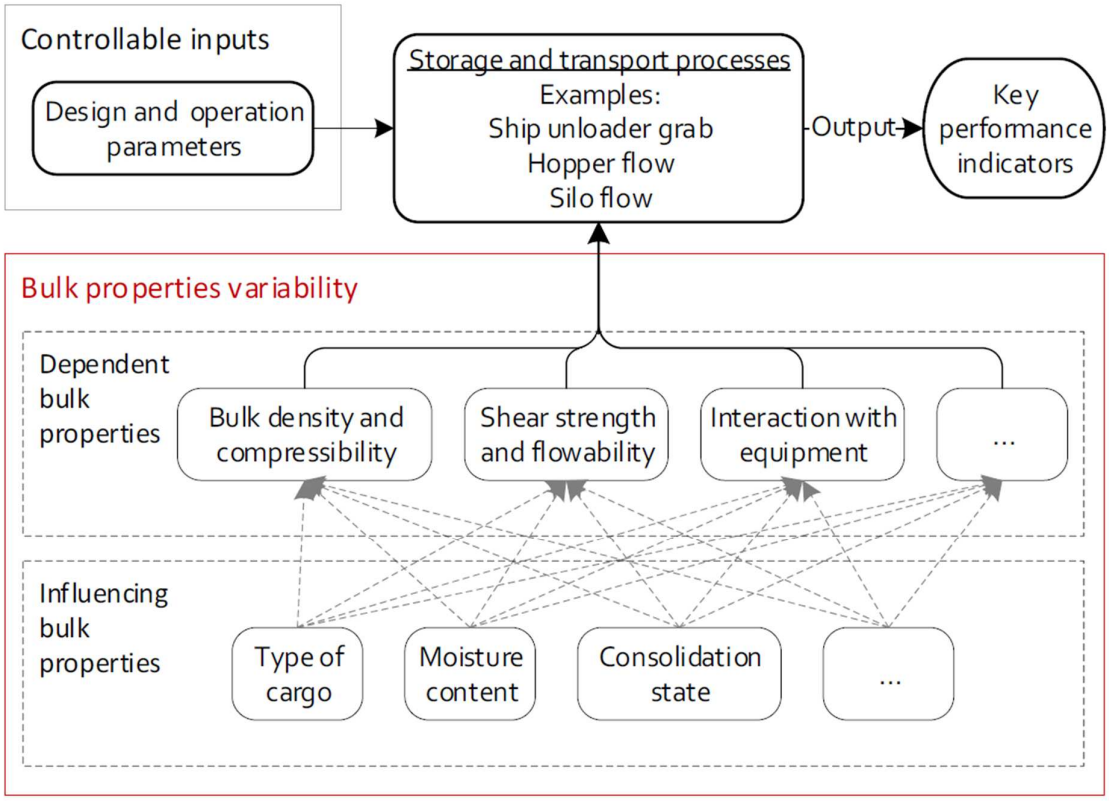

Figure 3-1. Controllable and uncontrollable inputs in bulk storage and transport processes, including ship unloader grabs

In [22], stress-strain responses and bulk density of two Swedish iron ore sample are quantified in uni-axial consolidation tests under various combinations of moisture content. Additionally, the Jenike shear test is applied to quantify the shear strength of the bulk materials at dry and moist conditions, however, without creating a pre-consolidated situation. In [48], the influence of moisture content variation and pre-consolidation on flowability of four different Australian cohesive iron ore samples were investigated. Free surface flow of the samples (e.g. angle of repose) as well as interaction of iron ore fines with handling equipment were out of scope of the two mentioned studies, and thus they need to be considered when the grabbing process is being investigated.

In [38], effects of type of iron ore and level of moisture content on the bulk density and angle of repose of two samples of iron ore fine are investigated. Also, the bulk density measurements are performed under the effect of consolidation and vibration at various levels of

moisture content. The results show that bulk density is sensitive to type of iron ore, level of moisture content and consolidation. However, the relationship between consolidation states and shear strength, or consolidation states and penetration resistance of iron ore fines are not researched.

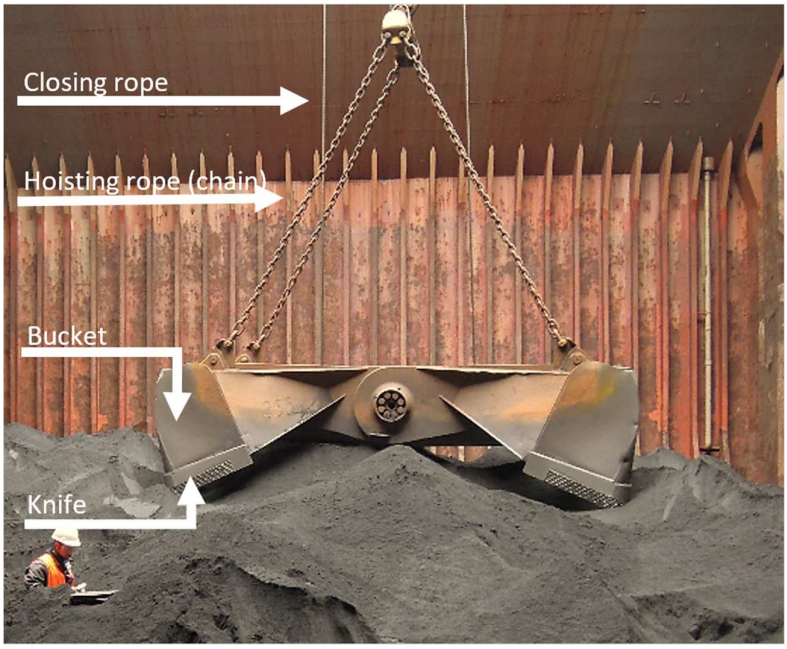

Figure 3-2. A rope grab lowered on iron ore cargo

As discussed above, even though a number of studies are conducted that can help to incorporate the variability of bulk properties in handling process, some links remained unquantified. First, the effect of level of pre-consolidation stress on the penetration resistance of iron ore is unknown. Identifying this relationship is essential in some bulk handling applications, such as ship unloading and excavation in stack yards. Second, by quantifying the interdependency of flowability, pre-consolidation and moisture content for cohesive iron ore, the uncertainty of bulk properties variability can be introduced into the design procedure of bulk handling equipment. Furthermore, relationships between influencing and dependent bulk properties are not fully established in the literature. For instance, the effect of pre-consolidation stress on the penetration resistance might be dependent to type of iron ore.

Based on the literature review, the influential bulk properties are categorized into three different groups as follows: I) type of iron ore, II) moisture content, and III) consolidation state. The first group, type of iron ore, covers those characteristics of samples that can be assumed constant during storage and excavation, such as chemical composition, particle size distribution, clay type and content. Also, variations of particle size distribution due to possible segregation

during transport of iron ore cargoes is considered to be negligible in the current investigation. More than five dependent bulk properties are also measured in this chapter that can be categorized under three main groups, as follows: I) bulk density and compressibility, II) shear strength and flowability, and III) interaction with equipment.

3.1.1. Influencing bulk properties

Three different influencing bulk properties are included in this chapter, which are also suggested in Figure 3-1. The first property is the type of iron ore cargo, which will be referred with *I* in this chapter. In general, iron ore products are produced in four different particle size ranges: lump, pellet, sinter feed and pellet feed. Lump ore products have particle size between 6.3 and 40 mm [18]. Particle size range of pellets is between 8 and 14 mm; because of size and characteristics of particles in iron ore pellets, the variations of moisture content or consolidation state does not play a role on the dependent bulk properties [8]. Therefore, pellet as well as lump size iron ore products are out of scope of the current investigation, as discussed in the previous chapter. Figure 3-3 displays three different iron ore samples, pellets, sinter feed and pellet feed categories, indicating the difference in their particle size distribution. Sinter feed and pellet feed products, which are included in this study, have a particle size usually less than 11 mm [19,20]. In [20], a Scanning Electron Microscope (SEM) was used to take high magnification photos of the sinter feed type products. All the tested samples had porous particles of irregular shapes and a range of particle sizes. Pellet feed type iron ores tend to be more uniformly sized, compared with sinter feed type products.

Figure 3-3. Various size range in iron ore products; pellets, sinter feed and pellet feed [21]

Second influencing bulk property is the level of moisture content. Iron ore cargoes are found in a wide range, from relatively dry condition to saturated condition [4]. The dry-based moisture content, denoted by MC in this dissertation, is the portion of a representative sample consisting of water, or other liquid express as a percentage of the total dry mass of that sample [32].

The last important influencing bulk property that is included in this investigation is the consolidating state. In general, the consolidation occurs due to the consolidating stress, σ, acting

on bulk solids [50]. Also, the kinetic energy coming from releasing bulk solids from height leads to a more consolidated condition [20].

3.1.2. Dependent bulk properties

The dependent bulk properties are basically sensitive to the level of influencing ones. First dependent property, bulk density (ρ_b) as shown in Eq. (3.1), follows from the solid density (ρ_s), and the density of the fluid within the voids (ρ_f) [50].

$$\rho_b = (1 - \varepsilon)\, \rho_s + S\, \varepsilon\, \rho_f \tag{3.1}$$

where S and ε are the degree of saturation (with fluid) and porosity respectively. The porosity indicates the ratio of void volume to total volume of bulk solids, and decreases by applying the consolidating effort. The fluid density, ρ_f, is assumed to be constant in this investigation, and equal to the density of water.

On an element of iron ore normal stresses as well as shear stresses may act. It can be expected that if the ratio of shear stress and normal stress exceeds a certain value, the particles will start to slide over each other, which will lead to relatively large deformations. The resistance against shear force or *Shear strength* depends mainly on two factors: *frictional strength*, which is the resistance to movement between the slope material's interacting constituent particles, and *cohesion strength*, which is the bonding between the particles. The cohesion strength of the liquid bridge in an iron ore bulk is dependent on the volume of the bridge, and hence the amount of moisture present [22]. Therefore, the cohesive behavior of iron ore is created due to the capillary force mainly, contrary to rock or dust materials. According to [59], three bonding states can be identified in moist bulk solids, pendular, funicular and capillary states. The bonding strength is weak at the pendular state. By increasing quantity of liquid in bulk solids, the bonding strength of liquid bridge increases to a peak at funicular state. A fully saturation point may be reached by further increasing the moisture content, which causes the drop of capillary pressure near fully saturation [60]. Fine-grained bulk solids with moderate or poor flow behavior due to cohesive forces are called cohesive bulk solids [50]. If the influence of the cohesive forces can be neglected, a bulk solid is called non-cohesive or free-flowing.

Jenike [61] as well as Schulze [50], suggested to characterize flowability of a bulk solid by its unconfined yield strength, σ_c, as a function of the consolidation stress, σ_1. The unconfined yield strength, σ_c, is the stress causing failure under an unconfined compression. Usually, flow function, ff_c, is used to characterize the flowability numerically, as shown in Eq. (3.2).

$$ff_c = \frac{\sigma_1}{\sigma_c} \quad (3.2)$$

The larger ff_c is the better a bulk solid flows. The flow behavior is categorized based on its flow function in Table 3-1.

Table 3-1. Flow behavior based on flow function [50]

Range	$ff_c < 1$	$1 < ff_c < 2$	$2 < ff_c < 4$	$4 < ff_c < 10$	$10 > ff_c$
Flow behavior	NF: not flowing	VC: very cohesive	C: cohesive	EF: easy-flowing	FF: free-flowing

Furthermore, for a design procedure the quantities characterizing the interaction between bulk solids and equipment have to be known. Essentially, this can be quantified by measuring the shear strength between the geometry surface of equipment and bulk solids, generally referred in literature as wall friction. In addition to frictional forces, adhesive forces may contribute to the shear strength between wall material and bulk solid specimen. The wall friction, is important for the design of grab, silo, transfer chute, hopper, and other equipment that contact with bulk solids during their transport [50].

3.1.3. Iron ore samples

The selected samples are different in various aspects, such as the size and shape of particles and their origin. First two samples belong to the Carajas mines that are one of the largest iron ore resources in the globe [62]. I_1 and I_2 are pellet and sinter feed types of iron ore respectively. Third sample, I_3, is a pellet feed type that is extracted from Minas-Rio mine that is located in the southern part of Brazil. All the three iron ore samples are collected at a destination port located in the Netherlands, where the iron ore cargoes are unloaded from ocean going bulk carriers.

The particle size distribution of the samples is determined according to [63], and the results are displayed in Figure 3-4. Smallest and largest sieve sizes of respectively 0.053 and 1.4 mm are used. In first sample, I_1, 50% of weight consists of particles larger than 0.053 mm, indicating the median size of particles, d_{50} as defined in [64]. Next sample, I_2, has a median value of 0.880 mm, that is more than 16 times larger than I_1. The d_{50} value of I_3 could not be determined using the sieves. This indicates particles size of I_3 is considerably smaller than the Carajas samples. Therefore, a large variation of particles size is covered in experiments.

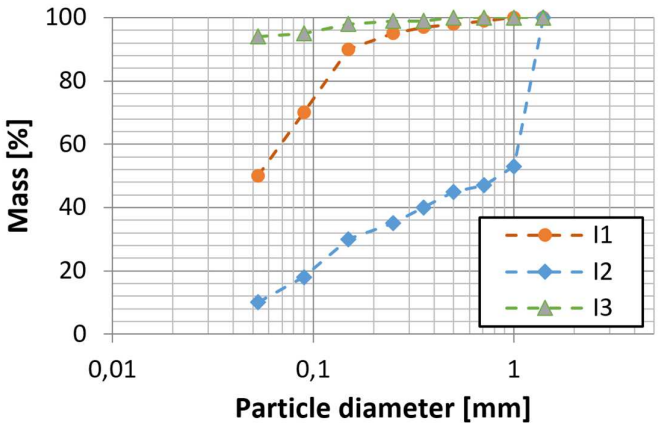

Figure 3-4. Particle size distribution of the iron ore samples

The as received moisture content (dry-based), $MC_{as,rec}$, of the samples is determined according to the method described in [65], in which the water content is dried using a ventilated oven. Table 3-2 displays the as received moisture content of the iron ore samples.

Table 3-2. As received moisture content of the iron ore samples, based on three measurements per type

I: Type of iron ore	I_1	I_2	I_3
$MC_{as,rec}$	13.3	8.7	6.8

3.2. Test Apparatus

3.2.1. Ring shear test

Shear cells are used commonly to quantify the flowability of granular materials [66]. Jenike [67] established a methodology to apply shear test results in the design procedure of hoppers and silos. Shear cells are able to measure the three dependent properties of iron ore under investigation here and is therefore selected.

The Schulze ring shear tester RST-01.01 type M, is used that its main function and dimensions are described in [68]. In the test procedure, first the shear cell is filled with a bulk solid specimen. Next the normal stress, σ, is applied on the bulk solid specimen through the top lid. Both normal stress and the vertical displacement of the lid are recorded over time. Thus, the bulk density of the specimen are captured for various levels of normal stresses. Also, two horizontal tie rods prevent the top lid from rotating; forces in the tie rods are denoted by F_1 and F_2. So, during the rotation of the bottom ring, a shear deformation in the bulk solid specimen is created. A schematic cross-sectional view of this process is shown in Figure 3-5 with. Figure 3-5a shows a cross section schematic view of ring shear test, before starting the rotation. In the next one, the shearing is commenced once the bottom ring starts to rotate with an angular velocity of

ω, and X_m denotes the shear deformation. Figure 3-5c shows the shear deformation when shear failure occurred. The shear stress is directly proportional to F_1 and F_2; with the equations found in [68], the forces F_1 and F_2 are converted to the shear stress as displayed in Eq. (3.3).

$$\tau = \frac{r_s\,(F_1 + F_2)}{r_m\,A_d} \tag{3.3}$$

where r_s and r_m are the moment arms of the tie rod forces and the lid force ($\tau\,A_d$) respectively. The stress in the horizontal plane at steady-state flow is measured and referred as the shear stress, τ. If the shear stress does not reach a constant, steady-state flow is assumed after 30 mm of shear displacement with variations of less than 0.05% per mm of shear displacement [68].

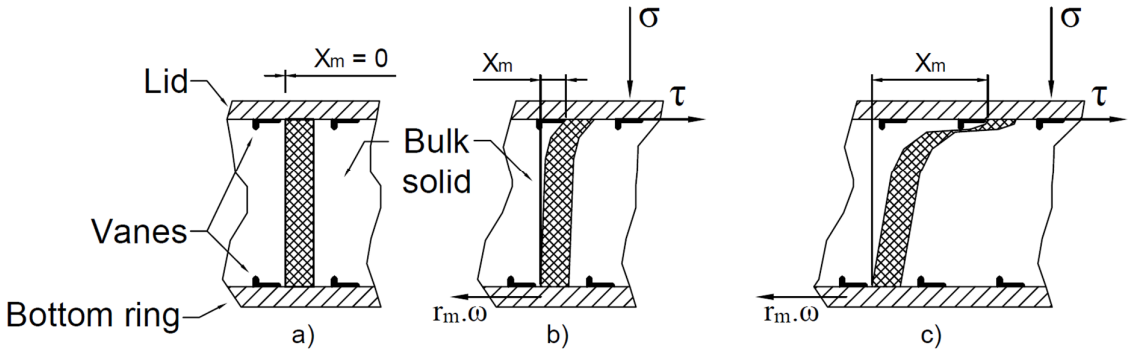

Figure 3-5. The shearing mechanism in the Ring Shear Test - based on [50]**; a) before shearing, b) during shearing, c) shear failure**

With a proper test procedure and correct design of the ring shear tester, test results close to those achieved with the Jenike shear tester can be obtained, but the reproducibility is clearly better [50]. Table 3-3 provides an overview of the measured dependent bulk properties in the ring shear test as well as wall friction test. With small adjustments in the shear cell, the wall friction test can also be conducted using the same test device [50]. The measurement method for the wall friction using the ring shear test is similar to the ring shear test procedure. The difference is that in the wall friction test, the base cell is replaced by a wall material. In Figure 3-6, half of the cross section views of both ring shear cell and wall friction cell are shown. The cell depth is 12 mm in the wall friction test to ensure the shear failure occurs between particles and the wall material. A blasted hot-rolled stainless steel plate is used in our experiment as the wall material.

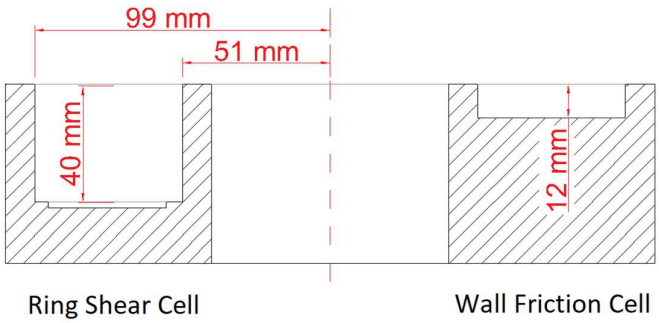

Figure 3-6. Cross-sectional view of the ring shear cell (left side) and the wall friction cell (right side)

Table 3-3. List of measured dependent bulk properties in ring shear and wall friction tests

Test Setup	Raw measurement	Dependent bulk properties
Ring Shear Test	ΔL Lid displacement	ρ_b: Bulk density
	τ Shear Stress	Mohr-Circle, including: φ_{lin}: Linear internal friction τ_c: Cohesion strength σ_c: Unconfined yield strength ff_c: Flowability
Wall Friction Test (using shear cell)	τ_w Wall shear stress	ϕ_x: Wall friction angle τ_a: Adhesion strength

3.2.2. A test to determine angle of repose

When a bulk solid material is experiencing a free surface flow, its surface forms an angle. This angle, which is referred as the angle of repose, α_M, usually measures the maximum slope angle of bulk solid material between a horizontal plane and the free surface angle [40]. The angle of repose represents the shear strength of bulk solid materials in their loosest state [69]. According to the Mohr-Coulomb equation, the shear strength of bulk solids materials in a failure plane, τ_s is often approximated by Eq. (3.4) [70]:

$$\tau_s = \tau_c + \sigma_\alpha \tan(\varphi) \tag{3.4}$$

where $tan(\varphi)$ indicates the friction coefficient of the bulk solid. σ_α is the normal stress in the failure plane, and τ_c denotes the cohesion of the bulk material: In other words, τ_c is the shear strength of the bulk material if $\sigma_\alpha = 0$. By increasing σ_α, due to increasing the height of bulk solids material for instance, it is expected that the contribution of τ_c in the shear strength decreases. When τ_c is

negligible, α_M represents φ mainly. Failure will occur once shear stress in an arbitrary cutting plane exceeds the shear strength of the bulk material. The remaining bulk solids in the box forms an angle of repose, α_M. This parameter represents the shear stress of bulk material under the force of gravity. Therefore, angle of repose, α_M, can be used to investigate the effect of type and moisture content of iron ore on its free surface flow.

α_M is an important characteristic in the handling processes; according to [71] angle of repose results are useful to categorize flow properties. It is used commonly to design silos and hoppers. For example, in [72] the correlation between the angle of repose and flow pattern in silos is discussed. Additionally, [73] formulated the correlation between the angle of repose and discharge mass flow rate from hoppers. In an application oriented study, [74], silo discharge of wood chips material is improved by using angle of repose tests.

Also, in the excavation application, the volume of the collected bulk material is mainly determined by its angle of repose. During closing of buckets, the excess material flows out the buckets from its open sides, and so, with a higher angle of repose this results in a higher volume of the collected bulk material. For instance, Figure 3-7 shows two different types of iron ore in the grab's buckets. Figure 3-7a shows iron ore pellets that is a free flowing material, while Figure 3-7b shows a fine and moist iron ore cargo that has a considerably higher angle of repose.

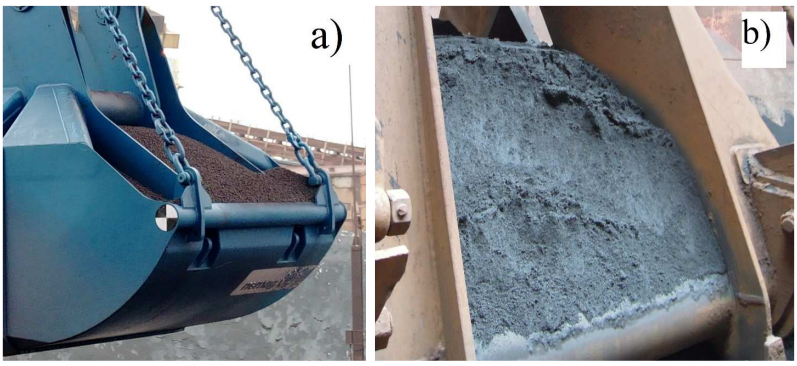

Figure 3-7. Forming an angle of repose inside grab buckets; a) A free-flowing cargo with a low angle of repose, b) cohesive iron ore with a high angle of repose

A ledge method set up [9] for measuring the angle of repose is used. The test setup and its procedure, is also referred under other names in literature, such as shear box [75] and rectangular container test [14]. Figure 3-8a displays the test box dimensions. The container is 250 mm high, 215 mm long and 80 mm wide. In the ledge angle of repose test the bulk material is poured from a small height, around 10 cm, into the test box slowly to minimize the effect of consolidation. Next, the door opens to allow the sample to flow. Once a static angle of repose is created, photos

are taken from a horizontal view. α_M is determined from the images by taking the coordinates of ten equally spaced points on the slope of the material, as shown in Figure 3-8b. Then, the linear regression technique is used to fit a straight line to the data points and the angle of the line with the horizontal represents the angle of repose.

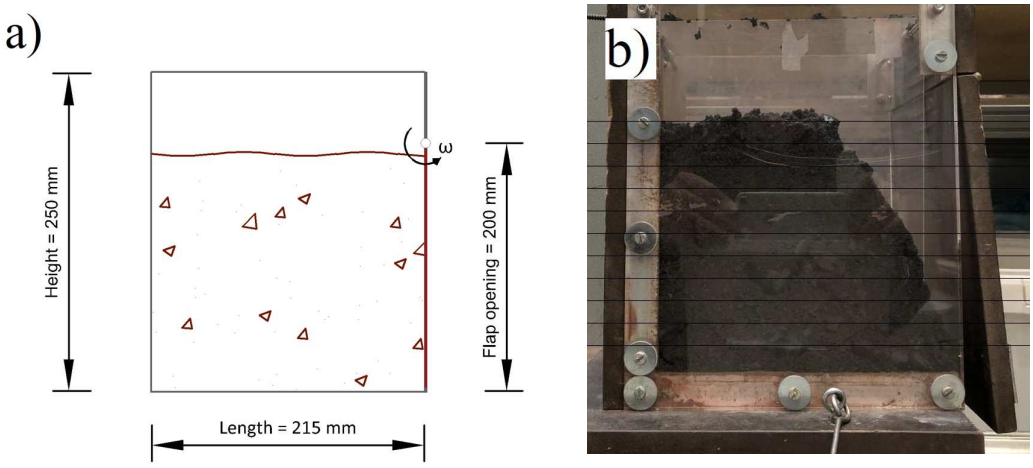

Figure 3-8. The test box to determine angle of repose; a) the initial condition and dimensions, b) formed angle of repose

3.2.3. Consolidation-penetration test

When the surface of bulk solid material is touched by an excavating equipment (i.e. grab), its knives penetrate the material. The resistance of the bulk material to penetration influences the initial penetration depth and the cutting trajectory of the knives. Therefore, characterizing the penetration resistance of a bulk solid material in interaction with the knives of a grab is essential for design of excavating equipment such as grabs.

As shown in Figure 3-9, a wedge-shaped penetration tool is used in our measurements; since its cross section resembles the penetration of grabs' knives in bulk solid materials. The tool dimensions are similar to the tool used in [8], with a 200 mm length. The container properties are displayed in Figure 3-10. The container volume is 15 litres.

Four dependent bulk properties are quantified in the consolidation-penetration test, as displayed in Table 3-4. According to [21], by recording the reaction force on the wedge-shaped tool during the penetration phase, the penetration resistance force is quantified. By integrating penetration resistance force over penetration depth, the penetration resistance is determined in Joules [9]. $W_{50,ratio}$ is the ratio between W_{50} measured at a specific level of pre-consolidation to W_{50} when no pre-consolidation is applied. The bulk density of the sample before and after the

consolidation phase is measured, which is used to discuss bulk compressibility under the effect of pre-consolidation.

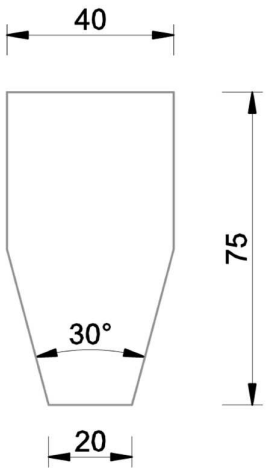

Figure 3-9. The penetration tool cross-sectional view

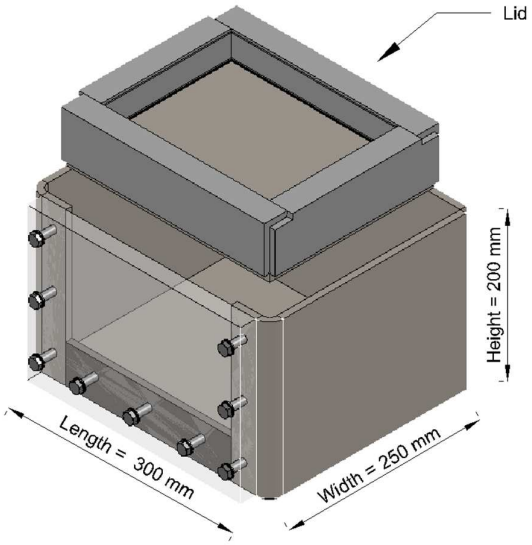

Figure 3-10. Dimensions of the container used in consolidation-penetration test

Table 3-4. List of measured dependent bulk properties

Test Setup	Raw measurement	Dependent bulk properties
Consolidation-Penetration Test	Δ_W Wedge displacement	ρ_b: Bulk density C_b: Compressibility
	F_W Reaction force on wedge	F_w-Δ_W: Penetration resistance as a function of penetration depth $W_{d,\sigma}$: Energy required to penetrate to depth d at the pre-consolidation of σ

Both the flowability and shear strength of a bulk solid material play a role in the test. As schematically illustrated in Figure 3-11, a shearing zone, as well as a compacted zone, are created during penetration of a wedge-shaped tool in bulk solid materials.

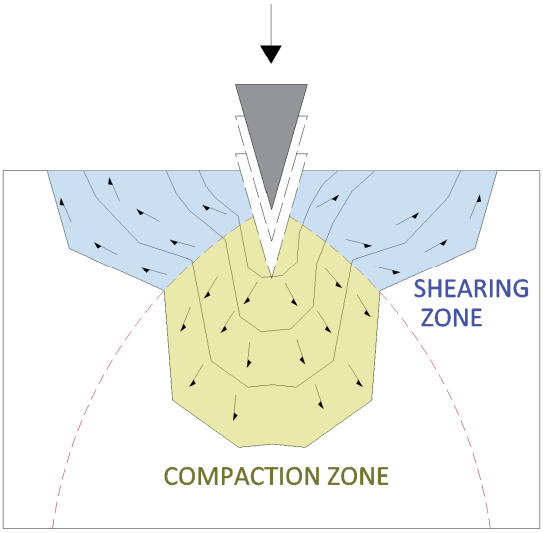

Figure 3-11. Zones during the penetration test – based on [76]

3.3. Experimental Design Diagram

A simple and popular method to design the experimental plan is one-factor-at-a-time method (OFAT). In this method, the variability of the dependent bulk properties can be determined by changing the level of one of influential bulk properties, while the others are kept constant [77]. However, since the influence of more than one influential bulk property are being investigated, using statistically designed experiments that several properties are varied simultaneously is more effective [53], and enables to identify interdependencies between the different properties. Within

experimental designs three types of variables are distinguished. First of all the variables that are kept constant throughout all experiments such as the dimensions and operational parameters of the tests. Second, the three independent variables that are varied and to which the system response, here bulk response, is measured. The bulk response is defined as the dependent variable.

3.3.1. Levels of influencing bulk properties

The three influencing bulk properties and their ranges are shown in Table 3-5. Each property is denoted by a letter and a number to indicate the variable name and its corresponding level respectively. According to the measurements done in [20], the variation of moisture content for a specific type of iron ore is less than ±2% in different cargoes. To gain a comprehensive insight on the influence of moisture content on the dependent bulk properties, a variation of ±4% with steps of 2% is investigated in this chapter.

On one hand, it is important to select pre-consolidation stress levels similar to stress levels that exist in the application under investigation. On the other hand, it is nearly impossible to measure the actual pre-consolidation stress acted on different layers of iron ore in an application [50]. Therefore, the range of pre-consolidation stress in the experimental design diagram is selected based on the available information in literature. The maximum vertical pre-consolidation stress in a ship's hold containing iron ore is estimated to reach 400 to 500 kPa at the bottom of cargo holds [78]. Additionally, the bulk material in the bottom of the cargo hold are usually trimmed using bulldozers or by the grab itself. This means that the efficiency of the grab closing process, in terms of its payload, does not play a significant role in the trimming stage, compared to prior unloading stages. Therefore, to choose a range relevant to the efficiency of the grab closing process, the highest stress level for the consolidation-penetration test is set to 300 kPa. The other levels of σ_{pre} are 0, 8, 20 and 65 kPa.

Table 3-5. Selected range of the influential bulk properties in experimental design diagram

Level	I: Type of iron ore	MC: Level of moisture content [%]	σ_{pre}: Pre-consolidation stress [kPa]
1	I_1- Carajas pellet feed	$MC_{as,rec-4\%}$	0
2	I_2- Carajas sinter feed	$MC_{as,rec-2\%}$	8
3	I_3- Minas-Rio pellet feed	$MC_{as,rec}$	20
4	-	$MC_{as,rec+2\%}$	65
5	-	$MC_{as,rec+4\%}$	300

The maximum consolidation stress is expected to be up to 20-30 kPa inside grab's buckets during its filling. Table 3-6 provides examples of the estimated range of static or quasi-static

consolidation stress that are expected to occur in various iron ore storage and transport applications. Additionally, to capture the stress-dependency of bulk materials in a higher resolution compared to the consolidation-penetration test, choosing a lower range of σ_{pre} is preferred. According to [50], the estimation of the consolidation stress for a comparative characterization of bulk materials must be adjusted to the capabilities of the particular shear tester. The ring shear tester used in the current investigation is able to apply up to σ_{pre} = 20 kPa. Therefore, as shown in Table 3-7, 2, 8 and 20 kPa are the three selected levels of vertical pre-consolidation stress for the shear test.

Table 3-6. Estimated range of static or quasi-static consolidation stress for handling iron ore in different applications

Application	consolidation stress range [kPa]
Ship's hold	0-450
Ship unloader grab	0-30
Conveyors	0-2
Silo and hoppers	Stress depends on silo and hopper dimensions

Table 3-7. Selected range for the pre-consolidation stress

σ_{pre}	Consolidation-penetration test	Ring shear test
$\sigma_{pre,0}$	0	2
$\sigma_{pre,8}$	8	8
$\sigma_{pre,20}$	20	20
$\sigma_{pre,65}$	65	-
$\sigma_{pre,300}$	300	-

3.3.2. Experimental plan

For each of the test setups a separate experimental plan is created as described hereafter.

A. Ring Shear Test

Table 3-8 displays a full factorial designed experiment that is used in the ring shear tests. This experimental plan includes all probable combinations of levels for all variables, which results in 60 different combinations. Since the reproducibility of results obtained by ring shear testers is adequate [50], each experiment is repeated once. $\sigma_{pre,20}$ is also chosen for the wall friction test.

Table 3-8. Experimental plan of the ring shear tests

List of independent variables	Level 1	Level 2	Level 3	Level 4	Level 5
I [-]	I_1	I_2	I_3	-	-
MC [%]	as,rec -4%	as,rec -2%	as,rec	as,rec +2%	as,rec +4%
σ_{pre} [kPa]	$\sigma_{pre,2}$	$\sigma_{pre,8}$	$\sigma_{pre,20}$	-	-

B. Angle of Repose measurements

In the angle of repose measurements, as shown in Table 3-9, a full factorial design is used to measure the effect of the two independent variables and their interrelation: type of iron ore and level of moisture content. This results in 15 experiments. Each experiment is repeated at least 5 times to ensure a good repeatability.

Table 3-9. Experimental plan of the angle of repose measurements

List of independent variables	Level 1	Level 2	Level 3	Level 4	Level 5
I [-]	I_1	I_2	I_3	-	-
MC [%]	as,rec -4%	as,rec -2%	as,rec	as,rec +2%	as,rec +4%

C. Consolidation-Penetration Test

In the excavation applications, the interaction between all the independent variables (I, MC and σ_{pre}) are not necessarily present. For example, in a cargo hold the consolidation pressure varies in the direction of the cargo depth, but the moisture content usually remains constant in this direction [20], except for the trimming stage. The moisture content can vary from ship to ship for a same type of iron ore, depending on for example excavation conditions in the mine and weather conditions during loading of the ship.

Therefore, two separate full factorial experimental plans are designed for the consolidation penetration test, that are displayed in Table 3-10. In the first set of experiments (I), the effect of consolidation is incorporated for different type of iron ore in the consolidation-penetration test. This results in 15 experiments. In the second set of experiments (II), all the possible combinations between the type of iron ore and the level of moisture content are included.. This results in 15 tests as well. This totals to 30 experiments for the consolidation-penetration test. Each experiment is repeated at least 3 times.

Table 3-10. Experimental plan of the consolidation-penetration test

List of independent variables	Level 1	Level 2	Level 3	Level 4	Level 5
Experiment set I. Interaction of type of iron ore and consolidation stress					
I [-]	I_1	I_2	I_3	-	-
σ_{pre} [kPa]	$\sigma_{pre,0}$	$\sigma_{pre,8}$	$\sigma_{pre,20}$	$\sigma_{pre,65}$	$\sigma_{pre,300}$
Experiment set II. Interaction of type of iron ore and moisture content					
I [-]	I_1	I_2	I_3	-	-
MC [%]	as,rec -4%	as,rec -2%	as,rec	as,rec +2%	as,rec +4%

3.4. Experimental Results

3.4.1. Ring shear test

Figure 3-12 presents results of the ring shear tests on iron ore sample I_1 at various combinations of MC and σ_{pre}. Figure 3-12a shows the yield locus lines at σ_{pre} = 2.0 kPa, in which the measured τ are plotted over the applied σ. The yield loci are relatively similar for $MC_{as,rec-4\%}$, $MC_{as,rec-2\%}$ and $MC_{as,rec}$ with the measured τ_{pre} of respectively 1.8, 1.9 and 2.0 kPa. The measured τ_{pre} at $MC_{as,rec+2\%}$ is equal to 2.6 kPa that is around 35% to 43% larger than the measured values at lower levels of MC. A similar trend applies to the measured values of τ_{shear} at σ_{pre} = 2.0 kPa for this sample.

Figure 3-12b shows the yield loci for σ_{pre} = 8.0 kPa. The measured shear values of τ_{pre} and τ_{shear} (at 4 different levels of σ_{shear}) are the lowest at $MC_{as,rec-4\%}$ compared to the other levels of MC. Similar to the previous level of σ_{pre}, the highest shear stress values are measured at $MC_{as,rec+2\%}$ for this sample, with a τ_{pre} around 18% to 31% larger than the measured values at lower levels of MC. However, the relative difference between measured peak values of τ_{shear} at 4 different levels of σ_{shear} between $MC_{as,rec+2\%}$ and $MC_{as,rec\%}$ is limited to 5%.

Figure 3-12c shows the yield loci for σ_{pre} = 20.0 kPa. A shear stress of 20.5 kPa is measured at $MC_{as,rec}$ during the pre-shearing stage. Changing moisture content from the lowest level to highest level caused an increase of 18% in τ_{pre}. The measured values of τ_{shear} at 4 different levels of normal stress show the highest shear strength values occurs at $MC_{as,rec}$ and $MC_{as,rec+2\%}$,and the lowest at $MC_{as,rec-4\%}$. With σ_{shear} = 8.1 kPa and $MC_{as,rec}$, a shear stress of 12.4 kPa is measured, which is 39% higher than the τ_{pre} at σ_{pre} = 8 kPa. A similar comparison can be done between σ_{pre} of 8 and 2 kPa. This clearly indicates that the level of normal stress that is applied during the pre-shear stage increases the shear strength. This stress-history dependent behavior of the shear strength occurs at all levels of moisture content for this iron ore sample.

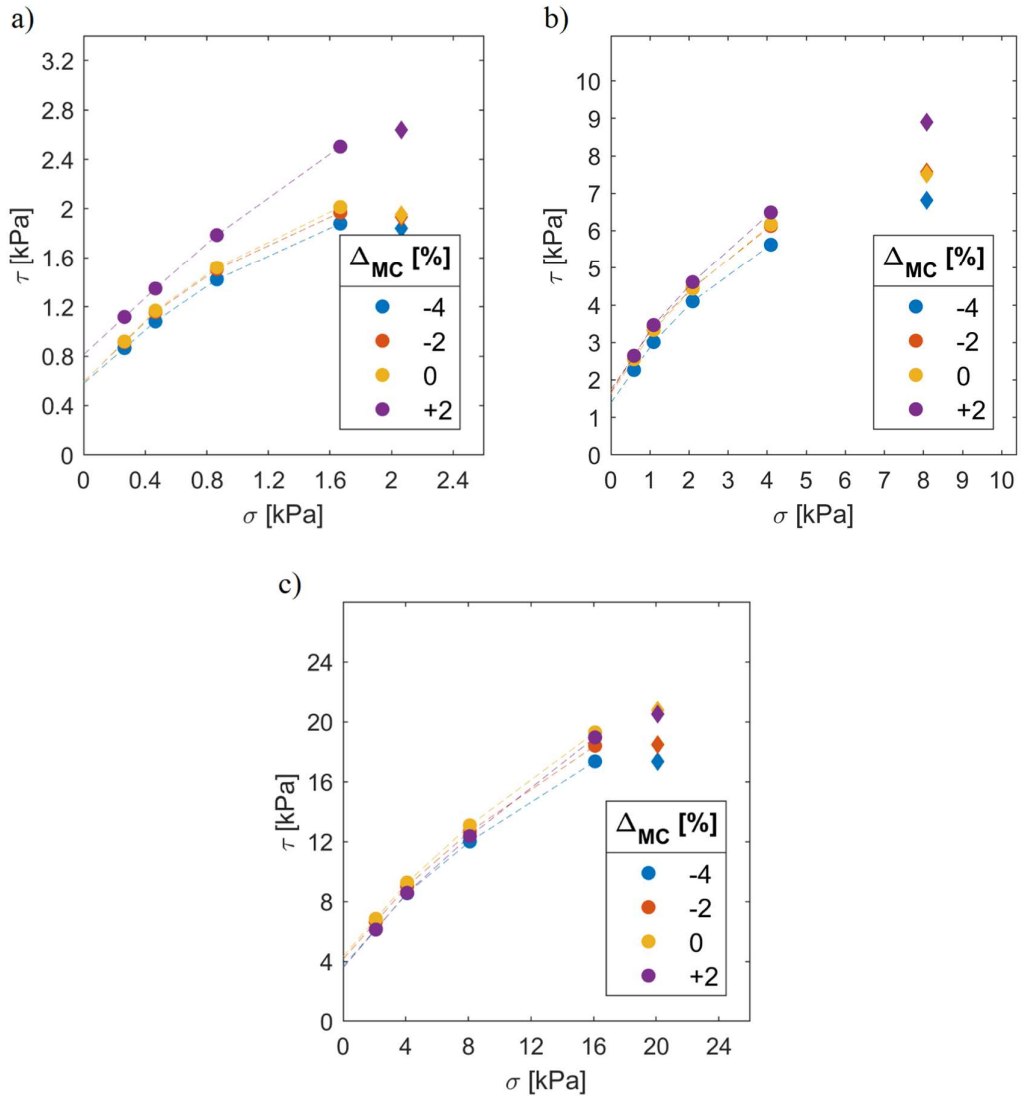

Figure 3-12. Yield locus of I_1 in various moisture content levels and pre-consolidation levels, σ_{pre} : a) 2 kPa, b) 8 kPa, c) 20 kPa

For iron ore sample I_1, the ring shear test could not be conducted for $MC_{as,rec+4\%}$. As shown in Figure 3-13, the particles start to form large agglomerates. Due to the large agglomerates it is impossible to create a flat surface in the shear cell without compressing the material, which must be avoided during preparing the test. Furthermore, according to [68], particles should be in general smaller than 6 mm in diameter to be used in this ring shear test.

Figure 3-13. Forming large agglomerates after adding 4% extra moisture content; a) $MC_{as,rec}$, b) $MC_{as,rec+4\%}$

Figure 3-14a and Figure 3-14b show the bulk density results of sample I_1 with including and excluding the weight of moisture respectively. A general trend is that by increasing the level of MC, the sample becomes more compressible. Similar trend also was observed in [48] for four Australian iron ore samples. The moisture content variation in iron ore samples is responsible of the change in the compressibility due the macro-shrink behavior of the clay content [79]. For that reason there is a positive inter-correlation between ρ_b, MC and σ_{pre}. The main outlier in this graph is the bulk density results of the sample at $MC_{as,rec+2\%}$; a considerably higher initial bulk density, $\rho_{b,0}$, is measured at this moisture level compared to the lower levels. The bulk density at $MC_{as,rec+2\%}$ is still distinct at $\sigma_{pre,20}$. This can explain the reason behind measuring higher shear stresses at $MC_{as,rec+2\%}$ in this pre-consolidation stress, compared with other levels of MC.

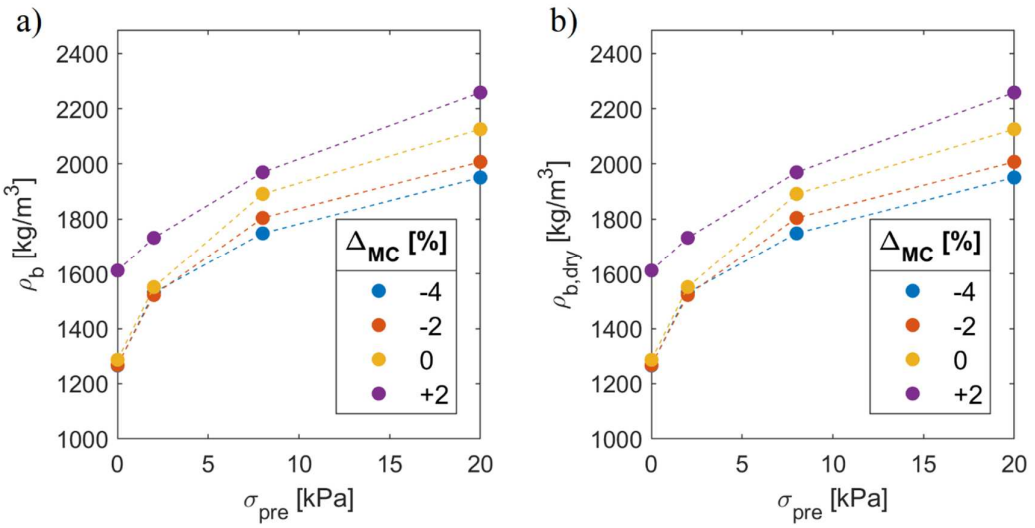

Figure 3-14. Bulk density measurements of I_1 using RST; a) bulk density, b) dry bulk density

Figure 3-15 presents results of the ring shear tests on the second iron ore sample, I_2. In Figure 3-15a, σ_{pre} = 2 kPa, a high dependency of shear stresses to the level of moisture content is

observed. At this level of σ_{pre}, higher shear stress values are measured overall at $MC_{as,rec}$, compared to other levels of MC. The lowest shear stress values are also measured at $MC_{as,rec-4\%}$, which is the driest condition of the sample in this experiment. At $MC_{as,rec+4\%}$, the highest level of moisture content, the $\tau_{shear,4}$ is 48% higher than τ_{pre}. This can be explained by Figure 3-16 that shows that the excessive water easily flows out of the sample under σ_{pre} = 2 kPa. For that reason, results of the tests at $MC_{as,rec+4\%}$ are neglected in interpreting the results, as partially saturated materials are the focus of current chapter.

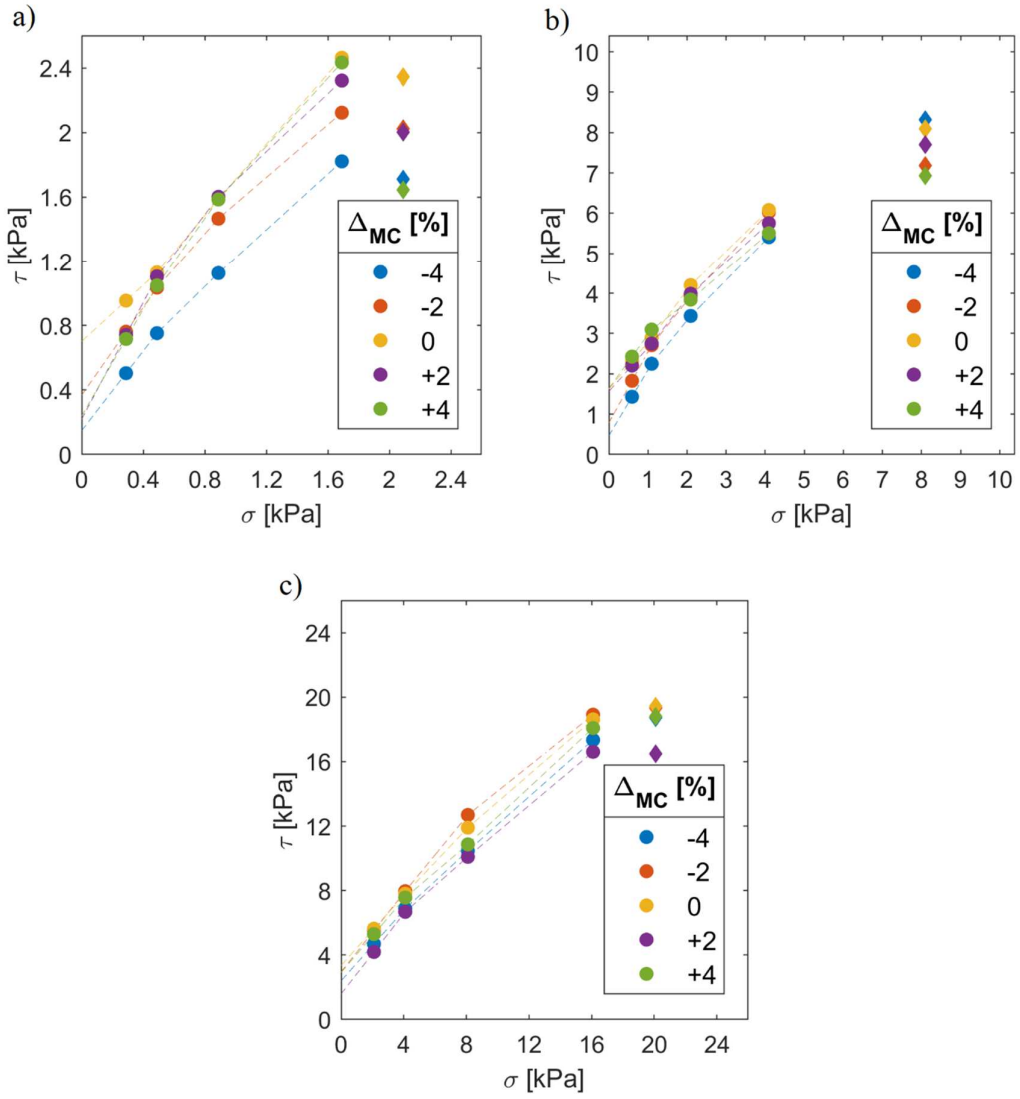

Figure 3-15. Yield locus of I_2 in various moisture content levels at σ_{pre} equal to: a) 2 kPa, b) 8 kPa, c) 20 kPa

In contrast to results of σ_{pre} = 2 kPa, at σ_{pre} = 8 kPa lower variations of shear stress values (in percentage) are measured at all the applied moisture content levels. The measured values of τ_{pre} do not show a clear trend by changing the levels of moisture content.

Figure 3-15c with the ring shear test results at σ_{pre} = 20 kPa shows a lower dependency of τ_{pre} to MC in general, compared to σ_{pre} = 8 kPa. Except τ_{pre} at $MC_{as,rec-2\%}$, the other measurements are close to τ_{pre} at $MC_{as,rec}$ with less than 4% variations. ϕ_{lin} changes by 8 degrees, corresponding to about 20% change, with the variation of moisture content. τ_c changes 1.3 kPa, corresponding to 77%, by varying MC. Therefore, τ_c of the sample is more sensitive than ϕ_{lin} to moisture content variation

Similar to sample I_1, a stress-history dependent shear strength is observed in sample I_2. For instance, at the normal stress of about 2 kPa for σ_{pre} equal to 2, 8 and 20 kPa in the as received condition, shear stresses of 2.0, 4.2 and 5.6 kPa are measured respectively. In other words, the shear strength is increased more than 100% at this material condition by pre-consolidating the sample. This stress dependent behavior is important in design of handling equipment, such as grabs. For instance, once cohesive iron ore bulk is consolidated by 20 kPa rather than 2 kPa during closing of grab's buckets, higher shear stress is required to mobilize the flow. Therefore, a better filling process could be expected by minimizing the consolidation on cohesive iron ore bulk during closing of grab's bucket.

Figure 3-16. Excessive water leaving the sinter feed sample in the wet test condition ($MC_{as,rec+4\%}$)

Figure 3-17 shows the bulk density results of sample I_2 in the ring shear test. $\rho_{b,0}$ at $MC_{as,rec}$ is 1995 kg/m^3 in the shear cell that increases to 2799 kg/m^3 after shearing at 20 kPa consolidation stress. The sample is less compressible at lower levels of MC; the difference between $\rho_{b,0}$ and $\rho_{b,20}$ (bulk density under 20 kPa normal stress) at $MC_{as,rec-4\%}$ and $MC_{as,rec-2\%}$ are respectively equal to 285 and 630 kg/m^3. Only for $MC_{as,rec+2\%}$ the bulk density decreases after pre-shearing at 2 kPa

normal stress. This is caused by the dilation of the sample during shearing that lifts the cell's lid over a recorded distance of 1 mm.

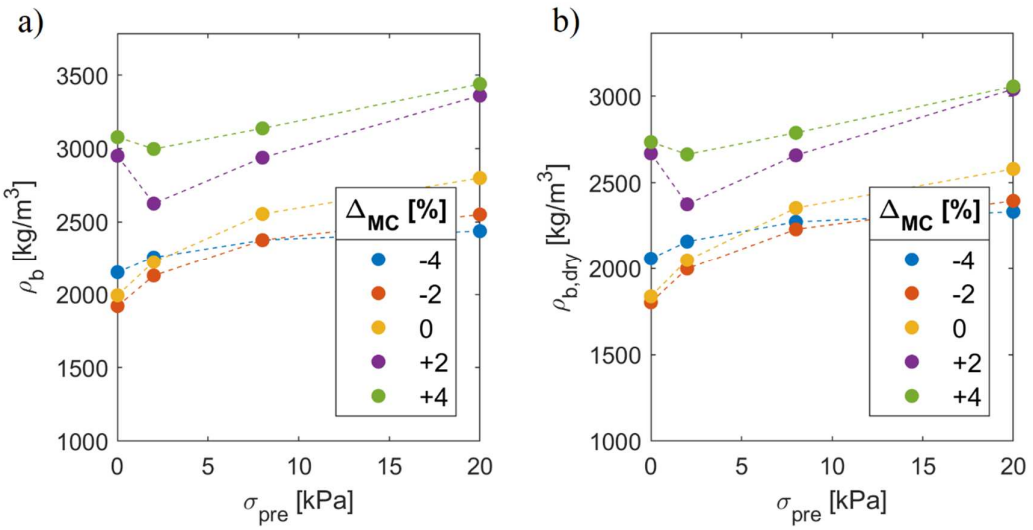

Figure 3-17. Bulk density measurements of I_2 using RST; a) bulk density, b) dry bulk density

Figure 3-18 presents the yield locus lines of sample I_3, Minas Rio pellet feed, at five different levels of MC. This sample is less dependent to the variations of moisture level, compared to the two Carajas samples. This can be clearly seen in all three graphs at σ_{pre} equal to 2, 8 and 20 kPa that are shown in Figure 3-18a, b and c respectively. For instance, in Figure 3-18a, σ_{pre} = 2 kPa, an average cohesion strength, τ_c, of 0.8 kPa with a deviation of less than 0.1 kPa is measured at all levels of MC. The cohesion strength values of I_3 are higher than two previous samples at 2 kPa pre-consolidation level. Relatively consistent values of ϕ_{lin} are also measured at various levels of MC; at σ_{pre} equal to 2, 8 and 20 kPa average linear internal frictions of respectively 29.8, 40.5 and 37.8 degree with a maximum standard deviation of 2 degree are measured. Based on the visual observations, the particles of Minas Rio sample are unlikely to form agglomerates by increasing moisture content. For that reason, the shear stress shows a low sensitivity to variations of MC. The stress-history dependent behavior of the shear strength is also captured in sample I_3, similar to two previously discussed samples.

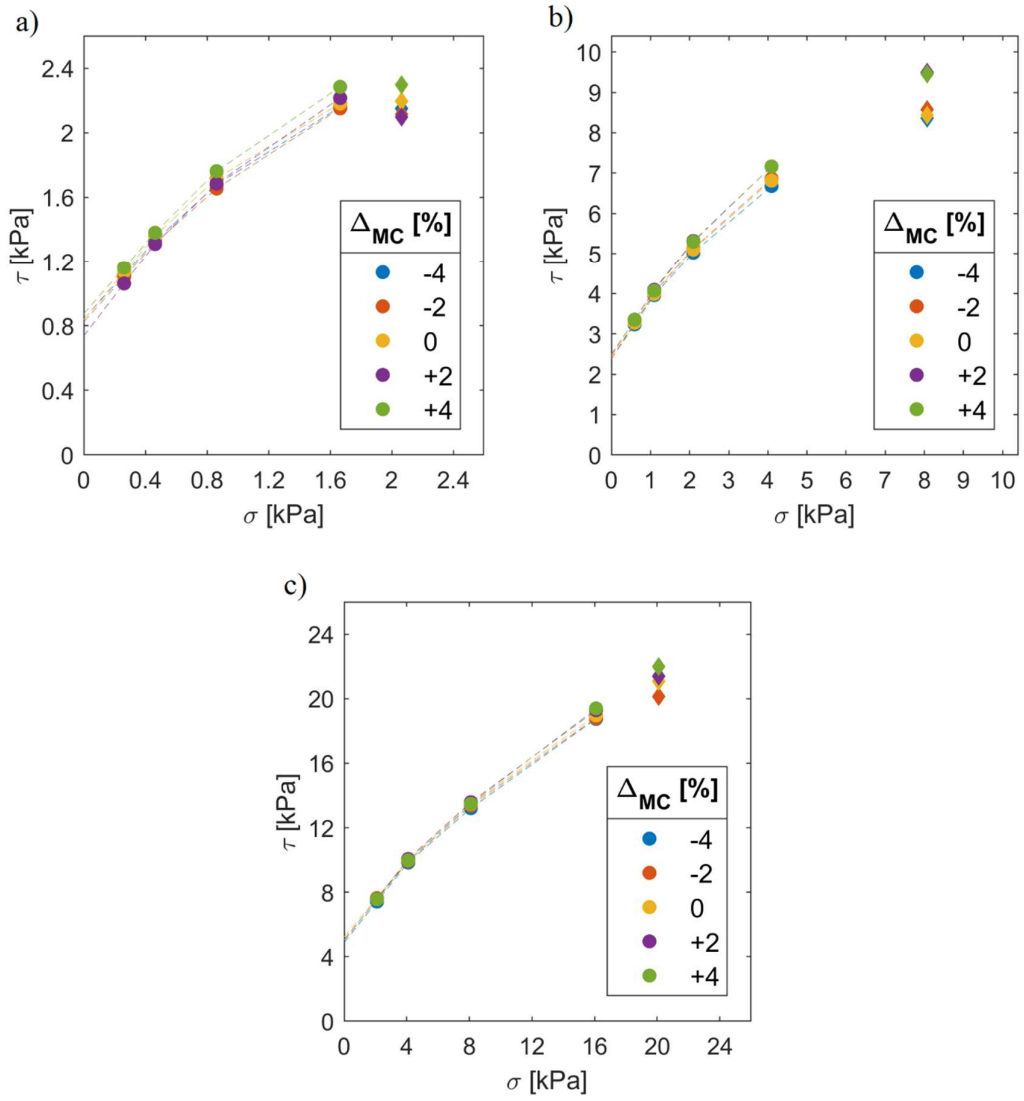

Figure 3-18. Yield locus of I_3 in various moisture content levels at σ_{pre} equal to: a) 2 kPa, b) 8 kPa, c) 20 kPa

Figure 3-19 shows the bulk density results of sample I_3 in the ring shear test. Both ρ_b and $\rho_{b\text{-}dry}$ show a positive correlation with the (pre-)consolidation stress. For example, $\rho_{b,0}$ at $MC_{as,rec}$ is equal to 1370 kg/m^3 that rises to 2336 kg/m^3 by shearing under consolidation stress of 20 kPa. Furthermore, both ρ_b and $\rho_{b\text{-}dry}$ tend to increase by adding moisture. This means that the bulk density of the sample is not only increased because of the additional weight of moisture, but also due to an additional compressibility. Similar to I_1, the other pellet feed size sample, no uplift of the cell's lid occurred during the ring shear test.

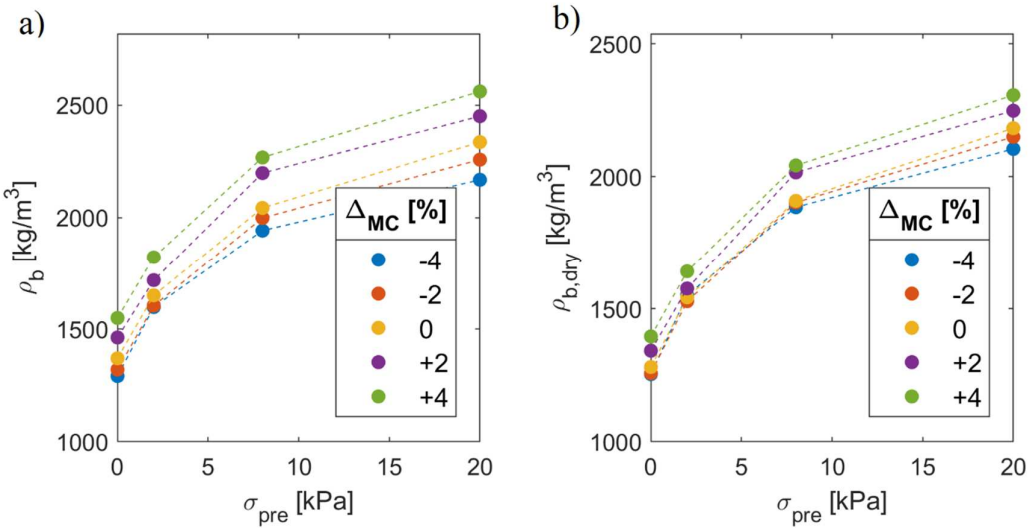

Figure 3-19. Bulk density measurements of I_3 using RST; a) bulk density, b) dry bulk density

Figure 3-20 shows results of the experiment using the wall friction test setup. In each graph, the effect of normal stress on the wall friction angle, ϕ_x, at various levels of MC is displayed. The measured values of ϕ_x in the first sample, I_1, at three first low levels of MC follow a similar trend. At the lowest and highest levels of normal stress, σ = 1.1 kPa and σ = 17.1 kPa, ϕ_x of 32.7˚, 34.4˚ and 31.5˚ are measured respectively. By increasing the moisture to $MC_{as,rec+2\%}$, higher values of ϕ_x are measured in average, compared to lower levels of MC. This behavior is caused by the adhesion strength created due to the extra water added to the sample.

Due to change in MC in sample I_2, a high variation of around 20˚ in ϕ_x is measured under σ = 1.1 kPa. By increasing the normal stress, the range of variation starts to decrease, and under σ = 17.1 kPa the values of ϕ_x are between 20.7˚ to 23.3˚.

In third sample, an average ϕ_x of 34.4º is measured under 1.1 kPa, with an outlier at $MC_{as,rec-4\%}$. In general, at all levels of MC, there is a negative correlation between wall friction angle and normal stress; there are some exception data points at $MC_{as,rec-4\%}$ and $MC_{as,rec-2\%}$.

3.4.2. Angle of repose and effective angle of internal friction

Figure 3-21 compares the angle of repose (α_M) measurements with effective angle of internal friction (φ_{eff}) for three samples of iron ore at various levels of MC. In left graphs, the average of measured α_M are shown with the vertical error bars indicating the standard deviation of 10 test repetitions. Overall, the measured values of α_M are between 55˚ to 70˚ in all the tests, except for the sample I_2 at $MC_{as,rec+2\%}$. The effective angle of internal friction, φ_{eff}, is the slope of effective yield locus in ring shear test as defined in [50], which is an important parameter in designing silos

and hoppers. φ_{eff} represents the ratio of the minor principal stress (σ_2) to the major principal stress (σ_1) at steady-state flow. For cohesive bulk solids, φ_{eff} usually decreases with increasing consolidation stress [50].

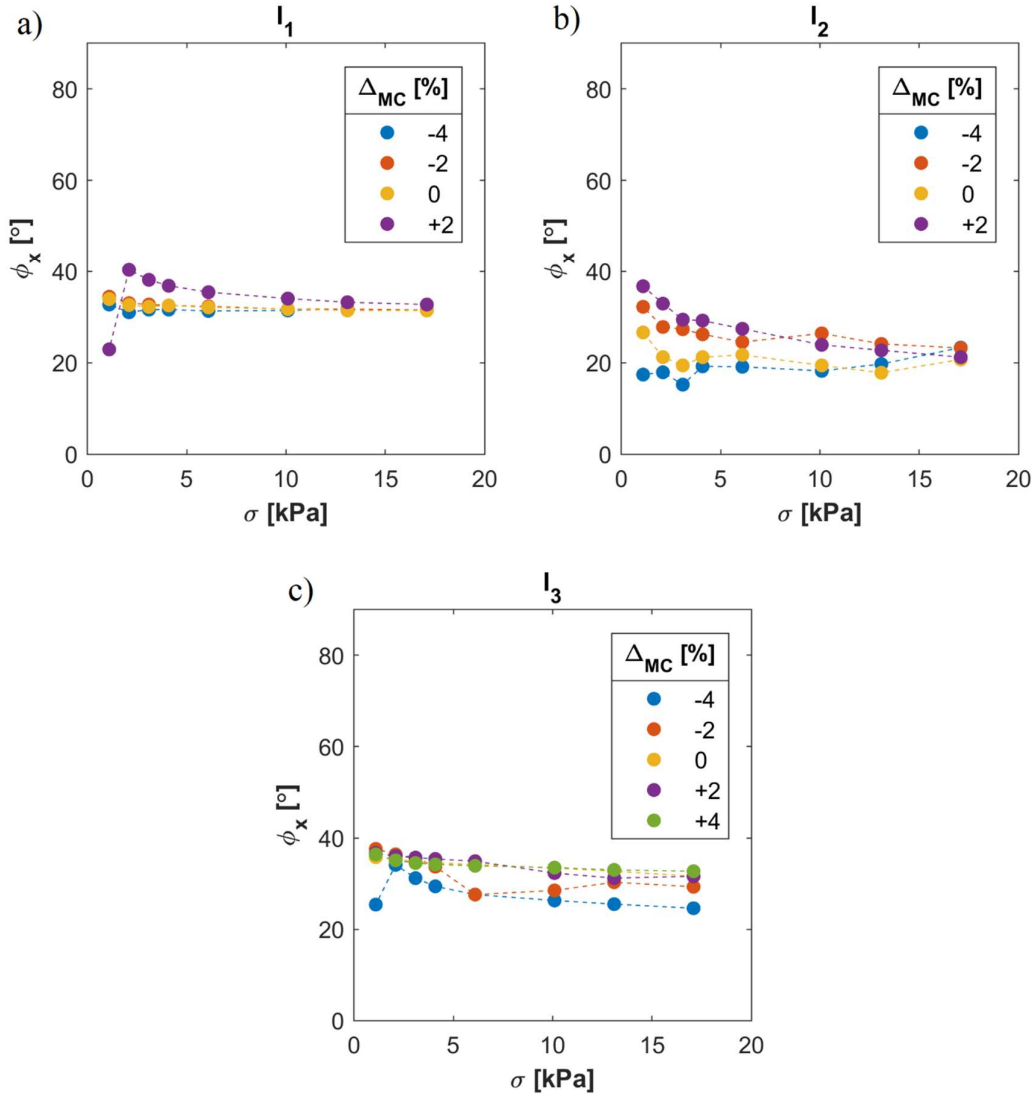

Figure 3-20. Results of wall friction test; a) I_1, b) I_2, c) I_3

In Figure 3-21a, the measurements on I_1 are shown, in which the $MC_{as,rec}$ is equal to 13%. A variation of only 1˚ is captured in α_M by reducing the MC. The test could not be executed properly at higher levels of MC, because the extreme stickiness of the bulk material led to an inadequate filling of the test box. By increasing MC, φ_{eff} increases at all levels of σ_{pre} for I_1. The negative correlation between σ_{pre} and φ_{eff} can be seen clearly in Figure 3-21a (right). For the current sample, considering standard deviation values of angle of repose measurements, α_M is comparable with φ_{eff} measured at σ_{pre} = 2 kPa.

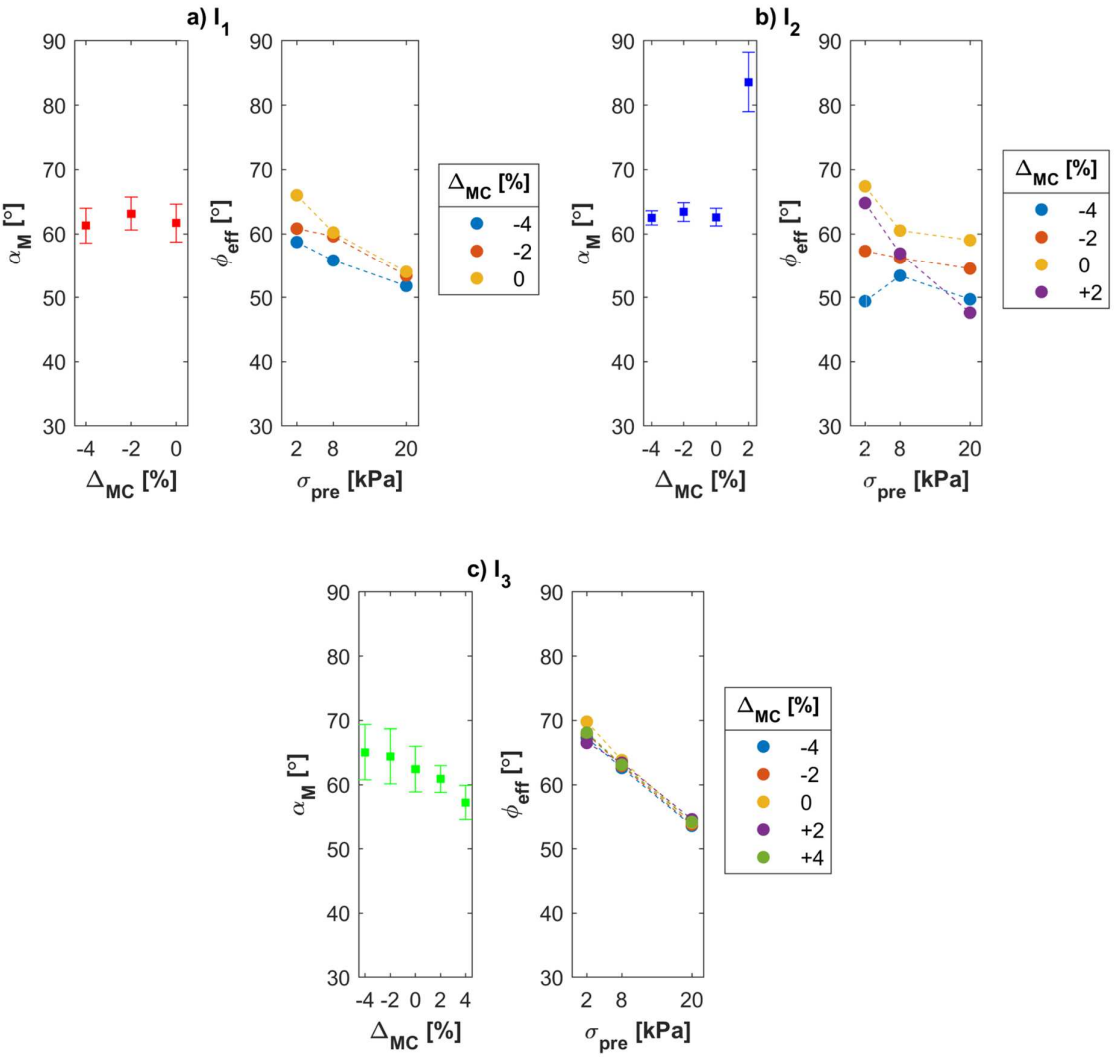

Figure 3-21. α_M and φ_{eff} results for three different iron ore samples; a) I_1, b) I_2, c) I_3

The results of angle of repose on the sinter feed sample, I_2, are shown in Figure 3-21b. An angle of repose of 63˚ is measured in average at $MC_{as,rec}$. The same value is measured at $MC_{as,rec-2\%}$ and $MC_{as,rec-4\%}$. A sudden increase of about 20˚ in the averaged angle of repose is observed by testing the sample at $MC_{as,rec+2\%}$. A higher standard deviation in the measurement is found as well at $MC_{as,rec+2\%}$; for which the bulk material does not flow in some of the repetitions. A possible explanation for the sudden increase in the angle of repose is that as the material's moisture content approaches liquidation, agglomerates merge and create inter-particle bonds. The inter-particle bonds are stronger than inter-agglomerate bonds [38], so the inter-particle friction in the material is higher, which leads to increase in the angle of repose. The test could not be executed at $MC_{as,rec+4\%}$ due to extreme stickiness behavior that was also observed in sample I_1 at high levels of moisture content. The test is also conducted on a dry sample to determine the effect of cohesion

strength on the angle of repose; this results in α_M = 58° for the dry sample that is 5° lower than measured α_M at $MC_{as,rec}$. The negative correlation between σ_{pre} and φ_{eff} can be seen in Figure 3-21b (right), expect for $MC_{as,rec-4\%}$. No decisive conclusion can be made by comparing α_M and φ_{eff} values for the sinter feed type sample, I_2.

In contrast with two previous samples, there seems to be a small negative correlation between MC and α_M for I_3, shown in Figure 3-21c. At the highest level, $MC_{as,rec+4\%}$, the bulk material tends to flow easier with an average measured value of α_M = 57˚. However, the error bars at different MC levels overlap with each other; a conclusive correlation between MC and α_M cannot be therefore found. φ_{eff} values show a consistent trend at all levels of σ_{pre} for I_3, independent of MC level. Comparable φ_{eff} and α_M are measured at two lowest levels of MC, which starts to diverge, up to 12°, by increasing MC.

Due to relatively consistent measured trends of α_M and φ_{eff} in I_1 and I_3, it is expected to not observe high variations of angle of repose in practice, such as after filling grab's buckets. In contrast, for sample I_2, a higher variation of angle of repose, and consequently equipment performance is expected to occur.

3.4.3. Consolidation-penetration test

Two sets of experiments are conducted using the consolidation-penetration test setup. In the first set, the effect of σ_{pre} on the penetration resistance is studied by investigating all possible combinations between defined levels of I and σ_{pre}; level of moisture content, MC, is kept constant. In contrast, in the second set, the interaction between I and MC is investigated to quantify their interaction with regards to the penetration resistance of iron ore samples.

Figure 3-22 shows an overview of the results obtained in first experiment set for three iron ore samples. The graphs in the left column (a, c, and e) display the reaction force recorded during penetration of the wedge tool into iron ore samples. Five different levels of σ_{pre} are applied, from 0 to 300 kPa. At $\sigma_{pre,0}$, the loose condition, no consolidation stress is applied; while only the bulk material surface is flattened. The right graphs (b, d, and f) show the accumulative penetration resistance in Joules that is calculated by integrating the reaction force over penetration depth. The lines represent the average of three measurements, and the vertical error bars indicate the standard deviation values.

In the loose condition, the highest resistance is measured in the sinter feed sample, I_2; an average reaction force of more than 1300 N is measured after penetrating 0.10 m into the sample. Considerably lower forces are measured for the other two pellet feed samples at their loose

condition. In sample I_1, the penetration tool could not be moved deeper than 0.08 m; therefore, the measured data are filtered out after 0.07 m.

Once sample I_1 is pre-consolidated by 8 kPa, a notable increase in the penetration resistance occurs. Similar behavior is captured in I_2 that is originated from the same mining site. The last sample, I_3, however shows a different behavior under the effect of pre-consolidation; the peak value of F_W only increases by 11% by applying a σ_{pre} = 8 kPa. After reaching the peak, a steady-state penetration resistance is observed after a certain depth for sample I_3.

In sample I_3 a positive correlation exists between σ_{pre} and the depth where the peak reaction force occurs. However, the peak value of F_W is less sensitive to σ_{pre}, in contrast with two other samples. There is a strong positive correlation between σ_{pre} and peak value of F_W in samples I_1 and I_2. This phenomena is probably correlated with the change in bulk density due to the pre-consolidation stage. Additionally, the peak occurs at smaller penetration depths in these two samples, compared to I_3.

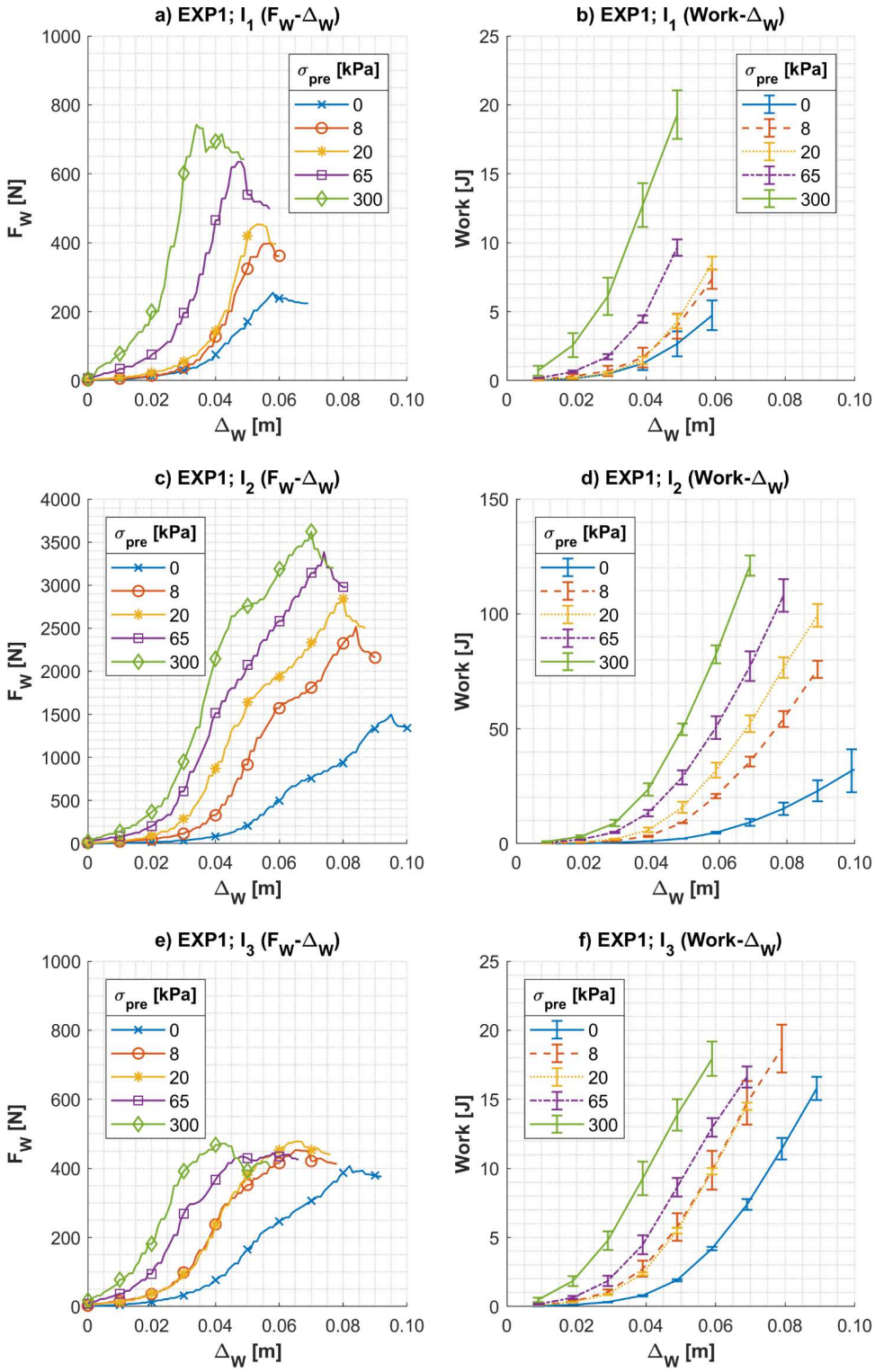

Figure 3-22. Results of experiment set I in the consolidation-penetration test, the effect of σ_{pre} at $MC_{ac\text{-}rec}$; a) I_1 (F_W-Δ_W), b) I_1 (Work-Δ_W), c) I_2 (F_W-Δ_W), d) I_2 (Work-Δ_W), e) I_3 (F_W-Δ_W), f) I_3 (Work-Δ_W)

Figure 3-23 displays results of experiment set II, in which the effect of variation of MC on the penetration resistance of iron ore samples in the loose condition, σ_{pre} = 0 kPa, is investigated. The first sample, I_1, has the highest value of $MC_{as,rec}$ among the other samples. According to the force-displacement graph, the average reaction force of three measurements is the highest at $MC_{as,rec}$ for I_1 compared to other levels of MC. However, by considering the standard deviation of the measurements, indicated in the Work-Δ_W graph, there is no conclusive correlation between level of MC and the penetration resistance of this sample. Only once the bulk material reaches $MC_{as,rec+4}$ that is equal to 17%, the resistance against penetration almost disappears. This results in a peak value of only 17 N in F_W.

Sample I_2 has the highest peak value of F_W at $MC_{as,rec}$, compared to other levels of MC of this samples, as well as compared to other samples. At the initial 0.03 m of the penetration depth, in all levels of MC in sample I_2, similar trend in F_W is captured. However, the reaction force increases exponentially at $MC_{as,rec}$ and $MC_{as,rec-4\%}$ by moving the penetration tool deeper. The exponential trend starts at greater depths at $MC_{as,rec-2\%}$ that results in a lower accumulative penetration resistance, compared to the two previous MC levels. This phenomena can be explained by the results that were obtained previously in our experiment with the ring shear test; the lowest compressibility of sample I_2 is measured at $MC_{as,rec-4\%}$. The low compressibility creates more penetration resistance in the compaction zone under the wedge-shape tool (see Figure 3-11). At $MC_{as,rec+2\%}$ and $MC_{as,rec+4\%}$ a considerably low values of F_W are recorded, with the peaks of less than 10 N. Due to the excessive water, the bulk material starts to behave more as liquid rather than solid materials.

In sample I_3, the peak value of F_W is the least sensitive to variation of MC, compared to two other samples. The peak values in this samples are between 600 to 800 that however, happens in different depths. For example, at highest level of MC, the peak force is located at 0.08 m, but at $MC_{as,rec-4\%}$ at 0.11 m. This results in a positive correlation between MC and accumulative penetration resistance (work) of sample I_3 that can be concluded from the right graph.

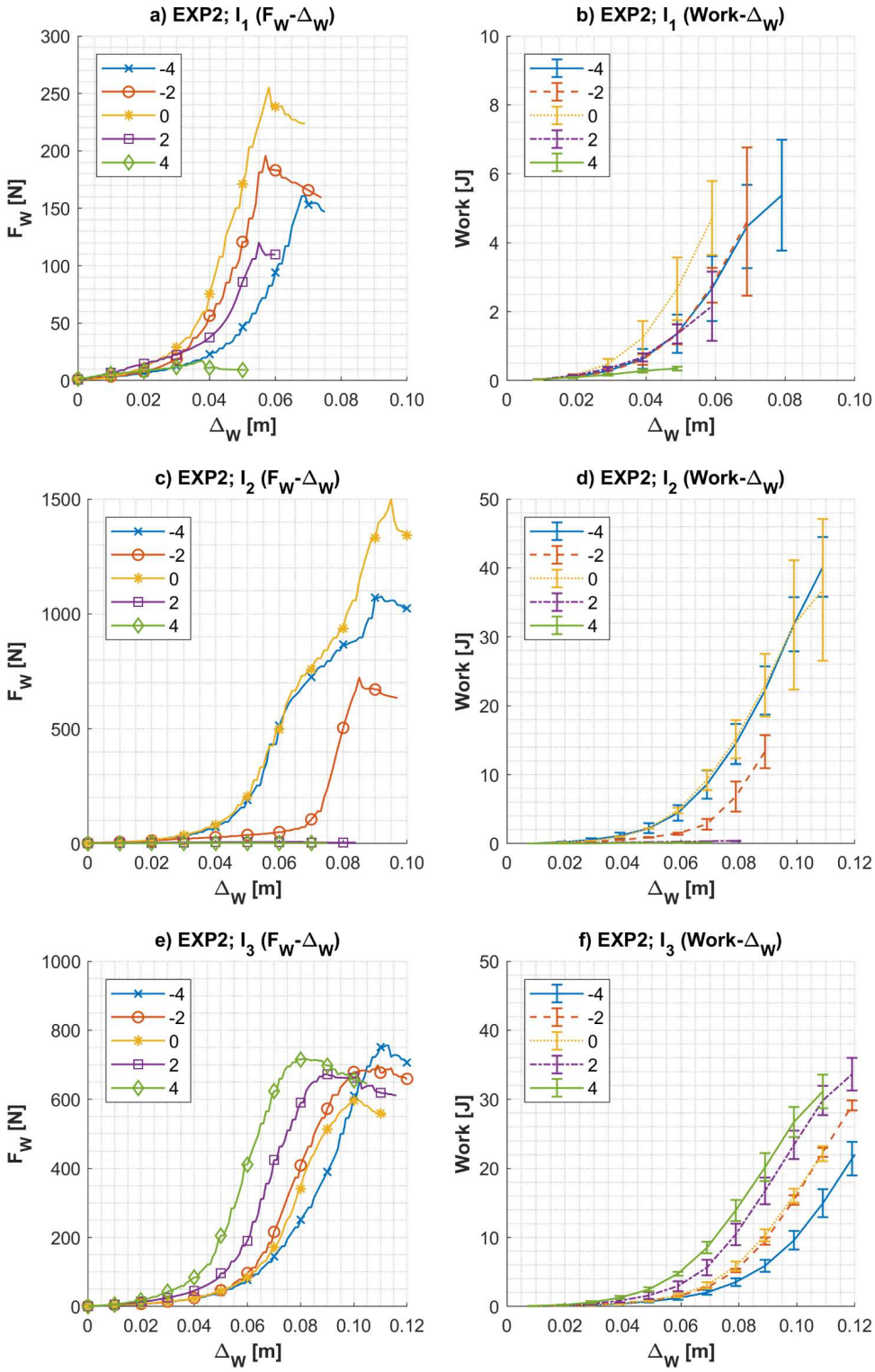

Figure 3-23. Penetration resistance of iron ore samples in different levels of MC; a) I_1 (F_W-Δ_W), b) I_1 (Work-Δ_W), c) I_2 (F_W-Δ_W), d) I_2 (Work-Δ_W), e) I_3 (F_W-Δ_W), f) I_3 (Work-Δ_W),

3.5. Correlations Between Influencing and Dependent Bulk Properties

In the previous section, results of the experiments using the ring shear, ledge angle of repose and consolidation-penetration tests were presented. In this section, the effect of the different influencing bulk properties on the flowability, penetration resistance and bulk density are discussed.

Figure 3-24 illustrates the comparative flowability analysis that is created using the ring shear test results. In Figure 3-24a and Figure 3-24b, the mean ff_c values derived respectively for different levels of MC and σ_{pre} are presented. The standard deviation values are also presented to indicate the variance of flowability due to the change of the third (absent) property. For instance, the standard deviations of the mean ff_c in the left graph is due to the variance of σ_{pre}.

According to Jenike classification [67], the sinter feed sized sample behaves as a cohesive (C) material, however easy-flowing (EF) and very cohesive (VC) flowability are also captured in some tests. Furthermore, high variations of ff_c in sample I_2 is notable. The two pellet feed sized samples, I_1 and I_3, are categorized as VC at almost all levels of MC and σ_{pre}. Only in sample I_1 at σ_{pre} = 20 kPa a ff_c value of higher than 2 is captured due to higher levels of applied σ_{shear} compared to other pre-consolidation levels. The range of measured flow functions for the three Brazilian samples, I_1 to I_3, is similar to the range measured for the Australian iron ores using Jenike direct shear tester [48], resulting in an ff_c between 1 to 4.

As suggested in [80], for cohesive iron ore material, cohesion forces tend to be less contributing to the shear strength at higher consolidation stresses. For that reason, a positive correlation between σ_{pre} and ff_c in all samples is expected. In Table 3-11, the correlation coefficients between σ_{pre} and ff_c, as well as between MC and ff_c are shown. The correlation coefficient quantifies the statistical correlation between two variables, which is bounded between -1 and +1 [53]. A correlation coefficient of ±1 indicates the strongest agreements between two variables, and 0 means no agreements. No conclusive correlation between MC and ff_c is found for the three samples. In contrast, an average correlation coefficient of 0.735 is found between σ_{pre} and ff_c for the samples. High values of correlation coefficients exists between σ_{pre} and ff_c for samples I_1 and I_2 values, however, a weaker agreement exists for sample I_2. This suggests that for sample I_2 the influence of σ_{pre} on ff_c is interdependent on the level of MC.

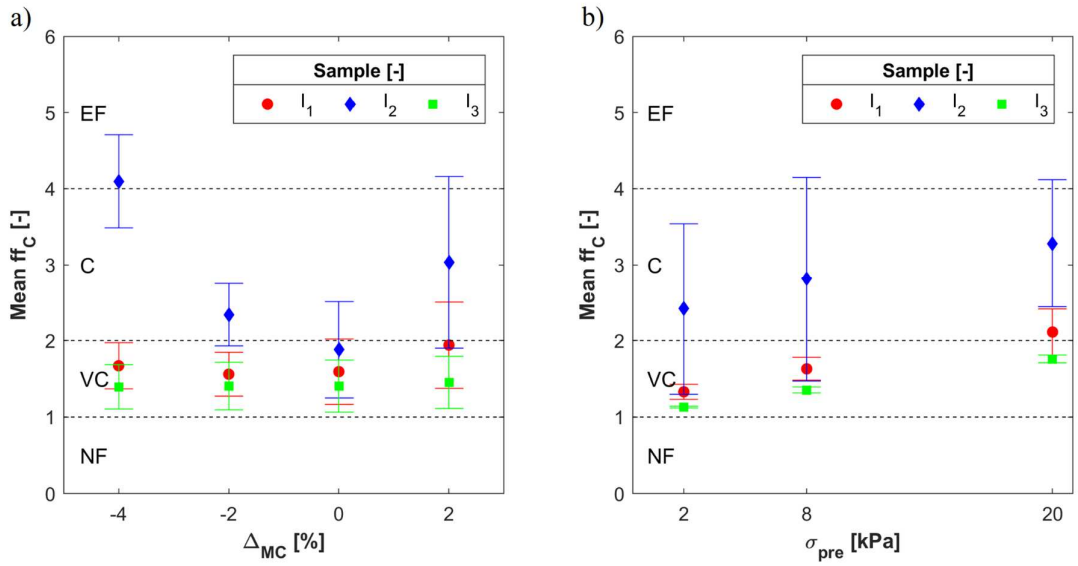

Figure 3-24. Comparative flowability analysis; a) Main effect of MC variation on ff_c, a) Main effect of σ_{pre} variation on ff_c

Table 3-11. Correlations coefficients in the ring shear tests

Sample	I_1	I_2	I_3	Average	Standard deviation
σ_{pre} and ff_c	0.875	0.338	0.992	0.735	0.285
MC and ff_c	0.258	-0.396	0.077	-0.020	0.276

Furthermore, the interaction between MC and σ_{pre} on the flowability of three samples is analyzed in Figure 3-25. Two properties have interaction when the effect of one influencing property (i.e. MC) on the output of the experiment (i.e. ff_c) is considerably affected by the level of the other influencing property (i.e. σ_{pre}) [53]. For instance, as predicted above, in sample I_2, the ff_c for $MC_{as,rec-4\%}$ is the highest at $\sigma_{pre,8}$, while the lowest flowability for $MC_{as,rec+2\%}$ is found at $\sigma_{pre,8}$. This suggests an interaction between MC and σ_{pre} on ff_c for sample I_2. In contrast, almost no interaction is found for sample I_1 and I_3.

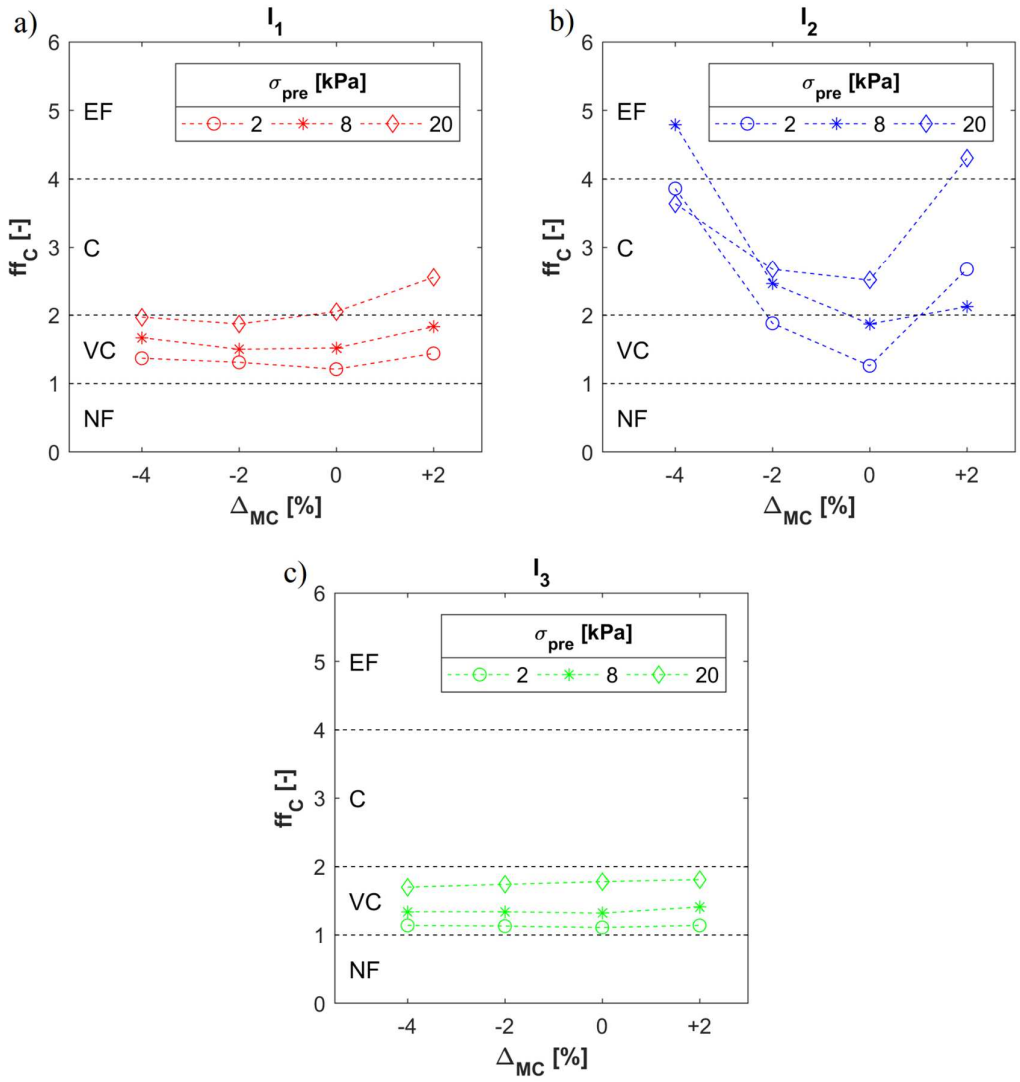

Figure 3-25. Interaction plots between MC and σ_{pre} on ff_c for different iron ore samples; a) I_1, b) I_2, c) I_3

Figure 3-26 presents the comparative analysis done on the penetration resistance results. In Figure 3-26a and Figure 3-26b, the $W_{50,ratio}$ values are shown respectively for different levels of MC and σ_{pre}. $W_{50,ratio}$ is calculated by dividing the accumulative penetration resistance, work in Joules, at $\Delta_W = 0.05$ m over the same parameter measured at $MC_{as,rec}$ and $\sigma_{pre,0}$. In I_1 and I_2, the MC variation leads to reduction in the penetration resistance, In I_3, by increasing MC the peak F_W is occurred at lower Δ_W, therefore a positive correlation between $W_{50,ratio}$ and MC is found. In Table 3-12 the correlations between MC and $W_{50,ratio}$, as well as σ_{pre} and $W_{50,ratio}$ are presented. σ_{pre} is responsible for a substantial increase in the penetration resistance of iron ore cargoes, especially for the sinter feed sized sample. For that reason, it is expected that there is a negative correlation between σ_{pre} and penetration depth of grabs into iron ore cargoes.

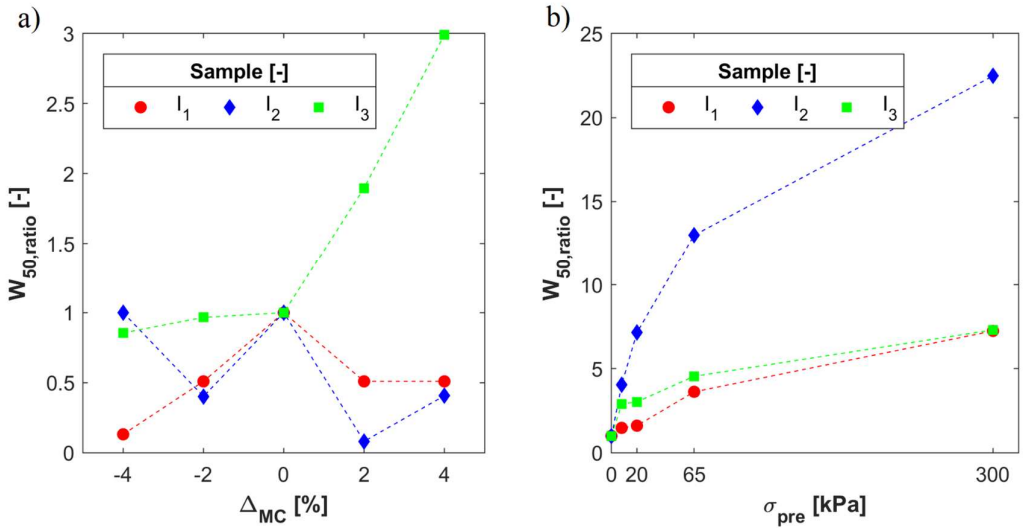

Figure 3-26. Comparative penetration resistance analysis; a) Interaction plot between MC and type of iron ore, b) interaction plot between σ_{pre} and type of iron ore

Table 3-12. Correlations coefficients in the consolidation-penetration tests

Sample	I_1	I_2	I_3	Average	Standard deviation
σ_{pre} and $W_{50,ratio}$	0.980	0.979	0.986	0.982	0.003
MC and $W_{50,ratio}$	0.39	-0.59	0.90	0.235	0.617

Figure 3-27 presents the effect of σ_{pre} on ρ_b of the three iron ore samples quantified using the consolidation-penetration test. The filled markers represent the average of three tests repetitions at a specific σ_{pre}, and the vertical error bars indicate the standard deviation of ρ_b. All the tests are executed at $MC_{as,rec}$. The values of $\rho_{b,0}$ are confirmed by comparing with measuring bulk density of three samples according to ISO 17828 [81]. Higher values of bulk density are obtained in the consolidation-penetration test setup compared to measurements in the shear cell. For example, for sample I_2 at the loose condition, average ρ_b is around 200 kg/m^3 higher that what was measured using the shear cell. The difference between the dimensions and the geometry of the cell and test container caused the difference in ρ_b results. In smaller geometries, wall effects are likely to be more influential on the packing of cohesive bulk materials.

By applying $\sigma_{pre,8}$, a sudden increase in ρ_b is measured in samples I_2 and I_3; at this level of σ_{pre} mainly rearrangements of particles and elastic deformations contribute to the densification process [22]. Then, bulk densities increase with a milder slope between σ_{pre} of 8 and 65 kPa. For example in sample I_2, $\rho_{b,65}$ is 7% higher than $\rho_{b,8}$. The compressibility of the bulk materials tend to converge to a maximum limit by applying σ_{pre} higher than 65 kPa. Overall, sample I_2 shows the

most sensitivity to σ_{pre}. A wide distribution of particle sizes makes sinter feed type iron ore capable to obtain a denser packing [78].

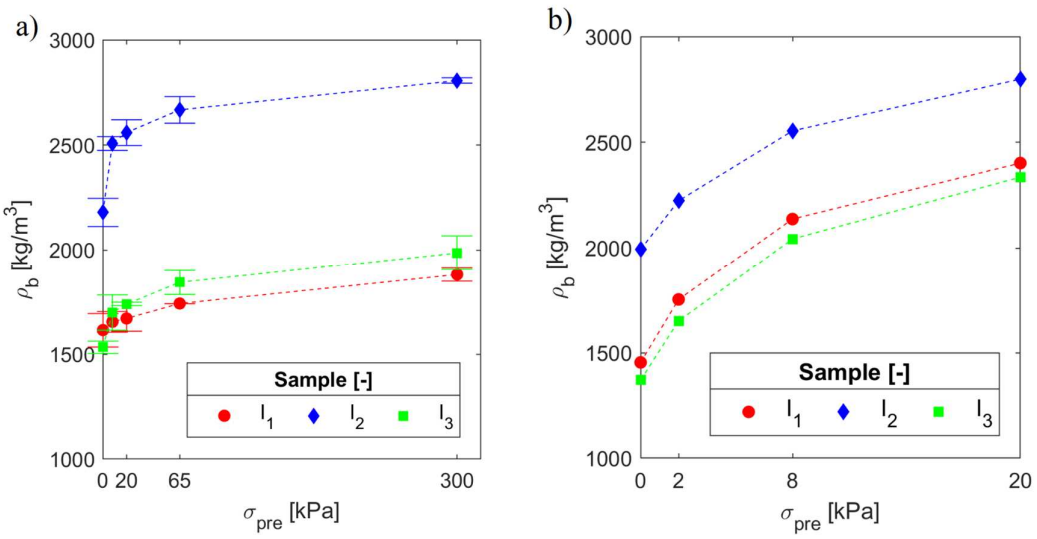

Figure 3-27. Bulk density results for $MC_{as,rec}$; a) consolidation-penetration tests, b) ring shear test

3.6. Conclusion

The aim of this chapter was to first establish links between the influencing and dependent bulk properties. Second the range of variations of bulk properties of iron ore was determined, which is applicable to design of various of types of handling equipment, including grabs. Using three different setups and by running five separate experiments in total, it was successfully shown that the three influencing bulk properties, type of iron ore, moisture content and pre-consolidation are responsible for the variations of the dependent bulk properties.

- In terms of variability of flowability, the three iron ore samples are categorized as cohesive to very cohesive based on the ring shear test results. In average, there is a strong positive correlation between pre-consolidation and flowability, independent of moisture content. However, in average a weak correlation exists between moisture content and flowability when the interdependency to pre-consolidation is considered.
- No conclusive correlation was found between moisture content and the angle of repose of the three iron ore samples. The variability of angle of repose, α_M, of these samples were measured using the ledge method. The test results are in the range of 55° to 70°, except for the Carajas sinter feed sample at $MC_{as,rec+2\%}$ that resulted in an angle of repose of 84° in average of multiple repetitions. The mentioned range is consistent with measurements done in [8], [38] and [82]

on moist iron ore samples using a similar test method. In contrast, [8] measured an angle of repose of 40° for free flowing iron ore pellets using the ledge method.

- The penetration resistance has a strong positive correlation with pre-consolidation, independent of moisture content. There is a weak correlation between moisture content and penetration resistance when the interdependency to the type of iron ore is considered.
- The bulk density has a strong positive correlation with pre-consolidation, independent of moisture content. There is also a strong positive correlation between moisture content and bulk density, independent of pre-consolidation.

Furthermore, a general conclusion is that the dependent bulk properties of cohesive iron ore samples are highly sensitive to the history of the applied stress, σ_{pre}. This phenomena was observed in both ring shear and consolidation-penetration tests, in which high correlations between pre-consolidation and respectively flowability and accumulative penetration resistance are found. Design of bulk handling equipment (e.g. grabs) for cohesive iron ore can be improved by minimizing the undesirable effect of pre-consolidation on the process. This can be done, for instance, by optimizing geometrical optimization of equipment; by applying a relatively low pre-consolidation stress on bulk solids during closing of grab's buckets. Then, the flow is expected to be mobilized requiring a lower shear force. Furthermore, both (moist) bulk density and dry bulk density, are also highly correlated with pre-consolidation. Therefore, choosing appropriate range of pre-consolidation in the design of equipment for handling cohesive iron ore is also crucial.

Highest variation of the dependent bulk properties, in total, was captured in the Carajas sinter feed sample, I_2. This sample showed a high sensitivity of the penetration resistance and bulk density results to pre-consolidation. Also, its angle of repose tends to reach a maximum by increasing the moisture content. Furthermore, the flowability of sample I_2 showed highest sensitivity to the variation of moisture content, in which an interaction between moisture content and pre-consolidation was found. Therefore, the highest inconsistency of the productivity (e.g. grab's payload) is expected to occur in the handling process of the Carajas sinter feed product. Therefore, using test results of sample I_2, the variability of iron ore properties can be incorporated in optimizing bulk handling equipment that are used in excavation and storage.

4

Minimizing computation cost for modelling cohesive bulk solids*

Discrete Element Method (DEM) is a suitable numerical tool to simulate bulk solids. DEM is able to capture the discontinuous behavior of bulk solids by modelling motion of individual particles and interaction with each other and equipment. The computation time of DEM simulations increases exponentially when particle size is reduced or the number of particles increased. This critical challenge limits the use of DEM simulation for industrial applications, including the grabbing process. Scaling techniques can offer a solution to reduce computation time. Therefore,

---

* This chapter corresponds to the following references:

M.J. Mohajeri, R.L.J Helmons, C. van Rhee, D.L. Schott, "A hybrid particle-geometric scaling approach for elasto-plastic adhesive DEM contact models". Powder Technology, Volume 369, 2020, 72-87. DOI: 10.1016/j.powtec.2020.05.012.

M.J. Mohajeri, C. van Rhee, D.L. Schott, "Penetration resistance of cohesive iron ore: a DEM study", 9th International Conference on Conveying and Handling of Particulate Solids, 2018.

a proper scaling approach is developed in this chapter to simulate cohesive materials with a minimum number of required computational nodes.

The previous chapter concluded that the pre-consolidation plays a significant role in the behavior of cohesive bulk solids. Thus, first, a DEM contact model that to simulate the stress-history dependent behavior of cohesive bulk solids is selected based on its feasibility. In Section 4.2, available scaling techniques for DEM simulation are evaluated. Next, a proper scaling technique is developed to consider elasto-plastic and cohesive behavior of bulk solids. Section 4.3 provides a simulation plan to include effect of particle as well as geometry scaling in a hybrid manner. In Section 4.4, the scaling technique is verified by simulating the ledge angle of repose, ring shear test, and uni-axial consolidation tests. Recommendations to apply the hybrid particle-geometry scaling technique are provided in Section 4.5. Finally, Section 4.6 presents conclusion for the proper scaling approach for an elasto-plastic adhesive DEM contact model.

4.1. Selecting a Stress-History Dependent Cohesive Contact Model

The consolidation-penetration is selected as a test case to investigate which DEM contact model is able to capture the stress-history dependent behavior of cohesive bulk solids. In this test case, the effect of pre-consolidation on bulk properties (i.e. bulk density) and interaction with equipment (i.e. the penetration resistance) can be analyzed.

4.1.1. Simulation setup of the consolidation-penetration test

The laboratory consolidation-penetration test method that was developed in Chapter 2, is used for determining the penetration resistance of a cohesive iron ore sample. A simplified virtual apparatus similar to the experimental apparatus is created in the DEM commercial software package EDEM®. The components of the virtual apparatus are displayed in Figure 4-1. The only difference between the real and virtual apparatus is that instead of the Plexi-glass, a periodic boundary condition is used in the simulation. In the container, the particles are created using a dynamic factory and placed in random positions. They are allowed enough time to reach a quasi-static condition, where the average velocity of particles is smaller than 10^{-5} m/s.

The simulation consists of two stages, the consolidation and the penetration. Once the DEM particles are relaxed, the consolidation stage is commenced, in which the lid plate moves downward with a small velocity of 0.02 m/s. After occurring first contact between the lid plate and particles, a constant pressure between them are maintained to mimic the consolidation stage in the real experiment. The magnitude of the applied pressure is referred as the pre-consolidation

stress. After compressing the particles for 1 second, the lid plate is moved upward at the same velocity.

After preparing a consolidated sample, the wedge-shaped penetration tool, which is 0.20 m long, moves downward with the constant velocity of 1 mm/s, similar to the penetration stage in the real experiment. The reaction force on the wedge-shaped tool during penetration into the cohesive iron ore sample is measured, a smoothing operation is used to reduce the possible effects of noise in the measurements: by integrating the resulting force, F [N], over the depth, s [m], the penetration resistance, W [J] is obtained.

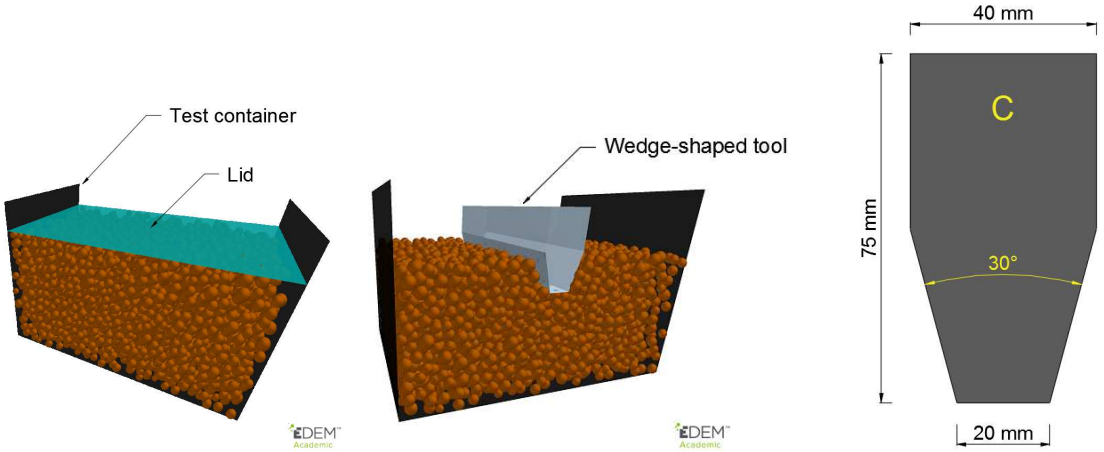

Figure 4-1. Virtual apparatus in EDEM®; left) the consolidation stage, middle) the penetration stage, and right) wedge-shaped tool

This chapter compares two DEM contact models, first the Hertz-Mindlin (no-slip) combined with Linear Cohesion (HMLC) [83], second the Edinburgh Elasto-Plastic Adhesion (EEPA) [24]. The first contact model, Hertz-Mindlin, is a non-linear elastic model and has been used in most recent DEM studies [11]. To replicate the cohesive behavior of the iron ore sample, the Linear Cohesion model is added to the base contact model that modifies the normal contact force by adding the following force:

$$F_c = 2\, k_c\, \pi\, R_p\, \delta_n \tag{4.1}$$

where, k_c, R_p and δ_n are the cohesion energy density [J/m^3], particle radius [m], and normal overlap between particles [m] respectively. A constant cohesion energy density of 50 kJ/m^3. The contact parameters of the EEPA model are selected similar to [84]; only a smaller Surface Energy value (8 J/m^2) is used that allows for creating bulk density and void ratio values comparable to values measured in the real experiment.

The wall friction test was done using a ring shear cell, according to [50]. Since no adhesion strength was observed between the iron ore particles and the steel material, the Hertz-Mindlin (no-slip) contact model is used for modelling the interaction of particles with the geometries.

Particles of iron ore fines are irregular in shapes having a wide size distribution [20]. In this chapter, however, particle shapes are simplified to spheres. To compensate the simplification of the particle shapes, the influence of restricting rotation of the particles on simulation output is therefore investigated. By restricting rotation of the particles, their angular motion is prevented. Thus, a better interlocking between particles is created, compared to the use of a rolling friction spring-damper model. When rotation of particles is allowed, the built-in rolling friction model of EDEM® software package is used, which is referred in literature as *model A* [85]. Additionally, a size distribution with the standard deviation of 0.1 is used. A mean particle size of 11 mm in diameter is used, which is around 10 times larger than the real particles; using a realistic particle representation of cohesive iron ore in the virtual simulation would have resulted in an unfeasible computational time per simulation.

The particle shear modulus (G) is also selected to be 5 MPa in the current section, which is close to the value used by [22] for modelling cohesive iron ore. However, [86] showed using a value smaller than 100 MPa might result in undesirable effects in the penetration of a wedge into bulk material. They advised that the approach should be verified when the particle shear modulus is altered.

Therefore, as displayed in Table 4-1, a simulation plan is designed to select a contact model that model the stress-history dependent behavior appropriately. Three different independent variables are included, contact model, integration time-step, and the ability of particle to rotate. The simulation output is analyzed though three dependent variables, $\Delta\rho_{b,0}$, W_{50} and W_{80}. Here, $\Delta\rho_{b,0}$ is defined as the change in bulk density in the loose condition (0 kPa) over the simulation time. If a DEM simulation is stable and reliable, $\Delta\rho_{b,0}$ prior to the penetration stage should be almost 0 kg/m^3. $\Delta\rho_{b,0}$ is calculated by comparing the bulk density after filling the container, and the bulk density before the first contact between the wedge tool and the particles. $W_{50/200}$ and $W_{80/200}$ are defined as the dimensionless penetration resistance at the penetration depths of 50 mm and 80 mm, respectively, which are calculated using Eq. (4.2). Once a stable DEM simulation of the compression-penetration test is developed, the influence of the contact models on capturing the dependency to the pre-consolidation stress is investigated.

$$W_{z/L}\,[-] = \frac{\text{Penetration resistance [J] at depth of } z}{\text{Weight of iron ore sample [kN]} \cdot \text{Length of the wedge tool [m]}} \tag{4.2}$$

Table 4-1. Simulation plan to select a stress-history dependent contact model

Independent variables	Range of investigation
Contact model	[HMLC EEPA]
Time-step	Percentage of Rayleigh time step [%]: [1.5 3 6.25 12.5 25 50] Corresponding absolute value [10^{-5} s]: [0.62 1.25 2.80 5.60 10.4 20.6]
Rotation of particles	[Allowed Restricted]

4.1.2. Simulation results

Figure 4-2 displays the influence of the investigated independent variables on the dimensionless penetration resistance, W_{50} and W_{80}. In the case of allowing particles to rotate, both contact models show a high sensitivity to the integration time-step. On the other hand, when the rotation of particles is restricted, the results are more stable, except for the 50% of Rayleigh time-step. When the time-step is too large, important data during contact detection and calculation is missed. Figure 4-3 also confirms the findings about effect of rotation; when the rotation of particles is activated, the bulk density changes during the simulation for both contact models. Therefore, the rotation of particles is capped for prospective simulations in this section.

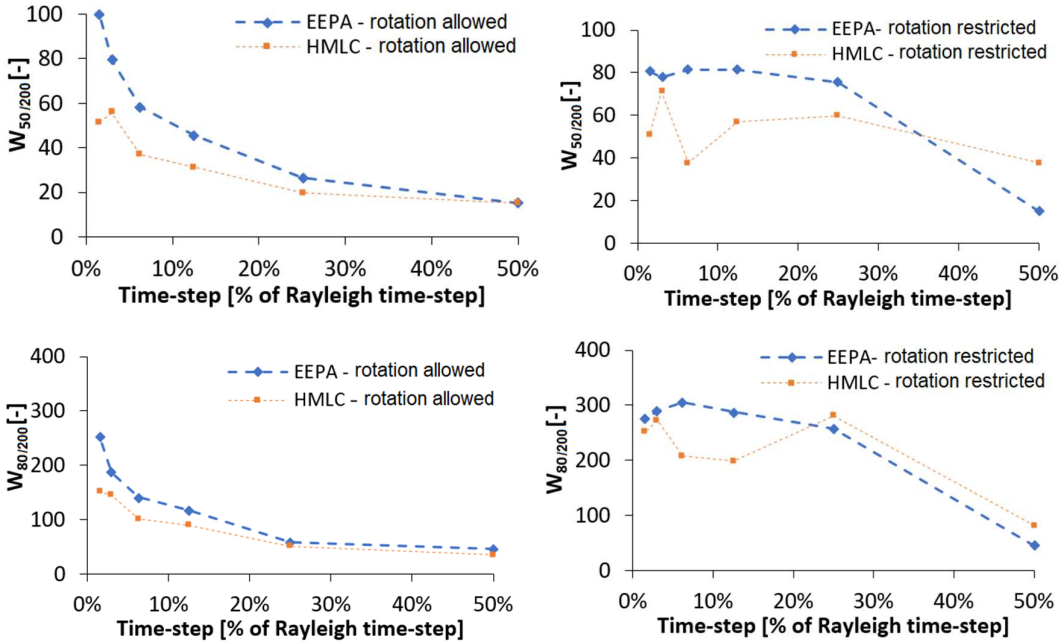

Figure 4-2. Influence of time-step on the dimensionless penetration resistance; left) rotation is allowed, and right) rotation is restricted

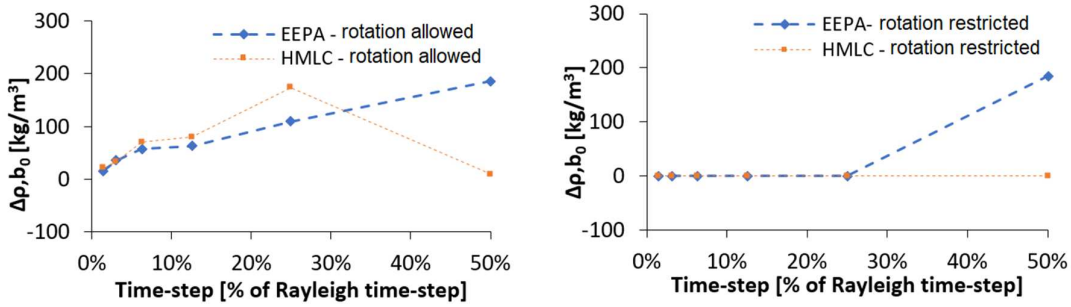

Figure 4-3. Influence of time-step on the bulk density change in the loose condition; left) rotation is allowed, and right) rotation is restricted

Next, the effect of contact model on the dependency of the simulation output on the applied pre-consolidation stress is investigated. In Figure 4-4, the results are compared with the experimental results obtained in Chapter 3 for the Carajas SF sample. In this experiment, three different levels of pre-consolidation stress are applied on the sample, 0, 8 and 65 kPa. As illustrated in Figure 4-4, a higher pre-consolidation stress results in a higher penetration resistance in both laboratory tests and the DEM simulations. The elastic contact model, HMLC (red squares), shows a lower dependency to the pre-consolidation stress, especially for the greater depth. This shows this contact model is unable to capture a realistic compressibility of the cohesive iron ore between the penetration tool and bottom of the container. On the other hand, the Elasto-plastic contact model, EEPA (blue diamonds), is capable to better replicate the dependency of the penetration resistance to the consolidation level. Although, the EEPA model underestimates W_{80} at the pre-consolidation of 8 kPa; calibrating the contact stiffness will probably improve the results.

Figure 4-5 displays the change in the bulk density before and after the consolidation stage. Similar to the penetration resistance, the EEPA model is more successful in replicating the laboratory results, with the exception in 8 kPa pre-consolidation stress.

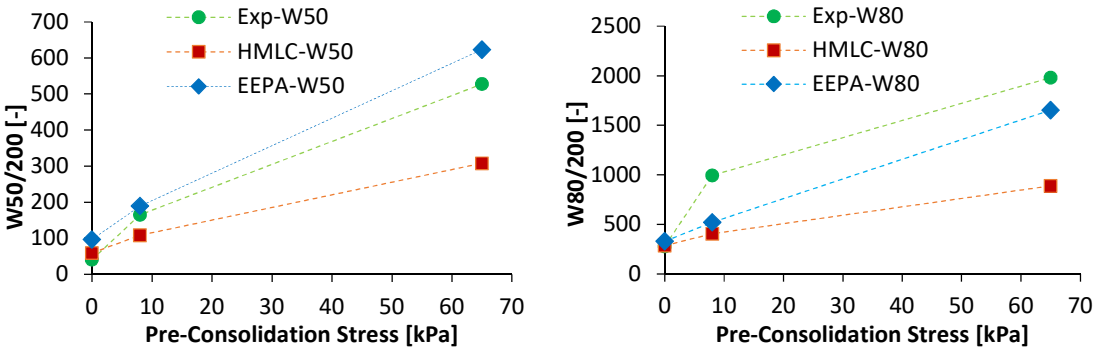

Figure 4-4. Effect of pre-consolidation stress on the penetration resistance; left) dimensionless penetration resistance at depth of 50 mm, and right) Dimensionless penetration resistance at depth of 80 mm

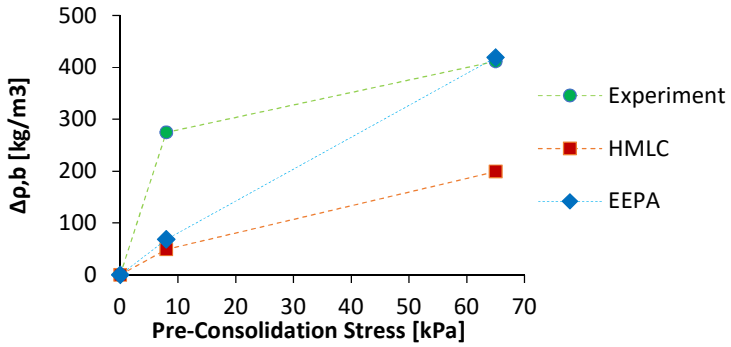

Figure 4-5. Effect of pre-consolidation stress on bulk density

Additionally, this section showed that the built-in rolling friction model of EDEM® software package, *model A*, produces simulations that are unstable. Restricting rotation of particles enhanced stability of the simulation. Another promising solution is to implement a rolling friction model in the software package that ensure a sufficient level of stability. Also, choosing an appropriate contact model is crucial for modelling cohesive materials properly. Further calibration of the EEPA contact model will minimize the mismatch between experimental and simulation results.

4.2. Scaling Technique

4.2.1. An overview of scaling techniques for DEM

To predict the outcome of the flow process accurately, the DEM parameters should be chosen carefully. To select the input parameters with confidence, the common procedure is to calibrate and to validate DEM simulations [9,28,87,88]. Three different calibration approaches for choosing DEM parameters can be named, as follows:

The first approach, *Direct Measuring*, requires measuring the input parameters directly at particle or contact level [11]. Accurate measurements of the micro-properties do not necessarily lead to a successful prediction of the bulk flow properties [2-3]. Furthermore, modelling the actual shape and size of particles leads to a computation time that is impractical for industrial applications, such as silo flow [4-5], transfer chutes [92–94], and ship unloader grabs [9], where the approximate number of particles required is greater than 10^7.

In the second approach, *in-situ calibration*, field experiments on a specific industrial process, at a scale of 1:1, are used to either calibrate or re-calibrate a DEM simulation replicating the real process. For example, Ilic et al. [93] have used the in-situ calibration approach in a qualitative way for modelling the accelerated flow in transfer chutes. Using this calibration approach, the shape and size of particles can be modelled in a simplified way that are different than those actually handled in full-scale operations [94]. In the in-situ calibration approach, a sufficient number of experiments must be conducted to avoid ambiguity of DEM parameter set [95]. Additionally, a disadvantage of the in-situ calibration approach is that the calibrated DEM parameter set depends on the design, and it might fail to simulate processes different than the in-situ calibration experiments.

In the third approach, *Bulk Calibration*, a laboratory experiment or series of experiments is/are first conducted to measure the bulk properties that are relevant to the application under consideration [11]. Next, the input parameters for DEM simulations are calibrated by minimising the mismatch between output simulations and laboratory measurements. In general, to produce comparable bulk responses, these calibration simulations replicate a laboratory setup and procedures at a scale of 1:1 [96].

Although the *Bulk Calibration Approach* can use a less detailed representation of particle shape and size, an important challenge remains the huge size of equipment used in bulk terminals, compared with particle size and the scale of calibration laboratory experiments. For instance, a Schulze Ring Shear Tester used to measure the bulk properties of particles smaller than 6 mm has an internal volume of less than 10^{-2} m^3 [97]. Equipment in bulk terminals, such as ship unloader grabs and silos, by contrast, have volumes that are 10^3 to 10^4 greater than laboratory devices. This challenge limits the use of DEM simulations for industrial applications [9-10].

Various approaches are used to reduce the computation time of DEM simulations. They can be categorized into two main groups. In the first group, computational techniques are used to speed up simulations, whereas particle size and geometry are kept constant. For instance, in [91]

reducing the stiffness of contact springs successfully led to more rapid simulation by allowing a larger integration time step to be chosen. [100] also proposed using a more efficient DEM solver to reduce the computation time.

In the second group, either geometric size or particle size or both is/are scaled. Table 4-2 provides an overview of the scaling techniques applicable to DEM simulations. Scaling can be done at either global or local level. At global level, scaling is applied to the entire simulation domain, influencing all the particles. For example, particle size can be scaled up in the entire domain by a constant scaling factor *s*. At local level, scaling is only applied to a specific region or a specific group of particles. For instance, in the *Scalping* or *Cut-off* technique [6, 15], finer fractions of particles are omitted by replacing them with the larger particle size fractions.

Table 4-2. An overview of scaling techniques applicable to DEM simulations (*s*: scaling factor)

Scaling technique	**Scaling factor of geometry**	**Scaling factor of particle**	**Level**
Local Particle Refinement	1	Variable *s* over domain	Local
Scalping (cut-off)	1	Finer fractions are up-scaled	Local
Exact Scaling	*s*	*s*	Global
Geometric Up- or Down-Scaling	*s*	1	Global
Coarse Graining (CG)	1	*s*	Global
Hybrid Particle-Geometric Scaling (current chapter)	S_{Box}	S_P	Global

The philosophy of *Local Particle Refinement*, which uses up-scaled particles outside the area of interest, is similar to Local Mesh Refinement [102]. This technique was successfully applied in [103] to model cone penetration into free-flowing materials using DEM. However, the main challenge when using local scaling techniques is that the speed of current DEM solvers depends mainly on the smallest particle size used in the simulation. The reduction in computation time is therefore limited by the critical integration time step.

In *Exact Scaling*, both particle size and geometric dimensions are scaled by the same scaling factor *s*. An example can be found in [104], which investigates the upscaling of the uni-axial confined, uni-axial unconfined and cone penetration test for cohesive elasto-plastic soils. An important uncertainty with the *Exact Scaling* method is that both micro-properties at particle scale (e.g. particle mass), and macro-properties at bulk scale (e.g. bulk volume, porosity) are varied simultaneously. For instance, to create comparable initial stress states during scaling, Janda and Ooi [104] suggested to reduce the gravity with the same scaling factor that is used to up-scale

particles and geometry sizes. Since the scaled system should have the same energy density as the original (unscaled) system [105], altering gravity during scaling is not recommended. *Schott et al.* [91] also proposed the *Geometric Downscaling* of excavation equipment, which did not result in confirmed scaling rules.

Another technique, referred to as *Coarse Graining (CG)*, substitutes larger grains for the original DEM particles, thus allowing for a lower number of particles in simulations. [9] successfully applied this technique, using the calibrated DEM parameters in a large-scale simulation of grabs and free flowing bulk materials. [106] investigated the coarse graining of the JKR contact model [9] combined with Hertz-Mindlin [107] in a shear tester, but no scaling rules for modelling cohesive bulk materials were established. A more successful study [30] investigated the Coarse Graining of an Adhesive Elasto-Plastic in the uniaxial consolidation process through a trial and error approach, and it found that the constant cohesion force of the contact spring (constant pull-off force) should be scaled up by the square of the particle scaling factor.

One or more combinations of the scaling techniques mentioned can be used to reduce the computation time of DEM simulations. For example, [96] used three different scaling techniques, *Exact Scaling*, *Coarse Graining* and *Scalping*, to simulate the angle of repose of a free-flowing bulk material. In practice, however, raw bulk materials and powders, such as moist iron ore fines and coal usually show cohesive elasto-plastic behaviour. Bulk responses of this type of materials, such as shear strength, bulk stiffness, and bulk density, depend on the history of applied normal pressure on the bulk specimen [21,22,48,108]. As discussed in the previous section, this stress-history dependent behavior can be simulated properly by using contact models that are based on an elasto-plastic adhesive spring. Thus, the question is how combinations of scaling solutions can be applied to a different contact model incorporating the behaviour of cohesive elasto-plastic materials.

In the remaining of this chapter, therefore, a hybrid particle-geometric scaling approach with the focus on an adhesive elasto-plastic DEM contact model is developed. This hybrid approach combines particle scaling with geometric scaling in a sequential manner. Figure 4-6 compares the idea behind the hybrid approach (Figure 4-6a) with Exact Scaling (Figure 4-6b) and particle upscaling (Figure 4-6c) techniques. In hybrid scaling, only particle properties (e.g. particle size, particle interaction parameters) or geometric properties (e.g. dimensions) are varied at a time, which is the main novelty over *Exact Scaling*. As discussed earlier, the main uncertainty with the *Exact Scaling* is that both micro-properties at particle scale, and macro-properties at bulk scale are varied simultaneously. In hybrid scaling, the geometric size is scaled each time after applying

particle upscaling, so basically larger particles can fit in the simulation setup. This creates a novelty for hybrid scaling over particle upscaling, in which up-scaled particles might not fit properly in the simulation setup. $\phi T_{Computation}$ is the ratio of the computation time of the scaled simulation to the computation time of the reference simulation.

By applying hybrid particle-geometric scaling on a simulation setup, its internal volume can be increased to a level comparable to equipment in solid bulk terminals. This allows to create DEM simulations of an industrial process that have practical computational time using scaled up particles.

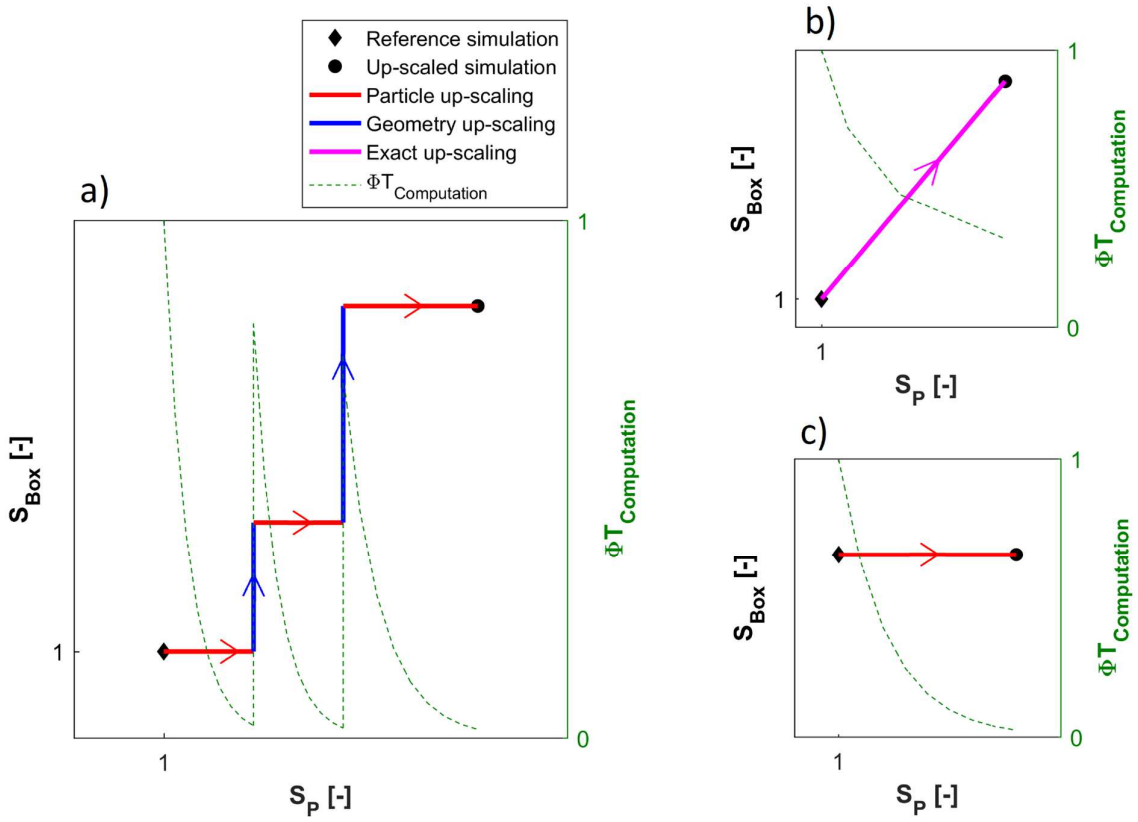

Figure 4-6. Scaling approaches, (a) hybrid particle-geometric scaling approach (b) Exact Scaling, and (c) particle upscaling

4.2.2. Particle scaling for an elasto-plastic adhesive contact model

The Coarse Graining technique substitutes coarse grains *s* times larger than the original particles for the original particles with radius R_p. In general, a higher scaling factor *s* leads to a lower computation time of DEM simulations. According to [105], the scaled system should have the same energy density as the original (unscaled) system. Using the same particle density maintains the same potential and kinetic energy densities through CG [9]. The contact stiffness and damping

should be also scaled precisely, to maintain the same energy losses between the scaled system and the original one.

Lommen et al. [9] establish the CG principles for the Hertz-Mindlin contact model in both the normal and tangential spring directions. Figure 4-7 shows the normal direction of the spring-damper system for both eight original particles and the substituted coarse grain with $s = 2$. If spherical particles are used, by maintaining the same Young's modulus in two systems, the contact stiffness and damping are identical to the equivalent stiffness and damping of the original system respectively.

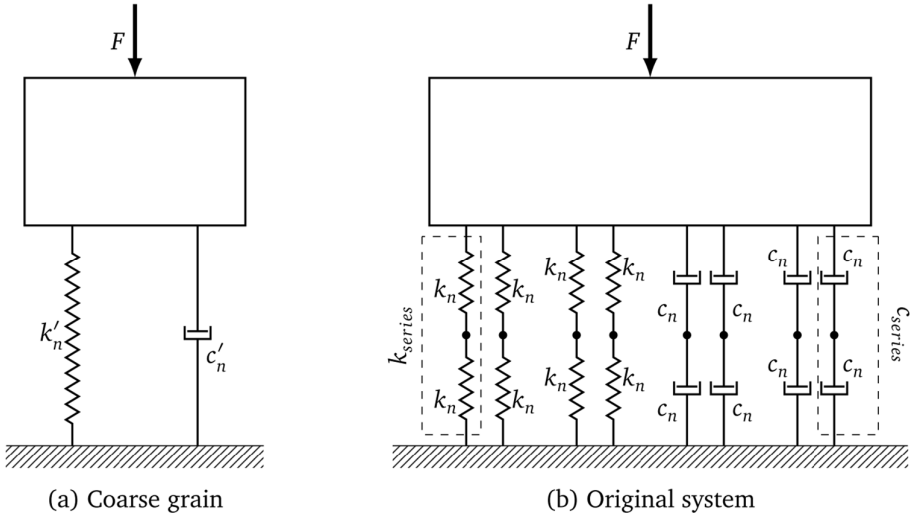

Figure 4-7. A coarse grain contact with a scaling factor of 2 and the equivalent contact of the original group of particles [9]

Figure 4-8 is a schematic diagram of the non-linear mode of the EEPA contact spring in the normal direction. The contact spring in the normal direction consists of four different parts:

- Constant pull-off force f_0 (N): an ever-present adhesive force that is added to other normal forces.
- *Branch* I, the loading spring: the contact follows the path k_1 when two particles are approaching each other. Choosing $n = 1.5$ makes the loading spring equivalent to the Hertz-Mindlin contact spring in the normal direction [84].
- *Branch* II, the unloading and reloading spring: due to plastic deformation, upon unloading the contact spring switches to the unloading and reloading spring k_2. The specific overlap corresponding to zero spring force during unloading is described as the plastic overlap δ_p. This plastic overlap is tracked and updated as the stress history-dependent parameter of the contact spring. The stiffness of the contact spring in *Branch* II, k_2, is a function of k_1 and the plasticity

ratio λ_P, and it is equal to $\frac{k_1}{1-\lambda_P}$. The plasticity ratio, λ_P, controls the ratio between stiffness in branch II (k_2) and stiffness in branch I (k_1), which shows the influence of plasticity ratio at contact scale. This means by increasing the plasticity ratio, a higher level of plastic overlap occurs during contact.

- *Branch* III, the adhesive spring: if unloading continues beyond δ_p, an adhesive (negative) force is created that is limited to the maximum adhesive force f_{min}. Once this point is reached, the adhesive spring is activated, whose stiffness is k_{adh}. If unloading continues, two particles separate if at $\delta_N = 0$ the absolute normal force is larger than the constant pull-off force f_0.

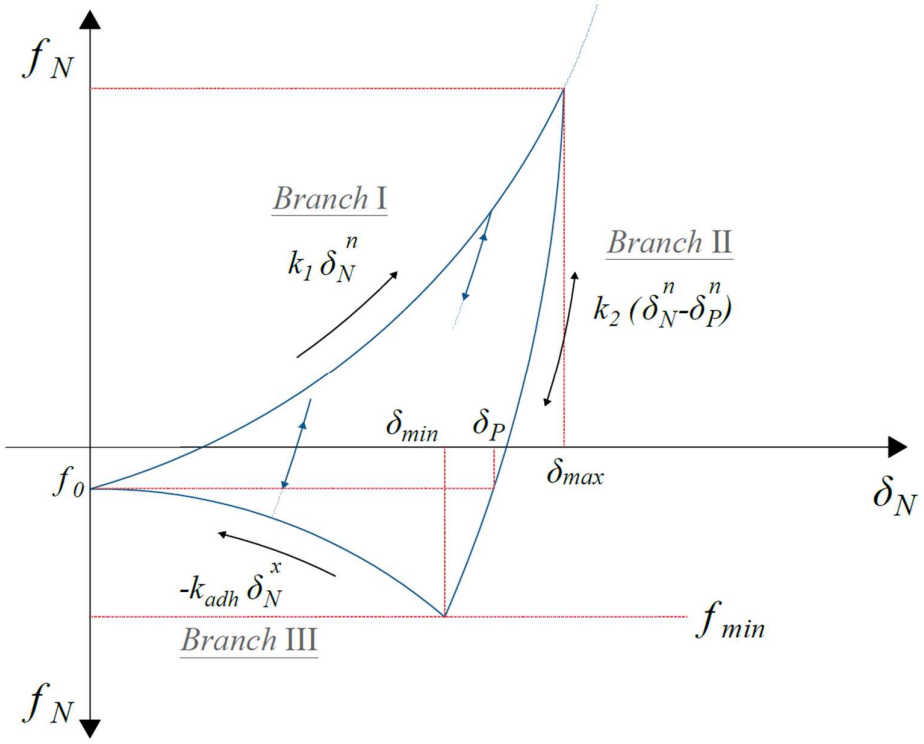

Figure 4-8. The relationships of the EEPA contact spring in the normal direction [84]

Eq. (4.3) shows the mathematical formulation of the sum of hysteretic force in the normal spring:

$$f_N = \begin{cases} f_0 + k_1 \delta_N^n & if\ k_2 (\delta_N^n - \delta_P^n) \geq k_1 \delta_N^n \\ f_0 + k_2 (\delta_N^n - \delta_P^n) & if\ k_1 \delta_N^n > k_2 (\delta_N^n - \delta_P^n) > -k_{adh} \delta_N^x \\ f_0 - k_{adh} \delta_N^x & if\ -k_{adh} \delta_N^x \geq k_2 (\delta_N^n - \delta_P^n) \end{cases} \quad (4.3)$$

If n = 1.5 is used, the stiffness of the contact spring in *Branch* I, k_1, is calculated as follows:

$$k_1 = \frac{4}{3} E^* \sqrt{R^*} \quad (4.4)$$

where E^* and R^* are the equivalent Young's modulus and radius of two particles that are in contact. By using $\lambda_P = 0$, the contact spring is converted to an elastic spring [24]. The plastic overlap is calculated in Eq.(4.5):

$$\delta_P = {\lambda_P}^{\frac{1}{n}} \delta_N \tag{4.5}$$

The stiffness of the adhesive spring, *Branch* III, is calculated as follows:

$$k_{adh} = \frac{(f_{min} - f_0)}{\delta_{min}^x} \tag{4.6}$$

where δ_{min} is the corresponding overlap with the maximum adhesive force f_{min}. Since the minimum overlap, δ_{min}, is the intersection between *Branch* II and *Branch* III, then it can be considered equal to $(\frac{f_{min}+k_2\ {\delta_P}^n}{k_2})^{1/n}$. The power value for *Branch* III is *x*. Similarly to JKR theory [109], the maximum adhesive force as formulated in Eq. (4.7) is a function of the contact patch radius *a* (m) and the adhesion surface energy $\Delta\gamma$ (J/m^2).

$$f_{min} = \frac{3}{2}\ \pi\ \Delta\gamma\ a \tag{4.7}$$

Figure 4-7 shows that the equivalent stiffness of the original system k_{eq}, which consists of s^2 pairs of series springs, can be derived using Eq. (4.8) for n = 1.5. Using the fact that in series springs, $\delta_{series} = s\ \delta_N$, and based on the definition of k_1 (Eq. (4.4), k_{eq} during loading is determined.

$$\begin{aligned} k_{eq,I} &= s^2\ k_{series} \\ &= s^2\ \frac{\frac{1}{4}F}{\delta_{series}^n} \\ &= s^2\ \frac{\frac{1}{4}F}{(s\ \delta_N)^n} \\ &= s^2\ \frac{k_1}{s^{1.5}} \\ &= \sqrt{s}\ k_1 \end{aligned} \tag{4.8}$$

Maintaining the same equivalent Young's modulus for the coarse system yields:

$$E^{*\prime} = E^* \tag{4.9}$$

Therefore, according to Eq. (4.10) in *Branch* I, the stiffness of the coarse system is equal to the equivalent stiffness of the original system. The same scaling rule is applicable to the tangential stiffness k_t [9].

$$\begin{aligned} k_1' &= \frac{4}{3}\, E^{*'} \sqrt{R^{*'}} \\ &= \frac{4}{3}\, E^{*} \sqrt{sR^{*}} \\ &= \sqrt{s}\, k_1 \\ &= k_{eq,I} \end{aligned} \tag{4.10}$$

Eq. (4.11) rewrites the normal force in unloading and reloading, *Branch* II, for the coarse system. First, k_2' and δ_P' are replaced by $\frac{k_1}{1-\lambda_P}$ and $\lambda_P{}^{\frac{1}{n}}\, \delta_N$ respectively.

$$\begin{aligned} f_{N,II}' &= k_2' \left({\delta_N'}^{\,n} - {\delta_P'}^{\,n} \right) \\ &= \frac{k_1'}{(1-\lambda_P')} \left({\delta_N'}^{\,n} - {\lambda_P'}^{\left(\frac{1}{n}\right)^n} {\delta_N'}^{\,n} \right) \\ &= \frac{k_1' \left(1 - {\lambda_P'}^{\left(\frac{1}{n}\right)^n}\right)}{(1-\lambda_P')} \left({\delta_N'}^{\,n} \right) \end{aligned} \tag{4.11}$$

Next, according to Eq. (4.10), k_1' is replaced by $\sqrt{s}\, k_1$. Also, since the coarse system is equivalent to s^2 pairs of series springs, $\delta_N' = s\, \delta_N$. If the same plasticity ratio λ_p is maintained for the coarse system, for n = 1.5:

$$\begin{aligned} f_{N,II}' &= \frac{\sqrt{s}\, k_1 \left(1 - \lambda_P^{\left(\frac{1}{n}\right)^n}\right)}{(1-\lambda_P)} s^{1.5}\, (\delta_N^n) \\ &= s^2 \frac{k_1 \left(1 - \lambda_P^{\left(\frac{1}{n}\right)^n}\right)}{(1-\lambda_P)} (\delta_N^n) \\ &= s^2\, k_2 \left(\delta_N^n \;\; - \delta_P^n \;\; \right) \\ &= s^2\, f_{N,II} \end{aligned} \tag{4.12}$$

Therefore, according to Eq. (4.12), during unloading and reloading, the stiffness of the coarse system is equivalent to the original system consisting of s^2 pairs of series springs.

The next step is to find scaling rules for cohesive forces. Figure 4-9 compares the constant pull-off springs between the original system and the coarse system with a scaling factor of 2. If the constant pull-off force is scaled up by s^2, according to Eq. (4.13), the force in the coarse system (F_A) is equal to the equivalent force in the original system (F_B). The equivalent constant pull-off forces in the original and coarse systems are therefore equal.

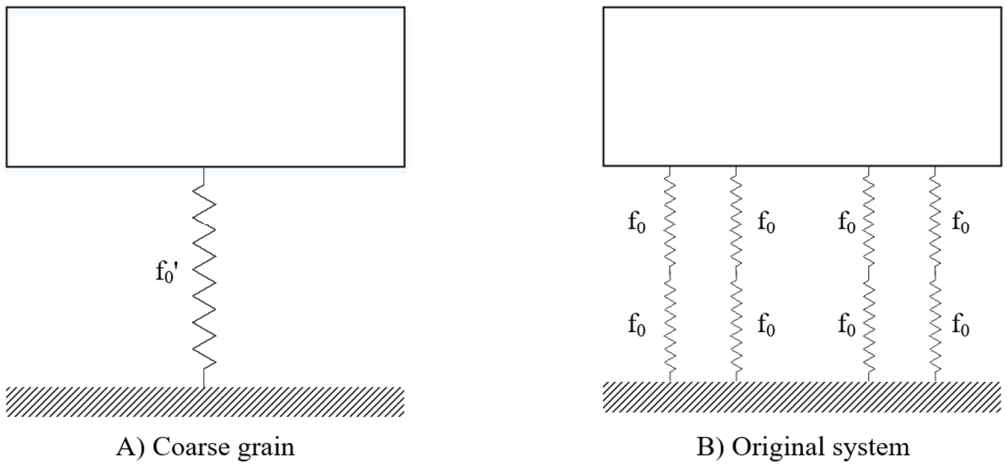

Figure 4-9. A coarse grain contact with a scaling factor of 2 during pull-off and the equivalent contact of the original group of particles

$$F_A = f_0' = s^2 f_0 = F_B \tag{4.13}$$

Similarly to Eq. (4.8), the equivalent stiffness of the original system in *Branch* III, $k_{eq.III}$, is derived in Eq. (4.14):

$$\begin{aligned} k_{eq,\mathrm{III}} &= s^2 k_{series} \\ &= s^2 \frac{\frac{1}{s^2} F_{series}}{\delta_{series}^x} \\ &= s^2 \frac{f_N}{(s\,\delta_N)^x} \\ &= s^{2-x} k_{adh} \end{aligned} \tag{4.14}$$

If the Surface Energy, $\Delta\gamma$, is scaled by the factor *s* for the coarse system:

$$\Delta\gamma' = s\,\Delta\gamma \tag{4.15}$$

Furthermore, since $\delta_N' = s\,\delta_N$, the contact radius *a* is proportional to the particle radius, which is scaled up by the scaling factor *s*. The minimum attractive force in the coarse system f_{min}' is therefore:

$$f_{min}' = \frac{3}{2} s^2 \pi\,\Delta\gamma\, a \tag{4.16}$$

Thus, according to Eqs. (4.6), (4.12), (4.13), (4.14), (4.16) and (4.17), in *Branch* III, for $n = 1.5$, the stiffness of the coarse system is proven to be equal to the equivalent stiffness of the original system. It is remarkable that changing the value of *x*, the power value of *Branch* III, leaves the

conclusion still valid. δ_{min} is replaced by $(\frac{f_{min}+k_2{\delta_P}^n}{k_2})^{1/n}$ using the fact that this point is the intersection between *Branch* II and *Branch* III.

$$
\begin{aligned}
k'_{adh} &= \frac{(f'_{min} - f'_0)}{{\delta'_{min}}^x} \\
&= \frac{s^2(f_{min} - f_0)}{(\frac{f'_{min} + k'_2\,{\delta'_P}^n}{k'_2})^{\frac{x}{n}}} \\
&= \frac{s^2(f_{min} - f_0)}{\left(\frac{s^2\,f_{min} + \sqrt{s}\;k_2\;\;s^n\,\delta_P^n}{\sqrt{s}\,k_2}\right)^{\frac{x}{n}}} \\
&== s^2(\frac{f_{min} - f_0}{s^x\,\delta_{min}^x}) \\
&= s^{2-x}\,k_{adh} \\
&= k_{eq,III}
\end{aligned}
\tag{4.17}
$$

4.2.3. Geometric scaling

Geometric dimensions are linearly scaled, which means that all the dimensions are scaled by the same factor, referred to in this chapter as S_{Box}. The scaling of geometric kinematics is also by the same scaling factor. This allows for maintaining a constant shear strain rate during geometric scaling.

4.3. Hybrid Simulation Plan for Particle and Geometric Scaling

In this section, a simulation plan is designed to firstly investigate the influence of the proposed particle scaling rules on bulk responses in quasi-static and dynamic regimes. Second, to evaluate the decoupled effect of scaling from both a particle and a geometric perspective, a hybrid particle-geometric simulation plan is created. To isolate the effects of S_{Box} from S_P, only one of them is varied at a time. In other words, when geometry dimensions are varied, particle properties (e.g. particle size, particle density, contact settings) are maintained constant. This allows for creating intersects between two levels of S_{Box}, as illustrated previously in Figure 4-6. Following test cases are used to study behaviour of bulk material from various aspects:

- Uniaxial confined consolidation simulation, which captures the stiffness of bulk material under vertical consolidation stresses. Using this case, it is evaluated whether bulk stiffness is scaled properly.

- Ledge angle of repose simulation, which is widely used to develop calibrated DEM simulations [9,14,82,96]. This test cases evaluates the performance of hybrid particle-geometric scaling when modelling the free-surface flow of cohesive bulk materials.
- Schulze ring shear simulation, which is used to model shear flow under the effect of consolidation stresses. Shear tests are commonly used to characterize bulk materials (free-flowing and cohesive) [50], and to calibrate DEM simulations [90,110–115].

The transition from a quasi-static to a dynamic regime can be characterized using the *Inertial Number*, I_{regime}, which has been used in [116] to study the shear flow. The ratio between inertial forces and confining pressure can be expressed using Eq. (4.18).

$$I_{regime} = 2\,\dot{\gamma}\,R_P\sqrt{\rho_P/_P} \tag{4.18}$$

where $\dot{\gamma}$ is the shear strain rate, R_P is the particle radius, ρ_P is the particle density, and P is the confining pressure. $I_{regime} \leq 0.01$ has been characterized as a quasi-static regime [116].

4.3.1. DEM input parameters

Main constant DEM parameters to model particles and their interaction are listed in Table 4-3a. These parameters are selected based on the calibrated DEM simulation of cohesive elasto-plastic coal in ring shear test that is developed in [29]. The calibrated DEM parameters have been verified in terms of shear strength and bulk density for various levels of consolidation pressure. A spherical shape is used to model DEM particles. A normal distribution of particle size with a standard deviation of 0.1 is used. A particle density of 1350 kg/m^3 has been used in [29]. In the current study, particle density is increased to 4500 kg/m^3 that allows to simulate density level of heavier bulk solids, including cohesive iron ore [8].

DEM input variables are listed in Table 4-3b. Main DEM variable in all tests is particle size. A reference particle radius of 5.5 mm has been used, corresponding to $S_P = 1$. The rotational freedom of particles can be suppressed artificially by either introducing a rolling friction model [85] or restricting rotation of particles [9,117]. Restricting rotation of particles has been done in [29] by applying a counterbalance torque in each time-step necessary to prevent rotational movement. This leads to increasing the resistance of particle against rotational torque. Restricting rotation of particles has been successfully used to resemble realistic material behavior [8,9,29,105,118]. A restricted rotation option as the reference value is used to consider the rotational torque between particles. The plasticity ratio is another DEM variable in this

investigation. A reference value of 0.75 is used to enable elasto-plastic behavior of the contact spring.

Table 4-3a. Constant DEM input parameters to model particles and their interaction - based on [29]

Item	Symbol	Units	Value
Shear Modulus	G	MPa	7.5
Poisson's ratio	υ	-	0.25
Particle shape	ψ_P	-	Sphere
Coefficient of restitution	$C_{R,p\text{-}p}$	-	0.01
Coefficient of static friction	$\mu_{s,P\text{-}P}$	-	0.25
Particle density	ρ_P	kg/m^3	4500

Table 4-3b. DEM input variables to model particles and their interaction

Item	Symbol	Units	Reference value
Particle radius at S_P=1	R_P	mm	5.5
Rolling friction model	-	-	Restricted rotation [29]
Plasticity ratio	λ_P	-	0.75 [29]

4.3.2. Uniaxial consolidation

Simulation setup

A virtual uniaxial confined consolidation simulation setup is used to evaluate the Coarse Graining technique under vertical consolidation stresses. Figure 4-10 shows the specifications of the simulation setup, including reference box dimensions. Particles are generated using a moving particle factory plate, which fills the box from bottom to top. This avoids compaction during the particle generation step, which might be caused by the kinetic energy of the particles. Next, particles are allowed to settle and to reach a static condition, where the ratio of the kinetic energy to the potential energy is less than 10^{-6}, as defined in [104]. Afterwards, the loading (consolidating) stage starts by moving the lid plate downward at a velocity of V_{Lid}. After the bulk material has been consolidated, the unloading stage starts by moving the lid plate upward at the same velocity. A lid velocity of 4 mm/s is used at $S_{Box} = 1$, which is equivalent to an axial strain rate of 0.02 s^{-1}. Based on Eq. (4.18), by using the axial strain rate, an Inertial Number, I, smaller than 0.01 during the consolidation (up to 200 kPa) is created, and therefore, the simulation procedure creates a quasi-static regime.

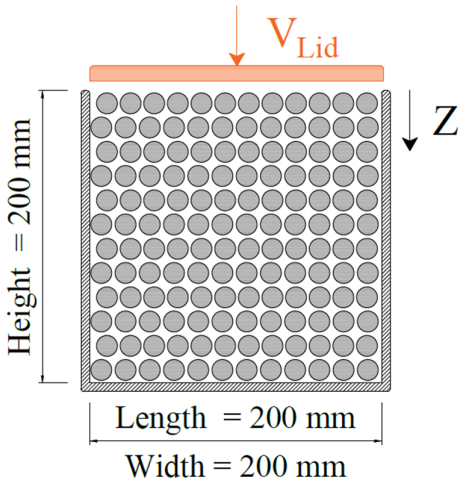

Figure 4-10. Schematic view of the uniaxial consolidation simulation setup (S_{Box} = 1)

Tests

Two different tests are conducted using the uniaxial simulation setup. The first test, 1.1, uses the non-adhesive non-linear Elastic mode of the contact model, which is basically similar to the Hertz-Mindlin contact model. In other words, λ_P, $\Delta\gamma$ and f_0 are set to zero in the first test with n = 1.5.

Figure 4-11 shows the experimental plan for Test 1.1 with the uniaxial consolidation simulation. Test 1.1 includes both the upscaling and downscaling of particle size and the upscaling of box size. The horizontal axis indicates the particle scaling factor S_P, and the vertical axis indicates the box scaling factor S_{Box}. The box dimensions and top lid velocity V_{Lid} are upscaled linearly, by scaling factors of 2.5 and 5, relative to the reference simulation setup. For each level of S_{Box}, five different levels of S_P are investigated. This results in smallest and largest particle radii of 2.2 and 33 mm respectively in Test 1.1.

In the second test, the contact plasticity is activated by setting λ_P = 0.75. Test 1.2 with uniaxial consolidation simulation uses the non-linear Elasto-Plastic mode of the *EEPA* contact model . S_P is varied from 2 to 6 while S_{Box} is kept constant at 5.

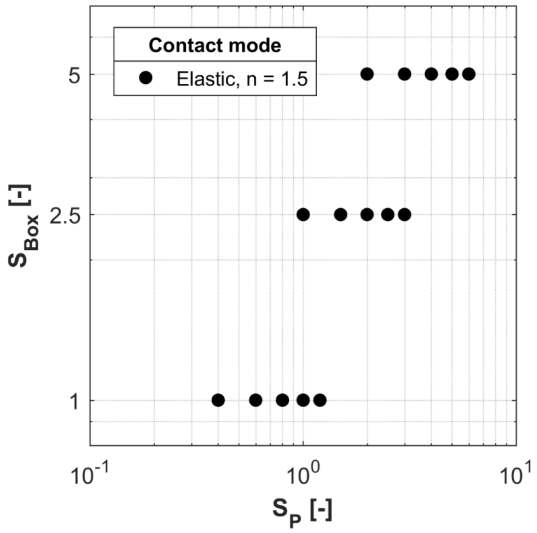

Figure 4-11. Experimental plan for hybrid particle-geometric scaling in Test 1.1 with the uniaxial consolidation setup

Objectives

The tests with the uniaxial consolidation setup determine two main responses. The first is the average porosity of bulk material, as formulated in [50]. This parameter compares the packing densities after filling the box in different simulations. The second response is the pressure on the moving lid σ_{Lid} during its displacement in the z direction. This enables the stiffness of bulk material during loading and unloading to be compared at different levels of S_P and S_{Box}.

4.3.3. Angle of repose

Simulation setup

The angle of repose (α_M) is an important characteristic in bulk handling processes; according to [71], angle of repose results are useful to categorise flow properties. Multiple test procedures are available in literature to determine α_M, some example are described in [50]. Using different test procedures, different values of angle of repose (α_M) for a same bulk material can be expected [9]. A ledge method setup or shear box is used to simulate the static angle of repose. Figure 4-12 shows the reference test box dimensions. The container is 200 mm high, 200 mm long and 80 mm wide. The fixed parts are coloured black. The red part, which is the flap opening, starts moving at a velocity of V = 1 m/s to initiate particle flow by removing the lateral support. This leads to a shear strain rate of up to 0.2 s^{-1}, and I larger than 0.01 during the flow under the gravity force. Based on (4.18), the simulation procedure creates a dynamic regime that ends with a static condition once an angle of repose is formed.

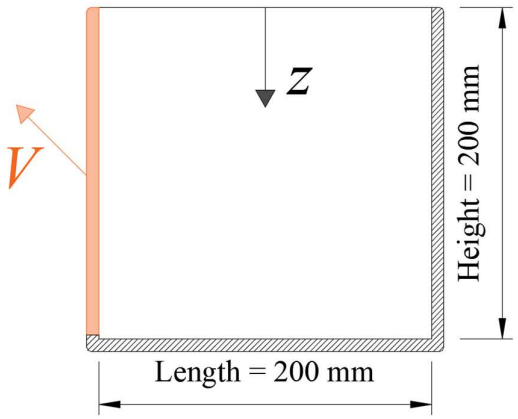

Figure 4-12. Dimensions of the angle of repose test setup; reference box size (S_{Box} = 1)

Tests

Three tests are conducted using the ledge angle of repose setup. To be consistent with the previous uniaxial consolidation test experiments, a reference particle radius of 5.5 mm, equivalent to $S_p = 1$, is used in the current experiments. Figure 4-13 shows the experimental plan for Test 2.1, which verifies the developed coarse graining technique by applying a hybrid particle-geometric scaling approach, in which both particle size and box size are varied in a sequential manner.

In the second test, 2.2, particle size and level of cohesion are varied using a full factorial experiment to verify the coarse graining technique for different levels of cohesion. In Table 4-4, a *relative cohesion* term is defined to distinguish between the expected levels of bulk cohesion, from a relative low angle of repose to high values. For example, at a medium level of relative cohesion for $S_P = 2$, $\Delta\gamma$ and f_0 are equal to 20 J/m^2 and -0.32 N respectively. To create relatively high bulk cohesion for $S_P = 2$, $\Delta\gamma$ and f_0 are increased by 50% respectively, compared to the medium level. A decrease of 50% is also applied to create relatively low cohesion.

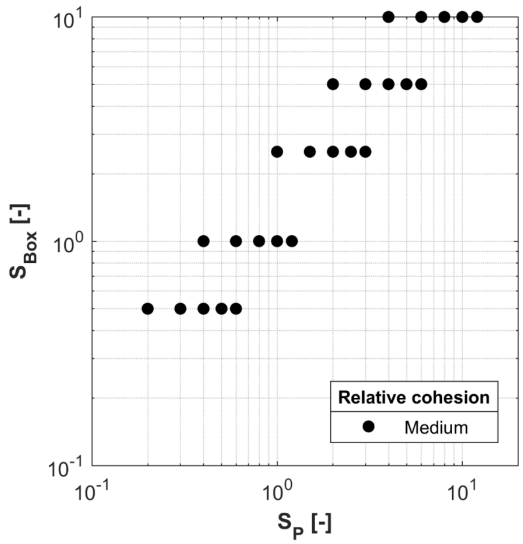

Figure 4-13. Experimental plan for hybrid particle-geometric scaling in Test 2.1 with an angle of repose setup

Table 4-4. Three different levels of relative cohesion for $S_P = 2$

Level of relative cohesion	$\Delta\gamma$ [J/m^2]	f_0 [N]
Low	10	-0.16
Medium	20	-0.32
High	30	-0.48

All the simulations in Test 2.1 are conducted at medium relative cohesion. Thus, $\Delta\gamma$ and f_0 are varied with respect to the particle scaling factor S_P according to equations (4.15) and (4.13) respectively. The test box dimensions are also scaled by geometric scaling factors S_{Box} of 0.5, 2.5, 5 and 10. Five levels of S_P, the particle scaling factor, are tested at each level of S_{Box}. This results in a total of 25 simulations in Test 2.1. First, in the smallest box size, $S_{Box} = 0.5$, five different particle scales are simulated, S_p equal to 0.2, 0.3, 0.4, 0.5 and 0.6. Next, five particle sizes are simulated in $S_{Box} = 1.0$, that are equal to $S_p = 0.4$, 0.6, 0.8, 1.0 and 1.2. S_p equal to 0.4 and 0.6 are simulated in both $S_{Box} = 0.5$ and 1.0. It is expected that by maintaining the particle size constant, the angle of repose can be compared under the effect of varying box dimensions. In other words, the link between $S_{Box} = 0.5$ and 1.0 in the experimental plan is $S_p = 0.4$ and 0.6, which allows to verify the adequacy of hybrid particle-geometric scaling using the ledge angle of repose simulations setup. The hybrid scaling is continued by using $S_{Box} = 2.5$ and $S_p = 1$, 1.5, 2, 2.5, 3. In $S_{Box} = 5$, particle scales of 2, 3, 4, 5, and 6 are simulated. Using the largest geometry dimension, $S_{Box} = 10$, particle scales of 4, 6, 8, 10 and 12 corresponding to particle radii of 22, 33, 44, 55 and

66 mm are simulated. Therefore, in Test 2.1 with the ledge angle of repose setup, adequacy of the following hypotheses are checked:

a) The particle scaling rules that are established through equations (4.8) to (4.17) is applicable for various particle sizes

b) The exact scaling, where both particle and geometry are scaled with a same scaling factor, is not applicable on cohesive materials when an elasto-plastic adhesive contact model is used. In other words, the effect of particle scaling should be decoupled from the effect of geometry scaling, which can be done using a hybrid particle-geometric scaling approach.

In Test 2.2, the dimensions of the text box are kept constant at $S_{Box} = 5$. The particle size is varied from $S_P = 1$ to 6, and three levels of relative cohesion are investigated. This results in running a total of 15 simulations.

In Test 2.3, the effect of coarse graining is also evaluated for the case of enabling rotation of particles. The following variables are included in Test 2.3: particle scaling factor, coefficient of static friction, and coefficient of rolling friction. The rolling friction model follows the recommendation by Ai et al. [85] to use model C for quasi-static conditions. Following the suggestion of [119], the rolling stiffness of [120] is used and the viscous rolling damping torque is disabled. By enabling rotation of particles, their mobility increases, so higher restrictive forces (e.g. cohesive and friction) needs to be used, compared to the case when the rotation restricted option is used. The reference values of coefficients of static friction and rolling friction are chosen according to the calibrated model of wet sand in [121], which are equal to 0.7 and 0.8 respectively. for $S_P = 2$, $\Delta\gamma$ and f_0 equal to 100 J/m^2 and -1.32 N are used respectively. This resulted in $\alpha_M = 53^\circ$, similar to the angle of repose measured for $S_P = 2$ in $S_{box} = 5$ with the medium relative cohesion level when the restricted rotation option is used. $\Delta\gamma$ and f_0 are varied with respect to the particle scaling factor S_P according to equations (4.15) and (4.13) respectively. In this test, the ledge angle of repose simulation is done using $S_{box} = 5$, and $S_p = 2$, 3, 4, 5, and 6. Using an one-variable-at-a-time approach, level of $\mu_{s,p\text{-}p}$ is varied between 0.3 to 0.9, and level of $\mu_{r,p\text{-}p}$ is varied between 0.4 to 1. This allows to confirm the particle scaling rules are independent of levels of coefficient of static and rolling friction.

Objectives

The equilibrium of forces and stresses can be drawn for a critical failure angle $\alpha_{M,critical}$, as illustrated in Figure 4-14. In an arbitrary cutting plane A_s, different normal and shear stresses will act, depending on $\alpha_{M,critical}$. All normal and shear stresses at the free surface are equal to zero.

Failure will occur once τ_α exceeds the shear strength of the bulk material. According to the Mohr-Coulomb equation, the shear strength of bulk material τ_s is often approximated by Eq. (4.19) [70]:

$$\tau_s = \tau_c + \sigma_\alpha \tan(\varphi) \tag{4.19}$$

where *tan(φ)* indicates the friction coefficient of the bulk material. τ_c denotes the cohesion strength of the bulk material: in other words, τ_c is the shear strength of the bulk material if $\sigma_\alpha = 0$. If the box dimensions in the Test 2.1 are scaled up, the vertical stress acting on A_s increases, due to the greater weight of bulk material. Although the exact location of A_s is unknown, Eq. (4.19) suggests that increasing the normal stress σ_α, decreases the contribution of *c* to the shear strength. A negative correlation between S_{Box} and α_M can therefore be expected. To enable the effect of box scaling on the angle of repose of cohesive materials to be evaluated, we need to ensure that the vertical pressure in the z direction (and consequently σ_α) is scaled correctly in DEM simulations.

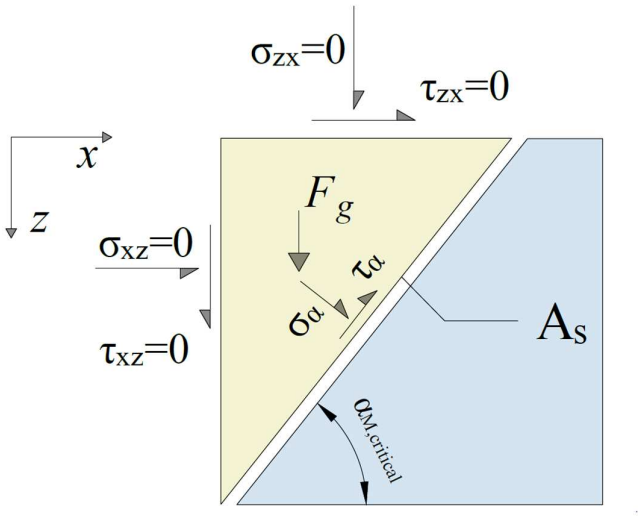

Figure 4-14. Equilibrium of forces at the critical failure angle

According to [122], normal stresses in vertical sections can be calculated using Eq. (4.20), in which the constant vertical stress σ_v is assumed to act across the cross-sectional area *A*.

$$\sigma_{v,z} = \frac{g\ \rho_b\ A}{K \tan(\varphi_x)\ U}\left[1 - e^{\frac{-K \tan(\varphi_x)\ U\ z}{A}}\right] \tag{4.20}$$

where *g*, ρ_b, *K*, φ_x, which denote standard gravity, bulk density, lateral stress ratio and wall friction angle respectively, are assumed to be constant [50]. *U* is the cross-sectional perimeter, and *z* is the bulk material height above the cross-section. Since in Test 2.1 all the box dimensions are scaled linearly, according to Eq. (4.21) a linear relationship exists between $\sigma_{v,bottom}$ and S_{box}.

$$\sigma_{v,bottom} = \frac{g\ \rho_b\ (S_{Box}^2\ A_1)}{K\ \tan(\varphi_x)\ (S_{Box}\ U_1)}[1 - e^{\frac{-K\ \tan(\varphi_x)\ (S_{Box}\ U_1)\ (S_{Box}\ z_1)}{(S_{Box}^2\ A_1)}}]$$
$$= S_{Box}(\frac{g\ \rho_b\ A_1}{K\ \tan(\varphi_x)\ U_1}\left[1 - e^{\frac{-K\ \tan(\varphi_x)\ U_1\ z_1}{A_1}}\right]) \quad (4.21)$$
$$= \alpha\ S_{Box}$$

where the parameters with subscript 1 refer to the original box dimensions with $S_{box} = 1$. $\sigma_{v,bottom}$ increases linearly when S_{box} is increased, where the constant α is the rate of change. To check whether a unique α can be obtained during hybrid particle-geometric scaling, and also to ensure that the simulation results match the analytical solution, $\sigma_{v,bottom}$ is measured for all the simulations.

The coordination number, or the average contacts per particle, is another important factor in quantifying particle packing [123]. This indicator is used here to evaluate the effect of both Coarse Graining and geometric scaling on particle packing. The average coordination number over all the particles is measured after the bulk material has reached a static condition. Since the number of contacts between geometry and particles is basically higher for simulations with smaller particles, only contacts between particles are included when calculating the average coordination number.

In addition, the angle of repose α_M is measured using a computer image-analysis technique as proposed in [124]. Once a static angle of repose is created, α_M is determined from the images by taking the coordinates of ten equally spaced points on the slope of the material. Then, the linear regression technique is used to fit a straight line to the data points and the angle of the line with the horizontal represents the angle of repose. Using the images, the bulk surface profiles after the creation of the angle of repose are also compared between simulations.

The four parameters mentioned, $\sigma_{v,bottom}$, average coordination number, α_M and bulk surface profile, are used to evaluate the effects of particle and box scaling on the angle of repose simulation.

4.3.4. Ring shear test

Simulation setup

A DEM simulation of the ring shear test (RST) is set up based on [97] and [125]. The RST is commonly used to characterise the flowability of cohesive and free-flowing materials. A schematic cross-sectional view of the RST cell filled with particles is shown in Figure 4-15.

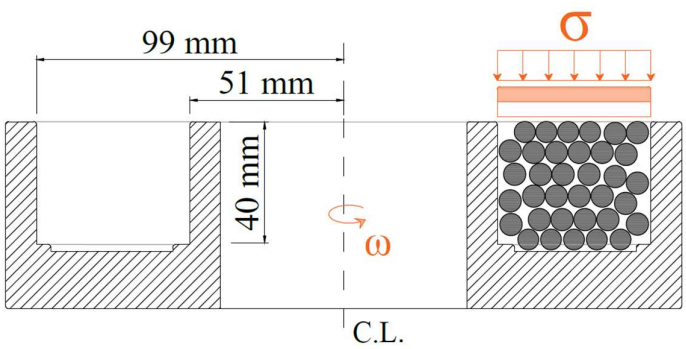

Figure 4-15. Schematic cross-sectional view of the original ring shear cell: (left) cell dimensions, (right) schematic view of process

The simulation setup and test procedure is similar to [29], in which the calibrated DEM parameters of cohesive material using the elasto-plastic adhesive contact model is developed. In the simulation, the shear cell is first filled with particles. After they reach the static condition, the pre-shearing stage starts. In this stage, a uniform normal pressure of 20 kPa is first applied to the bulk material surface using the lid plate. Next, the shear cell starts to rotate over the centre line (C.L.) with a rotational velocity of ω_{cell}. A range of rotational velocity between 5 to 20 degree/s was used. It was found that this range of velocity is enough to create a steady-state shear flow in the bulk material. Using a lower rotational velocity a longer time is required to to create the steady-state shear stress in simulation. For that reason, to ensure that the steady-state is always reached within the simulation time, a ω_{cell} = 15 deg/s is used in all simulations with ring shear test. This leads to a shear strain rate of 0.49 s^{-1}, and a dynamic regime. In the second stage of the test, the shearing stage, the normal pressure is reduced to 2 kPa to measure the shear stress of the pre-consolidated bulk material.

Test

Figure 4-16 shows the experimental plan designed to scale RST simulations. Three different shear cell sizes are created by scaling the reference cell by scaling factors of 2 and 5, while ω_{cell} is kept constant during this test. The particle radius is also varied from 2.2 to 27.5 mm.

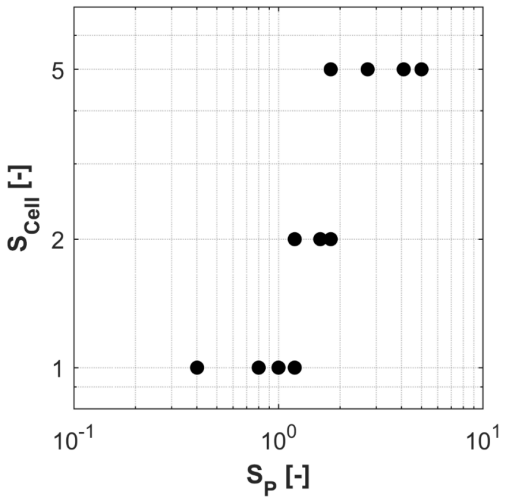

Figure 4-16. Experimental plan for hybrid particle-geometric scaling in Test 3 with RST

Objectives

The shear stress values are measured at both the pre-shearing and shearing stages, referred to in this chapter as τ_{pre} and τ_{shear} respectively. The measured values of τ_{pre} and τ_{shear} for different combinations of S_{Cell} and S_P are used to evaluate the hybrid particle-geometric scaling in RST simulations.

4.4. Results of Hybrid Particle-Geometric Scaling

4.4.1. Uniaxial consolidation

Figure 4-17 shows the porosity values measured for different levels of S_{Box}. The average porosity is measured after the particles reach a static condition, and before starting the loading stage. Upscaling the box dimensions decreases the porosity, due to a greater total mass of particles, which results in denser packing in general. These results show that S_{Box} and average porosity are strongly correlated, with a correlation coefficient of -0.985. The maximum porosity at each level of S_{Box} is measured for the smallest value of S_P/S_{Box}, thus the minimum porosity is measured for the highest value of S_P/S_{Box} respectively. Hence the minimum porosity occurs when $S_P = 6$ at $S_{Box} = 5$ and is equal to 0.385. This value is higher than the theoretical limit of minimum porosity for rigid spheres. According to [126], n_{min} (also known as $n_{Keppler}$) for rigid spherical particles = approximately 0.22. The maximum variation in porosity due to the scaling of particle radius is 0.5%. This variation is probably caused by the particle generation method, where the new particle is placed in the simulation domain without any contact with neighbouring particles. The initial conditions are therefore adequately comparable at each level of S_{Box}.

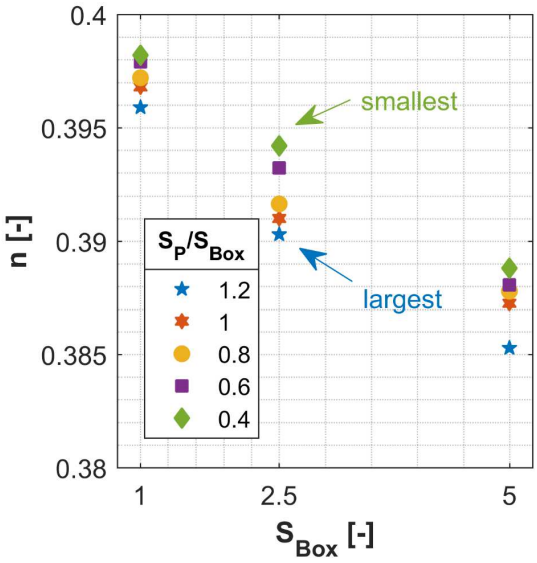

Figure 4-17. Porosity in Test 1 (uniaxial consolidation test) before loading

Figure 4-18 shows the outcome of Test 1.1, which illustrates the influence of both S_{Box} and S_P on the loading and unloading behaviour of bulk material. The vertical axis represents σ_{Lid} and the horizontal axis indicates the vertical location of the lid plate Z_{Lid} divided by the height of the box H_{Box}. The σ_{Lid} variation due to particle upscaling is determined by calculating the maximum difference between σ_{Lid} in the simulation with the smallest S_P and other simulations.

As shown in Figure 4-18a, for $S_{Box} = 1$, loading is continued until $Z_{Lid}/H_{Box} = 0.15$, and a maximum σ_{Lid} of 184 ± 6 kPa is measured for S_P from 0.4 to 1.2. The minimum σ_{Lid}, 0 kPa, during the unloading stage for $S_{Box} = 1$ occurs at $Z_{Lid}/H_{Box} = 0.0302 \pm 0.0020$. This value represents the residual deformation due to one complete cycle of loading (consolidating) and unloading the bulk material.

As shown in Figure 4-18b, for $S_{Box} = 2.5$, loading is continued until $Z_{Lid}/H_{Box} = 0.12$, and a maximum σ_{Lid} of 165 ± 4 kPa is measured. A residual deformation of 0.0243 ± 0.0000 is measured. As shown in Figure 4-18c, for $S_{Box} = 5$, loading is continued until $Z_{Lid}/H_{Box} = 0.12$, and a maximum σ_{Lid} of 151 ± 4 kPa is measured for S_P from 2 to 6. A residual deformation of 0.0276 ± 0.0004 is measured.

On average, a standard deviation of 3% is measured for both maximum σ_{Lid} and residual deformation at three levels of S_{Box}. Test 1.1 therefore confirms that the uniaxial confined consolidation simulation using the non-linear non-Adhesive mode of the contact model is adequately insensitive to particle scaling. This mode of the contact model is equivalent to Hertz-Mindlin.

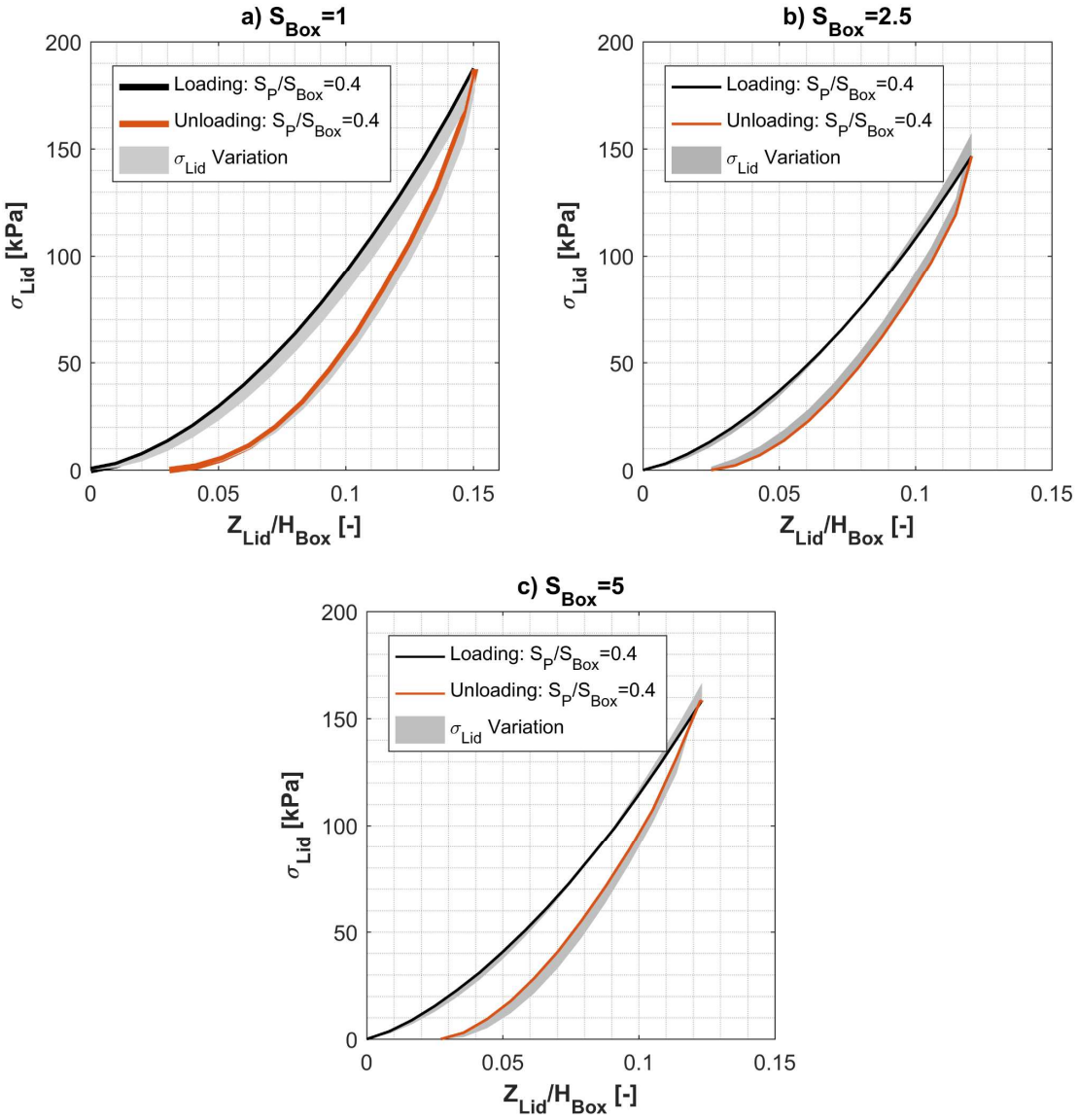

Figure 4-18. Influence of S_P and S_{Box} on the loading and unloading paths of the non-linear Elastic contact mode in the uniaxial consolidation simulation (Test 1.1)

Figure 4-19 shows the outcome of Test 1.2, which uses the non-linear elasto-plastic mode of the contact model. Loading is continued until Z_{Lid}/H_{Box} = 0.095, and a maximum σ_{Lid} of 120 ± 1 kPa is measured. This results in a standard deviation of less than 1% in maximum σ_{Lid} with varying the particle radius from 11 to 33 mm. A residual deformation of 0.0749 ± 0.0006 is measured in Test 1.2, which is 2.7 times the residual deformation in the equivalent S_{Box} in Test 1.1 when $\lambda_p = 0$. The considerable difference in the value of residual deformation, as well as the difference in maximum σ_{Lid}, is due to enabling the plasticity of the contact model, which has been discussed in [24] as well. A standard deviation of less than 1% is measured for the residual deformation in Test 1.2.

The above shows that, in both the elastic and elasto-plastic modes of the contact model, the loading and unloading paths are adequately independent from S_P. Coarse Graining as well hybrid particle-geometric scaling are therefore applicable to the uniaxial confined consolidation test.

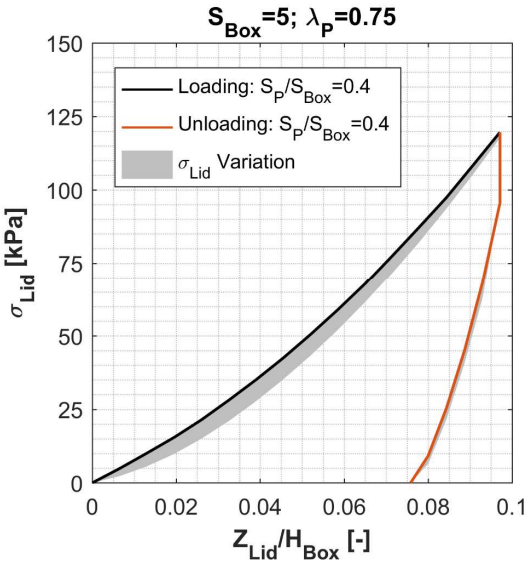

Figure 4-19. Influence of S_P and S_{Box} on the loading and unloading paths of the non-linear Elasto-Plastic contact mode in the uniaxial consolidation simulation (Test 1.2)

4.4.2. Angle of repose

Figure 4-20 shows the relationship between $\sigma_{v,bottom}$, S_{Box} and particle size. The vertical axis indicates $\sigma_{v,bottom}$; the horizontal axes in Figure 4-20a and Figure 4-20b show the box scaling factor S_{Box} and S_P/S_{Box} respectively. According to the fitted linear regression in Figure 4-20a, the simulation results match the analytical solution with $\alpha = 3.43$ and a coefficient of determination R^2 of 0.9989. This confirms that the simulation is able to capture the effect of geometry scaling on the vertical pressure distribution properly. A negligible effect of S_P/S_{Box} on $\sigma_{v,bottom}$ is measured in Figure 4-20b. The normal pressure on the cutting plane σ_α is therefore scaled correctly in DEM simulations, and it is comparable at every level of S_{Box}.

As Figure 4-21 shows, for the entire range of S_P/S_{Box}, the average coordination number follows a similar trend as S_{Box} increases. Particle packing therefore depends on S_{Box}. Although some deviations of the average coordination number, up to 10%, are captured for $S_{Box} = 0.5$ and 1, the influence of S_P/S_{Box} on particle packing is significantly less than the effect of S_{Box}. The increase in the average coordination number due to the scaling of box dimensions is caused by the strong correlation between S_{Box} and vertical pressure in the bulk material, as demonstrated previously in Figure 4-20. As illustrated in Figure 4-22, the coordination number (averaged in

horizontal directions) increases in the *z* direction. In other words, particle packing is in the loosest state near the bulk surface ($z \rightarrow 0$), and the bulk material becomes denser as z/H_{Box} increases. In general, increasing H_{Box} in Test 2.1 creates denser packing at a higher level of S_{Box}.

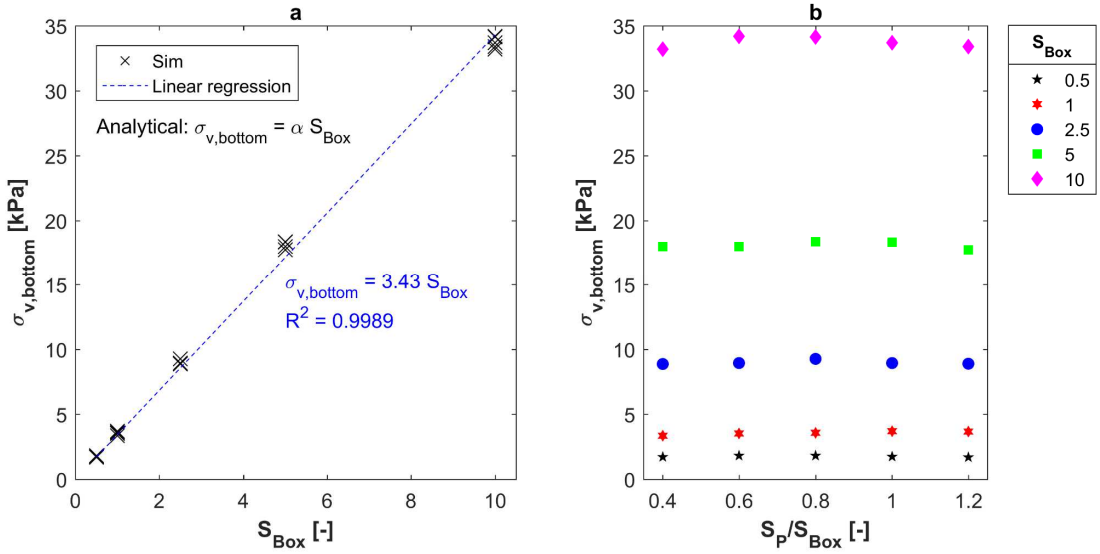

Figure 4-20. $\sigma_{v,bottom}$ in Test 2.1; (a) linear relationship between $\sigma_{v,bottom}$ and S_{Box}, (b) negligible sensitivity of $\sigma_{v,bottom}$ to particle size

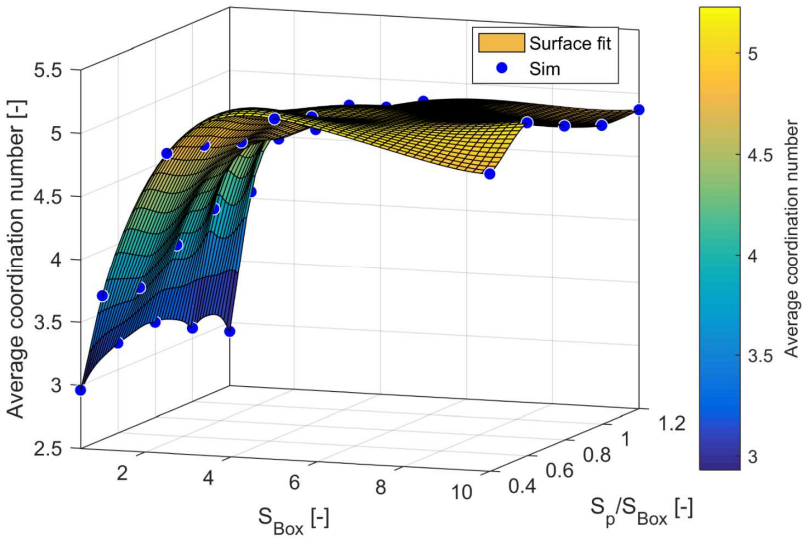

Figure 4-21. Average coordination number in Test 2.1

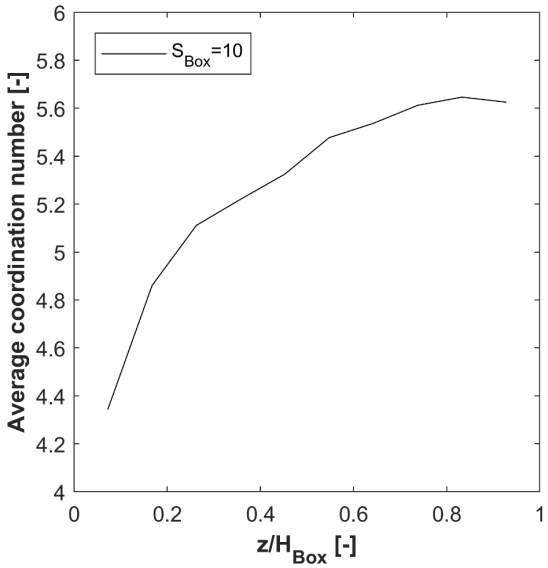

Figure 4-22. Increasing particle packing over box height (S_P = 4)

Figure 4-23 shows the angle of repose results of Test 2.1, in which S_P and S_{Box} are varied. With S_{Box} = 0.5 and 1, an angle of repose of 90° is measured for all the particle sizes. If the box dimensions are scaled up with S_{Box} = 2.5, the particles start to form an angle of repose smaller than 90°, which is equal to 63° in average. A standard deviation of only 1° is measured for S_{Box} = 2.5. The average values of α_M at S_{Box} = 5 and 10 are 53° and 43° respectively; standard deviations of less than 1° are measured in these tests when varying the particle size. Considering the low standard deviation values, the particle-scaling thus successfully replicated similar angles of repose for the S_P/S_{Box} range investigated at each level of S_{Box}. Therefore, hypothesis *a* (described in Section 4.3.3) on the adequacy of the particle scaling rules in the ledge angle of repose simulation is confirmed.

Furthermore, the performance of Exact Scaling, where both S_P and S_{Box} are scaled at the same time, is analysed in the angle of repose simulation. Figure 4-24 shows the α_M of the simulations where S_P = S_{Box}. Increasing the scaling factor, as Eq. (4.20) suggests, makes the cohesion term *c* less of a contributory factor to the shear strength compared to the friction coefficient, tan(φ). This led to a negative non-linear relationship between the geometry scaling factor and α_M. Exact Scaling is therefore an inadequate solution to scaling the angle of repose simulation for cohesive materials when an elasto-plastic adhesive contact model is used. This is consistent with findings of [94] in DEM modelling of a draw-down test. This confirms hypothesis *b*, which was described in Section 4.3.3.

In addition, in the hybrid experimental plan designed, at each level of S_{Box} at least one S_P intersects with a higher level of S_{Box}. For example, $S_P = 1$ is simulated in both S_{Box} equal to 1 and 2.5, corresponding to S_p/S_{Box} equal to 1 and 0.4 respectively. According to Figure 4-23, for $S_P = 1$ at $S_{Box} = 1$, an $\alpha_M = 90^\circ$ is captured, while at $S_{Box} = 2.5$ using the same particle size and contact settings, α_M is equal to 64˚. The difference in the angle of repose is caused due to the differences in level of normal pressure and average coordination number, that were demonstrated earlier in this section. For that reason, following a hybrid particle-geometric scaling, first particles are scaled up from $S_P = 0.4$ to 1.2. Second, geometry dimensions are scaled up from $S_{Box} = 1$ to 2.5, by keeping the particle size and contact settings constant for $S_P = 1$. Next, particles are scaled up from $S_P = 1$ to higher scales i.e. $S_P = 3$. Given the success of the particle scaling rules, α_M is adequately equal between $S_P = 1$ and 3 at $S_{Box} = 2.5$. Additionally, the intersection between $S_{Box} = 1$ and 2.5 is $S_P = 1$. Therefore, up-scaling is done from $S_P = 0.4$ to 3 in this case, by decoupling the geometry scaling from particle scaling. This is done by using an intersection point between $S_{Box} = 1$ and 2.5, which is $S_P = 1$. Applying a similar rationale, the effect of geometry scaling is decoupled from the particle scaling for the other levels of $S_{Box.}$ Using hybrid particle-geometric scaling, the ledge angle of repose simulation is therefore scaled up by increasing the particle size 60 times, from a particle radius of 1.1 mm to 66 mm.

Keeping S_{Box} constant in the Test 2.2 enables the effect of the cohesion parameters $\Delta\gamma$ and f_0 under Coarse Graining to be investigated. To analyse the results of Test 2.2, in addition to α_M, the difference in bulk surface profiles is shown. Figure 4-25 illustrates an example of comparing bulk surfaces between two DEM simulation outputs. The left image shows the reference image, in which $S_P = 2$ and relative cohesion is set at a low level. The right image compares the outcome of the simulation with $S_P = 5$ and a similar level of relative cohesion with the reference image. The green area indicates the missing area in the second image compared with the reference image. Red lines, which represent the bulk surface offset by particle radius in the simulation with $S_P = 2$ ($2\ R_{P,ref.} = 11$ mm), are used to evaluate the variation in bulk surface. The bulk surface in the coarse grained simulation therefore matches the reference simulation well.

Figure 4-26 compares the bulk surfaces between simulations with low (left) and high (right) relative cohesion levels. The magenta area indicates the difference due to the increase in cohesion. Both the angle of repose and the bulk surface irregularity increase as the relative cohesion increases.

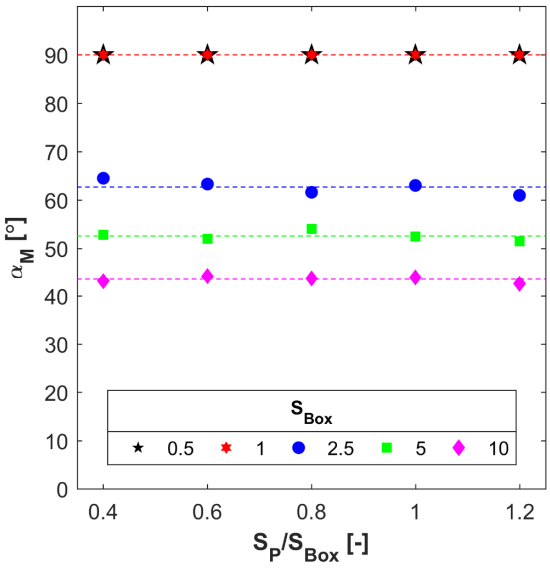

Figure 4-23. Influence of particle and geometric scaling on the angle of repose results in Test 2.1

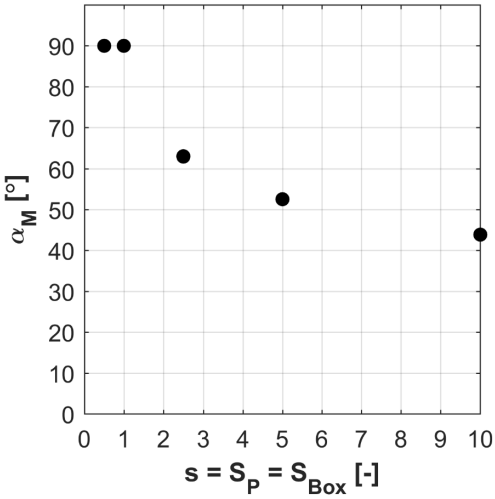

Figure 4-24. Inadequacy of Exact Scaling in angle of repose simulation of cohesive materials

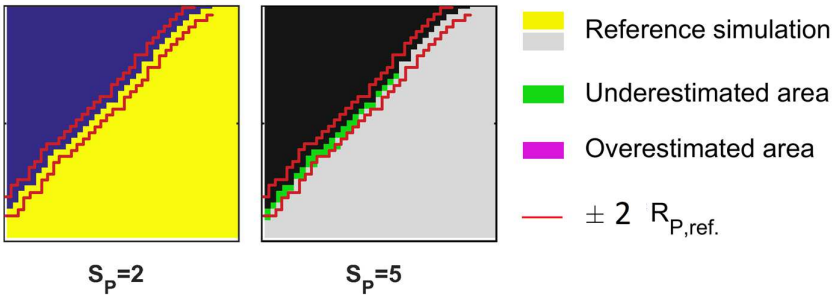

Figure 4-25. Comparing bulk surface between two particle scaling factors (low relative cohesion)

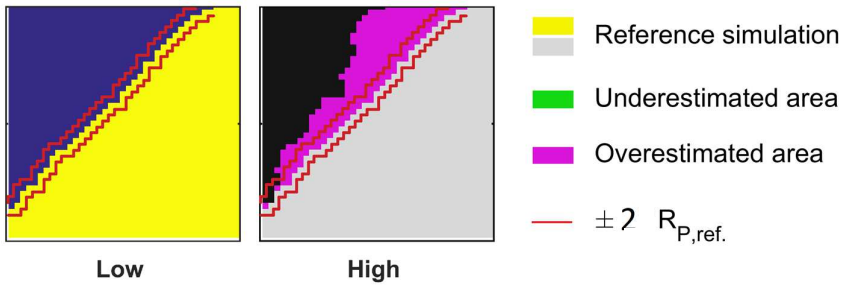

Figure 4-26. Comparing bulk surface between two different levels of relative cohesion at S_P=2

Figure 4-27 shows comparative bulk surfaces at low, medium and high levels of relative cohesion. In general, the mismatch is zero in the upper part of piles, and is only present in the middle and lower parts of the pile. Overall, at all three levels of relative cohesion, the difference in bulk surface between coarse grained particles and the simulation with R_P = 11 mm (S_P = 2) is limited to 2 $R_{P,ref}$ = 11 mm.

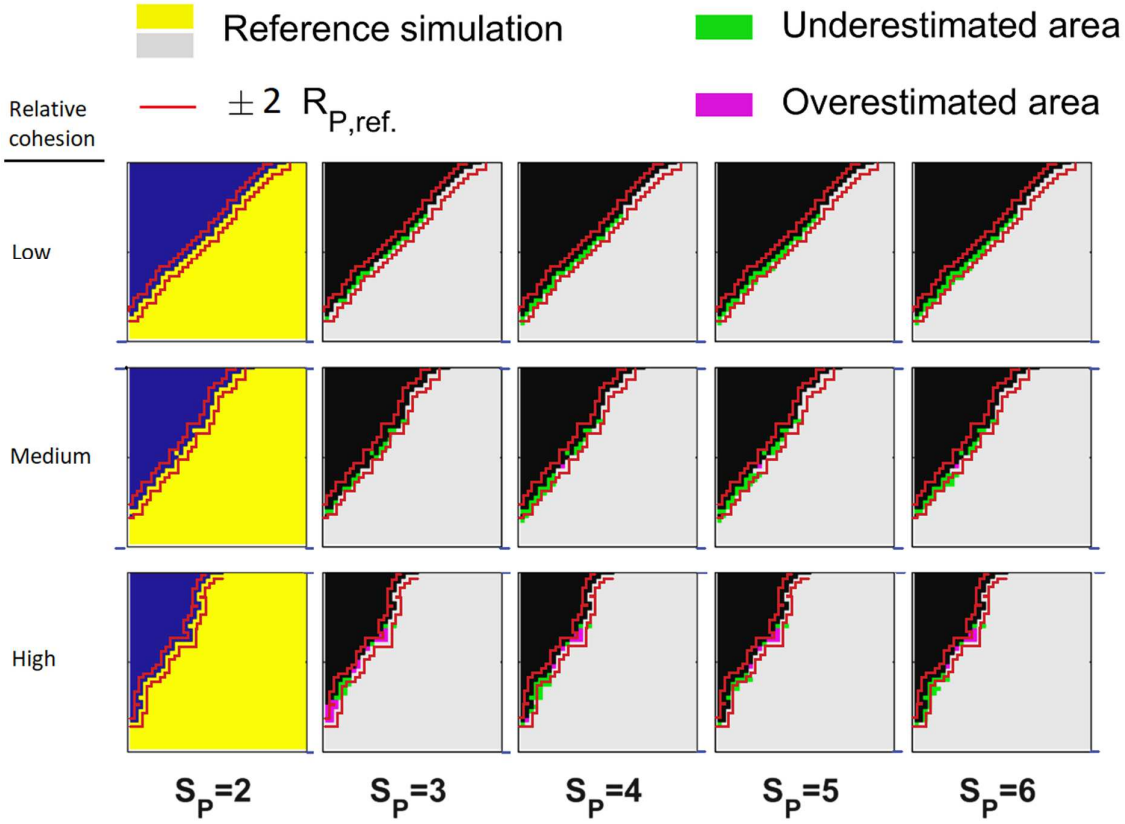

Figure 4-27. Angle of repose results in Test 2.2

Figure 4-28 compares α_M in Test 2.2. The dashed line shows the average α_M at all five levels of S_P. The average α_M with low relative cohesion is equal to 47° with a standard deviation of less than 1°. Increasing the relative cohesion to a medium level increases the average α_M to 53°, and

an average α_M of 62° is measured at high relative cohesion with a standard deviation of 1°. This confirms that the Coarse Graining technique is applicable to different levels of relative cohesion.

Angle of repose results in Test 2.3, in which the rolling friction C is used, are presented in Table 4-5. By increasing coefficient of static friction from 0.3 to 0.9, the average α_M is increased from 45˚ to 56˚. By increasing coefficient of rolling friction from 0.4 to 1, and maintaining a constant coefficient of static friction at 0.7, average α_M is increased from 47˚ to 54˚. In all cases, by varying particle scaling factor, a standard deviation of 1˚ or less is captured for α_M. This shows that the particle scaling rules were established in Section 4.3 are applicable when a rolling friction model (e.g. model C) is used. Additionally, scalability of particles in the ledge angle of repose simulation for elasto-plastic cohesive materials is confirmed independent of values of coefficients of static and rolling friction.

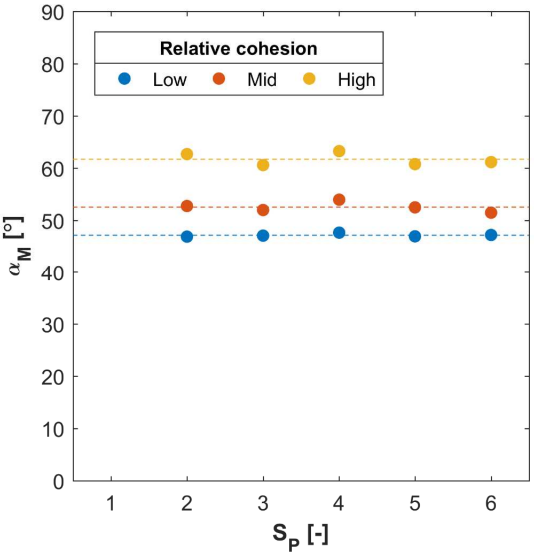

Figure 4-28. Angle of repose results in Test 2.2

Table 4-5. Effect of coefficients of static and rolling friction on the angle of repose for different particle scaling factors, S_P =2 to 6, at S_{Box} = 5

$\mu_{s,P-P}$	$\mu_{r,P-P}$	α_M [˚]
0.3	0.8	45±0.6
0.5	0.8	48±1.0
0.7	0.8	53±0.7
0.9	0.8	56±0.6
0.7	0.4	47±0.9
0.7	0.6	50±0.4
0.7	1	54±0.8

4.4.3. Ring shear test

Figure 4-29 shows the outcome of the test with the RST simulation. For each simulation, two different shear stress values are plotted. The results of the pre-shearing stage τ_{pre} and the shearing stage τ_{shear} are plotted in the left and right graphs respectively. τ_{pre} and τ_{shear} of 20.5 kPa and 5.3 kPa respectively are measured for S_P = 0.4, the smallest particle size. ±20% of the measured shear stress values for S_P = 0.4 is used to evaluate the influence of particle and geometric scaling. In other words, a variation of ±20%, compared to the measured shear stress values for the smallest particle size, is considered acceptable during scaling of the ring shear test. As the left graph shows, τ_{pre} increases by 20% when particle size is scaled up from S_P = 0.4 to S_P = 5 and the geometry of S_{Box} is scaled up from 1 to 5. Similarly to the pre-shear stage, the shearing stage results show that τ_{shear} increases by 20%, due to the scaling up of particles and geometry. In addition, a comparison of the results of the pre-shear and shearing stages shows that during the shearing stage, a relatively higher variation in τ due to upscaling is measured. The measured values of τ_{shear} for intersects of different levels of S_{Cell} (i.e. S_P = 1.2 and 1.8) vary considerably when geometric size is scaled up. The hybrid particle-geometric scaling approach therefore enables the upscaling of both particles and geometry in this test by using the intersect points that decouples the effect of particle and geometric scaling on shear stress .

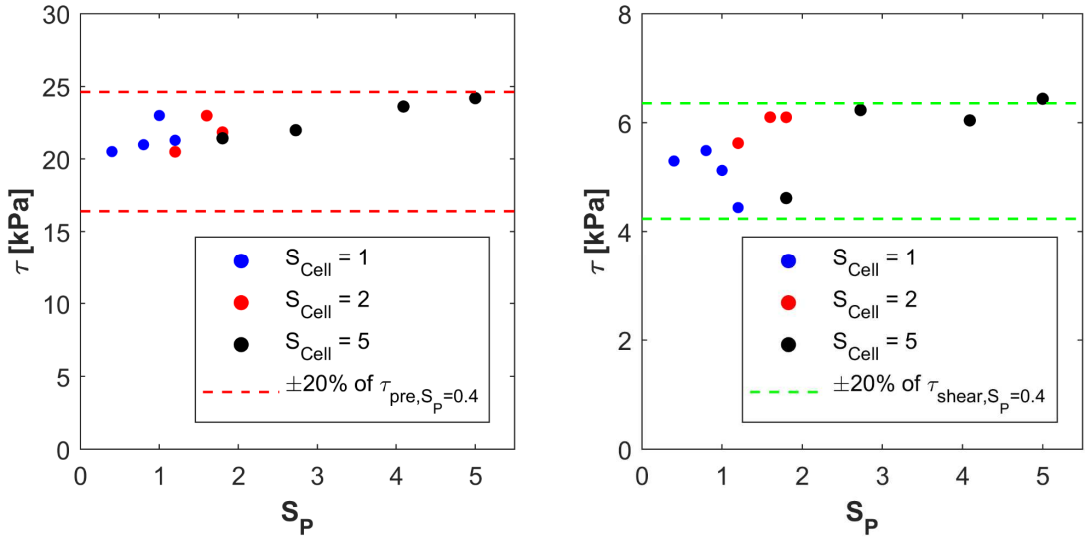

Figure 4-29. Ring shear test results: (left) pre-shear stage, (right) shearing stage

4.5. On Applying Hybrid Particle-Geometric Scaling

Using a hybrid particle-geometric scaling, the upscaling of particles and geometry can be used to develop large-scale DEM simulations of industrial granular processes, such as grabs, silo flow

and transfer chutes, while a minimized computational time is maintained. To achieve this, steps shown in Table 4-6 are recommended to follow.

Table 4-6. Necessary steps to apply hybrid particle-geometric scaling in combination with DEM calibration

	I) Laboratory test	II) Calibrated DEM simulation	III) Simulating geometric scaling	IV) Simulating particle scaling
S_{Box}	1	1	>1 (e.g. 5)	>1 (e.g. 5)
Sp	1	1	1	>1 (e.g. 5)
Response 1 (e.g. bulk stiffness)	y_1	y_1	y_1'	y_1'
Response 2 (e.g. angle of repose)	y_2	y_2	y_2'	y_2'
Response 3 (e.g. shear strength)	y_3	y_3	y_3'	y_3'

- Step I is to conduct the laboratory tests to characterize complex behaviour of cohesive and elasto-plastic materials for various bulk responses, denoted by *y*.
- Step II is to calibrate the DEM simulation replicating the laboratory tests at a scale of 1:1, which is a common calibration procedure.
- Step III is to vary the geometry scale by maintaining constant particle size and contact settings. Values of bulk responses are expected to be affected by geometric scaling.
- Step IV is to vary the particle scale and to compare bulk responses with outcome of step III. More scaling steps can be added to reach the desired trade-off between computational time and accuracy. Once a scaled up simulation with a reduced computational time is developed, validation should be achieved using in-situ experiments [9]. Validation experiments can be done in quantitative and qualitative ways; some examples can be found in [8,28,92–94,127–131].

4.5.1. Implementation for other contact models

The current chapter applies hybrid particle-geometric scaling to the Edinburgh elasto-plastic adhesive (EEPA) contact model. In general, the hybrid scaling approach can be used for other cohesive DEM contact models simulating cohesive materials. For instance, the Hertz-Mindlin contact model combined with the Linear Cohesion model, as formulated in [22], can be used to model elastic adhesive (cohesive) bulk materials. Using the Linear Cohesion model adds an

additional normal cohesive force to the Hertz-Mindlin model. The additional normal cohesive force is calculated according to Eq. (4.22):

$$f_{adh} = k_{adh}\, A \tag{4.22}$$

where k_{adh} is the cohesion energy density (J/m^3) and A is the contact area (m^2). The particle scaling rules can be established similarly to the approach that was used earlier in Section 4.2. Using the superposition principle, the equivalent force of the original system $f_{adh,eq}$, which consists of s^2 pairs of series springs, can be derived using Eq. (4.23). Using the fact that in series springs, $\delta_{series} = s\, \delta_N$, the contact area is scaled by s^2. Maintaining k_{adh} constant during scaling makes the additional normal cohesive force f_{adh} scale-invariant.

$$f_{adh,eq} = s^2\, f_n = s^2\, k_{adh}\, A \tag{4.23}$$

The concept of the *EEPA* contact model is similar to the Adhesive Elasto-Plastic contact model that was earlier developed by *S. Luding* in [23]. The main difference between these two contact models is that in *Luding's* model, the contact stiffness during unloading and reloading also depends on the plastic overlap δ_P. This allows the level of non-linearity of plastic displacements during unloading and reloading to be adjusted. This difference should be taken into account if Coarse Graining is applied to the contact model described in [23].

4.6. Conclusion

In this chapter, a hybrid particle-geometric scaling approach was developed that allows for scaling DEM simulations by isolating the effects of varying particle size and geometric dimensions on bulk properties. Additionally, particle scaling rules were derived by extending the Coarse Graining technique to incorporate two important aspects of bulk materials, their elasto-plastic behaviour and their cohesive forces.

- Three different types of tests were used to confirm that the proposed particle scaling rules as well as hybrid particle-geometric scaling are applicable to quasi-static and dynamic regimes.
- Uniaxial consolidation test at various vertical confining pressures, up to 190 kPa: the Coarse Graining technique is applicable to both the non-linear Elastic and non-linear Elasto-Plastic modes of the EEPA contact model. This was confirmed for a range of particle sizes, from a diameter of 2.2 mm until 60 mm.
- Ledge angle of repose that investigates the shear flow of cohesive materials under gravity force: first, the hybrid scaling approach was successfully applied to scale up the particle size as well

the geometry size. In other words, the particle size was scaled up to 60 times by isolating the effect of particle scaling from geometric scaling. Furthermore, the Exact Scaling technique, where both particle size and geometry are scaled using the same scaling factor, is inadequate for the ledge angle of repose test for cohesive (elasto-plastic) materials. Comparable initial conditions (e.g. average coordination number) cannot be created using Exact Scaling. Second, the particle scaling rules have been successfully applied to different levels of cohesion parameters f_0 and $\Delta\gamma$. There was a positive correlation between cohesion and ledge angle of repose.

- Shear stress values in ring shear test for both the pre-shear (τ_{pre}) and shearing (τ_{shear}) stages: the variations were limited to 20% by applying the hybrid particle-geometric scaling.

It was demonstrated that the constant pull-off force f_0 and the surface energy $\Delta\gamma$ should be scaled by the factors s^2 and s respectively during particle scaling. Furthermore, in hybrid particle-geometric scaling, only particle properties (e.g. particle size, particle interaction parameters) or geometric properties (e.g. dimensions) are varied at a time, which is the main novelty over Exact Scaling or Coarse Graining. Using a hybrid scaling, the upscaling of particles and geometry can be used to develop large-scale DEM simulations of cohesive (elasto-plastic) bulk solids with a minimized computational time. Next chapter will focus on calibrating DEM input parameters using the EEPA contact model.

5

A multi-objective DEM calibration procedure for cohesive and stress-history dependent bulk solids*

DEM simulations can only predict bulk level responses accurately if their input parameters are calibrated appropriately. Calibration aims at finding an optimal combination set of DEM input parameters that replicates the captured bulk responses. This chapter presents a reliable and novel calibration procedure for simulating the bulk responses of Carajas SF that were captured in Chapter 3.

Multiple challenges are experienced when calibrating DEM input parameters for cohesive materials. Section 5.1 discusses major challenges, including that DEM calibration may lead to either an "ambiguous parameter combination" or an empty solution space. In other words, a calibration procedure might fail to meet definiteness and feasibility criteria. Another major

---

* This chapter corresponds to: M.J. Mohajeri, C. van Rhee, D.L. Schott, "Replicating cohesive and stress-history dependent behavior of bulk solids: feasibility and definiteness in DEM calibration procedure". Accepted in Advanced Powder Technology, 2021.

challenge in DEM calibration is that the categorical-type DEM variables (e.g. contact module) have not yet been considered when optimization methods are used. A multi-step multi-objective procedure is introduced to address definiteness and feasibility, including both continuous and categorical DEM variables. In each step, the variables' solution space is narrowed down to be further optimized in the next step. The specific DEM calibration targets, simulation setups, and initial sampling strategy are also introduced in Section 5.2. Section 5.3 presents results of the multi-step DEM calibration. The adequacy of calibrated input parameters are verified in Section 5.4. Section 5.5 presents conclusion on the adequacy of the calibration procedure, in terms of definiteness, feasibility evaluation, sampling techniques, number of variables and calibration targets.

5.1. Feasibility and Definiteness in DEM Calibration Procedure

To simulate, design, and optimize processes and equipment for handling bulk solids, such as iron ore and coal, the discrete element method (DEM) is an adequately accurate computational method. However, DEM simulations can only predict bulk level responses (e.g. shear strength) accurately if their input parameters are selected appropriately. To select the input parameters with confidence, the common procedure is to calibrate [9,28,87,88].

Over the past decade, reliable DEM calibration procedures have been developed to model free-flowing bulk solids, such as iron ore pellets [9], glass beads [12], sinter ore [13], sand [14,15], and gravel [16,17]. By setting multiple targets for the DEM calibration, more than a single bulk response can be considered. This prevents the "ambiguous parameter combinations" problem in the DEM calibration procedure, which is discussed in detail in [17]. For example, to calibrate DEM input variables for simulating iron pellets in interaction with ship unloader grabs, Lommen et al. [9] considered at least three different calibration targets. They replicated the static angle of repose using the ledge and free-cone methods; the penetration resistance of iron pellets was also replicated, using a wedge penetration test setup.

In general, DEM calibration is performed following the generic procedure shown in Figure 5-1 To find an optimal combination of DEM input parameters that satisfies multiple calibration targets, optimization methods can offer a solution. Various optimization methods have already been applied to calibrate the *continuous* type of DEM variables successfully [12,13,16,132]. Continuous DEM variables are numerical variables that have an infinite number of values between any two values [133]. For example, the coefficient of static friction is an

important continuous DEM variable during calibration [11]. Richter et al. [16] concluded that surrogate modeling-based optimization methods are most promising for DEM calibration when continuous variables are included.

Categorical-type DEM variables have not yet been included in the calibration procedure when optimization methods are used. Categorical variables are finite numbers of groups or categories that might not have a logical order [133]. For example, shape of particles is a DEM categorical variable that plays an important role during calibration [134]. One can use design of experiments (DoE) methods to include categorical variables in the DEM calibration procedure. However, a high number of simulations might have to be run with no guarantee of finding an optimal set of DEM input parameters [16]. Additionally, iron ore fines and other similar bulk solids (e.g. coal) have an irregular distribution of particle shape [20] as well as fine particle sizes [30]. Modeling accurate particle shapes and sizes for cohesive bulk solids in DEM simulations thus leads to a computation time that is generally impractical for studying industrial bulk handling processes, such as flow in silo [30].

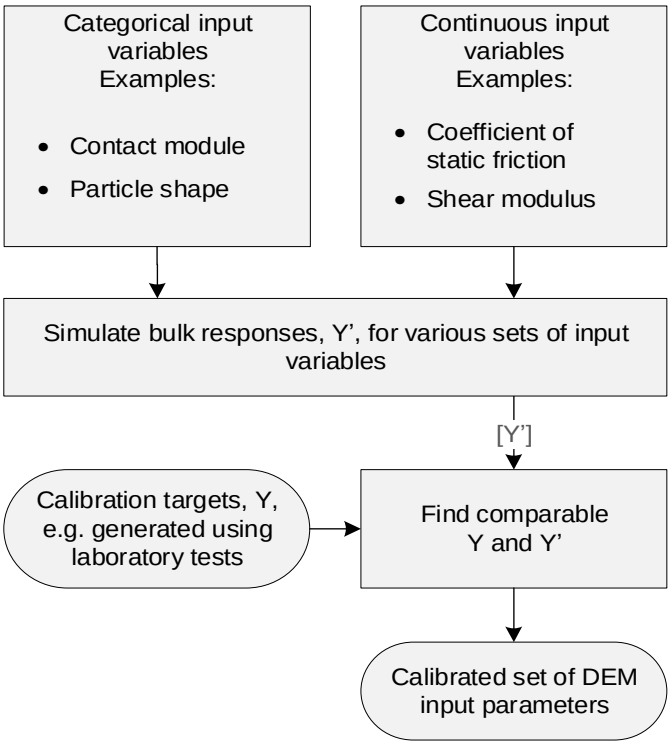

Figure 5-1. Main components of a generic DEM calibration procedure.

Furthermore, selecting an appropriate contact model from the available options is an important challenge in the DEM calibration. Applying optimization methods without choosing a proper

contact model might, for example, lead to an empty solution space or inadequacy in meeting macroscopic bulk behaviors other than the selected calibration targets [13]. A contact model generally includes multiple modules to calculate forces and torques between elements (e.g. particles). Figure 5-2 schematically illustrates a contact spring-damper system between two particles, *a* and *b*. Here, three main modules are identified: contact force in the normal direction is denoted by f_N, while f_T and τ_R represent force in the tangential direction and rotational torque respectively. Contact modules can be selected independently of each other. For instance, a rolling friction module can be implemented in various ways to determine rotational torque between two particles [9,85,119]. Therefore, each module of the contact model can be considered as a categorical variable in DEM calibration.

By contrast with free-flowing materials, cohesive bulk solids such as moist iron ore fines usually show a stress-history-dependent and cohesive behavior [108]. Their bulk responses, such as shear strength, bulk density, and penetration resistance, depend on the history of applied normal pressure on the bulk specimen [22,48,108]. As shown in the previous chapter, this stress-history-dependent and cohesive behavior can be simulated by using contact models based on an elasto-plastic adhesive spring. Orefice and Khinast [25] used a multi-stage sequential DEM calibration procedure to model cohesive bulk solids using a linear elasto-plastic adhesive model; the calibration was done by replicating a specific bulk response at each stage, starting with the angle of repose (measured using the funnel test) as the first calibration target. Three continuous DEM variables were included during the calibration; other DEM input parameters, continuous and categorical, needed to be kept constant during their calibration procedure. The multi-stage sequential calibration procedure might fail to meet the following criteria.

- Feasibility. Replicating all the selected bulk responses can be infeasible using chosen values for the input parameters that are constant during the calibration, such as a specific contact module. Therefore, considering the necessity of including multiple calibration targets, the calibration procedure can lead to an empty solution space for one or more than one of the calibration targets.
- Definiteness (or avoiding ambiguous parameter combinations [17]). To meet this criterion, a bulk response independent of the calibration targets needs to be simulated successfully using the calibrated set of DEM input parameters. Additionally, properly selecting all modules of the DEM contact model is a prerequisite. Otherwise, the calibrated set of input parameters might fail to capture a bulk response different than the selected calibration targets.

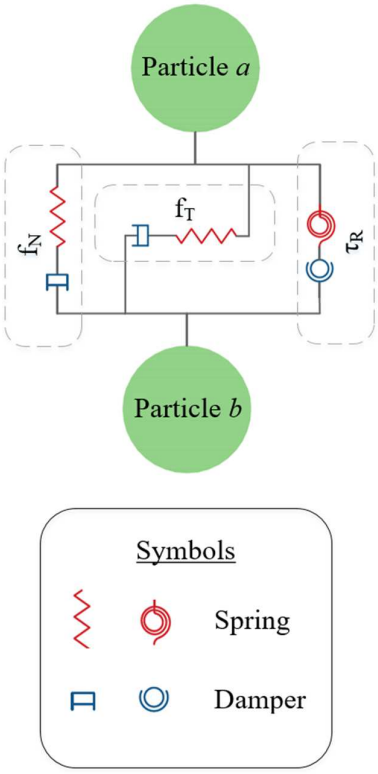

Figure 5-2. A contact spring-damper system between two particles, including normal, tangential, and rotational directions.

For example, the "definiteness" criterion has been focused on in the automated calibration procedure developed by [29], which is based on a genetic algorithm to replicate stress-history-dependent and cohesive behavior of bulk solids in the ring shear test. By introducing cohesive forces as well as elasto-plastic stiffness into the DEM calibration procedure, the number of DEM input variables and the number of required bulk responses increase [23,25–27]. For that reason, the abovementioned criteria become important in developing a reliable calibration procedure to simulate cohesive and stress-history-dependent behavior of bulk solids. As yet, however, no literature has addressed how to ensure that both criteria, feasibility and definiteness, are met in a DEM calibration procedure considering both continuous and categorical DEM input variables. Additionally, calibrating DEM input parameters is still a challenge when a high number (i.e. >2) of variables in combination with a high number of bulk responses (i.e. >2) is involved. Therefore, a reliable DEM calibration procedure is needed to capture the cohesive and stress-history-dependent behavior of bulk solids.

5.2. DEM Calibration Procedure

5.2.1. A Multi-Step Optimization Framework

In general, a calibration procedure aims at identifying an optimal combination of DEM input parameters, $X^* = x_1^*, \dots, x_{Ns}^*$, that leads to simulated bulk responses, $Y' = y_1', \dots, y_{Ny}'$, adequately similar to responses captured in physical laboratory or in-situ tests, $Y = y_1 , \dots, y_{Ny}$ [11]. *Ns* is the number of DEM input parameters and *Ny* the number of calibration targets. Bulk responses such as bulk density and shear strength thus need to be determined first, using appropriate physical tests. This allows for setting calibration targets and for quantifying the difference in bulk responses between simulated and physically determined values. To ensure that feasibility and definiteness criteria are satisfied for multiple calibration targets, a multi-step DEM calibration procedure considering categorical input parameters is proposed in Figure 5-3. The following four steps are included: (I) feasibility; (II) screening of DEM variables; (III) surrogate modeling-based optimization; and (IV) verification.

To apply surrogate modeling-based optimization, the parameter space needs to be searched effectively to be able to approximate Y'. Accordingly, *F(X)* maps relationships between new calibration targets, $Y = y_1, \dots, y_{My}$, and (significant) DEM variables. Although the full factorial design can be used to create multi-variate samples, all the possible combinations between significant DEM variables must be included. This leads to a high number of simulations needing to be done. Fractional factorial designs, such as Taguchi [135], Placket-Burmann [136], and Box Behnken [137] designs, can be used to generate multi-variate samples required for surrogate modeling without the need to create all the possible combinations of variables. For example, if a full factorial design is used for 4 input variables having 3 levels each, that leads to $3^4 = 81$ combinations to run. Using the Taguchi (orthogonal) method, a fractional factorial design can be created by running only 9 or 27 possible combinations.

The accuracy of the surrogate model is evaluated using the coefficient of determination, R^2. This coefficient quantifies the surrogate model accuracy in representing variability of values obtained from DEM simulations. To ensure that the surrogate model converges to a verifiable X^*, a minimum R^2 value of 0.75 is considered to be met for all calibration targets. Otherwise, more samples are used to train the surrogate model.

Next, the response optimizer searches for an optimal combination of input variables, X^*, that jointly meets a set of calibration targets, *Y*. To find X^* using the surrogate model, the response optimizer toolbox available in Minitab [138] is used in the current investigation.

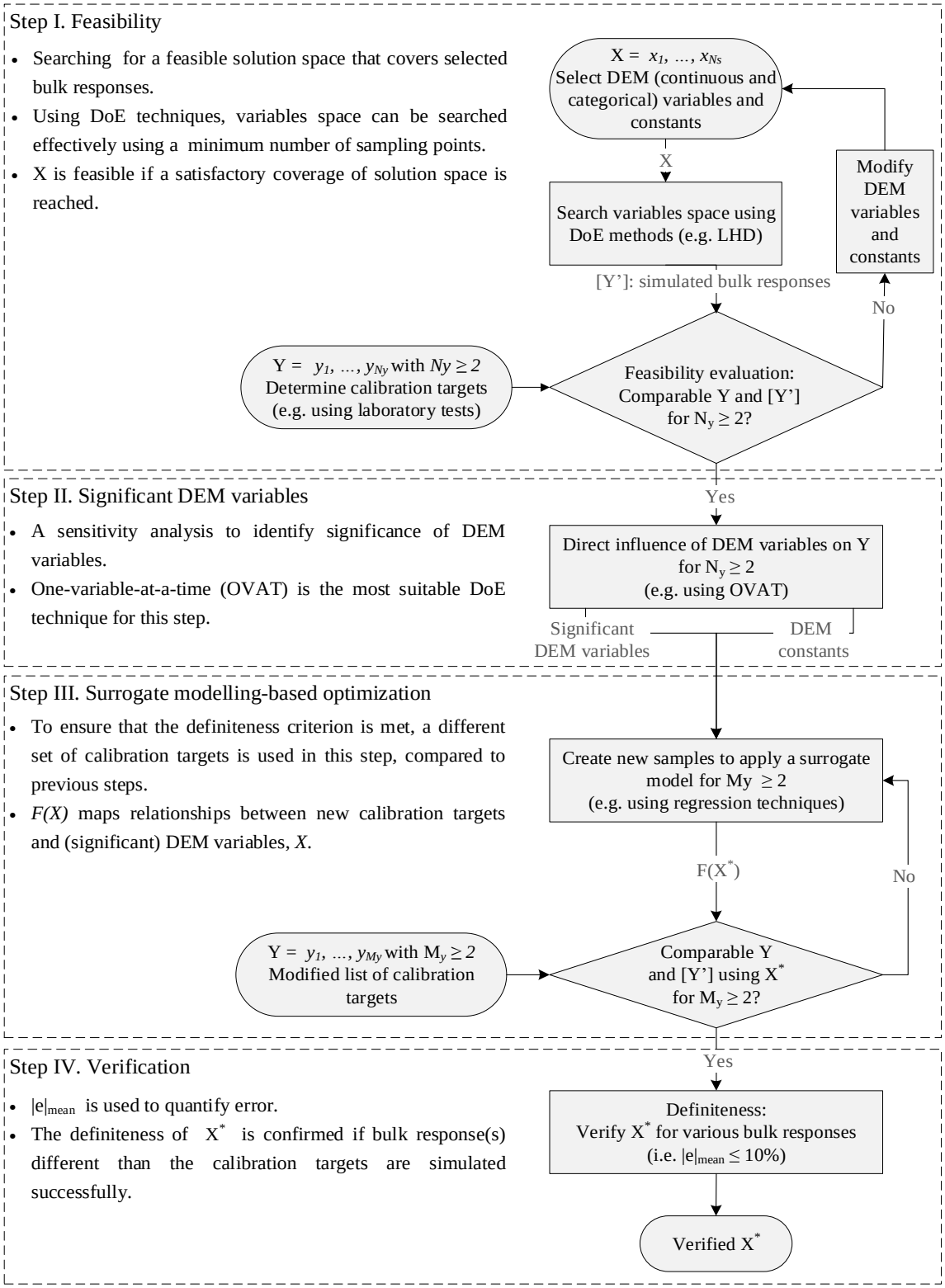

Figure 5-3. Main steps of the DEM calibration procedure considering feasibility and definiteness criteria.

The mean of absolute relative differences is used to quantify error in the verification step. If y and y' represent measured bulk responses in the experiment and the simulation, respectively, then $|e|_{mean}$ is determined according to Eq. (5.1) for a number of bulk responses, N_e. In the current study, an $|e|_{mean} \leq 10\%$ is considered an acceptable outcome during verification.

$$|e|_{mean} = \sum_{k=1}^{N_e} 100 \left| \frac{y_k - y'_k}{y_k} \right| \tag{5.1}$$

Therefore, in each step of the calibration procedure the variables space is narrowed down to be further optimized in the next step. In the final step, a verified parameter set is found by checking $|e|_{mean}$.

5.2.2. DEM Calibration Targets: Y

In this chapter, DEM calibration targets are set to values reported in Chapter 3. Bulk property variability of cohesive iron ores has been characterized using the following laboratory tests:

A) Schulze ring shear test;
B) ledge angle of repose; and,
C) consolidation-penetration test.

Additionally, three influencing parameters related to bulk properties were varied in the laboratory tests: (1) iron ore sample; (2) moisture content, denoted by *MC*; and (3) vertical consolidation pressure, denoted by σ. The results obtained in the laboratory tests listed above (A, B, and C) are used in the current chapter to set DEM calibration targets. During the calibration procedure, two out of three influencing parameters, *MC* and σ, are considered as sources of possible bulk property variability. Below characteristics of the selected bulk solid sample as well the measured bulk responses are described briefly.

5.2.3. Bulk solid sample

The bulk solid sample is a sinter feed type of iron ore from the Carajas mines, one of the largest iron ore resources on earth [62]. The average density of the particles is 4500 kg/m^3, with a standard deviation of 125 kg/m^3. The median particle size, d_{50}, is equal to 0.88 mm [64]. The dry-based moisture content was determined according to the method described in [65], in which the sample is dried using a ventilated oven. This resulted in *MC* = 8.7%. An overview of measured properties of the sample is presented in Table 5-1.

Table 5-1. Overview of measured properties of the cohesive iron ore sample (based on measurements of Chapter 3).

Property	Symbol	Unit	Average value
Dry-based moisture content	MC	%	8.7
Particle density	ρ_p	kg/m^3	4500
Median particle diameter	d_{50}	mm	0.88

5.2.4. Measured bulk responses

Table 5-2 displays physically measured bulk responses of the sample using the ring shear and ledge angle of repose tests when $\sigma_{pre} \leq 20$ kPa and $\Delta_{MC} = \pm 2\%$. Pre-consolidation or pre-shear stress, σ_{pre}, is a normal confining pressure that is applied initially. In the ring shear test, for example, a normal confining pressure of 20 kPa is applied initially during the pre-shear stage, and next a normal confining pressure of 2 kPa (σ_{shear}) is applied. Figure 5-4 shows the results of shear stress measurements in the ring shear test, including one pre-shear stage and one shearing stage. In general, σ_{shear} is smaller than σ_{pre}, which allows us to investigate a stress-history-dependent bulk response, such as shear strength in the case of shear tests. The ledge angle of repose test has been conducted under no pre-consolidation stress, which represents the free-surface flow of bulk solids under gravity force. Maximum and minimum values of physically measured bulk responses are shown under $\Delta_{MC,}$ up to ±2%, compared to its as-received condition. By considering the maximum and minimum measured values of bulk responses, extreme values can be included in the feasibility evaluation step of the DEM calibration procedure. In other words, the feasibility is evaluated for a range of bulk response values.

The wall friction was also determined in Chapter 3. The test was done with a σ_{pre} equal to 20 kPa and then the wall friction was measured for eight different levels of σ_{shear} between 2 and 17 kPa. The wall friction measurements resulted in a wall yield locus with an average wall friction angle of 19˚ and a negligible adhesion strength of 0.1 kPa.

Table 5-3 displays measured bulk responses of the sample using the consolidation-penetration test when $\sigma_{pre} \geq 65$ kPa and $\Delta_{MC} = 0\%$. To consider the stress-history dependency, two levels of σ_{pre} are included in the calibration procedure, equal to 65 and 300 kPa, respectively. As the first bulk response parameter, accumulative penetration resistance [J] on the wedge-shaped penetration tool is determined by integrating the reaction force over penetration depth [8]. The secondary measured bulk response in the test is the bulk density after removing σ_{pre}. For example, after removing σ_{pre} of 300 kPa, the bulk density was measured according to the procedure

described in [21], which for this sample was equal to 2807 kg/m^3 on average for three test iterations.

Table 5-2. Physically measured bulk responses with Δ_{MC} up to ±2% when $\sigma_{pre} \leq 20$ kPa (based on measurements of Chapter 3).

Test	Bulk response	Symbol	Unit	Minimum Value	Maximum value
Ring shear	Shear strength in pre-shear stage (σ = 20 kPa)	$\tau_{pre=20}$	kPa	16.5	19.4
	Shear strength in shearing stage (σ = 2 kPa)	$\tau_{2:20}$	kPa	4.2	5.6
	Bulk density in the loose condition	$\rho_{b,0}$	kg/m^3	1803	1840
	Bulk density after pre-shear of 20 kPa	$\rho_{b,20}$	kg/m^3	2400	2580
Ledge angle of repose	Angle of repose (σ_{pre} = 0 kPa)	α_M	°	63	84

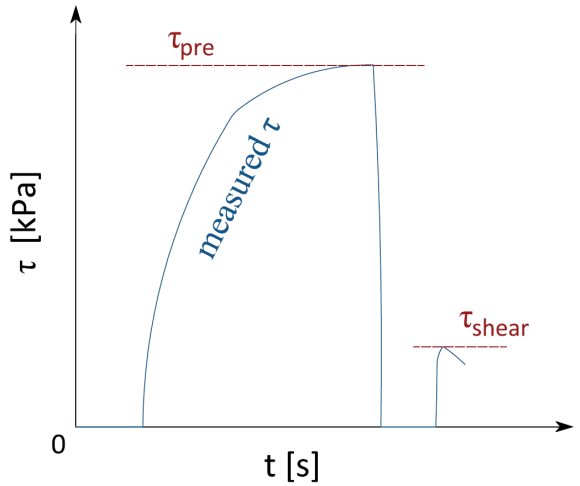

Figure 5-4. Schematic shear stress measurements in ring shear test, including pre-shear and shearing stages.

Table 5-3. Physically measured bulk responses when $\sigma_{pre} \geq 65$ kPa (based on measurements of Chapter 3).

Test	Bulk response	Symbol	Unit	Average Value	Standard deviation
Consolidation -penetration	Accumulative penetration resistance at 80 mm depth when σ_{pre} = 65 kPa	$W_{80,65}$	J	108	7
	Accumulative penetration resistance at 70 mm depth when σ_{pre} = 300 kPa	$W_{70,300}$	J	121	5
	Bulk density after applying σ_{pre} = 65 kPa	$\rho_{b,65}$	kg/m^3	2668	65
	Bulk density after applying σ_{pre} = 300 kPa	$\rho_{b,300}$	kg/m^3	2807	14

Therefore, bulk property variability of the cohesive iron ore sample has been determined under variation of confining pressure as well as moisture content. This provides a comprehensive set of measurement data to be used in the DEM calibration procedure (illustrated in Figure 5-3).

5.2.5. Initial Sampling Strategy for Step I (Feasibility) Using LHD

The initial sampling aims at evaluating the feasibility of capturing calibration targets using selected DEM input constants and variables. This allows for selecting a suitable solution, including levels of categorical variables and constants. Two simulation setups, ring shear and ledge angle of repose tests, are used in step I, feasibility. This means that the shear flow in two different test setups is simulated for σ_{pre} of up to 20 kPa. Three different bulk responses, $\tau_{pre=20}$, $\tau_{2;20}$, and α_M (angle of repose), are analyzed using DEM simulations for various combinations of input parameters.

During a calibration procedure, DEM input parameters, $X = x_1 \, , \ldots , x_{Ns}$, are divided into two groups: input variables and constants. Level input variables are varied in a range to meet calibration targets. Levels of DEM input constants are chosen based on available literature, if applicable; otherwise, their level is selected based on rational assumptions, as recommended by [25], or by the direct measurement method, as discussed in [11]. For example, modeling the actual shape and size distribution of a cohesive iron ore sample leads to a computational time that is impractical [139,140]. Thus, a simplified representation of particle shape and size can be used to develop a DEM simulation of cohesive iron ore. This technique has been applied successfully by [22,29,96] to model bulk solids that have fine particles with irregular shape distribution.

Nevertheless, the rotational torque between particles needs to be considered; according to [105], two options are possible: (a) introducing a certain level of non-sphericity in particle shape; and/or (b) suppressing the rotational freedom of particles. In this chapter, option (b) is applied, as – compared to using multi-spherical particles – it does not have a negative influence on the computational time. The rotational freedom of particles can be suppressed artificially by either introducing a rolling friction module [85] or restricting the rotation of the particles [9,29,117]. Both techniques are included as a categorical variable in step I, feasibility. The rolling friction module is implemented according to [119]. This implementation was classified as “rolling model C” by [85], so the rolling friction module as *RC* in this chapter. The rotation of particles is restricted by applying a counterbalance torque in each time-step necessary to prevent rotational movement. This leads to an increase in the particles’ resistance to rotational torque. Restricting the rotation of particles has been used successfully to resemble realistic material behavior

[8,9,105,118]. Additionally, the number of input variables is reduced because, when using the restricted rotation (*RR*) technique, rolling friction coefficient does not play a role in rotational torque.

DEM input variables for RC option

Table 5-4 displays DEM input variables when the *RC* option, rolling friction module C, is used. Based on the available literature, the coefficient of static friction between particles, $\mu_{s,p\text{-}p}$, is probably the most influential parameter on the internal shear strength of bulk solids [7,28,51-62]. Coefficient of rolling friction is also usually considered as an influential variable on shear flow [11]. To calibrate the shear flow of cohesive bulk solids, [121] found that a range of 0.2 to 1.0 is reasonable for coefficients of static friction and rolling friction when rolling model C is used. Particle shear modulus determines the stiffness of the contact spring. Therefore, *G*, particle shear modulus, is included as a continuous DEM variable in the current investigation. A range between 2.5 to 10 MPa is used for *G*, which covers values used by other researchers modeling cohesive bulk solids using the same elasto-plastic contact model [22,29].

Constant pull-off force (f_0) and surface energy ($\Delta\gamma$) are included in the calibration to control the magnitude of adhesive forces in the contact spring. f_0 is varied between -0.0005 and -0.005 N, and $\Delta\gamma$ between 5 and 50 J/m^2. These ranges are expected to be sufficient to capture a realistic shear flow based on the DEM calibration done in [29].

Table 5-4. DEM input variables to model interaction between particles when *RC* option is used.

Input variable	Symbol	Unit	Range
Coefficient of static friction	$\mu_{s,p\text{-}p}$	-	[0.2 1.0]
Coefficient of rolling friction	$\mu_{r,p\text{-}p}$	-	[0.2 1.0]
Particle shear modulus	G	MPa	[2.5 10]
Constant pull-off force	$-f_0$	N	[0.5 5] e-3
Surface energy	$\Delta\gamma$	J/m^2	[5 50]
Contact plasticity ratio	λ_P	-	[0.05 0.9]

DEM input variables for RR option

Table 5-5 displays DEM input variables when the *RR* option, rotation restricted, is used. First, based on our simulation results reported in [29], the ranges of coefficient of static friction and surface energy are changed, compared to the values in Table 5-4. By restricting the rotation of particles, their mobility decreases and so lower restrictive forces (e.g. cohesive and friction) can be used during the calibration procedure, compared to the case when the *RC* option is used. The

coefficient of static friction is varied between 0.2 and 0.4, while the surface energy variation is between 2.5 and 25 J/m^2. Second, ranges of other input variables are similar to the case when the *RC* option is used.

Table 5-5. DEM input variables to model interaction between particles when *RR* option is used.

Input variable	Symbol	Unit	Range
Coefficient of static friction	$\mu_{s,p\text{-}p}$	-	[0.2 0.4]
Particle shear modulus	G	MPa	[2.5 10]
Constant pull-off force	$-f_0$	N	[0.5 5] e-3
Surface energy	$\Delta\gamma$	J/m^2	[2.5 25]
Contact plasticity ratio	λ_P	-	[0.05 0.9]

DEM input constants

Table 5-6 presents other DEM input parameters that are kept constant during initial sampling for step I, feasibility. Particle density is set to 4500 kg/m^3, similar to the measured value (Table 5-1). As discussed earlier, the representation of particles' shape and size is simplified. Spherical particles are used and the mean particle diameter value is set to 4 mm including a normal particle size distribution with a standard deviation of 0.1. In addition to a reasonable computation time when spherical particles are used, the coarse graining principles for the elasto-plastic adhesive contact model [140] can be applied during the calibration procedure to further minimize the computation time. For example, the ledge angle of repose simulations are done using coarse grained particles with a scaling factor of S_P = 2.25, as per [140]. Constant pull-off force and surface energy are scaled with factors of S_P^2 and S_P to maintain comparable bulk responses with the unscaled simulation. For further details of particle scaling rules, please refer to [140].

The tangential stiffness multiplier, $k_{t,mult.}$, is recommended as 2/3 [148] for non-linear elastic contact springs. According to [149], to maintain simultaneous harmonic oscillatory positions between normal and tangential elastic springs, a value of 2/7 is recommended. However, no recommendation was found in literature to select $k_{t,mult.}$ when a non-linear elasto-plastic normal spring is used. For that reason, a range of $k_{t,mult.}$ bounded to 0.2 to 1 was used in the ledge angle of repose simulation. Within this range, no significant influence on the simulation stability and simulated bulk responses were found, and therefore $k_{t,mult.}$ is set to 0.4.

As suggested by [29], if a negligible adhesion strength is measured in the wall friction test, the Hertz-Mindlin (no-slip) contact model [150] can be used to describe interaction between particles and geometry. $\mu_{s,p\text{-}w}$, the sliding friction coefficient between particles and wall geometry,

is therefore determined directly by Eq. (5.2), which results in $\mu_{s,p\text{-}w}$ = 0.37 for the measured average angle of the wall yield locus φ_x of 19˚. The rolling friction coefficient between particles and wall geometry has a negligible influence on simulated shear stress [90], and therefore $\mu_{r,p\text{-}w}$ is set to 0.5.

$$\mu_{s,p-w} = \tan(\varphi_x) \tag{5.2}$$

Table 5-6. DEM input constants.

Particle and geometry input parameter	Symbol	Unit	Value
Poisson's ratio	υ	-	0.25
Particle density	ρ_p	kg/m^3	4500
Mean particle diameter at the reference particle scale (S_P = 1)	d_p	mm	4
Particle shape	Ψ_p	-	single sphere
Coefficient of restitution, particle-particle	$C_{r,p\text{-}p}$	-	0.01
Normal and tangential contact modules, particle-particle	$f_{N,p\text{-}p}$ and $f_{T,p\text{-}p}$	-	EEPA
Slope exponent	n	-	1.5
Tensile exponent	$\chi_{p\text{-}p}$	-	1.5
Tangential stiffness multiplier	$k_{t,mult.}$	-	0.4
Normal and tangential contact modules, particle-wall	$f_{N,p\text{-}w}$ and $f_{T,p\text{-}w}$	-	Hertz-Mindlin (no-slip)
Sliding friction coefficient, particle-wall	$\mu_{s,p\text{-}w}$	-	0.37
Coefficient of restitution, particle-wall	$C_{r,p\text{-}w}$	-	0.01
Time step	Δt	s	1.2e-5

Initial samples

Using design of experiments (DoE) techniques, parameter spaces – including their levels and possible combinations – can be searched effectively using a minimum number of sampling points. A Latin hypercube design (LHD) is constructed in such a way that each of the parameters is divided into *p* equal levels, where *p* is the number of samples. Based on the Φ_P criterion [151], the location of levels for each parameter is randomly, simultaneously, and evenly distributed over the parameter spaces, maintaining a maximized distance between each point. The LHD is constructed according to the algorithm developed in [152], which satisfies the Φ_P criterion for up to 6 parameters. This allows for including up to 6 DEM input parameters in a feasibility evaluation.

Figure 5-5 displays levels of the 5 continuous DEM input variables at S_P = 1 when the RR option, restricted rotation, is used. Forty different samples are created using the LHD to simulate

ring shear and ledge angle of repose tests. Similarly, using the LHD, 40 different samples are created for the 6 continuous DEM input variables (based on Table 5-5) at $S_P = 1$ when the RC option, rolling friction module C, is used.

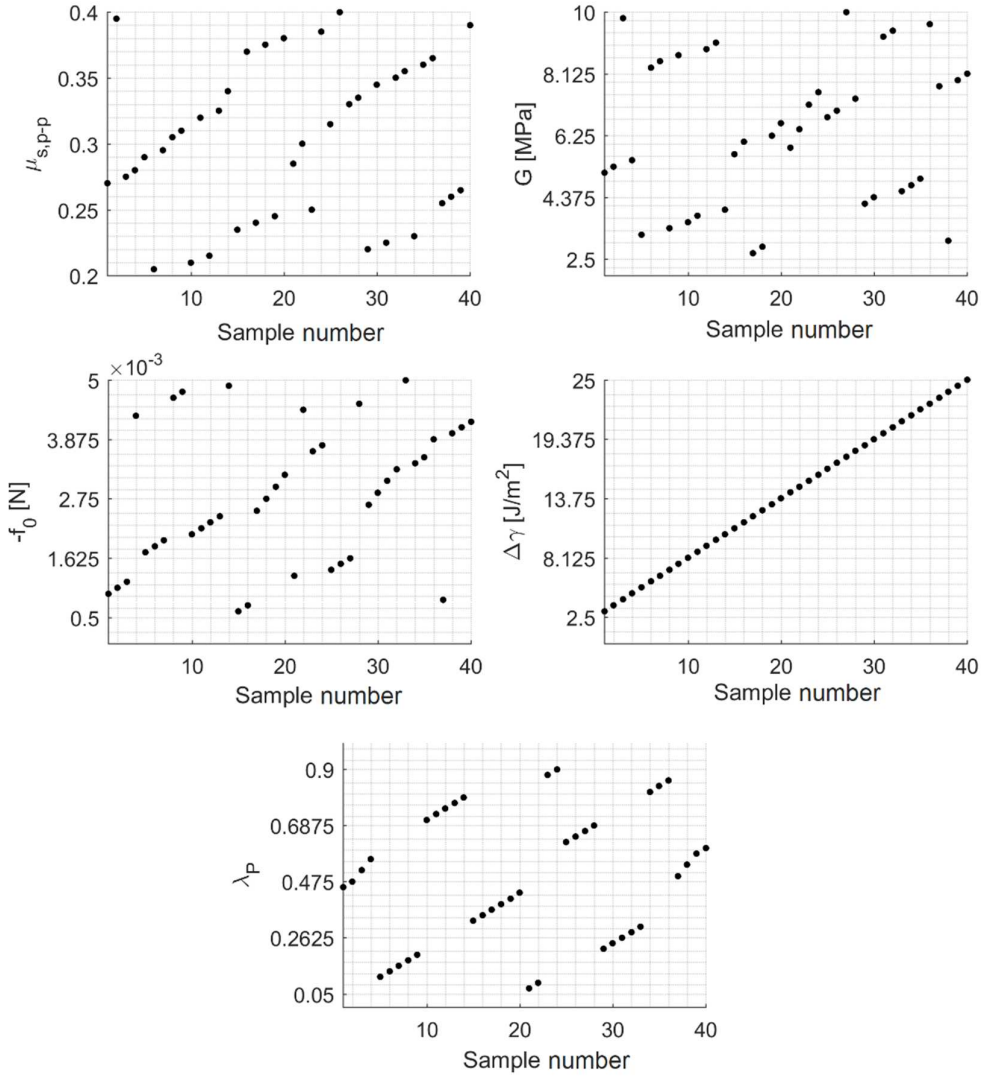

Figure 5-5. Forty different samples for RR option at S_P = 1, are created using Latin hypercube design for 5 variables.

In total, 160 simulations are run during step I, feasibility, which cover 2 categorical variables and 6 continuous variables.

5.3. Results

In this section, first the simulation results of the initial samples (step I) are presented. Then, a feasible solution is chosen to continue the calibration procedure when executing its next steps.

Additionally, new samples are created at the beginning of each new step to meet its specific objective.

5.3.1. Step I: feasibility

Figure 5-6 displays the simulation results of the 40 initial samples when the *RC* option, rolling friction module C, is used. Three different bulk responses are quantified:

- shear stress in the pre-shear stage, $\tau_{pre=20}$;
- shear stress in the shearing stage, $\tau_{2:20}$; and,
- average angle of repose in the ledge test, α_M.

Thus, N_y = 3 in step I, feasibility evaluation. Simulation results are also compared with the maximum and minimum values that were measured in the laboratory environment (shown in Table 5-2). For example, $\tau_{exp.max}$ and $\tau_{exp.min}$ are shown using blue and red dashed lines respectively.

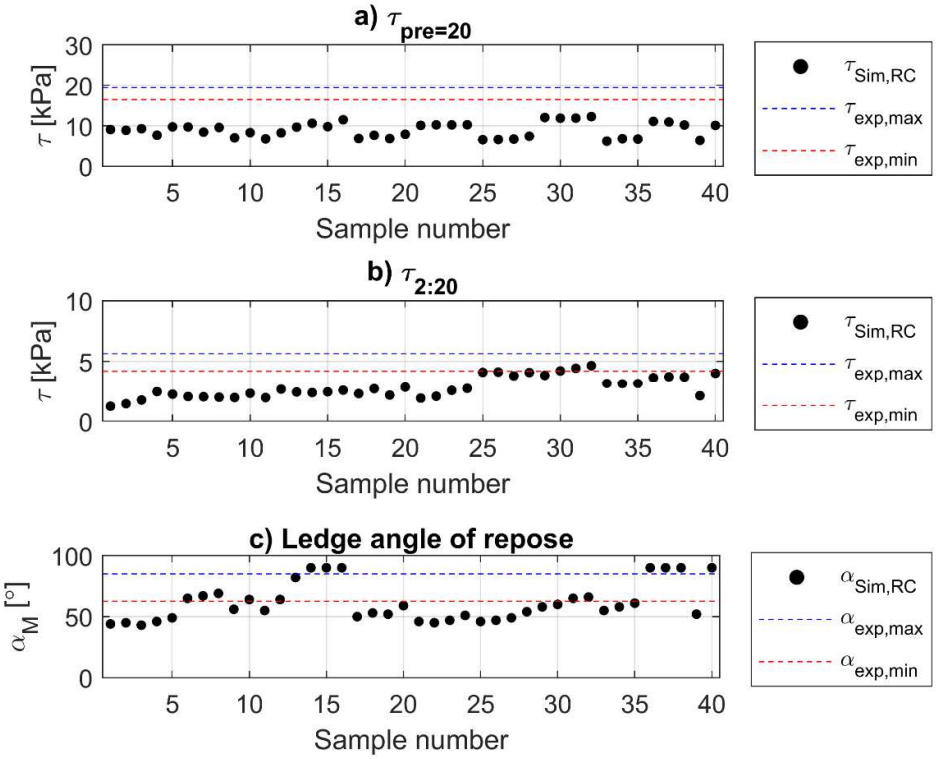

Figure 5-6. Shear strength and angle of repose values captured in 40 samples when RC option is used: a) $\tau_{pre=20}$; b) $\tau_{2:20}$; c) ledge angle of repose (α_M).

Using the *RC* option, a range of $\tau_{pre=20}$ bounded to 6.2 and 12.3 kPa is captured. This shows that the 40 samples created using LHD could vary $\tau_{pre=20}$ by around 100%. The maximum simulated $\tau_{pre=20,}$ 12.3 kPa, is around 25% lower than $\tau_{exp.min}$. This means that simulating a comparable $\tau_{pre=20}$

is probably infeasible using the *RC* option. To confirm whether this conclusion is limited to the selected ranges of the 6 DEM input variables, additional simulations using extreme values of DEM input variables are conducted. Extreme values are selected outside the selected ranges shown in Table 5-4. For example, using sample 32, which produced $\tau_{pre=20}$ = 12.3 kPa, an additional sample is created by increasing particle shear modulus, *G*, to 100 MPa. This leads to only a marginal increase in simulated $\tau_{pre=20}$. Even though the angle of repose, α_M, is simulated in a range of 43˚ to 90˚, simulating comparable bulk responses is infeasible in the ring shear test. Therefore, according to Figure 5-6 an empty solution space is reached when the *RC* option is used.

Figure 5-7 displays the simulation results of the 40 initial samples when the *RR* option, rotation restricted, is used. The same list of bulk responses as in Figure 5-6 analyzed here, and therefore the feasibility is evaluated for N_y = 3.

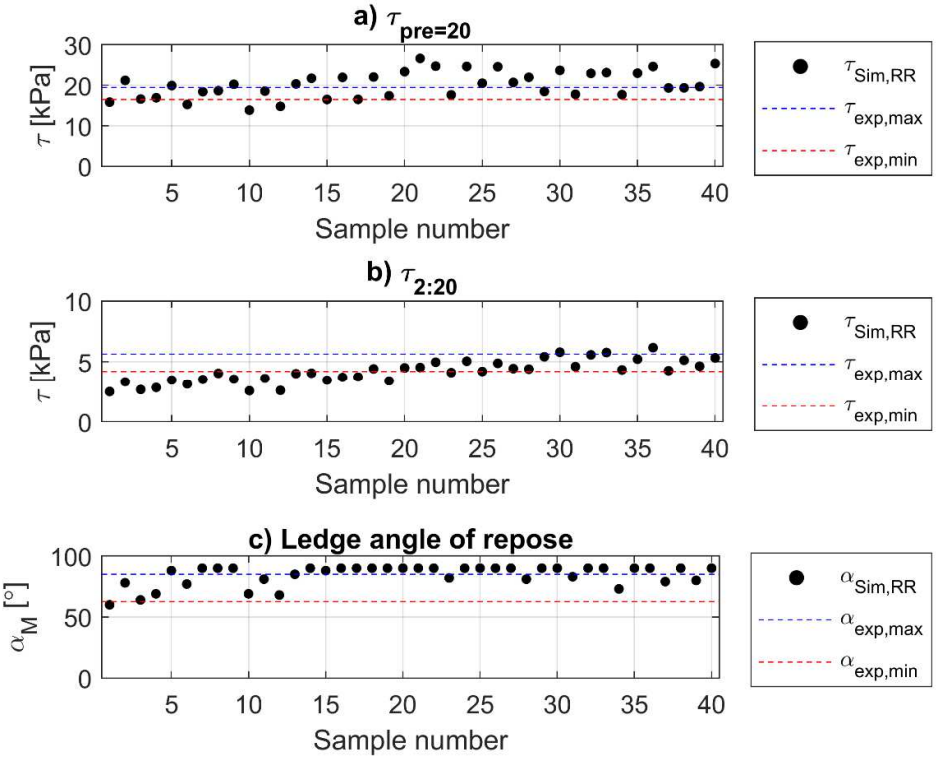

Figure 5-7. Shear strength and angle of repose values captured in 40 samples when *RR* option is used: a) $\tau_{pre=20}$; b) $\tau_{2:20}$; c) ledge angle of repose (α_M).

First, a range of $\tau_{pre=20}$ bounded to 13.9 and 26.6 kPa is simulated; this covers both $\tau_{exp.max}$ and $\tau_{exp.min}$. Second, a range of $\tau_{2:20}$ bounded to 2.5 to 6.5 kPa is simulated. This range covers both $\tau_{exp.max}$ and $\tau_{exp.min}$. Third, a range of α_M bounded to 60˚ and 90˚ is simulated; this covers the maximum and minimum values measured in the laboratory environment. Thus, according to

Figure 5-7, a non-empty solution space is reached when the *RR* option is used. However, no sample satisfies all three calibration targets jointly. For example, sample 39 seems to be an optimal parameter set, however the simulated bulk responses compared to $\tau_{exp,max(pre=20)}$, $\tau_{exp,max(2:20)}$ and $\alpha_{exp,max}$ have errors, |e|, of 1.13%, 22.53% and 5.88% respectively. By establishing mathematical relationships between input variables and each calibration target, such errors can be minimized. Therefore, the *RR* option is used in the next steps as a feasible solution to be optimized further.

5.3.2. Step II: significant DEM variables

A one-variable-at-a-time (OVAT) technique is used to create samples that allows for investigating the direct effect of each DEM variable, x_j, on simulated bulk responses by running a limited number of simulations.

Table 5-7 displays the samples created for this step, including 6 DEM input variables at the reference particle scale (S_P = 1), when the RR option is used. This results in 60 samples in total, to be simulated in the ring shear and ledge angle of repose tests. When one variable is changed, the others are maintained at the displayed reference values. Reference values are based on one of the samples that was used in step I. In addition to 5 DEM input variables that were included in step I, the tangential stiffness multiplier, $k_{t,mult.}$, is also varied in this step. This allows for checking whether $k_{t,mult.}$ has any significant influence on the selected bulk responses. A similar list of bulk responses including $\tau_{pre=20}$, $\tau_{2:20}$, and α_M is analyzed in step II. Furthermore, larger ranges for the DEM input variables, compared to the previous step, are used to create samples. This allows for running a comprehensive sensitivity analysis showing relationships between the DEM input variables and the selected bulk responses.

Table 5-7. Sampling for step II, finding significant DEM variables.

Variable	Unit	Reference value	Low	Step	High
$\mu_{s,p-p}$	-	0.3	0.1	increase by 0.1	1.0
G	MPa	7.5	1	multiply by 2	1024
λ_P	-	0.2	0	increase by 0.1	0.99
$-f_0$	N	1e-3	0	increase by 0.5 e^{-3}	5e-3
$\Delta\gamma$	J/m^2	5	0	increase by 2.5 and 5	25
$k_{t,mult.}$	-	0.4	0.2	increase by 0.2	1.0

Figure 5-8 displays isolated effects of the 6 DEM input variables at S_P = 2.25 on the simulated angle of repose. Since the ledge test box is performed in a rectangular container, α_M would be always equal or smaller than 90˚. By varying coefficient of static friction, the maximum possible

angle of repose, α_M = 90˚, being reached when $\mu_{s,p\text{-}p} \geq 0.6$. As expected based on the Mohr-Coulomb theory, there is a positive strong correlation between $\mu_{s,p\text{-}p}$ and α_M, as shown in Figure 5-8a. A higher particle-particle friction results in a higher shear strength when normal pressure and cohesion strength are constant. By contrast, there is a negative correlation between G and α_M, as can be seen in Figure 5-8b. By increasing G from 1 to 128 MPa, α_M decreases by around 20˚. By increasing G, a lower contact overlap, δ, is created. This is expected to result in lower forces in the adhesive branch of the contact spring (part III). Increasing G to higher values has negligible influence on α_M. The ledge angle of repose simulations using λ_P equal to 0 and 0.99 result in unstable simulations, in which the stable situation (as discussed in Section 2.4) is not reached. As shown in Figure 5-8c, by increasing λ_P from 0.1 to 0.5, α_M decreases by around 20˚, and further increasing λ_P has a negligible influence on α_M. Constant pull-off force and tangential stiffness multiplier are found to have negligible effects on α_M in the investigated range, as shown in Figure 5-8d and Figure 5-8f, respectively. There is a strong positive correlation between $\Delta\gamma$ and α_M, showing a non-linear trend near the extreme values (Figure 5-8e). According to the Mohr-Coulomb theory, a higher cohesion strength results in a higher shear strength.

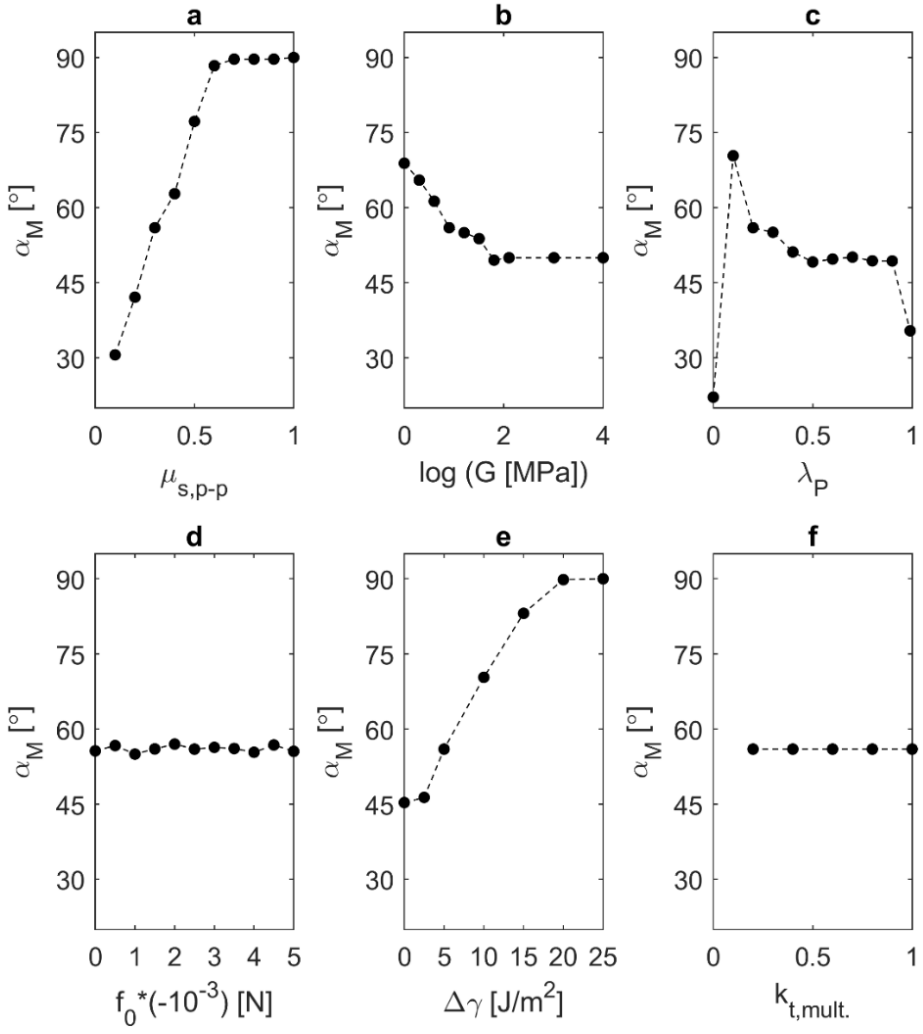

Figure 5-8. Isolated effects of 6 DEM input variables at S_P = 2.25 on the average angle of repose: a) coefficient of static friction; b) particle shear modulus; c) contact plasticity ratio; d) constant pull-off force; e) surface energy; f) tangential stiffness multiplier.

Coefficient of static friction, particle shear modulus, surface energy, and plasticity ratio are significant DEM variables influencing the angle of repose.

Figure 5-9 displays the results of the OVAT-based sensitivity analysis for simulated $\tau_{pre=20}$. According to the Mohr-Coulomb theory, the higher angle of internal friction of bulk material results in a higher shear strength when normal pressure and cohesion strength are constant. A linear trend seems to exist between these two parameters. The other 5 DEM input variables, compared to $\mu_{s,p-p}$, have a weaker influence on $\tau_{pre=20}$. Particle shear modulus and surface energy have positive correlation values with $\tau_{pre=20}$. The surface energy contributes in the cohesion strength of bulk material, thus contributing in the shear strength too.

Figure 5-10 displays the results of the OVAT-based sensitivity analysis for simulated $\tau_{2:20}$. Coefficient of static friction has a strong positive correlation with $\tau_{2:20}$, similar to its correlation with $\tau_{pre=20}$. The surface energy plays a more important role in $\tau_{2:20}$, compared to $\tau_{pre=20}$. Increasing surface energy, $\Delta\gamma$, from 0 to 25 J/m^2 causes an increase of more than 200% in $\tau_{2:20}$. According to the Mohr-Coulomb theory, at relatively low vertical pressure values, the cohesion strength, *c*, has a higher contribution to the shear strength, compared to shear flow at high vertical pressure values. As expected, based on the results of the ledge of repose simulations, *G* has a negative correlation with $\tau_{2:20}$. This is probably due a lower normal overlap created in the contact spring by increasing the value of *G*. Contact plasticity ratio, λ_p, also has some level of influence on $\tau_{2:20}$, but not in a predictive manner.

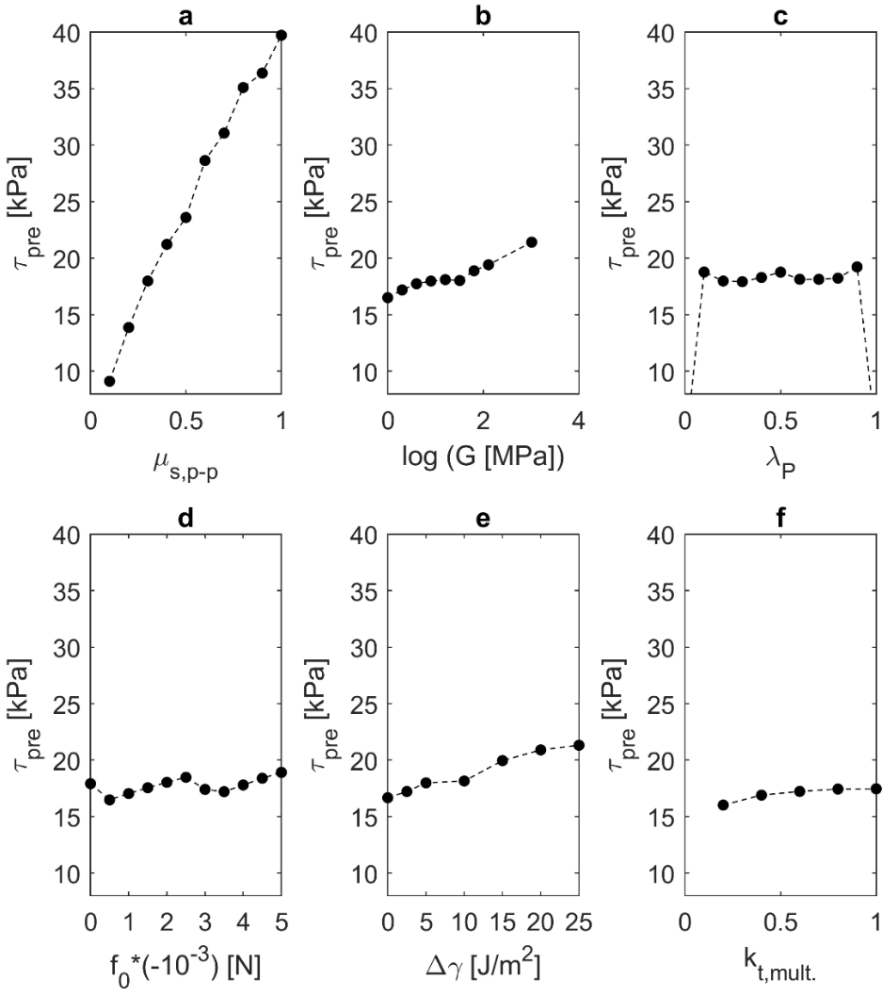

Figure 5-9. Isolated effects of 6 DEM input variables on the shear stress in the pre-shear stage ($\tau_{pre=20}$): a) coefficient of static friction; b) particle shear modulus; c) contact plasticity ratio; d) constant pull-off force; e) surface energy; f) tangential stiffness multiplier.

In conclusion, only one input variable, $k_{t,mult.}$, has a negligible influence on the investigated bulk responses. Therefore, all the other 5 input variables are included in the surrogate modeling-based optimization in the next step.

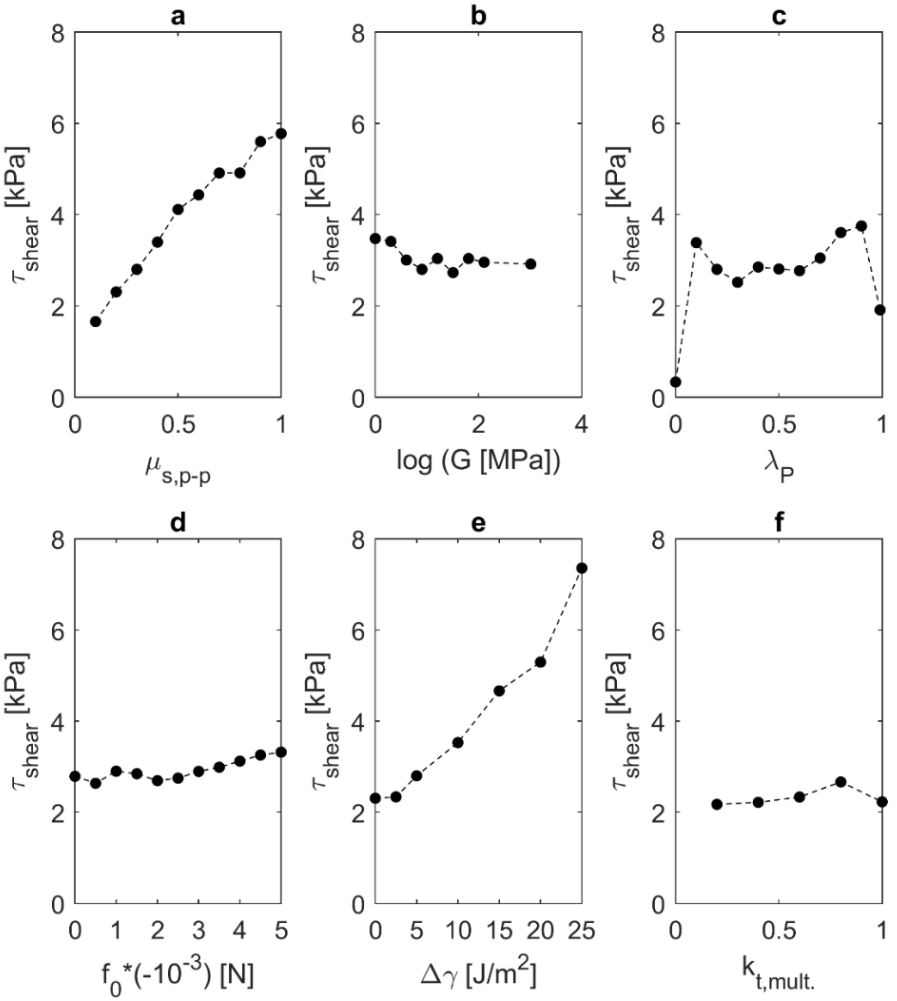

Figure 5-10. Isolated effects of 6 DEM input variables on the shear stress in the shearing stage ($\tau_{2:20}$): a) coefficient of static friction; b) particle shear modulus; c) contact plasticity ratio; d) constant pull-off force; e) surface energy; f) tangential stiffness multiplier.

5.3.3. Step III: surrogate modeling-based optimization

In this step, first the Taguchi method is used to create multi-variate samples to include variations of 5 significant DEM input variables when the *RR* option is used. Second, relationships between each calibration target and the DEM input variables are mapped to create *F(X)*. This is done using the multiple linear regression technique. As discussed in Section5.1, to consider the definiteness criterion, calibration targets are modified by excluding the ledge angle of repose test and by including $W_{80,65}$ and $W_{70,300}$ measured in the consolidation-penetration test. This means that four

calibration targets are included in step III, and therefore $M_y = 4$. Additionally, the maximum values of shear strength (shown in Table 5-2) are used as calibration targets in the simulation of a ring shear test. Third, an optimal set of DEM input parameters is found; these jointly satisfy the four selected calibration targets.

Table 5-8 presents the levels of the 5 significant DEM input variables at $S_P = 1$ that are used to create multi-variate samples. Given the adequate simulated bulk responses in step I, the coefficient of static friction is bounded to 0.2 and 0.4. For the same reason, levels of G are set to 2.5, 5, and 7.5 MPa. Three levels are selected for G to capture any possible non-linear relationship between G and the DEM calibration targets. λ_p is bounded to 0.2 and 0.6. This range is expected to be enough to capture a wide range of plasticity in the contact spring. Two other parameters, f_0 and $\Delta\gamma$, which control cohesive forces in part III of the contact spring, are confounded. In other words, their levels are varied simultaneously in a way that allows us to minimize the number of samples. Thus, 4 coded variables are used in the Taguchi design to create samples. In total, 18 samples are created using the Taguchi method.

As investigated in [9], the reaction force on the wedge-shaped penetration tool is affected by the particle scaling factor. For that reason, the consolidation-penetration simulation is calibrated only for level of particle size ($S_P = 2.25$), which is similar to the particle size used in the ledge angle of repose simulations.

Table 5-8. Levels of DEM input variables at $S_P = 1$ in step III: surrogate modeling-based optimization.

Coded variable	Variable name (uncoded)	Level		
		1	2	3
1	$\mu_{s,p\text{-}p}$ [-]	0.2	0.4	-
2	G [MPa]	2.5	5.0	7.5
3	λ_P [-]	0.2	0.4	0.6
4	$-f_0$ [N]	0.5e-3	2.5e-3	5.0e-3
	$\Delta\gamma$ [J/m2]	4	8	12

Next, the matrix of simulated bulk responses, *[Y']*, including 4 different bulk responses for 18 samples, is created. This matrix is used to map relationships between DEM variables, X, and simulated bulk responses, Y'. Details of *F(X)* are presented in Table 5-9, including coefficients of the DEM variables in linear regressions fitted on simulated bulk responses, Y'. *Cte.* stands for the constant term in the regression model. Remarkably, in all the fitted linear regression models the coefficient of static friction has the highest level of significance. Values of coefficient of determination, R^2, are also presented; in all the regression models, these are higher than 0.75.

Table 5-9. *F(X)* when $i \in M_y$; mapped relationships between DEM variables and simulated bulk responses.

Y' Bulk response	Symbol	Unit	Coefficients in fitted linear regressions					R^2
			Cte.	$\mu_{s,p-p}$ [-]	G [MPa]	λ_p [-]	$\Delta\gamma$ [J/m^2]	
Accumulative penetration resistance at 80 mm depth when σ_{pre} = 65 kPa	$W_{80,65}$	J	-86.7	435	6	22	3	0.77
Accumulative penetration resistance at 70 mm depth when σ_{pre} = 300 kPa	$W_{70,300}$	J	-111	550	1	113	4	0.80
Shear strength in shearing stage (σ = 2 kPa)	$\tau_{2:20}$	kPa	259	6797	-5	-415	143	0.89
Shear strength in pre-shear stage (σ = 20 kPa)	$\tau_{pre=20}$	kPa	3382	41455	171	-385	175	0.97

Therefore, the multiple linear regression model is found to be adequate for us to continue with response optimization. If insufficient values of R^2 are reached in this step of the calibration procedure, either a higher number of training samples or more advanced surrogate modeling techniques can be used.

Figure 5-11 presents an optimal set of DEM input variables that jointly satisfies four different calibration targets in step III with a composite desirability, $d_{composite}$, equal to 0.61. Composite desirability, $d_{composite}$, represents the geometric mean of individual desirability values, d, as shown in Eq. (5.3) and Eq. (5.4), respectively.

$$d_{composite} = \left(\prod_{i=M_y}^{M_y} d_i\right)^{1/n} ; i \in M_y \tag{5.3}$$

$$d = \begin{cases} \dfrac{\mathrm{f(X)} - y'_{min}}{y - y'_{min}}, & y'_{min} < \mathrm{f(x')} < y \\ \dfrac{y'_{max} - \mathrm{f(X)}}{y'_{max} - y}, & y < \mathrm{f(x')} < y'_{max} \end{cases} \tag{5.4}$$

where $f(X)$ is the predicated bulk response using the linear regression, and y is the target bulk response that is measured physically. y'_{min} and y'_{max} respectively represent the lowest and highest simulated values of a specific bulk response among all samples in step III. Each row in Figure 5-11, except the top one, represents a specific simulated bulk response with its maximum possible d value obtained by finding an optimal set of DEM input variables. For example, the last

row represents the response optimization for shear strength in the pre-shear stage, $\tau_{pre=20}$. For this bulk response, the physically measured value, y, is equal to 19.4 kPa.

Using the mapped relationship between DEM variables and y', simulated bulk response, a combination of variables is found that is predicted to lead to $f(X^*)$ = 18.7 kPa. This means that the outcome predicted in the simulation of a ring shear test using the current solution, shown in red, is a $\tau_{pre=20}$ equal to 18.7 kPa, with d = 0.80.

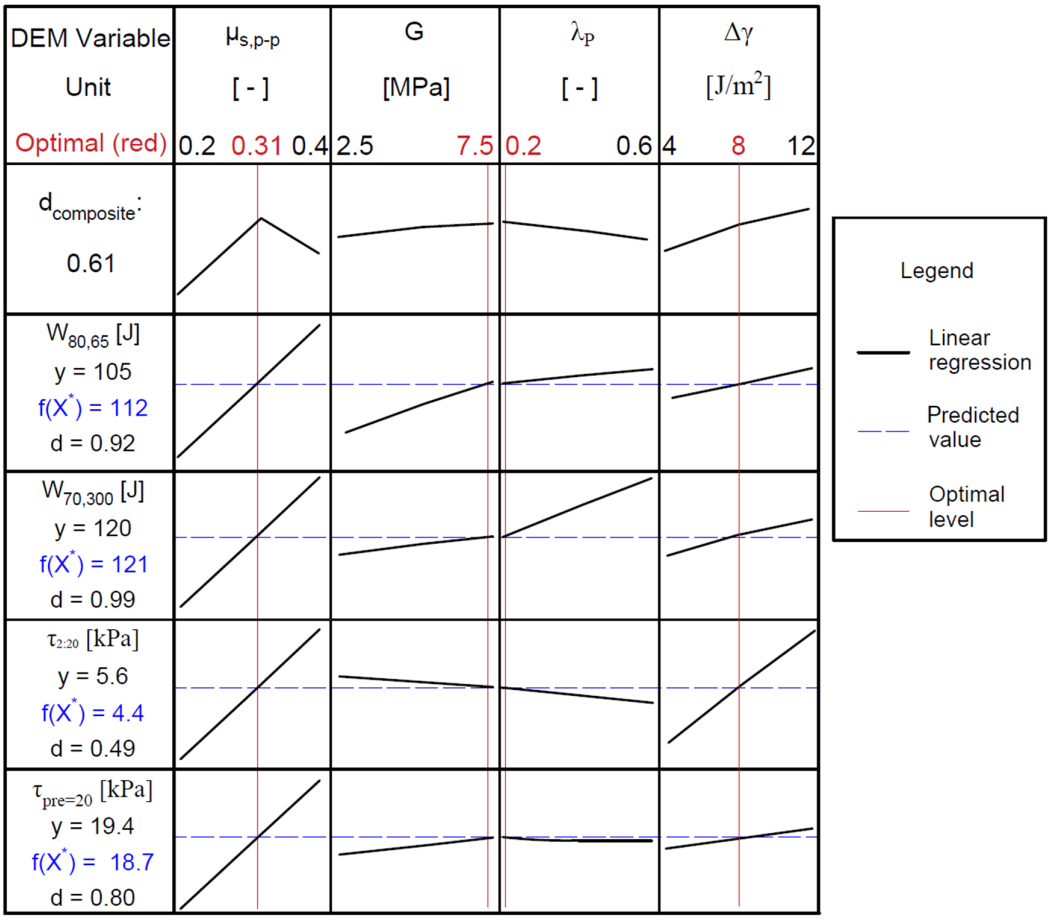

Figure 5-11. Finding an optimal set of DEM input variables that jointly satisfies calibration targets using response optimization.

5.4. Verifying the Calibration Procedure

This section discusses verification of the calibration procedure, step IV. First, it should be verified whether the outcome of surrogate modeling-based optimization is adequate. This is verified by running simulations using the optimal set of DEM input parameters and comparing simulated bulk responses to predicted values, $f(X^*)$. Second, $|e|_{mean}$ is used to compare simulated bulk responses

– using the optimal set – with all the calibration targets, corresponding to the maximum values in Table 5-2 and the target values in Table 5-3. Third, the entire yield locus in the ring shear test, including 1 level of σ_{pre} and 4 levels of σ_{shear}, is compared between the calibrated simulation and experiment. Fourth, the wall friction test as an independent bulk response is verified for various stress states.

First, ring shear and consolidation-penetration tests are simulated using the optimal set found Figure 5-11. In Table 5-10, four different simulated bulk responses are compared with values predicted using the surrogate-based optimization.

Table 5-10. Comparing simulated bulk responses using the optimal set with predicted values of surrogate modeling-based optimization.

Test	**Ring shear**		**Consolidation-penetration**	
Parameter	$\tau_{pre=20}$	$\tau_{2:20}$	$W_{80,65}$	$W_{70,300}$
Unit	kPa	kPa	J	J
y' Simulated bulk response	19.6	4.9	115	130
$f(X^*)$ Predicted value	18.7	4.4	112	121
$\lvert e\rvert = 100 * \lvert\frac{y'-f(X^*)}{y'}\rvert$	4.6	10.0	2.6	6.9

The relative difference is ≤10% in all cases, and therefore the adequacy of the multiple linear regression technique together with the response optimizer is confirmed for our DEM calibration problem. If large differences between *y'* and $f(X^*)$ had been captured, a higher number of samples or more advanced regression techniques could have been used to minimize the relative difference. Second, $|e|_{mean}$ is used to compare simulated bulk responses – using the optimal set – with all the calibration targets, corresponding to the maximum values in Table 5-2 and the target values in Table 5-3. In other words, bulk density, shear strength, ledge angle of repose, and accumulative penetration resistance values are verified here. Table 5-11 compares 9 different simulated bulk responses with their target values, which were measured physically using the laboratory tests. Four parameters in the ring shear test are compared, indicating shear strength and bulk density.

Table 5-11. Verification of calibration procedure; comparing simulated bulk responses with their calibration targets.

Test	Parameter	Unit	y' Simulated response	y Target value	$\|e\| = 100 * \|\frac{y'-y}{y'}\|$	$\|e\|_{mean}$
Ring shear	$\tau_{pre=20}$	kPa	19.6	19.4	1.0	5.2
	$\tau_{2:20}$	kPa	4.9	5.6	12.5	
	$\rho_{b,0}$	kg/m^3	1850	1963	5.8	
	$\rho_{b,20}$	kg/m^3	2760	2800	1.4	
Consolidation-penetration	$W_{80,65}$	J	115	105	9.5	4.8
	$W_{70,30}$	J	130	120	8.3	
	$\rho_{b,65}$	kg/m^3	2680	2668	0.4	
	$\rho_{b,300}$	kg/m^3	2830	2807	0.8	
Ledge angle of repose	α_M	°	90	84	7.1	7.1

The shear stress in the pre-shear and shearing stages is simulated with $|e|$ equal to 1% and 12.5% respectively. Bulk density values in loose and pre-sheared conditions, $\rho_{b,0}$ and $\rho_{b,20}$, are simulated with $|e|$ equal to 5.8% and 1.4%. On average, a relative deviation of 7% is captured in a ring shear test including four calibration targets. In the consolidation-penetration test, four different calibration targets are evaluated, including accumulative penetration resistance and bulk density values measured at two different pre-consolidation levels. In the consolidation-penetration test, accumulative penetration resistance parameters, $W_{80,65}$ and $W_{70,300}$, are simulated with $|e|$ smaller than 10%. Additionally, bulk density values at two different levels of σ_{pre}, 65 and 300 kPa, are simulated with negligible $|e|$ values (smaller than 1%). This confirms that, using the elasto-plastic adhesive contact model, the calibration procedure was successful in capturing history-dependent behavior of the cohesive iron ore sample in terms of penetration resistance and bulk density. Finally, the ledge angle of repose, which was not used during the surrogate modeling-based optimization, is replicated with $|e|$ = 7.1%. Therefore, considering simulated bulk density values in four different stress states and α_M, the definiteness criterion is met using the optimal set of calibrated parameters, X^*.

Third, the entire yield locus is verified for the ring shear test conducted with $\sigma_{pre=20}$. Figure 5-12 compares the results of the ring shear test simulation using the optimal parameter set.

Comparable shear stress values are measured in both simulation and experiment, with $|e|_{mean}$ = 6.7%. This verifies that the calibration procedure is able to replicate shear strength in various stress states and is able to capture the non-linear yield locus.

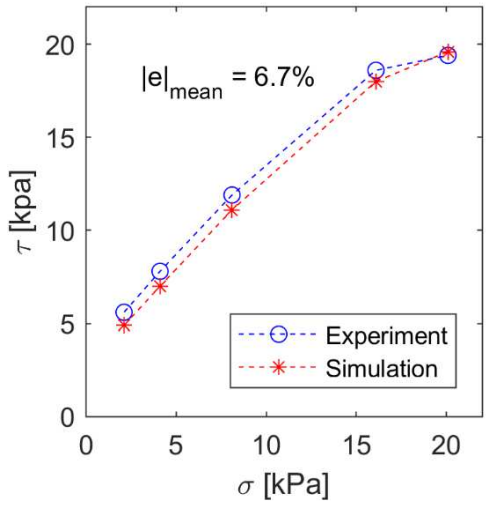

Figure 5-12. Verification of yield locus for $\sigma_{pre=20}$.

Finally, wall friction measurements as a bulk response independent of the calibration targets are compared in Figure 5-13, including 8 different stress states. The simulated wall yield locus shows a linear trend that replicates experimental values, with $|e|_{mean}$ = 5.5%. Since the Hertz-Mindlin (no-slip) contact model (without adhesive forces) was used to model particle-wall interactions, this linear trend could be expected. This finding is similar to the conclusion of [29], obtained by modeling a cohesive coal sample in a wall friction test.

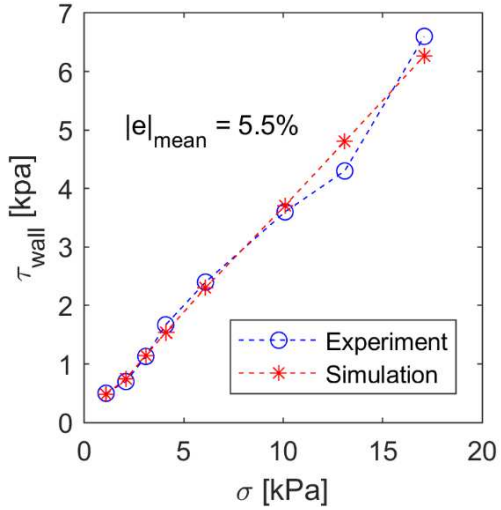

Figure 5-13. Verification of wall friction measurements.

5.5. Conclusion

In this chapter, a reliable and novel DEM calibration procedure is established by incorporating two important criteria: feasibility and definiteness. The DEM calibration procedure was applied successfully to model cohesive and stress-history-dependent behavior of moist iron ore based on an elasto-plastic adhesive contact module. The definiteness of the calibrated parameter set has been verified using 20 different bulk response values in four test cases, such as ring shear, consolidation-penetration, and wall friction tests.

- The established calibration procedure can be used to calibrate material models when a high number of DEM input variables (e.g. 6) as well as multiple calibration targets (i.e. >2) are involved.
- Both continuous and categorical variables can be used in step I, feasibility. Using the Latin hypercube design (LHD) method, it has been shown how a categorical DEM variable (i.e. rolling friction module) can be used during calibration.
- During the calibration procedure, significant DEM variables can be screened using the one-variable-at-a-time (OVAT) method in step II. For ring shear and ledge angle of repose simulations, coefficient of static friction between particles ($\mu_{s,p\text{-}p}$) was found to be the most significant DEM variable. In general terms, this outcome is consistent with findings by other researchers [11]. Particle shear modulus (G), surface energy ($\Delta\gamma$), and contact plasticity ratio (λ_P) were the other significant variables when the elasto-plastic adhesive contact module was used.
- It was shown in the current chapter that surrogate modeling-based optimization is applicable when a high number (i.e. > 5) of DEM input variables is involved.
- The combination of Taguchi and multiple linear regression techniques was successful in the surrogate modeling-based optimization, with coefficient of determination values larger than 0.75 for all the calibration targets.

Next chapter will focus on validating the calibrated model of the cohesive iron ore in simulating the grabbing process where all the bulk responses (discussed in Section5.4) play a role.

6

Validating co-simulation of a grab and cohesive iron ore*

A novel design approach of grabs is to test virtual prototypes of new concepts in interaction with bulk solids. To confirm the simulation accuracy of the grabbing process of cohesive and stress-history dependent iron ore cargo, this chapter develops and validates a full-scale co-simulation. The calibrated material model of Chapter 5 is used to set up the co-simulation.

First, by executing in-situ measurements during the unloading of a vessel, grab-relevant bulk properties of the cargo, such as penetration resistance, are determined. Second, full-scale grabbing experiments are conducted in the cargo hold, which allows the process to be recorded in realistic operational conditions. Third, full-scale co-simulation is set up using the material model that has been calibrated in the previous chapter. By applying the particle scaling rules of Chapter 4, the co-simulation can be run with a practical computation time. Fourth, the co-simulation is validated by comparing its predictions to experimental data from various aspects,

---

* This chapter corresponds to: M.J. Mohajeri, W. de Kluijver, R.L.J. Helmons, C. van Rhee, D.L. Schott, “A validated co-simulation of grab and moist iron ore cargo: replicating the cohesive and stress-history dependent behaviour of bulk solids”. Accepted in Advanced Powder Technology, 2021.

such as the force in cables and the torque in winches. The grabbing process of cohesive of iron ore and free-flowing iron ore (pellets) are compared with each other. The validated co-simulation proves that the stress-dependent behaviour of cohesive cargo as it interacts with the grab were captured successfully.

6.1. Introduction on the Validation Method

The general model of the grabbing process of bulk cargo (i.e. iron ore) using cable-based grabs is shown in Figure 6-1a. The crane operator controls the grab using cables that are connected to driving winches. In addition to the grab design itself, the dimensions of a ship's hold, the properties of bulk cargo, the crane operator, winches and cables are all contributing elements in the grabbing process. Thus, predicting the performance of new design concepts is still challenging as it requires consideration of the interaction between multiple contributing elements.

A novel approach to design grabs is virtual prototyping in interaction with bulk solids [8,153,154]. Lommen et al. [9] have developed a real-scale co-simulation between grabs and free-flowing iron ore material [108]. The co-simulation has been validated for simulating the grabbing process of iron ore pellets [155]. As shown in Figure 6-1b, the co-simulation uses the framework developed by coupling two solvers, MultiBody Dynamics (MBD) and Discrete Element Method (DEM) [6]. The co-simulation requires a virtual crane operator, a CAD model of a grab, and a calibrated DEM material model as inputs.

In contrast to iron ore pellets, the majority of iron ore cargoes exhibit cohesive and stress-history dependent behaviour [22,108]. Cohesive forces between particles are created due to the liquid bridge, and hence the amount of moisture present influences material behaviour and its interaction with equipment. Furthermore, as the unloading starts and proceeds to greater depths, grabs touch the cohesive material that is pre-consolidated with a higher level of overburden pressure [21]. Consequently, during the unloading of a bulk carrier, the bulk responses of cohesive iron ore cargo, such as bulk density, shear strength, and bulk stiffness, are expected to vary over the cargo depth (z direction) [108]. The cohesive and stress-history dependent behaviours of bulk materials are not yet investigated in terms of interaction with grabs. Therefore, a test method first needs to be developed to determine the grab-relevant properties of cohesive bulk materials during the unloading of a cargo hold; second, a reliable DEM material model for cohesive bulk solids needs to be included in the co-simulation to enable the virtual prototyping of grabs.

In the previous chapter, DEM parameters were calibrated to simulate the cohesive and stress-history dependent behaviour of moist iron ore cargo with an elasto-plastic adhesive contact model. The common procedure to assure the validity of the model is to first calibrate with laboratory scale experiments [29,156] and next validate DEM simulations with industrial scale experiments [9,28,87,88,157–159]. Validation is achieved by comparing the results of the simulation and experiment, either in quantitative or qualitative ways [8,28,92–94,127–131]. To ensure design concepts can be evaluated under actual operational conditions, validating the model in full-scale is required [160,161].

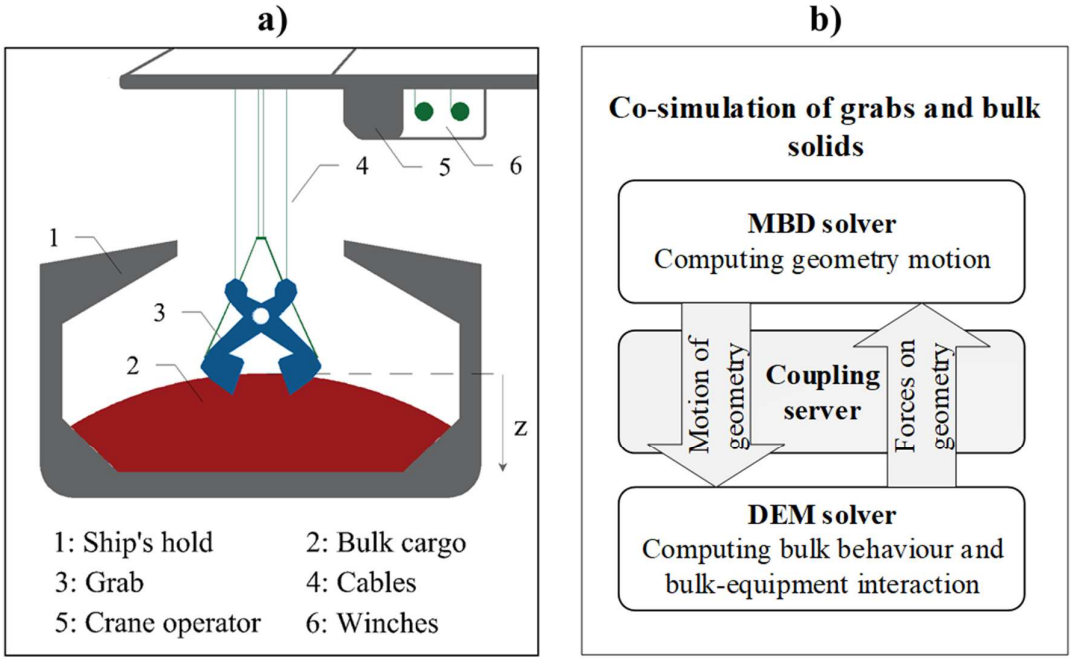

Figure 6-1. a) General model of the grabbing process (i.e. of iron ore) during unloading bulk carriers, b) the co-simulation framework of grabs and bulk solid materials based on [6]

Figure 6-2 displays the main steps required to develop the validated co-simulation of grabs and cohesive iron ore. In the first step, iron ore cargo is characterized during the unloading of a bulk carrier, as well as in the laboratory environment. The second step is to record the grabbing process under actual operational conditions, including the cargo depth as a variable, thus capturing the stress-history dependent behaviour of bulk material. The third step is to create a large-scale co-simulation of grabs and cohesive bulk solid cargo that has a practical computation time. The forth step is to validate that the co-simulation captures the grabbing process of the cargo accurately, considering essential outputs such as the static forces, dynamics, and kinematics of equipment.

6.2. Bulk Material Characterization and Validation Method

This section describes further the steps required to characterize bulk material and to validate the co-simulation modelling of the grabbing process of cohesive iron ore cargo.

6.2.1. Characterizing bulk solid cargo

The bulk solid cargo is characterized in both laboratory and ship hold environments. The cargo is a sinter feed type of iron ore from the Carajas mines, which is one of the largest iron ore resources on earth [62]. The average density of the particles is 4500 kg/m^3, with a standard deviation of 125 kg/m^3. The median particle size, d_{50}, is equal to 0.88 mm.

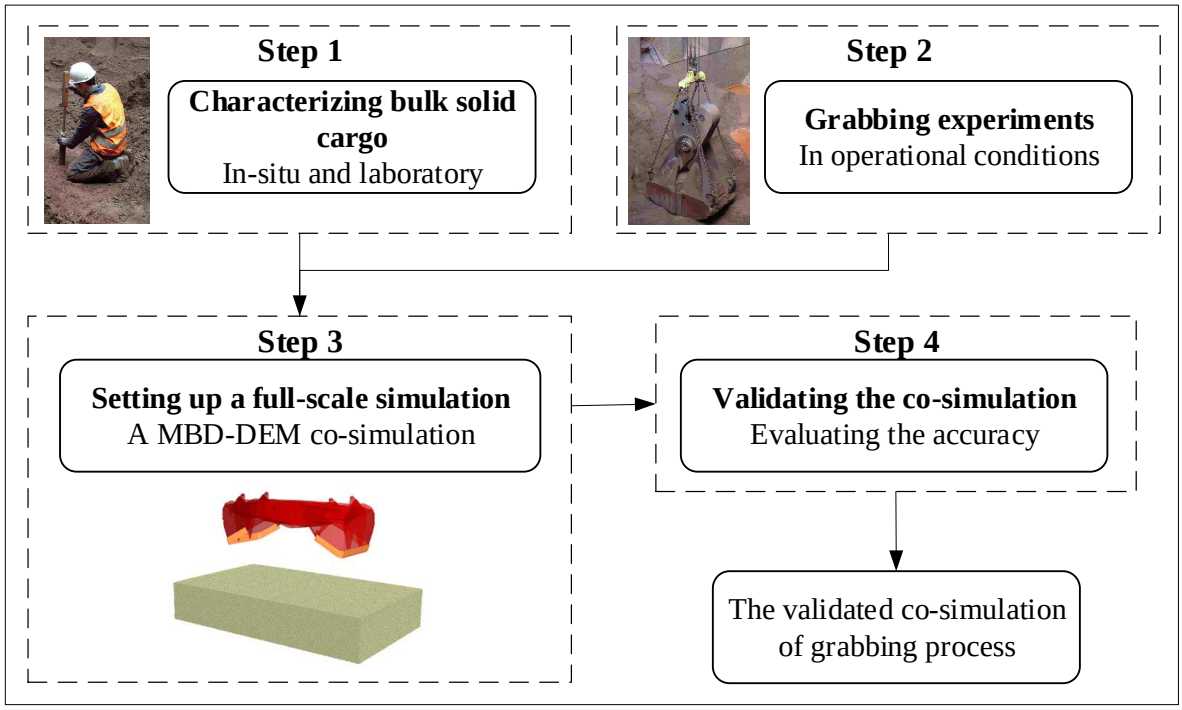

Figure 6-2. Main steps to develop a validated co-simulation of grabbing process

The objective of in-situ measurements during unloading is to determine the properties of the cohesive iron ore cargo over its depth, *z*. The following bulk properties are relevant to the grabbing process [108], and are thus selected:

- Penetration resistance through initial penetration depth, $\Delta_{initial,S66}$
- Bulk density, ρ_b
- Moisture content, MC

Measuring penetration resistance and bulk density during the unloading process allows for quantitatively investigating the level to which the cargo is densified over its depth. It is expected that moisture content also shows variation over cargo depth [4].

A test procedure is designed to determine the penetration resistance and bulk density using a single test device. Figure 6-3 displays a schematic view of the designed test device, which is named *sampling tube & sliding hammer* (S66). It consists of two main components, a sampling tube (Figure 6-3a and b) and a sliding hammer (Figure 6-3c). The effective length of the sampling tube is 260 mm, with an inner diameter of 66 mm, and thickness of 2 mm. The hammer is 400 mm long with a mass of 0.855 kg, which is connected to a slide with a length of 278 mm. The sliding hammer can be fixed to the sampling tube using a connecting head.

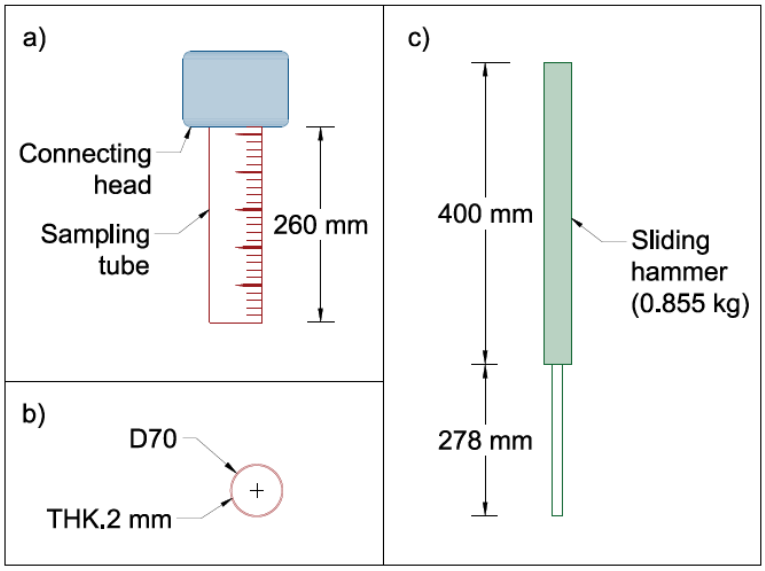

Figure 6-3. Schematic view of sampling tube & sliding hammer (S66): a) sampling tube and connecting head to hammer, b) cross section view of the sampling tube, and c) the sliding hammer

Penetration resistance is determined based on a modified version of the *Standard Penetration Test* (ISO 22476-3). The tube is driven into the bulk surface with five consecutive drops of the sliding hammer, and next, the initial penetration depth of tube ($\Delta_{initial,S66}$) is recorded. The number of hammer drops is sufficient, as more hammer drops may result in a penetration depth greater than the effective length of the sampling tube.

The test continues by driving the sampling tube further into the bulk surface until the final penetration depth is reached. Next, the tube is carefully extracted to weigh the collected bulk solid specimen. It is ensured that the tube is extracted without losing the bulk specimen. Bulk density, ρ_b, is then determined by Eq. (6.1).

$$\rho_b = \frac{M_s}{A_e\, L_s} \tag{6.1}$$

where M_s is the weight of the collected specimen. L_s is the final penetration depth of the sampling tube that is determined by using the ruler, as shown in Figure 6-3a. A_e is the inner cross-sectional area of the tube. The moisture content of samples is also measured in the laboratory using a drying oven, according to the method described in [65].

During the unloading process of bulk carriers, the bulk responses of fine moist iron ore ($\Delta_{initial,S66}$, ρ_b and MC) are expected to vary, as shown by the trends in Figure 6-4. This hypothesis is based on field measurements [20], including the Cone Penetration Test (ASTM D3441), and moisture content over cargo depth, *z*, prior to commencing the unloading process.

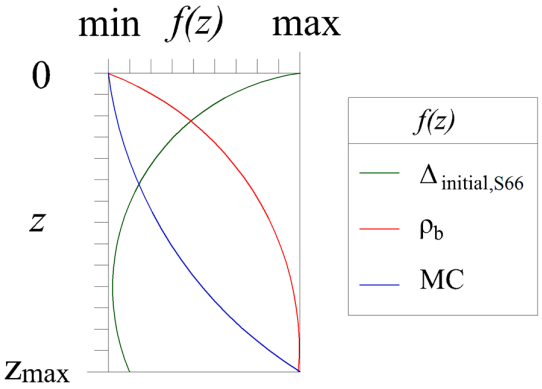

Figure 6-4. Expected distribution of grab relevant bulk properties over cargo depth (*z*)

Firstly, due to the void between particles, moisture is expected to transfer to greater depths during the voyage of bulk carriers. This results in the accumulation of moisture near the bottom of cargo holds [4]. Secondly, due to increasing vertical confining pressure over the cargo depth, lower initial penetration depth and higher bulk density values are respectively expected to occur by increasing *z* [108]. However, a saturated condition usually occurs at the "wet bottom" of iron ore carriers [19], usually for $z/z_{max} \geq 0.8$.

Verifying the accuracy of the sampling tool (S66)

It needs to be verified whether the S66 device is accurate in determining bulk density of the cohesive iron ore sample. For this purpose, two different test methods, ISO 17828 [81] and S66, are used in the laboratory environment. In ISO 17828, bulk density is determined by using a rigid cylinder with the inner volume of 5 litres. The bulk density results, including both average and standard deviation values, are compared in Table 6-1. Bulk density measurements using ISO 17828 are repeated five times, resulting in an average bulk density of 1774 kg/m^3 with an

acceptable standard deviation of 20 kg/m^3. Measurements using the S66 device result in an average ρ_b of 1780 kg/m^3 with a standard deviation of 40 kg/m^3 in ten test repetitions.

Table 6-1. Verifying the accuracy of the sampling tool (S66) in determining bulk density

Measurement method	Repetitions	Average ρ_b [kg/m^3]	SD [kg/m^3]	SD [%]
ISO 17828	5	1774	20	1.1
S66	10	1780	40	2.2

Comparable average bulk density values can be measured using ISO 17828 and S66, with a minor difference in standard deviation values. Therefore, the accuracy of S66 in determining bulk density of the cohesive iron ore sample is verified.

Measurement plan

A primary variable is considered in the measurement plan: cargo depth (z). Bulk cargo is characterized in the in-situ conditions from the top of the cargo pile, z = 0 m, until z/z_{max} = 0.85. As grabs unload the bulk carrier, greater depths (z > 0 m) can be accessed. At each cargo depth, the measurement is repeated between three to five times, ensuring test repeatability. Three different cargo holds are accessed during the in-situ measurements.

The cargo depth, z, is determined using a laser ruler (HILTI PD 40). When standing on the bulk cargo surface, the hold depth index is read using the laser ruler device. The device is only able to measure the distance to the depth index, but unable to measure the laser beam orientation. Thus, the distance to three different points are measured for each cargo depth, that allows for determining z with a maximum error of 0.5 m.

It usually takes more than a day to unload an ocean-bound bulk carrier. Therefore, unloading continues over a “night shift”. No data can be collected during this time, as the in-hold environment is unsuitable for taking such measurements during that period.

6.2.2. Grabbing experiments

Figure 6-5 shows five stages of the grabbing process, as introduced in [155]. In this figure, the red arrows indicate the cable velocity direction. The grab is lowered onto the bulk surface (Figure 6-5a), ending with a certain penetration depth as the grab digs into the material (Figure 6-5b). This continues by closing the grab and collecting the bulk solid (Figure 6-5c). Once the grab is almost filled with the bulk solid, the hoisting stage commences (Figure 6-5d). During experiments, the grabbing process usually ends with the suspension stage (Figure 6-5e), which

allows for conducting further measurements, such as weighing the grab and collected mass together.

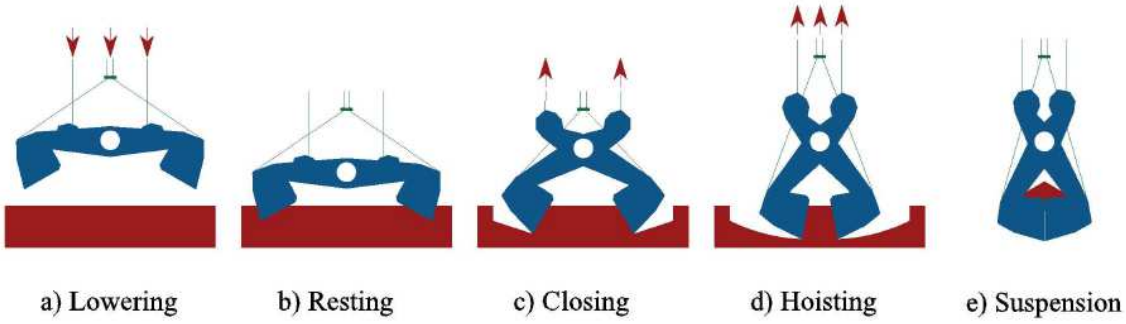

Figure 6-5. The operation of the grabbing process consists of five stages: a) Lowering onto the bulk surface, b) Resting with slacked cables, c) Closing by tensioning two cables, d) Hoisting using all cables, and e) Suspending the grab if required

Table 6-2. Measured parameters during the grabbing experiments

Stage	**Measured parameter**
All stages	Force in cables Torque in winches Kinematics of geometry
Suspension	Payload Average porosity of collected bulk solids In-grab bulk sampling

Table 6-2 presents the list of parameters measured in grabbing experiments. Two different types of parameters are measured. The signal type parameters are the following: the force in cables, the torque in winches, and the kinematics of grab geometry. Scalar type parameters are also recorded, such as payload and average porosity.

- Force in cables: the grab is operated on four cables and the tensile forces in these cables are measured using load cells. The load cells are located adjacent to driving winches of the crane. These load cells as well as other sensors are calibrated by the terminal operator on a regular basis. The load cells measure force in cables with a frequency of 2 Hz. The payload of grab, M_{DWT} can be determined using Eq. (6.2).

$$M_{DWT} = M_t - M_e \tag{6.2}$$

where M_t is the total force in cables once the grab is hoisted after collecting bulk solids, and M_e is the total force in cables before collecting bulk solids. In other words, M_e corresponds to the weight of an empty grab.

- Torque in winches: the torque in each winch is determined separately with a frequency of 100 Hz.
- Kinematics of geometry: to record kinematics of the grab geometry, a video tracking technique similar to [155] is used. Basically, the grab geometry consists of two rigid bodies that revolves over a main hinge. For that reason, three markers are used that are sufficient to track the geometry movements in X-Z plane.
- Average porosity of collected bulk solids: once the grab is suspended, 3D-scanning technology is used to determine the volume of the collected bulk solids, V_{DWT}. First, point cloud images are taken using the Intel RealSense™ depth (SDK) camera. Second, a surface mesh is fitted on point cloud images, according to the method described in [162]. Figure 6-6a shows an example of generated surface mesh, including the grab that contains collected bulk solids. Third, V_{DWT} is determined by importing the mesh surface of collected bulk solids into a 3D CAD model of the grab. The porosity of collected bulk solids, n_{DWT}, can then be calculated using Eq. (6.3).

$$n_{DWT} = 1 - \frac{M_{DWT}}{V_{DWT}\,\rho_s} \tag{6.3}$$

where ρ_s, particle solid density is equal to 4500 kg/m^3 [108].

- In-grab bulk sampling using S66-1000: once the grab is suspended, a sampling tube, *S66*, with the effective length of around 1 m is used to collect samples from the area highlighted in Figure 6-6b. The tube is then carefully extracted from the bulk material. The sample is weighed, which allows for quantifying the porosity in a similar way compared to Eq. (6.3). The sampling using S66-1000 is repeated at least three times, ensuring the repeatability of the test.

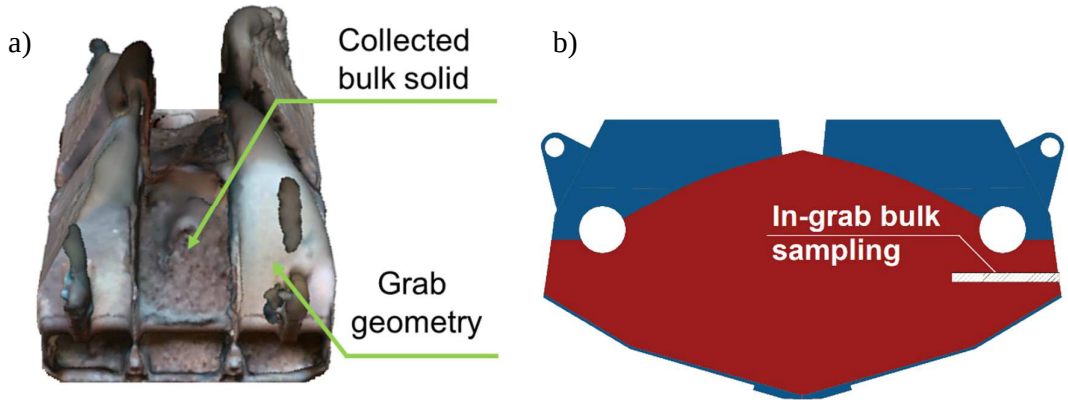

Figure 6-6. a) generated 3D surface mesh, including grab geometry and collected bulk solid, b) schematic cross-sectional view of grab and collected bulk solid, indicating the in-grab sampling area

Experimental plan

Two sets of experiments with different consolidation states are defined, of which multiple repetitions are performed.

- In the first experiment set, the process is recorded at the cargo depth of z = 7 m. The first experiment set includes: test 1.1, test 1.2 and test 1.3.
- In the second experiment set, the process is recorded at is z = 2.5 m. The second experiment set includes: test 2.1 and test 2.2.

The crane operator and bulk surface geometry are other possible influencing variables in our experiments. The motion of closing and hoisting winches are recorded with a frequency of 100Hz, thus a virtual crane operator can be modelled in the co-simulation. To minimize the influence of bulk surface geometry, grabbing experiments are executed on an adequately flat bulk surface.

6.2.3. A full-scale simulation setup

The co-simulation between MultiBody Dynamic (MBD) and DEM solvers uses the framework of [6], as shown schematically in Figure 6-1b. The MBD simulation of the grab is set up in ADAMS® using the real dimensions of the grab. In the virtual environment, the operation of the grab is simulated using a combination of winches, sheaves and cables [7].

A material model of the cohesive iron ore has been calibrated in the previous chapter. The calibrated model is used in the current chapter to set up the DEM simulation. By applying the particle scaling rules of [140], a mean particle diameter of 55 mm is used in the simulation. The surface energy and constant pull-off force needs to be adjusted during the scaling of particles.

Table 6-3 presents the main input parameters of the DEM simulation. For other DEM input parameters and the calibration procedure refer to the previous chapter.

To replicate a pre-consolidated condition in the simulation, DEM particles are compressed using a pressure-controlled plate. A quasi-static condition, as defined in [140], is maintained during compression. Once the desired pressure, i.e. 65 or 200 kPa, is reached, the pressure-controlled plate is moved upward. Thus, a pre-consolidation condition is replicated in the DEM simulation.

Table 6-3. Main input parameters of DEM simulation

Parameter	Symbol	Unit	Value
Particle density	ρ_p	kg/m^3	4500
Particle diameter	d_p	mm	55
Particle shape	Ψ_p	-	Single sphere
Normal and tangential contact modules, particle-particle	$f_{N,p-p}$ and $f_{T,p-p}$	-	EEPA [84]
Rolling contact module	f_R	-	Rotation restricted
Coefficient of static friction, particle-particle	$\mu_{s,p-p}$	-	0.31
Coefficient of static friction, particle-geometry	$\mu_{s,p-w}$	-	0.37
Constant pull-off force	$-f_0$	N	-0.2
Surface energy	$\Delta\gamma$	J/m^2	100
Plasticity ratio	λ_P	-	0.2

Figure 6-7 displays the DEM simulation environment, including the grab's geometry components. The dimensions of the material bed are selected after running a sensitivity analysis so that the grabbing process is not influenced by the boundaries. The in-situ measured winch velocity history is used as input in the co-simulation to replicate the grabbing process. In addition, modelling the actual distance between the grab and the trolley system of the crane could complicate the simulation setup unnecessarily. Thus, only the vertical position of the main hinge is analysed, as in the MBD simulation where the grab is positioned in the similar x-y coordinates compared to the winches.

To set up a full-scale DEM simulation of the grabbing process, the grab's components are separated into buckets and knives, as suggested by *Lommen et al.* [9]. The reaction forces from DEM particles on the bucket part is independent of particle size, thus the particle scaling rules of [140] can be applied. The penetration resistance against knives depends on the particle size [9], thus $\mu_{s,p-w}$ is adjusted to 0.2 for the interaction between knives and particles. This results in a

comparable penetration depth of grab due to its own weight, when the simulation and experimental setups are compared.

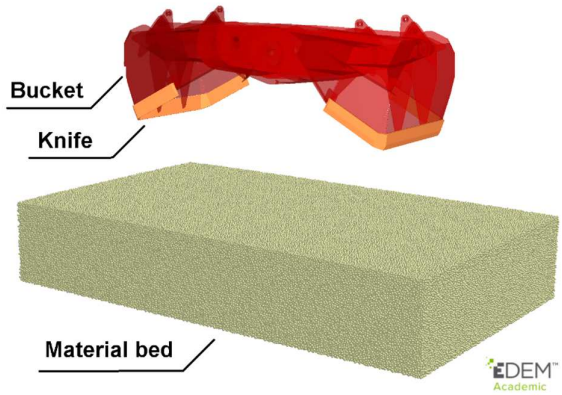

Figure 6-7. Main components in the DEM simulation, including material bed, the grab's buckets, and the grab's knives

6.2.4. Evaluating accuracy of the co-simulation

For scalar type parameters (e.g. payload, average porosity), the mean of absolute relative differences is used to quantify error in the co-simulation. If y and y' represent measured scalar parameters in the experiment and the co-simulation, respectively, then $|e|_{mean}$ is determined according to Eq. (6.4) for a number of test repetitions. In the current study, an $|e|_{mean} \leq 10\%$ is considered an acceptable outcome for validating the accuracy of the co-simulation.

$$|e|_{mean} = \sum_{k=1}^{N_e} 100 \left| \frac{y_k - y'_k}{y_k} \right| \tag{6.4}$$

Signal type parameters (e.g. force in cables, torque in winches) are compared between the experiments and simulations using the coefficient of determination, R^2, as described by Weisberg [163]. To validate the force in cables and the torque in winches, *Lommen et al.* [155] suggested that minimum R^2 values of 0.9 and 0.8 are required respectively.

6.3. In-situ and Validation Results

In this section, the results of in-situ bulk cargo characterization, as well as the validation of the DEM-MBD model, are presented.

6.3.1. Bulk cargo characterization during unloading

Figure 6-8 presents the outcome of the in-situ measurements on bulk properties over cargo depth, including initial penetration depth (Figure 6-8a), bulk density (Figure 6-8b), and level of moisture

content (Figure 6-8c). The purple-coloured area indicates the "night shift" period in which no data was measured.

According to Figure 6-8a, $\Delta_{initial,S66}$ in the first 2.5 m of the cargo depth is larger than 75 mm in all three measurements; while in other data points, when $z \geq 6$ m, the initial penetration depth of S66 is smaller than 75 mm. A higher deviation in results is observed when $z \leq 2.5$ m, compared to when $z \geq 6$ m. However, a clear trend is that $\Delta_{initial,S66}$ in the later situation ($z \geq 6$ m) is always smaller than in the former ($z \leq 2.5$ m). Some level of increase in $\Delta_{initial,S66}$ is observed when $z \geq 8$ m, compared to $8 > z \geq 6$, which is probably due the correlation between the penetration resistance of material and its moisture content.

According to Figure 6-8b, bulk density values in the first 2.5 m of the cargo depth is lower than 2400 kg/m^3, and the bulk density of three out of four data points shows comparable values to the laboratory measurements (Table 6-1). In contrast, at greater depths ($z \geq 6$ m), the bulk density of the cohesive iron ore cargo increases significantly (up to around 3100 kg/m^3).

According to Figure 6-8c, the moisture content is between 8.4% and 9% when $z \leq 6$ m, while it increases up to 10% when $z > 6$ m. In general, due to the void between particles, moisture transfers to greater depths during the voyage of bulk carriers. Similarly, a non-linear increase in moisture content has been observed for other iron ore cargoes [20]. The average moisture content of the cargo is 9.1%, with a standard deviation of 0.5%.

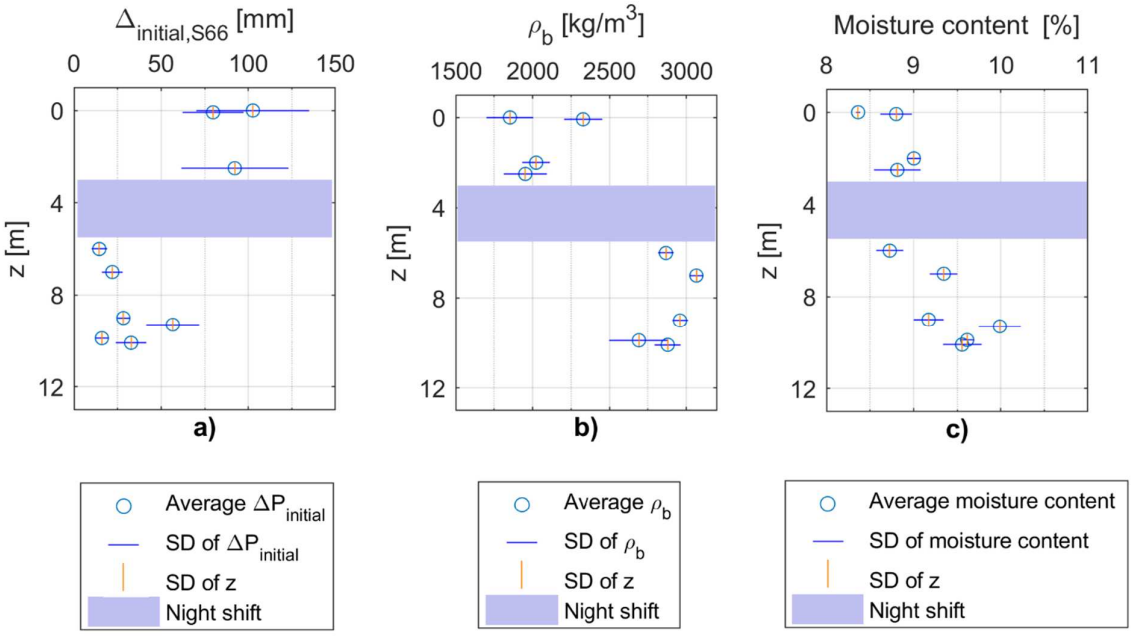

Figure 6-8. Grab-relevant properties of cohesive iron ore over cargo depth: a) intial penetration depth, b) bulk density, and c) level of moisture content

In conclusion, an increasing densification of the cohesive iron ore over the cargo depth is observed, which is in line with the expected trends shown in Figure 6-4. This has been supported by the considerable changes of $\Delta_{initial,S66}$ and bulk density values over cargo depth that have been determined during the unloading of the vessel. Thus, during the lowering stage, grabs penetrate into increasingly pre-consolidated bulk solids. To model the grabbing process of cohesive bulk solids in a realistic way, the increasing levels of pre-consolidation over the cargo depth needs to be replicated in the DEM simulation setup.

6.3.2. Validating the co-simulation

Two sets of grabbing experiments are conducted where the dry-based moisture content is 8.8±0.2%. The DEM material model is calibrated based on the moisture content of 8.7%, which is expected to replicate cargo conditions properly. Grabbing experiments are conducted at two different cargo depths, which correspond to z equal to 7 and 2.5 m. Due to cargo weight, the overburden pressure creates a pre-consolidated condition at mentioned cargo depths [21]. The overburden pressure, σ_{pre}, can be approximated by multiplying cargo depth and average cargo density together; the average cargo density is 2800 kg/m^3. For example, in the experiment set 1, corresponding to z = 7 m, the historical pressure is equal to approximately 200 kPa. Figure 6-9 compares the bulk density in simulated pre-consolidated conditions with experimental results of [108] on the same iron ore sample. Bulk density values at σ_{pre} equal to 65 and 200 kPa are adequately replicated in the DEM simulations.

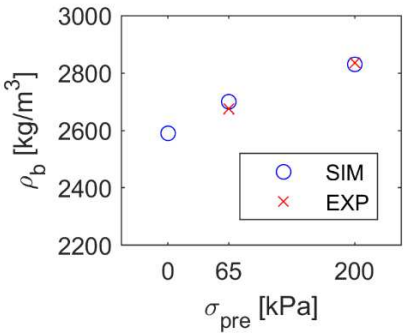

Figure 6-9. The DEM simulation setup adequately replicates the bulk density in pre-consolidation situations

Figure 6-10 shows the simulated grabbing process during four different stages of the operation: a) Lowering, b) Rest, c) Closing, and d) Hoisting. The suspension stage is not included in that simulation.

Experiment set 1: cargo depth of 7 m

The experimental results of the grabbing process are compared with predictions of the DEM-MBD co-simulation. Table 6-4 compares the payload in the experiments, $M_{DWT,exp}$, when the cargo depth is 7 m, to the simulated payload values, $M_{DWT,sim}$. The corresponding pre-consolidated situation is simulated by applying a uniform pressure of 200 kPa on the bulk surface prior to the grabbing process.

Table 6-4. Comparison between simulated payload and experimental measurements in test 1 (z = 7 m)

Test	$M_{DWT,exp}$ [ton]	$M_{DWT,sim}$ [ton]	|e| [%]
1.1	24.9	25.7	3.2
1.2	25.7	24.2	5.8
1.3	27.8	27.1	2.5
Mean	26.1	25.7	1.8

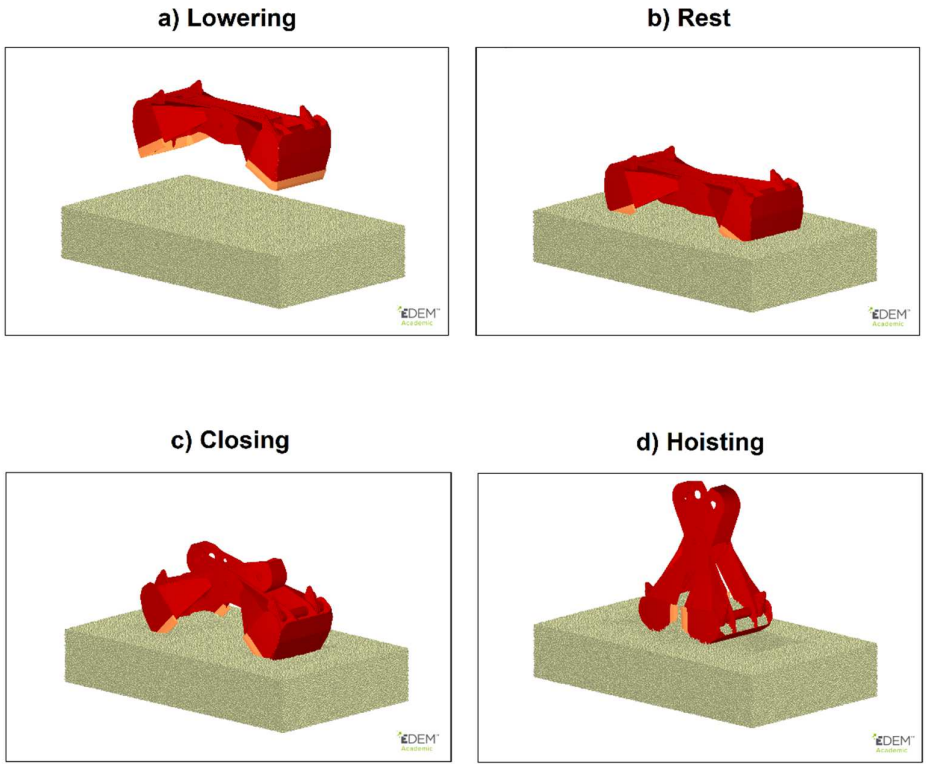

Figure 6-10. The simulated grabbing process in different operation stages: a) Lowering, b) Rest, c) Closing, and d) Hoisting

In the experiment set 1, an average $M_{DWT,exp}$ = 26.1 ton is determined with a standard deviation of 1.2 ton. The co-simulation replicates the payload values, with an average $M_{DWT,sim}$ = 25.7, with a standard deviation of 1.2 ton. The difference between simulated payloads and experimental

results, $|e|_{mean}$, is 1.8%, with the maximum value of |e| = 5.8%. The small error is probably caused by idealizing the bulk surface in the simulation and its operational characteristics. Also, *Schott et al.* [155] have validated the simulation of the grabbing process of free-flowing iron ore products with values of $|e| \leq 6.0\%$. Therefore, the payload values for test 1 are simulated adequately, compared to reality.

Test 1.1 is selected for further analysis in terms of the force in cables and the torque in winches. Figure 6-11 compares the total force in cables between the experiment and the co-simulation. The total force during the lowering stage (L) represents the empty weight of grab, M_e. Once the grab is resting on the bulk solid, cables go slack, thus, the total force drops. By tensing the closing cables during the next stage (C), the grab starts to collect the bulk solid. This continues by involving the hoisting cables and eventually lifting the grab out of the bulk solid. In test 1.1, the crane operator moves the grab toward the quay side, and therefore, no suspension stage (S) is present. The force over all stages is predicted accurately with an overall coefficient of determination of 0.959.

To validate the grab's dynamics, the torque of the closing and hoisting winches during a grabbing cycle are compared in Figure 6-12. Similar to the force data (Figure 6-11), the torque in the closing and hoisting winches are adequately predicted. Only during the hoisting stage (H) does the torque start to deviate slightly from the experimental data, for both closing (Figure 6-12a) and hosting (Figure 6-12b) winches. The predicted closing and hoisting winches have the coefficient of determination values of 0.947 and 0.934 respectively, for the entire time span. Therefore, the results confirm the grab's dynamics in test 1 are correctly predicted in the co-simulation.

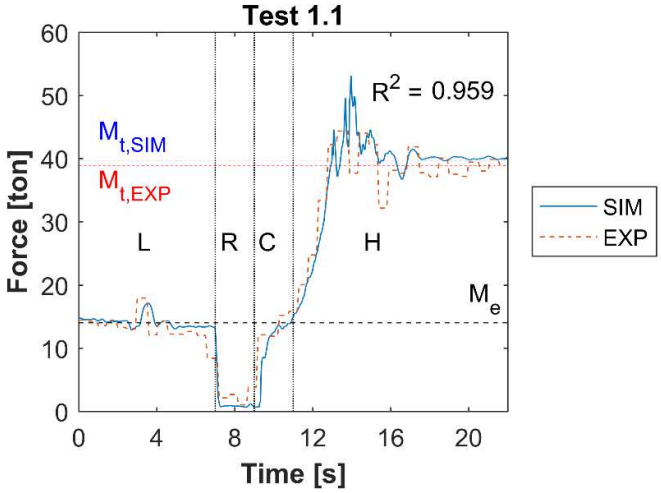

Figure 6-11. Load comparison in test 1.1.; Grab operation consists of lowering of the grab (L), resting on the surface (R), closing (C) and hoisting (H)

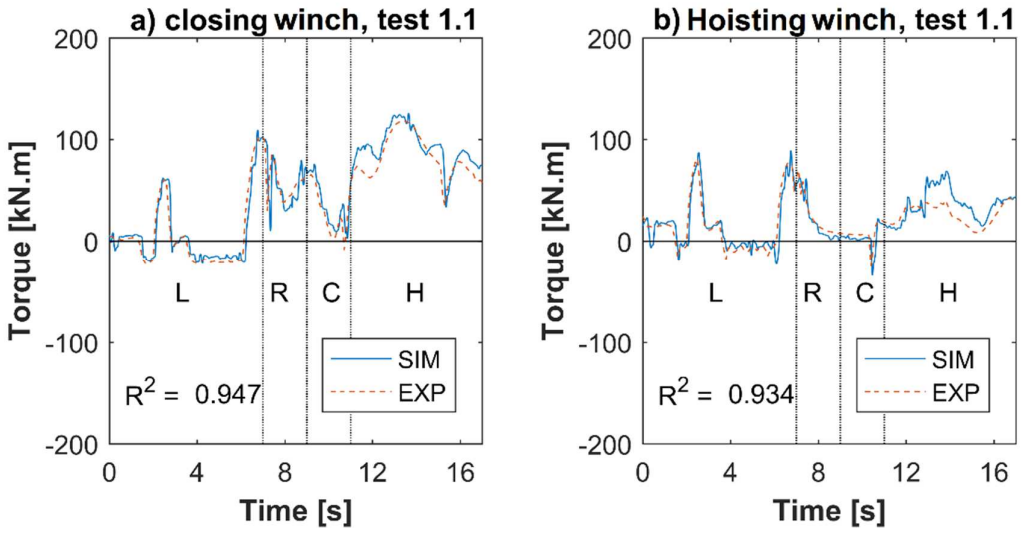

Figure 6-12. Torque comparison in test 1.1., a) closing winch, b) hoisting winch; Grab operation consists of lowering of the grab (L), resting on the surface (R), closing (C) and hoisting (H)

Figure 6-13 displays the three markers that we use to track the movements of the geometry during the grabbing process. Left and right markers represent the movement of the left and right grab's buckets respectively. The hinge marker represents the main hinge of the geometry where the grab's two buckets revolve.

Figure 6-14 compares the position of the markers between the simulation and the experiment. The position of the markers is analysed when the grab geometry is within reach of the video camera. In other words, the initial part of the lowering stage and the last five seconds of the hoisting stage are excluded from the analysis. These excluded areas are not of interest as the grab mechanism is not operational (no closing or opening) and there is no dynamic interaction with material (lowering and hoisting). For all markers, the desired coefficient of determination, $R^2 > 0.9$ is met with values exceeding 0.96. The observed comparisons in Figure 6-14 confirm that the co-simulation is capable of predicting the grab's kinematics for a pre-consolidated cohesive bulk solid cargo.

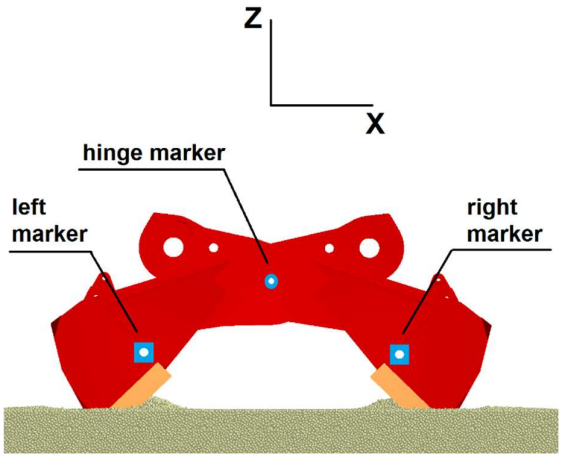

Figure 6-13. Three markers are used to quantify kinematics of the grab

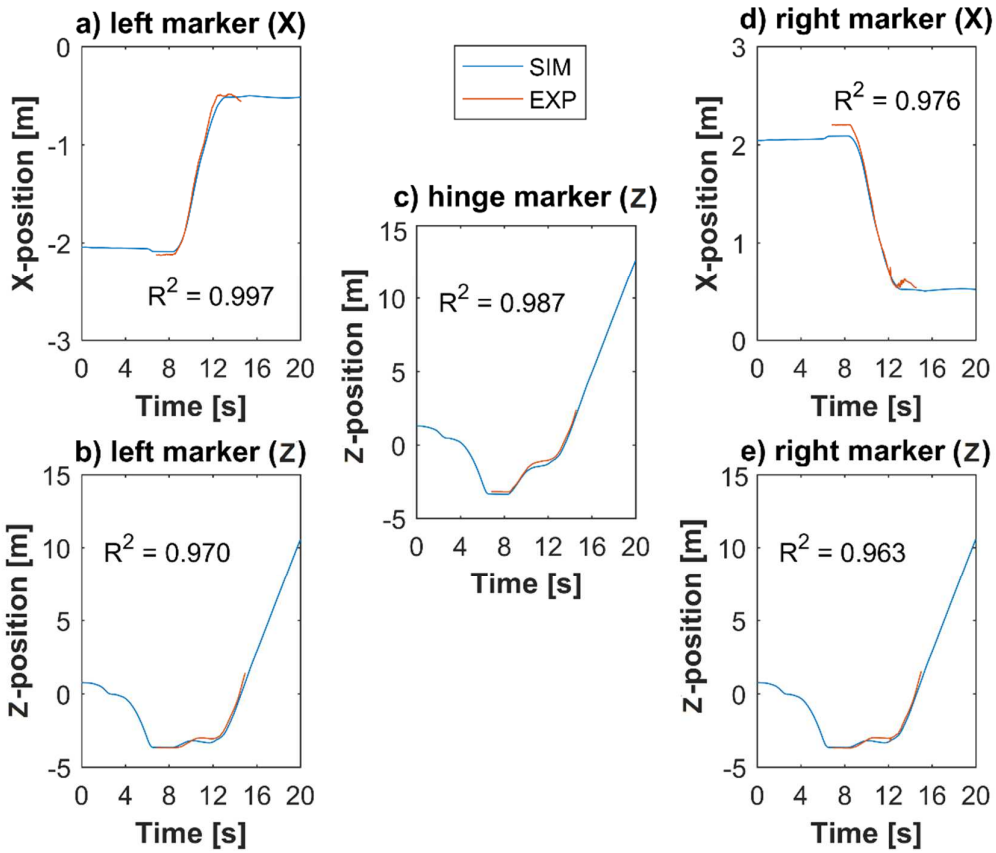

Figure 6-14. Comparison between simulating and video-tracking of the three applied markers on the grab, on pre-consolidation of 200 kPa in test 1.1. a) X-position of the marker on the left bucket, b) Z-position of the marker on the left body, c) Z-position of the marker on the main hinge, d) X-position of the marker on the right bucket, and e) Z-position of the marker on the right body

With the aid of 3D-scanning technology, the volume of collected bulk solids, V_{DWT}, in the grab is determined for test 1.3, and the average porosity, n_{DWT}, is calculated using Eq. (6.3). Figure 6-15a

presents how porosity is distributed in the simulation. The densification is at its lowest level near the free surface of bulk material, while due to existing compression forces, the material becomes more densified in its central region. The self-weight of bulk material, as well as the force applied by the grab geometry, are the acting compressive forces. A sampling tube, *S66*, is penetrated 0.60 m into the grabbed material and used to collect samples in the region highlighted in Figure 6-15b. The sampling is repeated three times, resulting in the average porosity of 0.468 for the highlighted region. The average simulated porosity for the same region is 0.480, indicating that simulated porosity distribution replicates reality accurately with |e| = 2.5%. Table 6-5 presents the comparison of M_{DWT} and n_{DWT}. The payload is replicated with a 2.5% difference between the simulation and the experiment. V_{DWT} is predicted accurately with |e| = 1%; this results in an adequate prediction of the average porosity with |e| = 5.8%.

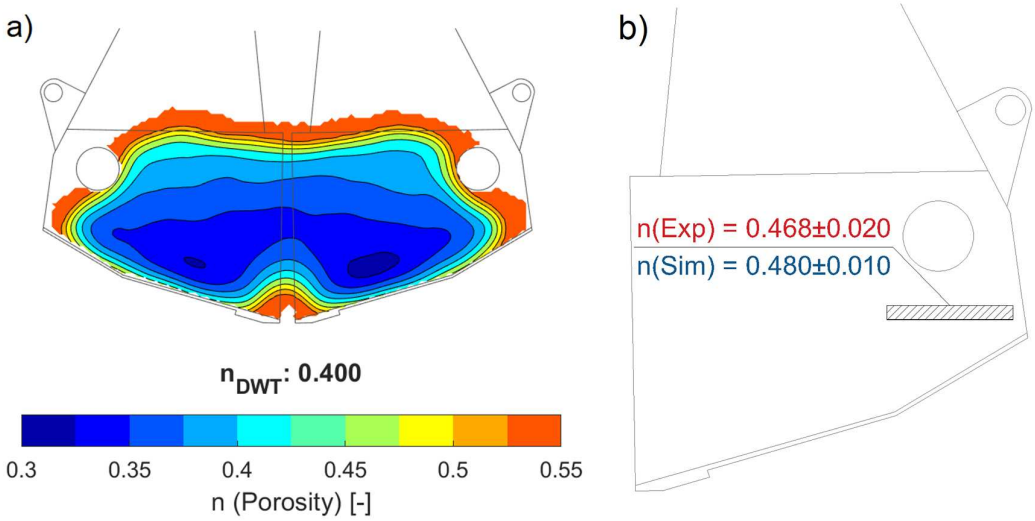

Figure 6-15. a) Simulated porosity distributon, and b) porosity comparison between experiment and simulation

Table 6-5. Validating mass and porosity of collected bulk solid

Test 1.3	**M_{DWT} [ton]**	**n_{DWT} [-]**
Experiment	27.8	0.375
Simulation	27.1	0.400
|e| [%]	2.5	5.8

Experiment set 2: cargo depth of 2.5 m

Table 6-6 compares the payload in experiments, $M_{DWT,exp}$, with the simulated payload, $M_{DWT,sim}$, when the cargo depth is 2.5 m. The corresponding pre-consolidated situation is created by applying a uniform pressure of 65 kPa on the bulk surface proceeding the grabbing process.

In the experiment set 2, an average $M_{DWT,exp}$ = 26.4 ton is determined with a standard deviation of 0.3 ton. The co-simulation replicates payload values accurately, with an average $M_{DWT,sim}$ = 26.3 with a standard deviation of 0.7 ton. Negligible differences between simulated payloads and experimental results are observed with $|e|_{mean}$ = 0.4%.

Table 6-6. Comparison between simulated payload and epxerimental measurements in test 2 (*z* = 2.5 m)

Test	$M_{DWT,exp}$ [ton]	$M_{DWT,sim}$ [ton]	|e| [%]
2.1	26.1	25.7	1.5
2.2	26.7	27.0	1.1
Mean	26.4	26.3	0.4

In addition, test 2.2 is selected to further validate the total force data. Figure 6-16 compares the total force in cables between the experiment and the co-simulation. The cables do not go fully slack during the rest stage (R), and therefore, the total force does not drop to zero. All four stages are replicated accurately in the co-simulation with R^2 = 0.957, confirming that the desired accuracy is also met when the cargo depth is 2.5 m.

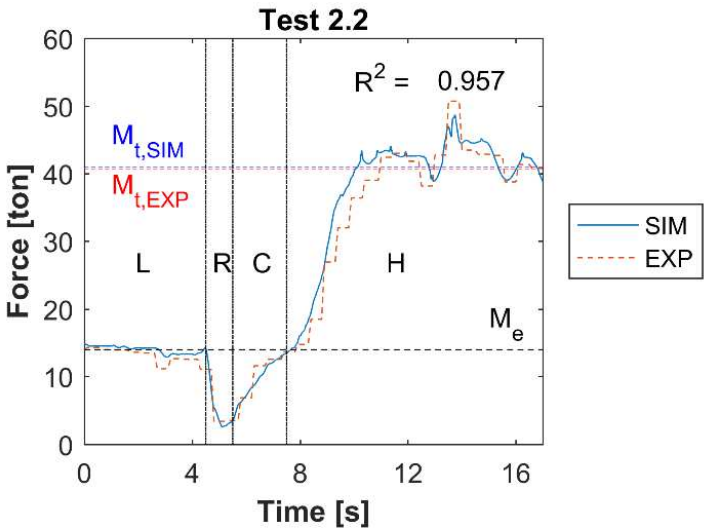

Figure 6-16. Load comparison in test 2.2.; Grab operation consists of lowering of the grab (L), resting on the surface (R), closing (C) and hoisting (H)

The volume of collected bulk solids, V_{DWT}, in the grab is determined for test 2.2 using the 3D-scan technology, and the average porosity, n_{DWT}. Table 6-7 presents the comparison of M_{DWT} and n_{DWT}. The payload is replicated with a 1.1% relative difference between the simulation and the experiment. V_{DWT} is predicted with |e| = 5.3%; this results in an adequate prediction of the average porosity with the absolute different of 0.029 and |e| = 8.8%. The sampling tube, *S66*, is penetrated 0.60 m into the grabbed material and used to collect samples in the region highlighted in

Figure 6-17. The sampling is repeated three times, resulting in the porosity of 0.410±0.020 for the highlighted region. The simulated porosity for the same region is 0.440±0.010, indicating that simulated porosity distribution replicates reality adequately with the absolute difference of 0.030 and |e| = 8.6%.

Table 6-7. Validating mass and porosity of collected bulk solid

Test 2.2	M_{DWT} [ton]	n_{DWT} [-]
Experiment	26.7	0.340
Simulation	27.0	0.369
|e| [%]	1.1	8.8

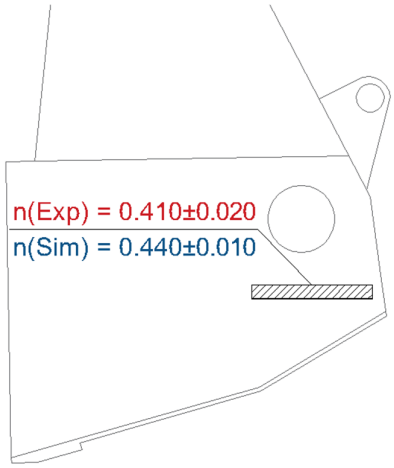

Figure 6-17. Porosity comparison between experiment and simulation in Test 2.2.

The grabbing process in two levels of pre-consolidation, corresponding to 65 kPa and 200 kPa, are validated. This confirms that the co-simulation is capable of capturing the grabbing processing of cohesive and stress-history dependent iron ore cargo. Further analysis on the grabbing process can help in gaining insight into the grabbing process of cohesive bulk solids.

6.4. Discussion of Stress-History Dependency

In the previous section was shown that the co-simulation can replicate a realistic grabbing process of cohesive iron ore, including two different levels of pre-consolidation. To further quantify the influence of pre-consolidation, additional simulations are carried out as shown in Table 6-8. The grabbing process of the cohesive iron ore, Carajas SF, in five different levels of pre-consolidation, is compared with the same process for free-flowing cargo: iron ore pellets. Pre-consolidation does not play a role in the grabbing process of iron ore pellets; thus, it is a proper option for our comparative analysis on the effect of σ_{pre} on the grabbing process. The validated co-simulation of

the grab with iron ore pellets is created in [155]. The grab dimensions and other inputs of the MBD simulation are kept as constants in the simulation plan, thus, the grabbing process can be investigated in comparable conditions. 300 kPa is selected as the highest pre-consolidation level, which is sufficient to create a pressure state existing at the cargo depth of around 11 to 14 m. Therefore, the grabbing process of cohesive and free-flowing iron ore products is compared for an operational range of cargo depths.

Table 6-8. Variables in the investigation on the effect of pre-consolidation on the grabbing process

Pre-consolidation levels [kPa]	[0 20 65 200 300]
Bulk materials	Carajas SF (cohesive iron ore) Pellets (free-flowing iron ore)

Figure 6-18 compares the footprint when the grabbing process is finished, and the grab has been lifted out of the material bed. Figure 6-18a shows the grab's footprint on the cohesive material bed. The cutting trajectory of the grab's knives can be seen clearly. In addition, the steep slope, which is clear at both sides, represents the initial penetration depth of the grab in resting state. A similar angle is observed during the grabbing process of cohesive iron ore in the cargo hold condition, allowing for the determination of the initial penetration of the grab, $\Delta_{grab,initial}$. At the cargo depth of around 7 m, an average $\Delta_{grab,initial}$ of 0.39 m, with a standard deviation of 0.05 m, is measured for the cohesive cargo.

Figure 6-18b shows the grab's footprint on the free-flowing material bed. Due to relatively low slope stability, particles flow once the grab has cut the bulk material. This results in a disturbed footprint, where the cutting trajectory of the grab's knives is no longer visible.

Figure 6-19a displays the effect of pre-consolidation on the initial penetration of the grab into bulk material in a resting state. Pre-consolidation does not play a role in $\Delta_{grab,initial}$ for free-flowing cargo. For cohesive cargo, the initial penetration of the grab decreases from 0.67 m to 0.37 m by increasing the pre-consolidation level from 0 to 300 kPa. A comparable $\Delta_{grab,initial}$ is measured between the experiments and simulation for σ_{pre} = 200 kPa.

Figure 6-19b displays the effect of pre-consolidation on the maximum cutting depth of the grab measured during the closing stage. $\Delta_{grab,max}$ is constant for free-flowing cargo, while it decreases considerably for cohesive cargo.

As shown in Figure 6-19c, cohesive cargo densifies under the effect of pre-consolidation, which is the reason behind the stress-history dependent behaviour captured for $\Delta_{grab,initial}$ and $\Delta_{grab,max}$. As expected, the bulk density of free-flowing cargo is constant under the effect of pre-

consolidation. Also, the bulk density of this free-flowing cargo is lower than the cohesive cargo, thus a higher grab payload is expected for Carajas SF.

The grab's payload under the effect of pre-consolidation is illustrated in Figure 6-20. The payload, M_{DWT}, at 0 kPa pre-consolidation is considerably larger for cohesive material compared to the free-flowing material. Bulk density and maximum cutting depth are the reasons behind such a difference. The stress-history dependent behaviour of the cohesive cargo results in a negative correlation between M_{DWT} and σ_{pre}, while a constant payload is captured for the free-flowing cargo.

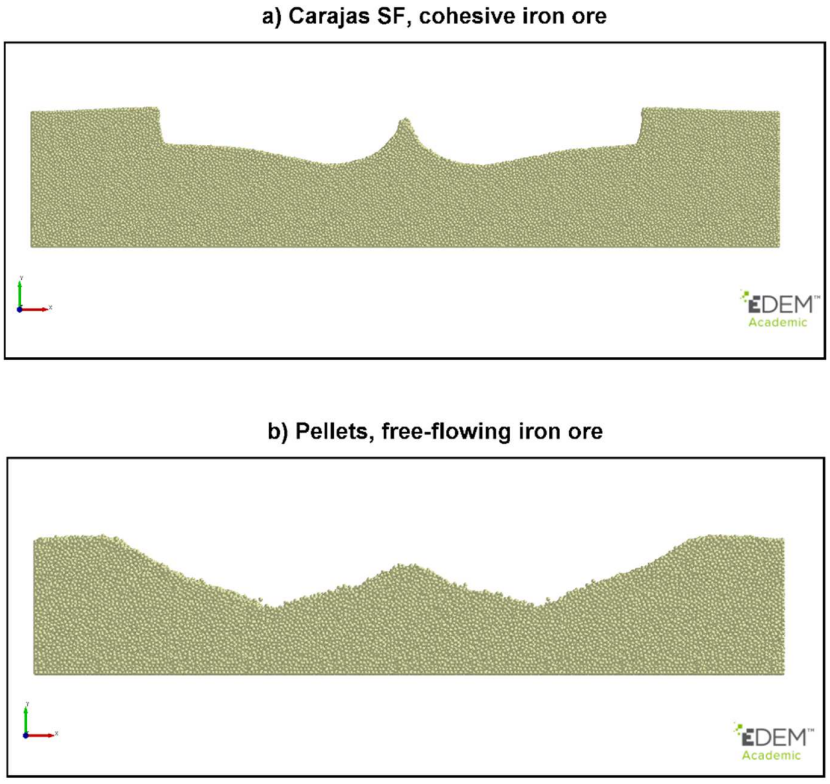

Figure 6-18. Footprint of the grabbing process on two types of iron ore: a) Carajas SF, and b) Pellets

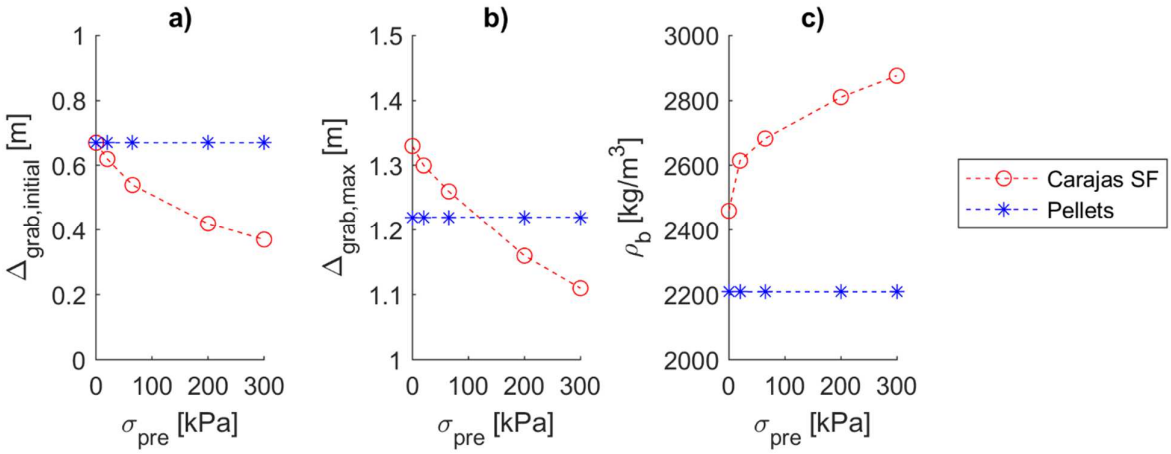

Figure 6-19. Effect of pre-consolidation on: a) the initial penetration depth of grab, b) the maximum cutting depth of grab, and c) the bulk density of cargo prior to the grabbing process

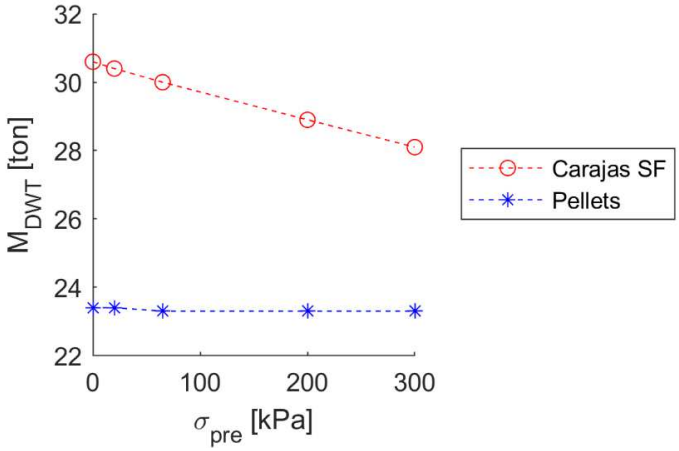

Figure 6-20. Direct effect of pre-consolidation on the grab payload for cohesive and free-flowing iron ore cargoes

6.5. Conclusion

This chapter successfully developed a validated co-simulation to accurately simulate the grabbing process of cohesive and stress-history dependent iron ore. Conducting full-scale grabbing experiments in the cargo hold allowed the process to be recorded under realistic operational conditions.

- The predictions of the co-simulation compared well to experimental data in all aspects, including force in cables, torque in winches, kinematics of geometry, payload, collected volume and average porosity of bulk solid. The used validation procedure can be applied to simulate the grabbing process of other materials, such as coal and biomass.

- In-situ measurements of bulk density and penetration resistance, using the developed test method (S66), quantified an increasing densification over the cargo depth. The co-simulation was validated for two different levels of cargo depth to ensure capturing the stress dependent behaviour of the bulk material.
- A negative correlation between pre-consolidation level and payload was observed. Multiple grab-relevant factors are affected when a pre-consolidation situation is created for cohesive materials; the increasing density of bulk material results in a lower penetration/cutting depth of grab, both at rest and closing stages.

Co-simulation setups allow for analysing the design performance of both free-flowing and cohesive iron ore under the effect of consolidation. Valuable information, such as the cutting trajectory, porosity distribution, and the volume of collected bulk solids can be extracted from the simulation. This can support designers and engineers in gaining insight into and improving grab performance. The co-simulation of grabbing process will be used in the next chapter to optimize a grab design including the effect of bulk variability, such as level of cohesion and pre-consolidation.

7

Grabs and bulk cargo variability*

Grabs usually handle a broad variety of iron ore cargoes that are different in their properties, such as moisture content, pre-consolidation and bulk density. On one hand, a fast and reliable unloading process is required to maintain a minimized cost for port operators and to deliver iron ore products to customers on time. On the other hand, the variability of bulk solid properties influences the grabbing process considerably, and thus, the grab's efficiency. To design a robust product, the consistency in the grab's efficiency needs to be maintained. The question is that how the bulk cargo variation can be included in the design procedure of grabs, thus achieving a maximized, and simultaneously, consistent grab's efficiency. Therefore, a multi-objective optimization framework is developed in this chapter to consider bulk cargo variability in the design process of grabs.

---

* This chapter is based on the following references:

A.J. van den Bergh, "Systematic design optimization of grabs handling cohesive materials". Delft University of Technology, 2019.TEL.8363, 2019.

M.J. Mohajeri, A.J. van den Bergh, J. Jovanova, D.L. Schott, "Systematic design optimization of grabs considering bulk cargo variability". Accepted in Advanced Powder Technology, 2021.

Discrete Element Method (DEM) is employed to first investigate how a virtual grab prototype can be tested considering the bulk cargo variability, including various levels of cohesive forces and bulk plastic compressibility. Such a sensitivity analysis allows for selecting bulk material classes that create significant deviation in the grab performance. This follows from optimizing a virtual prototype to reach a maximized Ψ_{mass} in handling a variety of significant bulk material classes while the deviation of grab performance is minimized. Multiple surrogate models are created to find optimal design settings, which are evaluated in a verification step.

7.1. Multi-objective optimization framework for including bulk cargo variability

Figure 7-1 shows an overview of how the bulk cargo properties contribute to the grabbing process as an uncontrollable input variable. Mohajeri et al. [108] measured grab-relevant bulk properties of a broad range of iron ore fines. Cohesive forces (i.e. liquid bridge) between iron ore particles are typically created when moisture is introduced [22]. Cohesive forces may influence the bulk properties of iron ore fines, such as shear strength and flowability [108]. Bulk compressibility and moisture content are also correlated for cohesive iron ore [38,108]. Pre-consolidation stress is another grab-relevant bulk property of cohesive iron ore that varies over the cargo depth during the unloading process [164]. Due to the increasing overburden pressure, a more consolidated cargo is stored at greater depths.

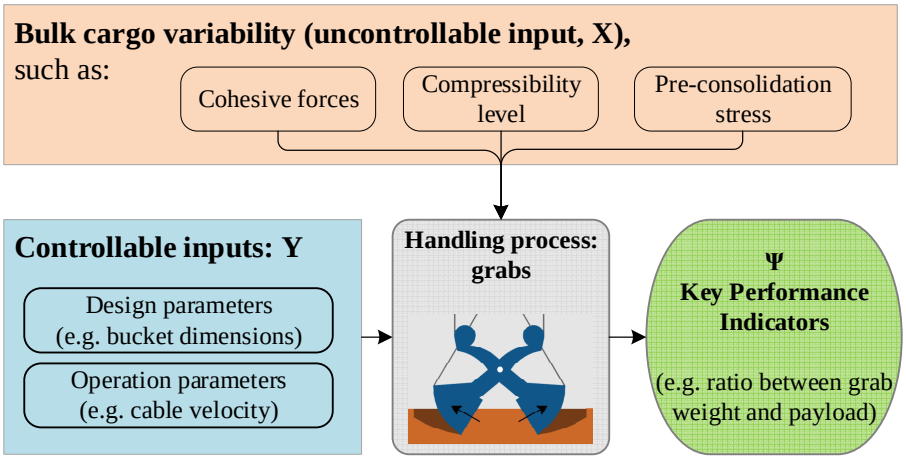

Figure 7-1. Contributing parameters in the grabbing process: controllable and uncontrollable inputs

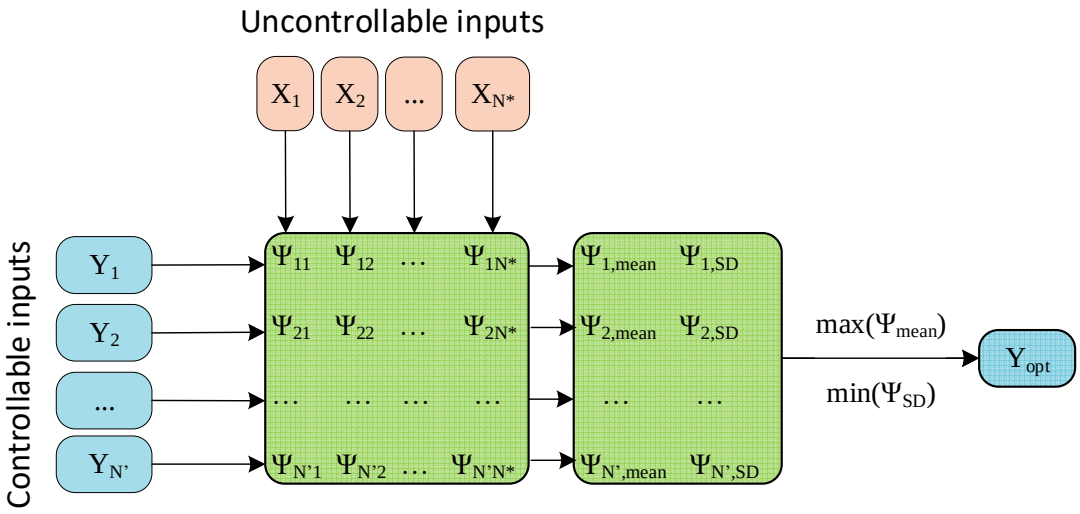

Figure 7-2. Quantifying a performance indicator, [Ψ], for a combination of controllable, Y, and uncontrollable, X, types of input

A multi-optimization framework is developed to incorporate the bulk cargo variability into the grab design process. Both controllable and uncontrollable types of input are included in the framework. A matrix, [Ψ], containing performance indicator values can be quantified for a combination of uncontrollable and controllable inputs, as shown in Figure 7-2. The primary aim is to minimize the undesirable effect of variability of X on Y. Thus, for an optimal design configuration, Y_{opt}, a maximized performance, Ψ_{mean}, is reached on average, while its standard deviation, $\Psi_{SD,}$ is minimized. The optimization framework is designed in four sequential steps where the output of each step is used in the next step as illustrated in Figure 7-3. This allows grab designers to follow a straightforward procedure when a new concept is being developed.

7.1.1. Step I. Sensitivity of the grab performance to bulk cargo variability

Reference material model of the cohesive iron ore - X_{ref}

A DEM material model of a cohesive iron ore cargo, named Carajas Sinter Feed (CSF), has been validated for the grabbing process in Chapter 6. In the current chapter, that validated material model is used as a reference material model, X_{ref}, to create a bulk cargo variability. To model interaction between particles in the reference material model, the elasto-plastic adhesive contact spring, EEPA [84], was used.

In the EEPA contact spring, the cohesive forces can be adjusted by varying the constant pull-off force (f_0) and surface energy ($\Delta\gamma$). Sensitivity studies on the dependency of bulk behavior (e.g. angle of repose, shear strength, bulk density) on the variation of f_0 and $\Delta\gamma$ have been

documented in [29,140,165]. For f_0 and $\Delta\gamma$, reference values of -0.2 N and 100 J/m^2 are used respectively.

The plasticity ratio (λ_P) controls the contact stiffness during unloading and reloading of the spring and, thus, this parameter controls the bulk compressibility. The plasticity ratio, λ_P, controls the ratio between stiffness in *branch II* (k_2) and stiffness in *branch I* (k_1), which shows the influence of plasticity ratio at contact scale. This means that by increasing the plasticity ratio, a higher level of plastic overlap occurs during contact and, thus, a higher level of bulk compressibility. For λ_P, a reference value of 0.2 is used.

The EEPA contact spring is able to capture a stress-history-dependent behaviour [118,164,166] and, therefore, no input parameters need to be adjusted in the material model for this purpose. A pre-consolidated situation can be simulated by applying a specific amount of pressure on the bulk surface and then releasing that pressure, as described in [165]. The reference material model has been validated in operational conditions for two different levels of pre-consolidation: 65 and 300 kPa. The grabbing process of the cohesive iron ore for various levels of pre-consolidation has been investigated in the previous chapter, which shows the negative effect of pre-consolidation on the grab performance.

Bulk cargo variability - [X]

This sensitivity analysis evaluates whether the variability of cohesive forces and bulk compressibility influences the grabbing process or not. The effect of a variable is considered significant if varying its level by ±100%, compared to its reference level, creates ±5% deviation in the mass indicator. As displayed in Table 7-1, a bulk variability, *[X]*, based on the reference material model is created.

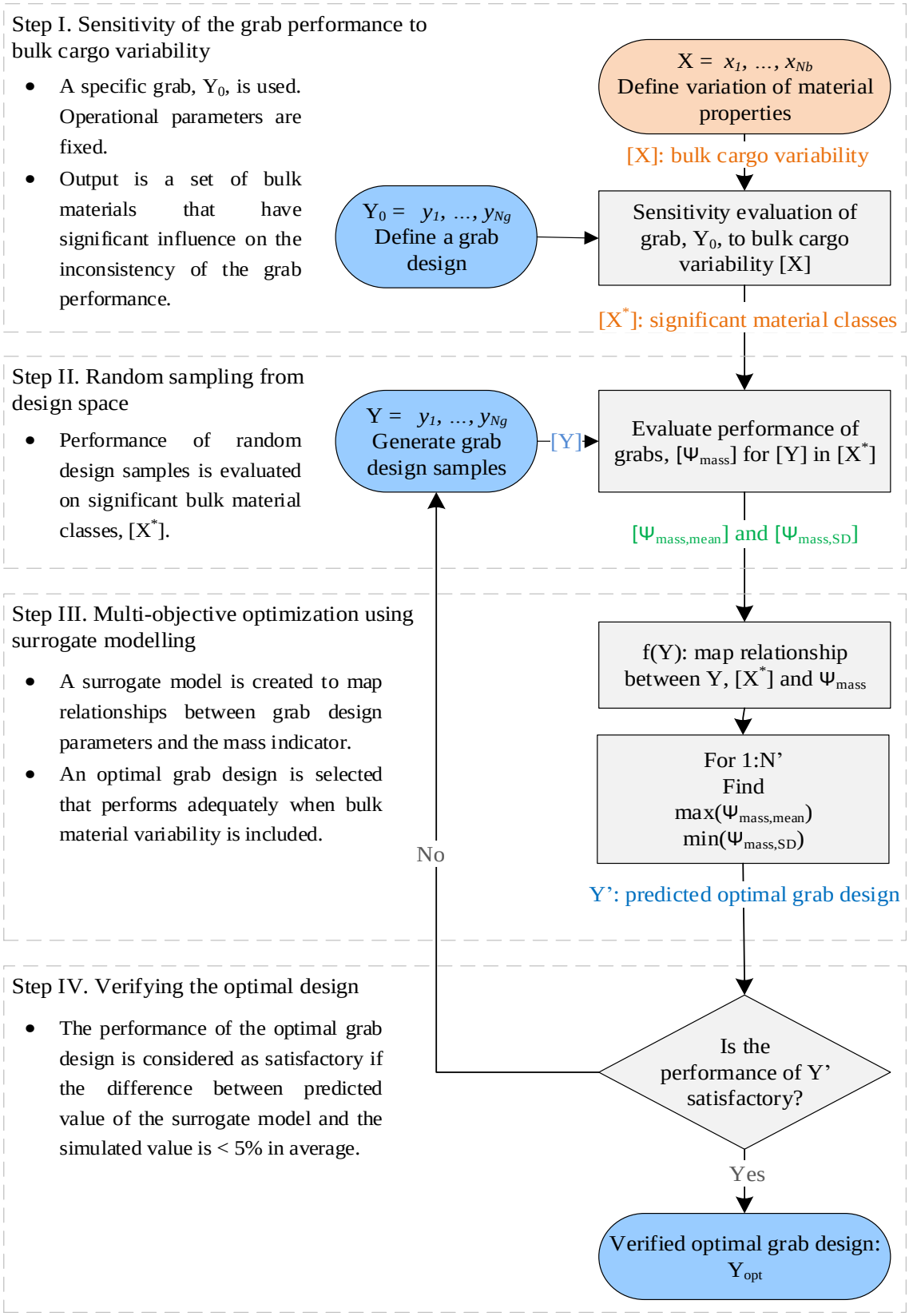

Figure 7-3. A systematic optimization framework to include the bulk variability in the grab design procedure

The relative cohesion term, as defined in Chapter 4, is used to vary the level of cohesive forces when the EEPA contact spring is applied. The relative cohesion, C_{bulk}, distinguishes between the expected levels of bulk cohesion in a qualitative way. To create a low relative cohesion, f_0 and $\Delta\gamma$ are decreased by 50% compared to the reference material model. An increase of 100% is also applied to create a high relative cohesion. C_{bulk} is set to "non" in bulk materials 1, 2, and 3, by setting both f_0 and $\Delta\gamma$ to 0.

The EEPA model behaves like an elastic spring if the plasticity ratio is set to 0, while using values close to 1 the model behaves like a plastic spring. In an elastic spring there is no residual overlap once the force drops to zero. Any values between 0 and 1 result in a certain level of plastic compressibility in the contact spring. The reference material has a plasticity ratio of 0.2, which we correspond to low relative plastic compressibility, λ_{bulk}. Medium and high levels of relative plastic compressibility are defined by using 0.55 and 0.9 for λ_P respectively. If λ_P, f_0 and $\Delta\gamma$ are all set to zero, then the material model behaves like a non-cohesive elastic bulk solid. The grabbing process of non-cohesive elastic iron ore has been already investigated in [155,164] and is, therefore, excluded from the current sensitivity analysis.

Table 7-1. Simulation plan to analyse the grabbing process for a bulk variability, [X]

Bulk material	**λ_{bulk} Relative plastic compressibility**	**λ_p [-]**	**C_{bulk} Relative cohesion**	**f_0 [N]**	**$\Delta\gamma$ [J/m^2]**
1	Low	0.2	Non	0	0
2	Medium	0.55			
3	High	0.9			
4	Low	0.2	Low	-0.05	50
5	Medium	0.55			
6	High	0.9			
7	Low	0.2	Medium	-0.1	100
8	Medium	0.55			
9	High	0.9			
10	Low	0.2	High	-0.2	200
11	Medium	0.55			
12	High	0.9			

Simulation setups

Grab-relevant behavior of all 12 bulk materials are evaluated in the following simulation setups:

- Angle of repose
- Uni-axial consolidation
- Penetration test

These preliminary simulations are executed to verify that the created virtual bulk variability represents various states of bulk cohesion and compressibility. Next, the grabbing process is simulated at full-scale, thus evaluating how the bulk variability influences the process. The particle diameter of the validated material model is relatively large (55 mm in diameter), compared to particle sizes used in typical laboratory scale DEM simulations. Therefore, relatively large domains are also created to fit enough numbers of particles without undesirable boundary effects.

The angle of repose is simulated by pouring particles from a specific height. The simulation setup is shown in Figure 7-4. Particles are created in a factory 1.5 meter above the bottom plate; due to the force of gravity, particles drop on the bottom plate to form an angle of repose over time. 2500 particles are created with a total mass of around 800 kg. Once the simulation is finished, a stable angle of repose is formed, and the position of particles that are on the slope is analyzed. A linear regression is then fit on the data points to determine the angle of repose. The angle of repose, $\alpha_{M,}$ is therefore the measurement objective of the simulation.

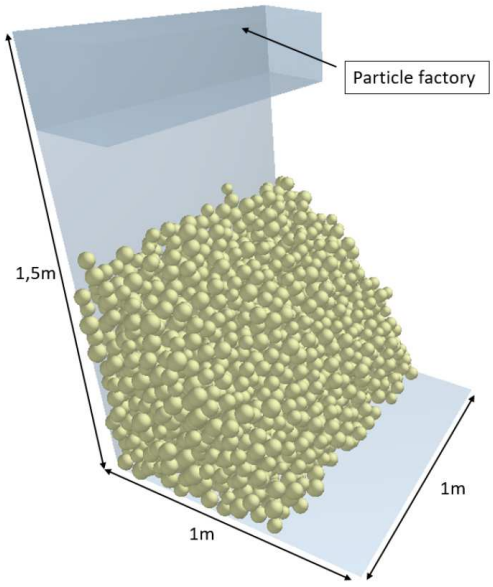

Figure 7-4. A simulation setup to measure the angle of repose

The uni-axial consolidation process, including loading and unloading, is simulated in four stages to evaluate the bulk compressibility as well as bulk density. The simulation domain is 1x1x2 meter. A block of material is created using a particle factory that moves upward. This kind of technique minimizes the impact force during the particle generation (Figure 7-5a). Next, the particles are allowed to settle for 2 seconds, and a low kinetic energy in the bulk material (i.e. ≤ 1e-4 J) is reached (Figure 7-5b). Next, the bulk material is consolidated by applying a uniform pressure (i.e. 65 kPa) on its surface by means of a geometry plate for 2 seconds (Figure 7-5c). The pressure is unloaded by moving the geometry plate upward with a velocity of 1 cm/s (Figure 7-5d).

The initial bulk density, $\rho_{b,0}$ is quantified when the particles relax in the second stage. The compressed bulk density, $\rho_{b,c}$ is measured at the end of loading in the third stage. The final bulk density, $\rho_{b,end}$ is quantified when the unloading is finished and a pre-consolidated situation is created.

The penetration resistance of the bulk material is the third grab-relevant property that is investigated here. The penetration resistance is an influential bulk property in the grabbing process [108], as a lower resistance to penetration of grabs into the bulk solids results in a higher payload generally. The penetration process is simulated for a material block that is pre-consolidated with a vertical pressure of 65 kPa, as shown in Figure 7-6a. A cube-shaped geometry with the volume of 8 m^3 is used to contain the material block.

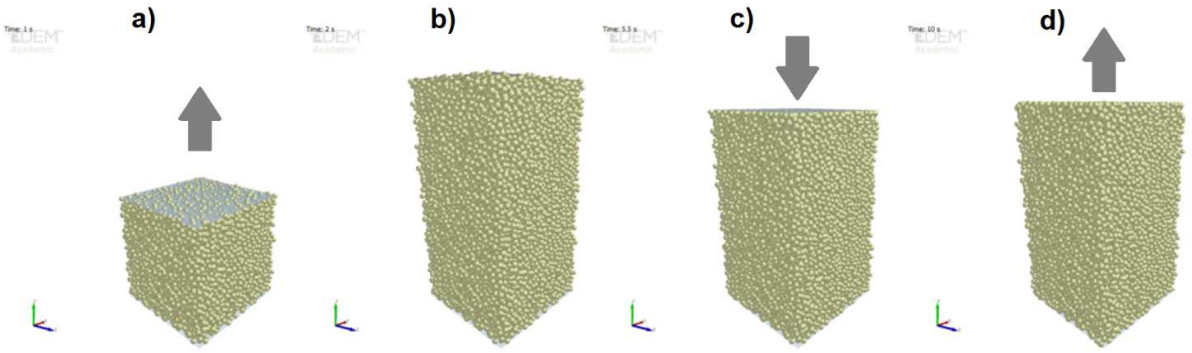

Figure 7-5. Uni-axial consolidation simulation consists of four stages: a) stage 1, particle generation, b) stage 2, particles relaxing, c) stage 3, uni-axial loading, d) stage 4, unloading. (The arrow indicates the direction of geometry kinematics)

In general, ship unloader grabs have wedge-shaped knives with a blunt tip to tradeoff between the penetration resistance and amount of wear. The wedge-shaped penetration tool has a width of 40 mm and its tip is 20 mm wide. That makes the cross-section of the penetration tool similar to the

setups used in [108,118,165] that focused on the grab application too. This tool (I) is driven into the pre-consolidated bulk material (II) with a constant velocity of 0.1 m/s. A plane contact 2000 mm in length is created during the penetration, which replicates the grab dimensions adequately. The reaction force on the penetration tool is quantified as the measurement objective.

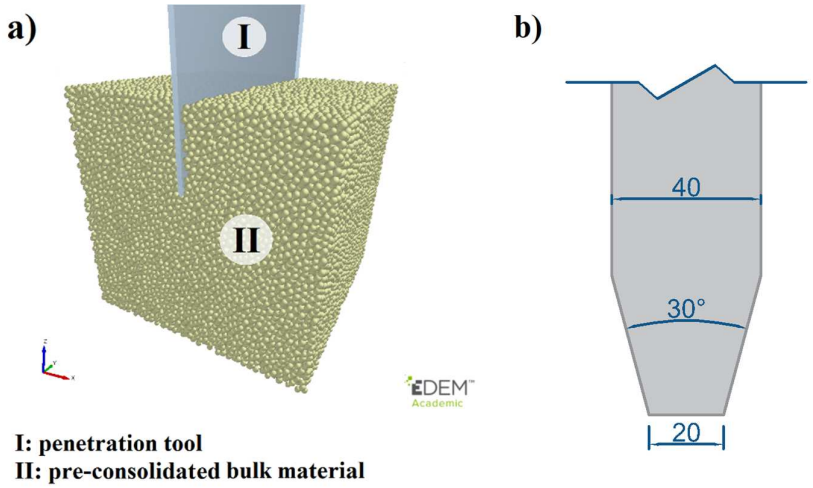

Figure 7-6. a) Simulation setup of the penetration test, b) Cross-section of the penetration tool (I)

Once the outcome of preliminary simulations confirms that an adequate bulk variability is achieved, the grabbing process can be simulated for the 12 bulk materials. The DEM simulation of the grabbing process is run on a combination of CPU and GPU. This allows for reducing the computation time of a MBD-DEM co-simulation by around 6 times, compared to a CPU-based co-simulation. NVIDIA Quadro GP100 is used as the graphics card in this study.

Once the co-simulation is finished, the grab performance is quantified for the 12 different bulk materials. The mass indicator, $\Psi_{mass.}$ is used to evaluate the sensitivity of the grab performance to the bulk variability. The outcome of Step I is [X^*], bulk material classes with significant influence on the grab performance.

7.1.2. Step II. Random sampling from design space (LHD)

Once the significant bulk material classes are created, a parametric variation of the grab design can be investigated. In Step II of the optimization framework, design space is searched effectively to create randomized variations of grab configurations. If all the possible combinations of variables with the design space are considered, a full factorial design is thus created. For each parameter, a series of levels, or values, N_s, is defined. When every possible combination is tested, the total number of samples, N', is given by Eq. (7.1).

$$N' = N_s^{N_g} \tag{7.1}$$

where N_g is the number of parameters. Even with a small number of parameters and levels, the number of samples can result in an extreme computation time. For example, if five design parameters are tested, each at three different levels, a total number of 3^5 samples need to be simulated. With an average computation time of 3.5 hours per grab simulation, this would result in about 35 days of computing for each bulk material.

Fractional factorial designs can offer more effective sampling methods compared to a full design, in terms of offering an affordable computation time [165]. The Latin Hypercube Design (LHD) method is selected in this chapter, as it allows for searching a parameter space effectively using a minimum number of sampling points [167]. A set of sampling points is constructed in such a way that each of the parameters is divided into p equal levels, where p is the number of samples. This is illustrated in Figure 7-7 using two examples and for two parameters. In example 1, the samples are constructed with an extremely poor space filling quality, while example 2 has a better filling quality with a fine filling of the design space.

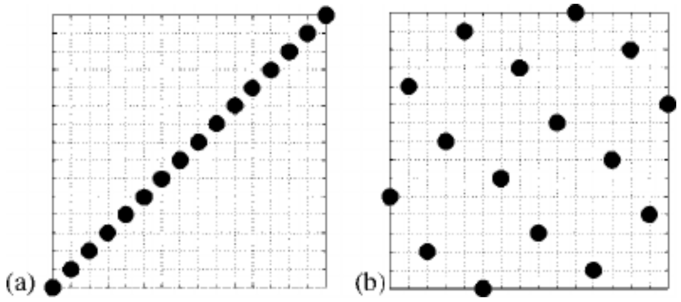

Figure 7-7. Examples of LHD including two parameters: a) poor filling of a design space, and b) reasonable quality of filling a design space

The LHD is constructed according to the algorithm developed in [152]. The Φ_P criterion was defined, as shown in Eq. (7.2), to measure the performance of a LHD-based sampling.

$$\Phi_p = \left[\sum_{i=1}^{n_p-1}\sum_{j=i+1}^{n_p} d_{ij}^{-p}\right]^{1/p} \tag{7.2}$$

where p is a positive integer, d_{ij} is the inter-point distance. In the current study, p = 50 is used following the recommendation of *Jin et al.* [168]. By minimizing the Φ_P criterion [151], the location of levels for each parameter is randomly, simultaneously, and evenly distributed over the

parameter space. Maintaining a maximized distance between each two points allows for satisfying the Φ_P criterion.

In total, five design variables are included in the optimization, referred here as D1, D2, D3, D4, D5. The variables and the range of variations are selected based on a previous parametric study [155] as well as in consultation with grab designers. For example, *Schott et al.* [155] demonstrated that the length of the grab bucket, D1, plays an important role in the grab performance. Also, the radius of a bucket, D2, is a significant design parameter as it influences the bucket shape, and, thus, its volume.

The construction of the LHD-based samples for D1 and D2 is visualized in Figure 7-8. Samples for three other design variables are randomly created in a similar way, thus, minimizing Φ_P for five variables. A range of 1650 mm to 2000 mm is considered for D1, as it is a typical range for such a grab prototype. For the same reason, D2 is also varied between 1200 mm and 2000 mm. Therefore, 25 different grab designs, N' = 25, are created, including 5 variables, N_g.

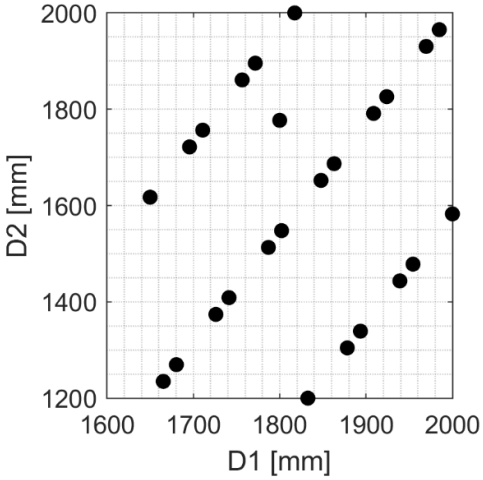

Figure 7-8. Sampling randomly generated for design variables D1 and D2 using Latin Hypercube Design.

7.1.3. Step III. Multi-objective optimization using surrogate modelling

A surrogate model is a computationally affordable mathematical model that can replace the actual simulation or experiment. Surrogate models approximate a function based on a set of available data points and can then predict the function at new points [13]. A surrogate model offers a faster computation time, compared to the actual DEM-MBD co-simulation, to predict performance of a new grab configuration. Surrogate models can be also used to obtain trends and identify the

influence of specific parameters on the grab performance. Three different types of regression-based surrogate models are tested in the current chapter:

- Linear regression
- Linear Support Vector Machine Kernel
- Polynomial Support Vector Machine Kernel

The linear regression model is the most widely used regression model. In general, this type of regression model is a linear function between variables, response of the system, and constant coefficients [169], as shown in Eq. (7.3).

$$f_k = \sum_{j=1}^{N_g} \beta_j \; y_j \tag{7.3}$$

where *f* is the regression model, β is a constant coefficient, and *y* is a (design) variable. A surrogate model can be created by fitting a regression function, f_k, for each bulk material. Therefore, f(Y) maps the relationship between the grab design variables, bulk materials, and the selected response of the system, which is the mass indicator, Ψ_{mass}, in the current study.

Kernel models transform variables using kernels. The transformed variables are measures for similarity or correlation between the data points. Multiplying the transformed variables with weights (constant coefficients), as with the linear models, gives an estimate of the output. The predictor function for a kernel-based regression is given by:

$$f_k = \sum_{i=1}^{n_p} \beta_i \, \Phi(y' - y_i) + b \tag{7.4}$$

where β_i is the weight factor corresponding to data point *i*, and *y'* indicates a vector of variable (at its new location) and y_i is an available data point. *b* is a constant to minimize the fitting error, ε. One difference between a linear regression model and a kernel model is that the latter has a number of coefficients, βi, corresponding to data points rather than variables. Φ is the kernel function that transforms data points into another space to handle the non-linearity. Linear and polynomial functions are used for Φ in the current study.

The support vector machine (SVM) regression uses a kernel function to first estimate the correlation between data points before fitting coefficients (Figure 7-9). The advantage of SVM is that it allows for an error between observations and predictions [170]. The cost function is not increased until the specified amount of error, ε, between observation and prediction is reached,

which forms an ε-tube around the prediction function. Outside the tube, the cost function increases and forces the prediction function to a specific range of data points.

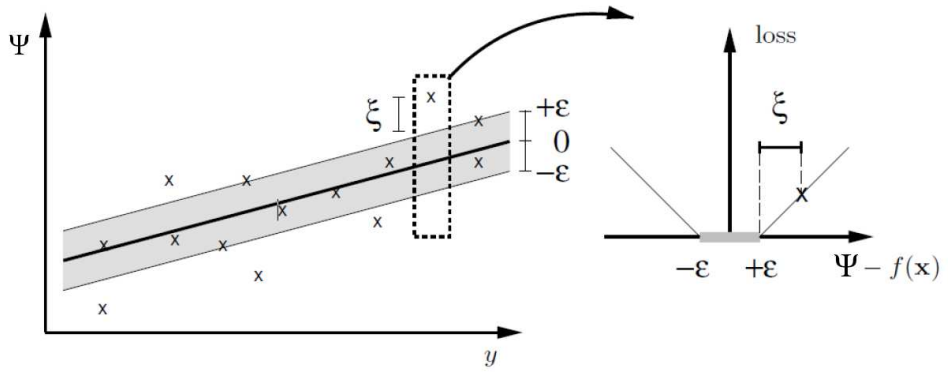

Figure 7-9. A tube with the radius of ε is fitted to data points in the SVM regression model [171]

As discussed earlier, two objectives are considered in the current optimization: a maximized average mass indicator ($\Psi_{mass,mean}$) and a minimized standard deviation for mass indicator ($\Psi_{mass,SD}$) measured in different bulk materials. The unloading frequency of a certain cargo is also considered in the optimization. For example, if a grab unloads a specific cargo 20% of time, and another cargo 80% of time, the second cargo should have a higher weighting factor in the optimization for maintaining an adequate productivity. The distance between origin mine and customer, production capacity of mine, and technical demands of customer are among the influencing factors on the frequency of receiving a specific bulk cargo at destination. The unloading frequency can usually be obtained by analyzing available databases of customers. Therefore, to consider the frequency distribution of bulk variability, weighting factors with $\sum_{k=1}^{N^*} w_k = 1$ are defined. w_k is the weighting factor of material k in the optimization.

Once different grab samples, Y, are simulated, one can select a design configuration that may jointly satisfy the optimization objectives. However, a response optimizer can find better design configurations, compared to the simulated samples, by using the surrogate models. Creating surrogate models allows for predicting the response of the system without the necessity of running a DEM-MBD co-simulation. Once a surrogate model is created, the optimal design can be found by selecting a combination of design variables that jointly satisfy the optimization objectives [165]. The NSGA-II genetic algorithm [172] is a proper tool to solve DEM-based optimization problems [15,26,27,132], and is therefore used in the current chapter to search for the optimal solution within the design range.

7.1.4. Step IV. Verifying the optimal design

The selected optimal design is verified by running conforming simulations. This allows for quantifying the error of surrogate models as well. The prediction error is quantified using Eq. (7.5).

$$|e|_{mean} = \sum_{k=1}^{N^*} 100 \left| \frac{f_k' - f_k}{f_k'} \right| \tag{7.5}$$

where $|e|_{mean}$ is the mean of absolute relative differences for the grabbing process in N^* different bulk materials. f_k is the prediction for system response, Ψ_{mass} in the current study. f_k' is the simulated response of the optimal design solution for bulk material k. The acceptable error of $|e|_{mean}$ is considered to be 5% multiplied by N^*. In other words, on average a prediction error of 5% for each bulk material is considered to be adequate. If the prediction error is not acceptable, the number of data points in step 2 can be increased to improve the accuracy. Additionally, based on the prediction error, the performance of the different surrogate models can be compared. The optimization ends with a verified optimal design configuration, Y_{opt}.

7.2. Results and Discussion

This section presents and discusses the outcome of four steps of the optimization in a sequential manner.

7.2.1. Results of step 1, sensitivity to cargo variability

Step I aims to identify a bulk material variability that has a significant influence on the grab performance. First, results of preliminary simulations are discussed. Second, the grab performance in handling the 12 different material models is analyzed. Third, a matrix, *[X*]*, containing the significant bulk material classes is created.

Angle of repose

Figure 7-10 shows the angle of repose results including two variables; relative cohesion (C_{bulk}) and relative plastic compressibility (λ_{bulk}). The angle of repose depends on the relative cohesion significantly. Increasing cohesive force values, f_0 and $\Delta\gamma$, results in a higher angle of repose. The relative plastic compressibility, also influences α_M. When a non-cohesive material is used, the relative plastic compressibility has a positive correlation with α_M. However, when the cohesive forces are present, the relative plastic compressibility has a negative correlation with α_M.

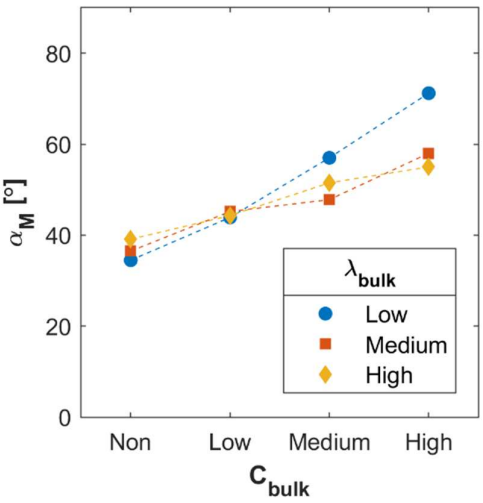

Figure 7-10. Angle of repose results including two variables: relative cohesion and relative plastic compressibility

In case of non-cohesive materials, a higher contact plasticity results in a larger contact area upon unloading, thus increasing the required sliding distance of particles relative to each other. However, when cohesive forces are active, a higher relative plastic compressibility results in a denser pile of material. Since the particle density is constant, a denser packing of material results in a heavier failure wedge in the slope, thus a lower angle of repose could be expected with increasing the contact plasticity. The effect of contact plasticity on the packing is discussed further in the uni-axial consolidation simulation setup.

Uni-axial consolidation

Figure 7-11 displays initial, compressed, and final bulk density values that are quantified for the 12 different bulk materials under 65 kPa pre-consolidation pressure. Results are presented in three separate graphs, each showing the outcome for a certain level of λ_{bulk}. All bulk density parameters decrease when cohesive forces increase, independent of the contact plasticity value.

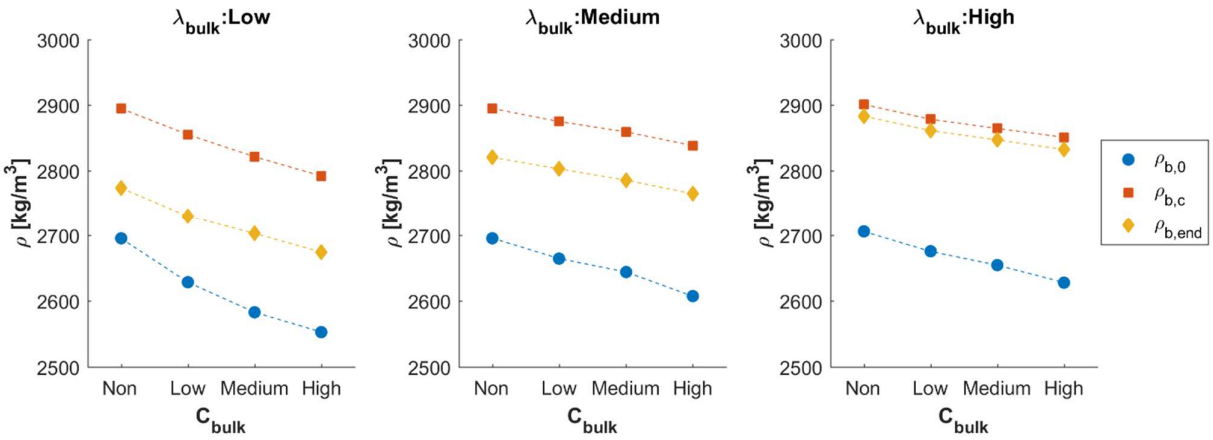

Figure 7-11. Bulk density values in the uni-axial consolidation simulation, including two variables: relative cohesion (C_{bulk}) and relative plastic compressibility (λ_{bulk})

The higher the cohesive forces, the larger the restrictive forces between particles to fill the voids; consequently, a lower bulk density is created. Furthermore, by increasing the contact plasticity, the residual overlap in contact spring increases [22], thus a smaller difference between $\rho_{b,c}$ and $\rho_{b,end}$ might be expected. Therefore, both variables, λ_{bulk} and C_{bulk}, have significant influence on the bulk compressibility and the bulk density.

Penetration resistance

W_{500}, the accumulative reaction force (in Joules) on the wedge-shape tool is quantified at the penetration depth of 500 mm. That is similar to the penetration depth that occurs in the grabbing process of the CSF cargo under 65 kPa pre-consolidation pressure [164]. The outcome of the penetration test simulations is shown in Figure 7-12, including two variables: λ_{bulk} and C_{bulk}.

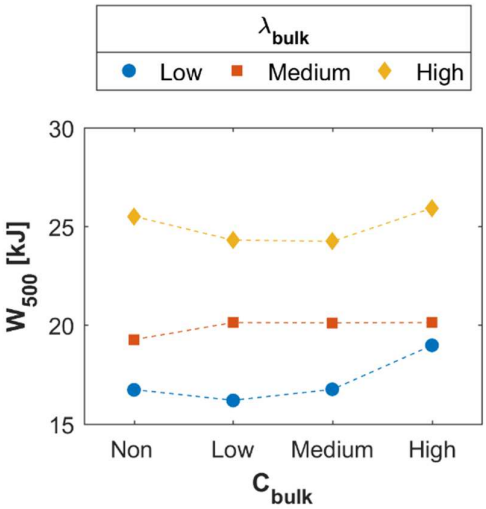

Figure 7-12. Effect of bulk variability on the penetration resistance

There is a positive correlation between the relative plastic compressibility, λ_{bulk}, and W_{500}. A higher contact plasticity results in a denser packing, thus, a higher resistance against the penetration of the wedge-shaped tool. There is no clear relationship between the relative cohesion and the penetration resistance. Therefore, only λ_{bulk} is a significant bulk variable influencing the penetration resistance.

The influence of each variable on the grab-relevant bulk properties is shown above. The relative cohesion has a significant influence on the angle of repose and bulk density, while the relative plastic compressibility plays a significant role in the angle of repose, bulk compressibility, and the penetration resistance.

Grabbing process

Figure 7-13 displays the influence of λ_{bulk} and C_{bulk} on the grab performance. The influence of relative plastic compressibility on the grab performance is significant. That could be expected, based on the penetration simulations. The relative cohesion also plays a role in the grabbing process, especially when a low λ_{bulk} is used.

Although the effect of the pre-consolidation pressure is not investigated in the current analysis, it is known that the pre-consolidation plays a significant role in the grabbing process of cohesive iron ore [164]. Three different bulk materials are selected for further optimization of the grab design, as presented in Table 7-2. Material IO-1* is a non-cohesive iron ore with no relative plastic compressibility which its DEM material model was developed within the Transport Engineering and Logistic section of Delft University of Technology [9]. Due to lack of compressibility of IO-1*, pre-consolidation is omitted. Material IO-2* is a cohesive iron ore with a low C_{bulk} and a high λ_{bulk} that is pre-consolidated with a relative high pressure of 200 kPa. By contrast, material IO-3* has a high C_{bulk} and a low λ_{bulk}, that is pre-consolidated with a relative low pressure of 40 kPa. Such pressure is expected at a cargo depth of around 1.5 m to 2 m. By analyzing an available database of a grab customer, the weighting factors are selected for each bulk material. Summarizing, three different bulk material classes with significant variability for the grabbing process are selected as the outcome of step I.

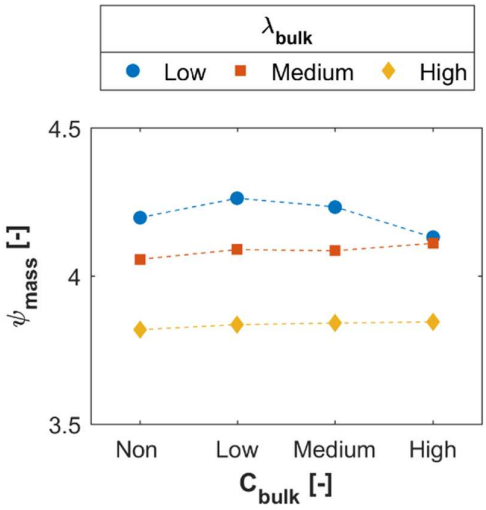

Figure 7-13. The grab performance under variation of relative cohesion and relative plastic compressibility

Table 7-2. *[X*]*: three different bulk material classes with significant influence on the grabbing process

Bulk material class	**λ_{bulk} Relative plastic compressibility**	**C_{bulk} Relative cohesion**	**σ_{pre} [kPa] Pre-consolidation stress**	**w Weight factor of the unloading frequency**
IO-1*	Non	Non	Not applicable	0.1
IO-2*	Low	High	40	0.4
IO-3*	High	Low	200	0.5

7.2.2. Results of Step II, performance indicators of random design samples

The 25 different grab design samples are simulated in three significant bulk material classes, *[X*]*, thus, 75 simulations are executed. The performance of grabs are analyzed using the mass indicator Ψ_{mass}, and the outcome is illustrated in Figure 7-14. The horizontal axis represents the mean value of Ψ_{mass} for a grab handling the three significant material classes, thus showing the performance of a design sample on average. The vertical axis represents the standard deviation value of Ψ_{mass} in handling *[X*]*, thus an indication for the performance consistency.

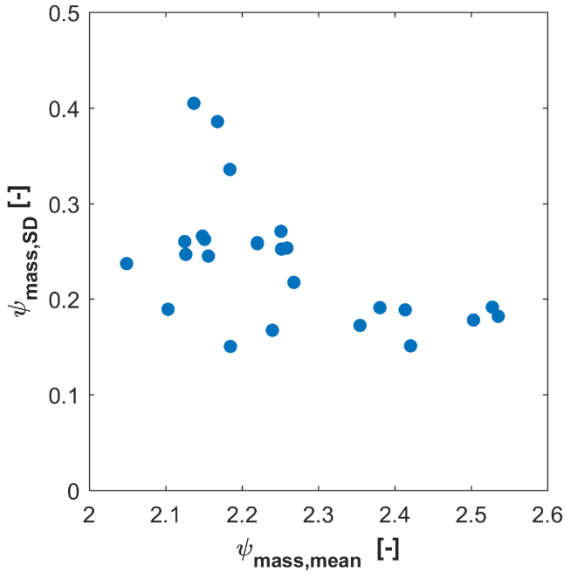

Figure 7-14. Performance of random grab design samples in three different bulk materials, *[X*]*

The mean Ψ_{mass} values are distributed between 2.05 and 2.54. A variation of around 24% in the performance of different design samples is captured. Next, surrogate models are fitted on the 25 data points.

7.2.3. Results of Step III, multi-objective optimization using surrogate modelling

Three different surrogate models are fitted on the available data points: linear regression, linear SVM kernel, and polynomial SVM kernel. Next, optimal solutions using the NSGA-II genetic algorithm are found for each surrogate model. The outcome is illustrated in Figure 7-15, indicating that different optimal solutions (red line) are found using different surrogate models. The available data points are shown in blue. The polynomial SVM kernel predicts optimal solutions that are better than the predictions of two other surrogate models. The non-linear relationships between optimization objectives and design variable were captured well using the polynomial SVM kernel.

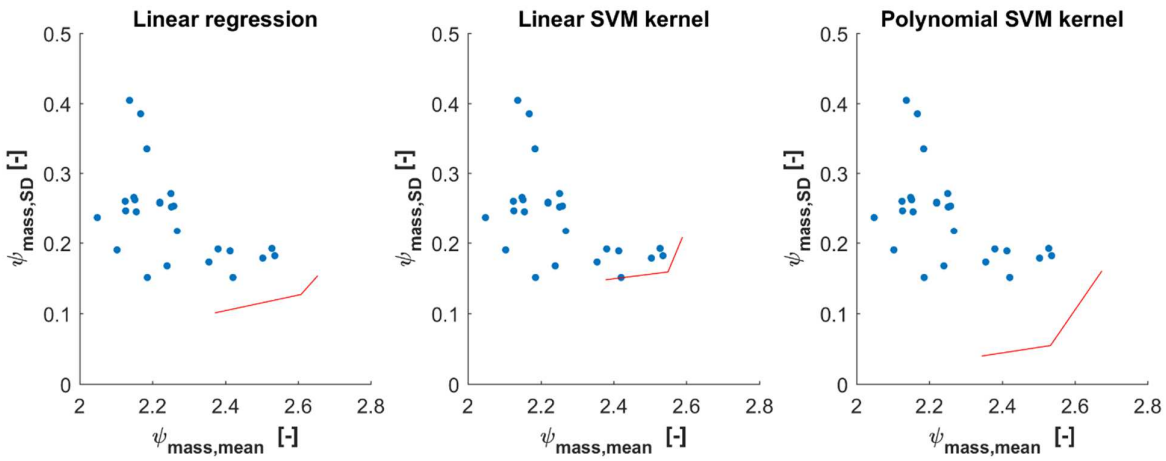

Figure 7-15. Optimal solutions are compared for three different surrogate models

7.2.4. Results of Step IV, verified optimal design

It needs to be verified whether the predications of the surrogate models and the optimization algorithm are sufficiently accurate. Therefore, the "knee-point" in the line presenting optimal solutions is selected, as recommended in [173]. Co-simulations are executed for each optimal solution in three significant bulk material classes, $[X^*]$; the outcome is shown in Table 7-3.

Table 7-3. Comparing simulated Ψ_{mass} in $[X^*]$ with predictions of the optimization algorithm

Bulk material	Linear regression	Linear SVM kernel	Polynomial SVM kernel
IO-1*	2.50	2.52	2.51
IO-2*	2.65	2.70	2.76
IO-3*	2.31	2.32	2.39
$\Psi_{mass,mean}$	2.49	2.51	2.56
$\lvert e \rvert_{mean}$ [%]	4.7	1.6	1.1

All three surrogate models have a prediction error smaller than 5% for $\Psi_{mass,mean}$. The polynomial SVM kernel shows the highest grab performance as well as the lowest prediction error, while the linear regression model shows the opposite. Therefore, the polynomial SVM kernel can be recommended as a surrogate model to find design configurations of an optimal grab, including the bulk cargo variability.

7.3. Conclusion

In this chapter, a sequential multi-objective optimization framework was established to include multiple grab design variables as well as a variety of bulk material properties in the design process.

A wide range of bulk material properties was used in the optimization, from a non-cohesive incompressible iron ore to a cohesive compressible cargo that is pre-consolidated. A maximized grab performance, $\Psi_{mass,\mathrm{mean}}$, was achieved, while a minimized value for the performance deviation was maintained. The established optimization framework offers a straightforward and reliable tool for designing grabs and other similar equipment, including the bulk cargo variability.

- A bulk variability was created to consider various levels of cohesion and compressibility of iron ore products. Three preliminary simulations were performed to verify that a realistic bulk variability is replicated using DEM. The outcome of simulations show that the relative cohesion has a significant influence on the angle of repose and bulk density, while the relative plastic compressibility plays an important role in the angle of repose, bulk compressibility, and the penetration resistance. The simulations of the grabbing process using a range of virtual bulk variability show that the relative plastic compressibility has a larger influence on the product performance, compared to the relative cohesion.
- 25 different random grab designs were created using the Latin Hypercube Design sampling method, including 5 different geometrical variables. A variation of 24% in the grab performance was captured using the random design samples, indicating the adequacy of the sampling method. Comparing the average mass indicator values, $\Psi_{mass,\mathrm{mean}}$, as well the corresponding standard deviation values allows for assessing performance of different grab designs.
- Three different surrogate models were created using linear regression, linear support vector machine kernel and polynomial supper vector machine kernel models. The outcome of the optimization was most promising and accurate when the surrogate model is constructed using a polynomial SVM kernel model, as it captures the non-linear relationships between variables and objectives.

Once a specific design concept is selected for handling iron ore, the bulk cargo variability can be included by following steps II, III and IV of the optimization framework. If a design concept needs to be optimized for a different type of cargo (e.g. coal), it is recommended that all steps of the optimization framework are followed in a sequential manner.

8

Conclusions and recommendations

8.1. Conclusions

A reliable and accurate DEM-MBD co-simulation was developed and utilised for optimizing the grabbing process of cohesive iron ore products. The grabbing process simulation was validated by full-scale grabbing experiments in the cargo hold under actual operational conditions. Both cohesive and stress-history dependent behaviour of moist fine iron ore were captured using the validated material model. Moreover, a novel multi-objective optimization framework was established that offers an affordable computation time to enhance design concepts in various operational conditions of varying bulk cargo properties.

The main findings regarding the main research questions of this dissertation are described below.

1. How can the effect of stress-history dependency of cohesive iron ore on the grabbing process be evaluated using a laboratory experimental setup?

- A consolidation-penetration test method was successfully developed to investigate the effect of consolidation stress on the penetration resistance. In this setup, a wedge-shaped tool penetrates into a moist sample of iron ore fine, that replicates the penetration process of grabs into bulk cargoes.

- A non-linear positive relationship between the pre-consolidation and the penetration resistance was found. Therefore, a strong link between the stress-history dependency of cohesive iron ore and the grabbing process was quantified.

2. What are variability and interdependency of iron ore properties and their interactions with equipment in realistic transport and storage conditions?

- Based on a range of experiments with three iron ore samples, it was shown that three bulk properties - type of cargo, moisture content, and pre-consolidation - are responsible for the variations of the dependent bulk properties: bulk density, angle of repose, penetration resistance, and shear strength.
- The tested iron ore samples are categorized as very cohesive to cohesive based on the ring shear test results. The angle of repose of these samples were measured using the ledge method; the test results are in the range of 55° to 70°, expect for Carajas SF sample (I_2) at the highest level of moisture content that resulted in angle of repose of 84° in average . The mentioned range is consistent with measurements of other researchers on moist iron ore samples using a similar test method.
- The dependent bulk properties of cohesive iron ore samples are highly sensitive to the history of the applied stress, σ_{pre}. This phenomena was observed in both ring shear and consolidation-penetration tests, in which high correlations between pre-consolidation and respectively flowability and accumulative penetration resistance are found. Therefore, choosing appropriate range of pre-consolidation in the design of equipment for handling cohesive iron ore is crucial.
- According to the obtained experimental results, it is expected that the variability of influencing bulk properties (type of cargo, moisture content and pre-consolidation) plays an important role in the performance consistency of transport and storage equipment, such as grabs.

3. How to minimize the computation cost for a large scale co-simulation of grabs and cohesive bulk solids?

- A hybrid particle-geometric scaling approach for DEM simulations of cohesive materials was developed and verified that allows for isolating the effects of varying particle size and geometric dimensions on bulk properties. Additionally, proper particle scaling rules were developed by extending the coarse graining technique to incorporate two important aspects of bulk materials, their elasto-plastic behaviour and their cohesive forces. It was demonstrated that the constant pull-off force, f_0, and the surface energy, $\Delta\gamma$, should be scaled by the squared of the scaling factor and the scaling factor respectively.

- To apply the hybrid particle-geometric scaling approach for simulating a cohesive and stress-history dependent bulk solid for using in an entirely different simulation scale, the following steps were required to be followed subsequently:
  - Step I is to conduct the laboratory tests to characterize complex behavior of cohesive and elasto-plastic materials for various bulk responses.
  - Step II is to calibrate the DEM simulation replicating the laboratory tests at a scale of 1:1, which is a common calibration procedure.
  - Step III is to vary the geometry scale by maintaining constant particle size and contact settings. Values of bulk responses are expected to be affected by geometric scaling.
  - Step IV is to vary the particle scale and to compare bulk responses with outcome of step III.

  Steps III and IV can be repeated until the desired trade-off between computational time and accuracy is reached. Once a scaled up simulation with a reduced computational time is developed, validation should be achieved using in-situ experiments.
- The scaling rules resulted in a reduction from 10^3 hours of computation time for around 8 million particles, to just under 4 hours for around 600 000 particles. This is sufficiently a short computation time to allow design optimisation of grabs.

4. What is a reliable calibration procedure to develop a realistic material model of cohesive iron ore for the grabbing process?

- To develop a realistic material model the following challenges in calibrating a DEM material model for complex bulk solids, such as cohesive and stress-history dependent iron ore, should be addressed:
  - Identifying proper contact modules that ensure multi-bulk responses can be captured properly: in this work, the Latin Hypercube Design technique was applied successfully to search for a non-empty solution space.
  - Including both types of input variables, categorical and continuous, in a multi-variable multi-objective calibration procedure: a categorical variable, rolling friction module, was included in the feasibility step of the calibration procedure. Once the level of categorical variable is set, levels of continuous variables, such as the coefficient of static friction, were optimized using the surrogate modelling.
  - Including a high number of DEM input variables in an optimization-based calibration procedure: by simply adjusting input parameters, numerous simulations should be run with no guarantee of finding a parameter set to fit the multi-bulk responses. The calibration procedure demonstrates how Design of Experiment techniques can be used in an effective way to create

samples for multiple DEM input variables (i.e. 6 continuous variables), while the number of required simulations is minimized.

- The calibration procedure addresses how a reliable procedure can be applied when the complexity of multi-bulk responses is included. It was shown that the surrogate modelling-based optimization is applicable when a high number (i.e. ≥ 5) of DEM input variables and a number of calibration targets (i.e. >2) are involved. The established calibration procedure can be applied to any type of unsaturated bulk materials, such as coal.

5. What is the accuracy of the MBD-DEM co-simulation of grabs and cohesive iron in replicating the actual process?

- The co-simulation of cohesive and stress-dependent iron ore was developed and validated successfully with full-scale grabbing experiments in the cargo hold. This allowed the process to be recorded under realistic operational conditions and ensured capturing the stress dependent behaviour of the bulk material at two different levels of cargo depth.
- The predictions of the co-simulation compared well to experimental data in all aspects, including force in cables, torque in winches, kinematics of geometry, payload, collected volume and average porosity of bulk solid.
- Using the co-simulation setup, a negative correlation between pre-consolidation level and payload was confirmed. When a pre-consolidation situation is created for cohesive materials, the increasing density of bulk material results in a lower penetration/cutting depth of grab, both at rest and closing stages.

6. How can bulk cargo variation be included in the design procedure of grabs?

- To include a variety of bulk material properties as well as multiple grab geometric variables in the design process, a sequential multi-objective optimization framework was established. A wide range of bulk material properties was used in the optimization, from a non-cohesive incompressible iron ore to a cohesive compressible cargo that is pre-consolidated. The optimization framework aimed successfully at a maximized grab performance (in terms of the mass indicator), and simultaneously, a maximized performance consistency. With the aid of this optimization framework, realistic operational conditions can be included in the design process of grabs.
- Three different surrogate models were created using linear regression, linear support vector machine kernel and polynomial supper vector machine kernel models. The outcome of the optimization was most promising and accurate when the surrogate model is constructed using

a polynomial SVM kernel model, as it captures the non-linear relationships between variables and objectives.

8.2. Recommendations

The developed and presented simulation-based optimization framework in this work is beneficial to grab manufacturers, terminal operators and other stakeholders of the grab industry:

Grab manufacturers should use the validated co-simulation to test the virtual prototypes of grabs as they interact with bulk solid cargoes, rather than the traditional approach of physical prototyping. Also, the simulation-based optimization framework offers application-driven design of grabs where the customer's specific requests, such as the list of cargoes being handled frequently, leads to a custom-made grab design.

Terminal operators can use the presented validated co-simulation to obtain valuable data regarding the grab performance under realistic operational conditions, and using obtained data in their logistic planning. In this dissertation, a surrogate model was created to include various design samples and bulk cargo properties. A more comprehensive surrogate model should be created in future work, capturing other aspects of operational conditions, such as bulk surface geometry. Once such a surrogate model is made more comprehensive, design and operational scenarios can be optimized without the necessity of running co-simulations. This allows for finding an optimal solution in near real-time. Various optimization targets can be included, such as unloading time of a bulk carrier, environmental impact, energy consumption, and fatigue of grab structure, therefore supporting the stakeholders in modernizing material handling systems.

Crane operators can utilize an automated monitoring system linked to a robust control system that enables the possibility of the operating grabs with a minimized unloading time. The developed co-simulation should be used for optimizing the control system in the grabbing process. The optimized control system requires near-real time data of bulk cargo and its interaction with equipment to be recorded in a remote way. The current common practice is using limited quantitative data, and by relying on visual observations and experience of the crane operator for controlling the grabs as well as laboratory-based measurements of similar cargoes.

The approach presented in this work can be implemented for other bulk solids and other handling equipment. Defining key performance indicators that take into consideration the impact of each piece of equipment on the entire chain of a bulk handling system can bring us closer towards revolutionizing the bulk material handling supply chain. The DEM material model

developed in this work was aimed for the grab application, which was simulated accurately. For a system approach, other applications, such as transfer chutes, that have flow regimes different than the grabbing process, require different material states to be considered. Therefore, a universal material model of a bulk solid independent of the flow regime should be established.

Bibliography

[1] United Nations Conference on Trade and Development (UNCTAD), Review of maritime transport, 2019. https://unctad.org/en/PublicationsLibrary/rmt2019_en.pdf.

[2] Natural Resources Canada, iron ore facts, (2019). https://www.nrcan.gc.ca/our-natural-resources/minerals-mining/minerals-metals-facts/iron-ore-facts/20517 (accessed May 5, 2020).

[3] D. Workman, Iron ore exports by country [online], (2020). worldstopexports.com/iron-ore-exports-country/ (accessed May 5, 2020).

[4] Iron Ore Technical Working Group, Marine report, 2013. Report.

[5] B. Vermeer, R.A.H. Schuurmans, D.L. Schott, G. Lodewijks, Analysis of the increased maximum load occurrences of bulk cranes, Bulksolids Europe 2012, Berlin. (2012).

[6] S. Lommen, G. Lodewijks, D.L. Schott, Co-simulation framework of discrete element method and multibody dynamics models, Engineering Computations. 34 (2018) 1481–1499.

[7] S.W. Lommen, D.L. Schott, G. Lodewijks, Multibody dynamics model of a scissors grab for co-simulation with discrete element method, FME Transactions. 40 (2012) 177–180.

[8] S.W. Lommen, Virtual prototyping of grabs: co-simulations of discrete element and rigid body models, Delft University of Technology, 2016. doi:PhD Thesis.

[9] S. Lommen, M. Mohajeri, G. Lodewijks, D. Schott, DEM particle upscaling for large-scale bulk handling equipment and material interaction, Powder Technology. 352 (2019) 273–282. doi:10.1016/j.powtec.2019.04.034.

[10] S.W. Lommen, The penetration of iron ore: calibrating discrete element parameters using penetration tests, 2011.TEL.7559, Delft University of Technology, 2011. MSc thesis.

[11] C.J. Coetzee, Review: Calibration of the Discrete Element Method, Powder Technology. 310 (2017) 104–142. doi:10.1016/j.powtec.2017.01.015.

[12] M. Rackl, K.J. Hanley, A methodical calibration procedure for discrete element models, Powder Technology. 307 (2017) 73–83. doi:10.1016/j.powtec.2016.11.048.

[13] L. Benvenuti, C. Kloss, S. Pirker, Identification of DEM simulation parameters by Artificial Neural Networks and bulk experiments, Powder Technology. 291 (2016) 456–465. doi:10.1016/j.powtec.2016.01.003.

[14] S.M. Derakhshani, D.L. Schott, G. Lodewijks, Micro–macro properties of quartz sand: experimental investigation and DEM simulation, Powder Technology. 269 (2015) 127–

138.

[15] H.Q. Do, A.M. Aragón, D.L. Schott, A calibration framework for discrete element model parameters using genetic algorithms, Advanced Powder Technology. 29 (2018) 1393–1403.

[16] C. Richter, T. Rößler, G. Kunze, A. Katterfeld, F. Will, Development of a standard calibration procedure for the DEM parameters of cohesionless bulk materials – Part II: Efficient optimization-based calibration, Powder Technology. 360 (2019) 967–976. doi:10.1016/j.powtec.2019.10.052.

[17] T. Roessler, C. Richter, A. Katterfeld, F. Will, Development of a standard calibration procedure for the DEM parameters of cohesionless bulk materials–part I: Solving the problem of ambiguous parameter combinations, Powder Technology. 343 (2019) 803–812.

[18] L. Lu, Iron ore: Mineralogy, processing and environmental sustainability, Elsevier, 2015. Book.

[19] M.C. Munro, A. Mohajerani, A review of the newly developed method used to prevent Liquefaction of iron ore fines on bulk carriers, Australian Geomechanics Journal. 51 (2016).

[20] Iron Ore Technical Working Group, Reference tests, 2013. Report.

[21] M. Mohajeri, F.M. Sickler, C. van Rhee, D.L. Schott, A Consolidation-Penetration Test for Wedge-Shaped Penetration Tools, FME Transactions. 46 (2018) 393.

[22] J.P. Morrissey, Discrete Element Modelling of Iron Ore Pellets to Include the Effects of Moisture and Fines, 2013. PhD Thesis.

[23] S. Luding, Cohesive, frictional powders: contact models for tension, Granular Matter. 10 (2008) 235. doi:10.1007/s10035-008-0099-x.

[24] S.C. Thakur, J.P. Morrissey, J. Sun, J.F. Chen, J.Y. Ooi, Micromechanical analysis of cohesive granular materials using the discrete element method with an adhesive elasto-plastic contact model, Granular Matter. 16 (2014) 383–400.

[25] L. Orefice, J.G. Khinast, A novel framework for a rational, fully-automatised calibration routine for DEM models of cohesive powders, Powder Technology. (2019) 687–703.

[26] J. Pachón-Morales, P. Perré, J. Casalinho, H. Do, D. Schott, F. Puel, J. Colin, Potential of DEM for investigation of non-consolidated flow of cohesive and elongated biomass particles, Advanced Powder Technology. (2020) 1500–1515.

[27] J. Pachón-Morales, H. Do, J. Colin, F. Puel, P. Perre, D. Schott, DEM modelling for flow of cohesive lignocellulosic biomass powders: Model calibration using bulk tests, Advanced Powder Technology. 30 (2019) 732–750.

[28] M. Ucgul, J.M. Fielke, C. Saunders, Three-dimensional discrete element modelling of tillage: Determination of a suitable contact model and parameters for a cohesionless soil, Biosystems Engineering. 121 (2014) 105–117. doi:10.1016/j.biosystemseng.2014.02.005.

[29] M.J. Mohajeri, H.Q. Do, D.L. Schott, DEM calibration of cohesive material in the ring shear test by applying a genetic algorithm framewrok, Advanced Powder Technology. 31 (2020) 112–125. doi:10.1016/j.apt.2020.02.019.

[30] S.C. Thakur, J.Y. Ooi, H. Ahmadian, Scaling of discrete element model parameters for cohesionless and cohesive solid, Powder Technology. 293 (2016) 130–137.

[31] R.K. Roy, Design of experiments using the Taguchi approach: 16 steps to product and

process improvement, John Wiley & Sons, 2001. Book.

[32] D.G. Fredlund, H. Rahardjo, Soil mechanics for unsaturated soils, John Wiley & Sons, 1993. Book.

[33] K.P. Panayiotopoulos, C.P. Papadopoulou, A. Hatjiioannidou, Compaction and penetration resistance of an Alfisol and Entisol and their influence on root growth of maize seedlings, Soil and Tillage Research. 31 (1994) 323–337.

[34] M.F. Nawaz, G. Bourrie, F. Trolard, Soil compaction impact and modelling. A review, Agronomy for Sustainable Development. 33 (2013) 291–309.

[35] K. Orzech, M. Wanic, D. Zaluski, A. Stepien, Influence of soil compaction and tillage methods on penetration resistance of soil and yields in the crop rotation system, Acta Agrophysica. 23 (2016) 662–680.

[36] Bureau of Infrastructure Transport and Regional Economics, Freightline 2 - Australian iron ore freight transport, (2014) 24. https://bitre.gov.au/publications/2014/files/Freightline_02.pdf.

[37] F.M. Sickler, Developing a test method to investigate effect of compaction on penetration resistance of moist iron ore and coal, 2016. TEL.8083, 2017. Report.

[38] A. Miszewski, S.W. Lommen, D.L. Schott, G. Lodewijks, Effect of Moisture Content on the Angle of Repose of Iron Ore, 7th International Conference for Conveying and Handling of Particulate Solids. (2012) 1–9.

[39] Delft University of Technology, NEN-EN 1097-5, Test methods for the determination of mechanical and physical properties of aggregates - Part 5: Determination of water content by drying in a ventilated oven, 2008. Technical report.

[40] International Maritime Organization, International maritime solid bulk cargoes code, 2013.

[41] Det Norske Veritas, Strength Analysis of Hull Structure in Bulk Carriers, 2003. Report.

[42] M.C. Munro, A. Mohajerani, Variation of the geotechnical properties of Iron Ore Fines under cyclic loading, Ocean Engineering. 126 (2016) 411–431. doi:10.1016/j.oceaneng.2016.09.006.

[43] Z. Asaf, D. Rubinstein, I. Shmulevich, Determination of discrete element model parameters required for soil tillage, Soil and Tillage Research. 92 (2007) 227–242. doi:10.1016/j.still.2006.03.006.

[44] R.S. Fowkes, D.E. Frisque, W.G. Pariseau, Materials handling research: penetration of selected/granular materials by wedge-shaped tools, US Dept. of Interior, Bureau of Mines, 1973.

[45] G.W. Turnage, D.R. Freitag, Effects of cone velocity and size on soil penetration resistance, Army Engineer Waterways Experiment Station Vicksburg MS, 1969.

[46] M.W. Gui, M.D. Bolton, J. Garnier, J.F. Corte, G. Bagge, J. Laue, R. Renzi, Guidelines for cone penetration tests in sand, in: Centrifuge, 1998: pp. 155–160.

[47] Y.K. Atemimi, Relationship between Compaction Ratio (RC) and Compacted Layer Thickness, Saudi Jounrnal of Engineering and Technol. (2016) 112–123.

[48] W. Chen, A. Roberts, K. Williams, J. Miller, J. Plinke, On uniaxial compression and Jenike direct shear testings of cohesive iron ore materials, Powder Technology. 312 (2017) 184–193. doi:10.1016/j.powtec.2017.02.037.

[49] S.P. Washington, M.G. Karlaftis, F. Mannering, Statistical and econometric methods for transportation data analysis, CRC press, 2010.

[50] D. Schulze, Powders and bulk solids: behavior, characterization, storage and flow, Springer Science & Business Media, 2007. Book.

[51] A. Costantini, Relationships between cone penetration resistance, bulk density, and moisture content in uncultivated, repacked, and cultivated hardsetting and non-hardsetting soils form the coastal lowlands of south-east Queensland, Powder Technology. (1995) 112–125.

[52] S. Herminghaus, Dynamics of wet granular matter, Advances in Physics. 54 (2005) 221–261.

[53] J. Antony, Design of experiments for engineers and scientists, Elsevier, 2014. Book.

[54] J. Yang, D. Sun, N. Hu, H. Ning, J. Zhang, W. Ye, J. Wu, Multi-objective robust design optimization of a two-dimensional tri-axial braided hollow pillar using an evolutionary algorithm, Composite Structures. 220 (2019) 105–113. doi:10.1016/j.compstruct.2019.03.058.

[55] P.G. Ceorgiev, Implementation of metamodels in ship design in ship design Implementation of metamodels, Maritime Industry. (2015). doi:10.13140/2.1.4336.6726.

[56] A.E. Ames, N. Mattucci, S. Macdonald, G. Szonyi, M. Douglas, Quality Loss Functions for Optimization across Multiple Response Surfaces, Journal of Quality Technology. 29 (2018) 339–346. doi:10.1080/00224065.1997.11979775.

[57] J. Yu, C. Chang, Robust design optimisation via surrogate network model and soft outer array design, International Journal of Production Research. 56 (2018) 1533–1547. doi:10.1080/00207543.2017.1356484.

[58] X. Zhou, D.K.J. Lin, X. Hu, T. Jiang, Robust parameter design based on Kullback-Leibler divergence, Computers & Industrial Engineering. 135 (2019) 913–921. doi:10.1016/j.cie.2019.06.053.

[59] W. Chen, A.W. Roberts, A modified flowability classification model for moist and cohesive bulk solids, Powder Technology. 325 (2018) 639–650. doi:10.1016/j.powtec.2017.11.054.

[60] W.J. Rawls, Infiltration and soil water movement, McGraw-Hill, 1993. Book.

[61] A.W. Jenike, Storage and flow of solids, bulletin no. 123, Bulletin of the University of Utah. 53 (1964) 198.

[62] A.R. Cabral, R.A. Creaser, T. Nägler, B. Lehmann, A.R. Voegelin, B. Belyatsky, Trace-element and multi-isotope geochemistry of Late-Archean black shales in the Carajás iron-ore district , Brazil, 362 (2013) 91–104. doi:10.1016/j.chemgeo.2013.08.041.

[63] American Society for Testing and Materials, Standard test methods for particle-size distribution (gradation) of soils using sieve analysis, ASTM International, 2004.

[64] Horiba Scientific, A guidebook to particle size analysis, 2012. Book.

[65] British Standard Institution, BS EN1097-5: Determination of water content by drying in a ventilated oven, 2008.

[66] U. Zafar, C. Hare, G. Calvert, M. Ghadiri, R. Girimonte, B. Formisani, M.A.S. Quintanilla, J.M. Valverde, Comparison of cohesive powder flowability measured by Schulze Shear Cell, Raining Bed Method, Sevilla Powder Tester and new Ball Indentation Method,

Powder Technology. 286 (2015) 807–816. doi:10.1016/j.powtec.2015.09.010.

[67] A.W. Jenike, Flow properties of bulk solids, American Society for Testing and Materials, 1960.

[68] Americal Society for Testing and Materials, D6773: Standard Test Method for Bulk Solids Using Schulze Ring Shear Tester, (2016) 1–27. doi:10.1520/D6773-16.2.

[69] M.A. Carrigy, Experiments on the angles of repose of granular materials, Sedimentology. 14 (1970) 147–158.

[70] K. Terzaghi, R.B. Peck, G. Mesri, Soil mechanics, 1996. Book.

[71] Y.S.L. Lee, R. Poynter, F. Podczeck, J.M. Newton, Development of a dual approach to assess powder flow from avalanching behavior, AAPS PharmSciTech. 1 (2000) 44–52.

[72] K. Saleh, S. Golshan, R. Zarghami, A review on gravity flow of free-flowing granular solids in silos – Basics and practical aspects, Chemical Engineering Science. 192 (2018) 1011–1035. doi:10.1016/j.ces.2018.08.028.

[73] W.E. Deming, A.L. Mehring, The gravitational flow of fertilizers and other comminuted solids, Industrial & Engineering Chemistry. 21 (1929) 661–665.

[74] H. Salehi, M. Poletto, D. Barletta, S.H. Larsson, Predicting the silo discharge behavior of wood chips-A choice of method, Biomass and Bioenergy. 120 (2019) 211–218.

[75] T. Roessler, A. Katterfeld, Scalability of angle of repose tests for the calibration of DEM parameters, in: 12th International Conference on Bulk Materials Storage, Handling and Transportation (ICBMH 2016), The, Engineers Australia, 2016: p. 201.

[76] W. Mairaing, Penetration resistance of soils in relation to penetrometer shape, Iowa State University, 1978. PhD thesis.

[77] V.C. Zitrom, One-Factor-at-a-Time Versus Designed Experiments, The American Statistician. 53 (1999) 126–131.

[78] Iron Ore Technical Working Group, Terms of Reference, 2013. Report.

[79] H.H. Murray, Traditional and new applications for kaolin, smectite, and palygorskite: a general overview, Applied Clay Science. 17 (2000) 207–221.

[80] A. Roberts, Handleability or Flowability, Centre for Bulk Solids and Particulate Technologies, The University of New Castle, 1999.

[81] P. ISO, ISO17828: 2016-Solid biofuels - Determination of bulk density, 2016.

[82] M.J. Carr, T. Roessler, H. Otto, C. Richter, A. Katterfeld, C.A. Wheeler, K. Williams, G. Elphick, K. Nettleton, Calibration procedure of Discrete Element Method (DEM) parameters for cohesive bulk materials, in: 13th International Conference on Bulk Materials Storage, Handling and Transportation (ICBMH 2019), Engineers Australia, 2019: p. 693.

[83] EDEMSimulation, EDEM2018 Documentation, 2018.

[84] J.P. Morrissey, S.C. Thakur, J.Y. Ooi, EDEM Contact Model : Adhesive Elasto-Plastic Model, 2014. Techincal report.

[85] J. Ai, J.-F. Chen, J.M. Rotter, J.Y. Ooi, Assessment of rolling resistance models in discrete element simulations, Powder Technology. 206 (2011) 269–282. doi:10.1016/j.powtec.2010.09.030.

[86] S. Lommen, D. Schott, G. Lodewijks, Particuology DEM speedup : Stiffness effects on

behavior of bulk material, Particuology. 12 (2014) 107–112. doi:10.1016/j.partic.2013.03.006.

[87] M. Obermayr, C. Vrettos, P. Eberhard, T. Däuwel, A discrete element model and its experimental validation for the prediction of draft forces in cohesive soil, Journal of Terramechanics. 53 (2014) 93–104. doi:10.1016/j.jterra.2014.04.003.

[88] L. Zhao, Y. Zhao, C. Bao, Q. Hou, A. Yu, Laboratory-scale validation of a DEM model of screening processes with circular vibration, Powder Technology. 303 (2016) 269–277.

[89] J. Quist, M. Evertsson, Framework for DEM model calibration and validation, in: Proceedings of the 14th European Symposium on Comminution and Classification, Gothenburg, Sweden, 2015: pp. 103–108.

[90] T.A.H. Simons, R. Weiler, S. Strege, S. Bensmann, M. Schilling, A. Kwade, A ring shear tester as calibration experiment for DEM simulations in agitated mixers - A sensitivity study, Procedia Engineering. 102 (2015) 741–748. doi:10.1016/j.proeng.2015.01.178.

[91] D.L. Schott, S.W. Lommen, R. van Gils, J. de Lange, M.M. Kerklaan, O.M. Dessing, W. Vreugdenhil, G. Lodewijks, Scaling of particles and equipment by experiments of an excavation motion, Powder Technology. 278 (2015) 26–34. doi:10.1016/j.powtec.2015.03.012.

[92] D. Ilic, A. Roberts, C. Wheeler, A. Katterfeld, Modelling bulk solid flow interactions in transfer chutes: Shearing flow, Powder Technology. 354 (2019) 30–44.

[93] D. Ilic, A. Roberts, C. Wheeler, Modelling bulk solid interactions in transfer chutes: Accelerated flow, Chemical Engineering Science. 209 (2019) 115–127.

[94] D. Ilic, Development of design criteria for reducing wear in iron ore transfer chutes, Wear. 434 (2019) 202–216.

[95] S. Kirsch, Avoiding ambiguity in DEM in-situ calibration for dry bulk materials, Minerals Engineering. 145 (2020) 94–106.

[96] T. Roessler, A. Katterfeld, Scaling of the angle of repose test and its influence on the calibration of DEM parameters using upscaled particles, Powder Technology. 330 (2018) 58–66. doi:10.1016/j.powtec.2018.01.044.

[97] American Society for Testing and Materials, Standard test method for bulk solids using Schulze ring shear tester, ASTM International, 2008.

[98] C.J. Coetzee, Particle upscaling: Calibration and validation of the discrete element method, Powder Technology. 344 (2019) 487–503. doi:10.1016/j.powtec.2018.12.022.

[99] M. Marigo, E.H. Stitt, Discrete element method (DEM) for industrial applications: Comments on calibration and validation for the modelling of cylindrical pellets, KONA Powder and Particle Journal. 32 (2015) 236–252. doi:10.14356/kona.2015016.

[100] M. Lemieux, G. Léonard, J. Doucet, L.-A. Leclaire, F. Viens, J. Chaouki, F. Bertrand, Large-scale numerical investigation of solids mixing in a V-blender using the discrete element method, Powder Technology. 181 (2008) 205–216.

[101] A.P. Grima, P.W. Wypych, Development and validation of calibration methods for discrete element modelling, Granular Matter. 13 (2011) 127–132.

[102] E. Bänsch, Local mesh refinement in 2 and 3 dimensions, IMPACT of Computing in Science and Engineering. 3 (1991) 181–191.

[103] O. Falagush, G.R. McDowell, H.-S. Yu, Discrete Element Modeling of Cone Penetration

Tests Incorporating Particle Shape and Crushing, International Journal of Geomechanics. 15 (2015) 04015003. doi:10.1061/(asce)gm.1943-5622.0000463.

[104] A. Janda, J.Y. Ooi, DEM modeling of cone penetration and unconfined compression in cohesive solids, Powder Technology. 293 (2016) 60–68. doi:10.1016/j.powtec.2015.05.034.

[105] C. Bierwisch, T. Kraft, H. Riedel, M. Moseler, Three-dimensional discrete element models for the granular statics and dynamics of powders in cavity filling, Journal of the Mechanics and Physics of Solids. 57 (2009) 10–31.

[106] D.S. Nasato, C. Goniva, S. Pirker, C. Kloss, Coarse graining for large-scale DEM simulations of particle flow - An investigation on contact and cohesion models, Procedia Engineering. 102 (2015) 1484–1490. doi:10.1016/j.proeng.2015.01.282.

[107] C. Kloss, C. Goniva, LIGGGHTS Users Manual, (2014).

[108] M.J. Mohajeri, M.J. van den Bos, C. van Rhee, D.L. Schott, Bulk properties variability and interdependency determination for cohesive iron ore, Powder Technology. 367 (2020) 539–557. doi:10.1016/j.powtec.2020.04.018.

[109] K.L. Johnson, K. Kendall, A.D. Roberts, Surface Energy and the Contact of Elastic Solids, Proceedings of the Royal Society A: Mathematical, Physical and Engineering Sciences. 324 (1971) 301–313. doi:10.1098/rspa.1971.0141.

[110] A. Salazar, E. Saez, G. Pardo, Modeling the direct shear test of a coarse sand using the 3D Discrete Element Method with a rolling friction model, Computers and Geotechnics. 67 (2015) 83–93. doi:10.1016/j.compgeo.2015.02.017.

[111] C. Thornton, L. Zhang, Numerical simulations of the direct shear test, Chemical Engineering & Technology. 26 (2003) 153–156. doi:10.1002/ceat.200390022.

[112] H. Huang, E. Tutumluer, Discrete Element Modeling for fouled railroad ballast, Construction and Building Materials. 25 (2011) 3306–3312. doi:10.1016/j.conbuildmat.2011.03.019.

[113] S.H. Liu, Simulating a direct shear box test by DEM, Canadian Geotechnical Journal. 43 (2006) 155–168. doi:10.1139/t05-097.

[114] C.J. Coetzee, E. Horn, Calibration of the Discrete Element Method Using a Large Shear Box, International Journal of Mechanical, Aerospace, Industrial, Mechatronic and Manufacturing Engineering. 8 (2014) 2105–2114. http://waset.org/Publications?p=96.

[115] I. Keppler, F. Safranyik, I. Oldal, Shear test as calibration experiment for DEM simulations: a sensitivity study, Engineering Computations. 33 (2016) 742–758.

[116] F. Cruz, S. Emam, M. Prochnow, J. Roux, F. Chevoir, Rheophysics of dense granular materials : Discrete simulation of plane shear flows, (2005) 1–17. doi:10.1103/PhysRevE.72.021309.

[117] C.S. Bierwisch, Numerical simulations of granular flow and filling, Citeseer, 2009. Book.

[118] M. Mohajeri, C. van Rhee, D.L. Schott, Penetration resistance of cohesive iron ore: A DEM study, in: 9th International Conference on Conveying and Handling of Particulate Solids, 2018: pp. 1–7.

[119] C.M. Wensrich, A. Katterfeld, Rolling friction as a technique for modelling particle shape in DEM, Powder Technology. 217 (2012) 409–417.

[120] K. Iwashita, M. Oda, Rolling resistance at contacts in simulation of shear band development

by DEM, Journal of Engineering Mechanics. 124 (1998) 285–292.

[121] M. Ajmal, T. Roessler, M.J. Carr, A. Katterfeld, Development of a Cohesive DEM Parameter Calibration Protocol for Bulk Materials using Rapid Flow and Low Consolidation Standard Tests, in: 13th International Conference on Bulk Materials Storage, Handling & Transportation, 2019.

[122] H.A. Janssen, Versuche uber getreidedruck in silozellen, Z. Ver. Dtsch. Ing. 39 (1895) 1045–1049.

[123] L.Y. Yi, K.J. Dong, R.P. Zou, A.B. Yu, Coordination number of the packing of ternary mixtures of spheres: DEM simulations versus measurements, Industrial & Engineering Chemistry Research. 50 (2011) 8773–8785.

[124] J. Frączek, A. Złobecki, J. Zemanek, Assessment of angle of repose of granular plant material using computer image analysis, Journal of Food Engineering. 83 (2007) 17–22.

[125] M.J. Mohajeri, C. van Rhee, D.L. Schott, Coarse graining of adhesive elasto-plastic DEM contact models in quasi static process, in: ICMBH 2019, 2019.

[126] C.A. Rogers, Packing and covering, University Press, 1964.

[127] R. Cai, Y. Zhao, An experimentally validated coarse-grain DEM study of monodisperse granular mixing, Powder Technology. 361 (2020) 99–111.

[128] M.Z. Tekeste, T.R. Way, Z. Syed, R.L. Schafer, Modeling soil-bulldozer blade interaction using the discrete element method (DEM), Journal of Terramechanics. 88 (2020) 41–52.

[129] D. Kretz, S. Callau-Monje, M. Hitschler, A. Hien, M. Raedle, J. Hesser, Discrete element method (DEM) simulation and validation of a screw feeder system, Powder Technology. 287 (2016) 131–138.

[130] A.P. Grima, Quantifying and modelling mechanisms of flow in cohesionless and cohesive granular materials, 2011. PhD thesis.

[131] A.P. Grima, T. Fraser, D.B. Hastie, P.W. Wypych, Discrete element modelling: trouble-shooting and optimisation tool for chute design, in: 2011: pp. 1–10.

[132] H.Q. Do, A.M. Aragón, D.L. Schott, Automated discrete element method calibration using genetic and optimization algorithms, in: EPJ Web of Conferences, EDP Sciences, 2017: p. 15011.

[133] D.S. Starnes, D. Yates, D.S. Moore, The practice of statistics, Macmillan, 2010. Book.

[134] C.J.J. Coetzee, Calibration of the discrete element method and the effect of particle shape, Powder Technology. 297 (2016) 50–70. doi:10.1016/j.powtec.2016.04.003.

[135] G. Taguchi, Introduction to quality engineering: designing quality into products and processes, Asian Productivity Organization, 1986. Book.

[136] R.L. Plackett, J.P. Burman, The design of optimum multifactorial experiments, Biometrika. 33 (1946) 305–325.

[137] M.D. McKay, R.J. Beckman, W.J. Conover, Comparison of three methods for selecting values of input variables in the analysis of output from a computer code, Technometrics. 21 (1979) 239–245.

[138] State College, Minitab 17 statistical software, (2010) PA: Minitab, Inc.

[139] J.Y.O. Subhash C. Thakur Hossein Ahmadian, Scaling of Discrete element model parameters for cohesionless and cohesive solid, Powder Technology. (2015) 130–137.

[140] M.J. Mohajeri, R.L.J. Helmons, C. van Rhee, D.L. Schott, A hybrid particle-geometric scaling approach for elasto-plastic adhesive DEM contact models, Powder Technology. 369 (2020) 72–87. doi:10.1016/j.powtec.2020.05.012.

[141] C.J. Coetzee, D.N.J. Els, Calibration of discrete element parameters and the modelling of silo discharge and bucket filling, Computers and Electronics in Agriculture. 65 (2009) 198–212. doi:10.1016/j.compag.2008.10.002.

[142] W. Smith, D. Melanz, C. Senatore, K. Iagnemma, H. Peng, Comparison of DEM and traditional modeling methods for simulating steady-state wheel-terrain interaction for small vehicles, in: Proceedings of the 7th Americas Regional Conference of the ISTVS, Tampa, FL, USA, 2013: pp. 4–7.

[143] C.J. Coetzee, D.N.J. Els, Calibration of granular material parameters for DEM modelling and numerical verification by blade-granular material interaction, Journal of Terramechanics. 46 (2009) 15–26. doi:10.1016/j.jterra.2008.12.004.

[144] Z. Wang, G. Jing, Q. Yu, H. Yin, Analysis of ballast direct shear tests by discrete element method under different normal stress, Measurement. 63 (2015) 17–24.

[145] A. Jensen, K. Fraser, G. Laird, Improving the precision of discrete element simulations through calibration models, 13th International LS-DYNA Conference, Detroit. (2014) 1–12.

[146] R. Briend, P. Radziszewski, D. Pasini, Virtual soil calibration for wheel–soil interaction simulations using the discrete-element method, Canadian Aeronautics and Space Journal. 57 (2011) 59–64.

[147] Y. Franco, D. Rubinstein, I. Shmulevich, Determination of discrete element model parameters for soil-bulldozer blade interaction, in: 15th International Conference of the ISTVS, September, 2005: pp. 25–29.

[148] A. Di Renzo, F.P. Di Maio, An improved integral non-linear model for the contact of particles in distinct element simulations, Chemical Engineering Science. 60 (2005) 1303–1312.

[149] O.R. Walton, Force models for particle-dynamics simulations of granular materials, in: Mobile Particulate Systems, Springer, 1995: pp. 367–380.

[150] R.D. Mindlin, Elastic spheres in contact under varying oblique forces, J. Applied Mech. 20 (1953) 327–344.

[151] M.D. Morris, T.J. Mitchell, Exploratory designs for computational experiments, Journal of Statistical Planning and Inference. 43 (1995) 381–402.

[152] F.A.C. Viana, G. Venter, V. Balabanov, An algorithm for fast optimal Latin hypercube design of experiments, International Journal for Numerical Methods in Engineering. 82 (2010) 135–156.

[153] H. Otto, A. Zimmermann, M. Kleiber, A. Katterfeld, Optimization of an orange peel grab for wood chips, Mechanics and Mechanical Engineering. (2019) 112–119.

[154] R.J. Kuiper, X. Chen, J.C.L. Frumau, S.A. Miedema, Reduction of Energy Consumption When Using a Grab for Deep-Sea Mining Operations, in: Offshore Technology Conference, Offshore Technology Conference, 2016.

[155] D.L. Schott, M.J. Mohajeri, J. Jovanova, S.W. Lommen, W. de Kluijver, Design framework for DEM-supported prototyping of grabs by industrial-scale validation, Journal of Terramechanics. (2021).

[156] F. Ye, C. Wheeler, B. Chen, J. Hu, K. Chen, W. Chen, Calibration and verification of DEM parameters for dynamic particle flow conditions using a backpropagation neural network, Advanced Powder Technology. 30 (2019) 292–301.

[157] M.R. Fatahi, A. Farzanegan, DEM simulation of laboratory Knelson concentrator to study the effects of feed properties and operating parameters, Advanced Powder Technology. 28 (2017) 1443–1458.

[158] S. Schmelzle, S. Leppert, H. Nirschl, Influence of impeller geometry in a vertical mixer described by DEM simulation and the dispersion model, Advanced Powder Technology. 26 (2015) 1473–1482.

[159] H. Wei, Y. Zhao, J. Zhang, H. Saxén, Y. Yu, LIGGGHTS and EDEM application on charging system of ironmaking blast furnace, Advanced Powder Technology. 28 (2017) 2482–2487.

[160] M. Ucgul, J.M. Fielke, C. Saunders, Defining the effect of sweep tillage tool cutting edge geometry on tillage forces using 3D discrete element modelling, Information Processing in Agriculture. 2 (2015) 130–141. doi:10.1016/j.inpa.2015.07.001.

[161] J.B. Barr, J.M.A. Desbiolles, J.M. Fielke, M. Ucgul, Development and field evaluation of a high-speed no–till seeding system, Soil and Tillage Research. 194 (2019) 104337.

[162] M. Kazhdan, H. Hoppe, Screened poisson surface reconstruction, ACM Transactions on Graphics (ToG). 32 (2013) 1–13.

[163] S. Weisberg, Applied linear regression, 528 (2005). Book.

[164] M.J. Mohajeri, W. de Kluijver, R.L.J. Helmons, C. van Rhee, D.L. Schott, A validated co-simulation of grab and moist iron ore cargo: replicating the cohesive and stress-history dependent behaviour of bulk solids, Advanced Powder Technology. (2021).

[165] M.J. Mohajeri, C. van Rhee, D.L. Schott, Replicating stress-history dependent behaviour of cohesive solid materials: Feasibility and definiteness in DEM calibration procedure, Advanced Powder Technology. (2021).

[166] S.C. Thakur, J.P. Morrissey, J. Sun, J.-F. Chen, J.Y. Ooi, A DEM study of cohesive particulate solids; plasticity and stress history dependency, in: International Conference on Particulate System Analysis Edinburgh, UK, 2011: pp. 1–5.

[167] F.A.C. Viana, A tutorial on Latin hypercube design of experiments, Quality and Reliability Engineering International. 32 (2016) 1975–1985.

[168] R. Jin, W. Chen, A. Sudjianto, An efficient algorithm for constructing optimal design of computer experiments, in: International Design Engineering Technical Conferences and Computers and Information in Engineering Conference, 2003: pp. 545–554.

[169] J. Fox, Applied regression analysis and generalized linear models, Sage Publications, 2015. Book.

[170] A.J. Smola, B. Schölkopf, A tutorial on support vector regression, Statistics and Computing. 14 (2004) 199–222.

[171] B. Scholkopf, A.J. Smola, Learning with kernels: support vector machines, regularization, optimization, and beyond, (2018) 112–125.

[172] K. Deb, A. Pratap, S. Agarwal, T. Meyarivan, A fast and elitist multiobjective genetic algorithm: NSGA-II, IEEE Transactions on Evolutionary Computation. 6 (2002) 182–197.

[173] K. Deb, Multi-objective optimization using evolutionary algorithms, John Wiley & Sons,

2001. Book.

Nomenclature

In this dissertation the following symbols have been used:

Symbol	Unit	Description
A	m^2	Area
μ_r	-	Coefficient of rolling friction
μ_s	-	Coefficient of static friction
$\|e\|$	-	Absolute relative difference
β	-	Constant term in regression model
C_{bulk}	-	Relative bulk cohesion
C_R	-	Coefficient of restitution
d_{50}	mm	Median particle size
$d_{composite}$	-	Composite desirability, geometric mean of individual desirability values
δ_n	m	Normal contact overlap
E^*	Pa	Equivalent Young's modulus
f_{adh}	N	Normal adhesive force
f_N	N	Normal contact force
f_T	N	Tangential contact force
f_0	N	Constant pull-off force
G	Pa	Shear modulus
g	m/s^2	Gravitational constant
H	m	Height
η_{grab}	-	Grab's efficiency

Symbol	Unit	Description
k_{adh}	N/m	Adhesive stiffness of contact spring
k_n	N/m	Normal stiffness of contact spring
k_t	N/m	Tangential stiffness of contact spring
$k_{t,mult}$	-	Tangential stiffness multiplier in the EEPA contact model
L_s	m	Final penetration depth of the sampling tube
M_e	ton	Grab's weight when it is empty
MC	%	Dry-based moisture content
M_{DWT}	ton	Weight of collected bulk solid
n_{DWT}	-	Porosity of collected bulk solid
$n_{Keppler}$	-	Theoretical limit of minimum porosity for rigid sphere
r	m	Moment arm
R^*	m	Equivalent radius
ρ_b	kg/m^3	Bulk density in moist state
ρ_d	kg/m^3	Bulk density in dry state
ρ_f	kg/m^3	Fluid density
R^2	-	Coefficient of determination
R_p	m	Particle radius
τ	Pa	Shear stress
τ_R	N.m	Rotational contact torque
U	m	Perimeter
V	m/s	Velocity
w_k	-	Weighting factor
W_z	J	Accumulated penetration resistance at penetration depth of *z*
α_M	Degree	Angle of repose
$\Delta_{initial,S66}$	m	Penetration resistance quantified through initial penetration depth of S66 tube
Δ_{MC}	%	Moisture content variation
$\Delta\gamma$	J/m^2	Surface energy
λ_{bulk}	-	Relative bulk compressibility
λ_P	-	Contact plasticity ratio

Symbol	Unit	Description
σ	Pa	Normal stress
σ_1	Pa	Consolidation stress
σ_c	Pa	Unconfined yield strength
σ_{pr}	Pa	Pre-consolidation stress
τ_a	Pa	Adhesion (shear) strength
τ_c	Pa	Cohesion (shear) strength
τ_w	Pa	Wall shear stress
ϕ_{lin}	Degree	Linear internal friction
φ_x	Degree	Wall friction angle
χ	-	Tensile exponent
ψ_P	-	Particle shape
ω	degree/s	Angular velocity

Acknowledgements

I would like to thank the supervision team, from both TU Delft and NEMAG BV, who put their trust in me to carry out this exciting research project. My research focused on linking design techniques, simulations, laboratory and field experiments, which made it an exciting experience for me. I have enjoyed working on this project and being part of this research team.

I would like to thank Dr Dingena L. Schott for being a truly supportive, motivating, and critical supervisor. I always looked forward to our progress meetings to share new results, ideas and challenges. Dingena always provided her point of view to help structuring my ideas and plans on both content and process of this research. We attended multiple conferences, project meetings and field experiments together, which were very helpful. I would also like to express my appreciation towards Prof. Cees van Rhee, who provided his expertise and feedback during this project. Our discussions on novel engineering ideas and challenges were always inspiring to me.

Support from NEMAG BV in initiating and sponsoring this project is acknowledged. I enjoyed working within their engineering team. Visiting NEMAG BV was always inspiring because of the fruitful meetings that helped to broaden my perspective on the grab application. Amazing Zeeland landscapes, splendid cake and dinner gatherings, as well as interesting conversations with companions such as Arjan, Niels and Kadir, were among other inspiring aspects of travelling to Zierikzee. Wilbert de Kluijver was a collaborative and supportive colleague at NEMAG BV, who contributed considerably in arranging, designing and conducting field experiments (Chapter 6). We co-supervised multiple graduation projects together, which resulted in improved insights into the grabbing process. Michel Corbeau was a responsible manager who was always ready to provide feedback to ensure that the project would be accomplished successfully. Technical discussions with Guido van Koeveringe, who shared his rich experience of the grab application, are also appreciated.

I would also like to acknowledge the support of Harry Post, Hans Schoorl and their colleagues from the Department of Raw Material Handling at Tata Steel, the Netherlands, for their contribution in conducting in-situ experiments (Chapter 6).

Discussions with Dr Rudy L. J. Helmons were inspirational and useful, contributing towards chapters 4 and 6 of this thesis. Dr Jovana Jovanova also helped with brainstorming and feedback on chapters 5 and 7. I would like to thank my colleagues, Hamid Gilvari, Vittorio Garofano and Marc Fransen, too, for sharing their time to discuss technical challenges and to brainstorm.

It has been a great pleasure to coach Arjan, Niels, Femke, Mats, Lars, Kesia and Kadir during their studies. The consolidation-penetration test method in Chapter 2 was developed with the help of Femke M. Sickler. The consolidation-penetration experiment in Chapter 3 was undertaken by Mats J. van den Bos. The ring-shear test simulation was created by Niels de Vries. The simulations in Chapter 7 were conducted by Arjan van den Bergh during his graduation project.

I would like to thank my colleagues in the Department of a Maritime and Transport Engineering, including the support staff, secretaries and department managers. Especially, I am grateful to Patty, Pauline, Anouk, Dineke, Monique and Gracia.

Many thanks to my partner, Farzaneh, firstly for being the most supportive person during these years, and secondly for helping me to finalize this book. Also, I appreciate the support of family and friends during this research project.

Curriculum Vitae

M. Javad Mohajeri is a researcher at Delft University of Technology working toward enabling robust design methods for ship unloader grabs. His main areas of research interest are Discrete Element Method, modelling bulk solids in interaction with equipment, and design optimization of bulk handling equipment. Aside from his career, Javad has a great passion for theatre, cinematography, hiking, psychology and literature.

2016-2020	Doctoral candidate in Maritime and Transport Technology PhD researcher at Delft University of Technology, Faculty of Mechanical, Maritime and Materials Engineering, Transport and Logistics Section. Working on a collaborative project with NEMAG B.V., a Dutch grab manufacturer to enable possibility of virtual prototyping of grabs as they interact with cohesive bulk solids.
2013-2015	Master degree in Civil Engineering, Tarbiat Modares University, Iran. Graduation project: Modelling stability of rubble-mound breakwaters using SPH method
2006-2011	Bachelor degree in Civil Engineering, Isfahan University of Technology, Iran.

Samenvatting

Wegens de grote vraag naar ijzerertsproducten in de staalindustrie hebben deze per jaar het grootste aandeel in de handel in droge bulkgoederen, groter dan kolen en graan. Ongeveer 9000 capesize-vrachtschepen met een draagvermogen tot 400 000 ton vervoeren jaarlijks ijzererts naar havens van bestemming. Voor het lossen van ijzererts uit scheepsruimen worden veelal grijpers gebruikt. Een snel en betrouwbaar losproces is nodig om de kosten voor havenexploitanten zo laag mogelijk te houden en om ijzerertsproducten op tijd bij de klanten te kunnen afleveren. In de praktijk zijn er vele factoren, zoals vocht, materiaaleigenschappen die variëren met de ladingdiepte, en de dynamische eigenschappen van de grijper, die het moeilijk maken om het losproces efficiënt te laten verlopen. Een oplossing voor een beter losproces is om met behulp van op simulatie gebaseerde methoden het ontwerp van grijpers te verbeteren. Hierdoor kan er per grijpercyclus een grotere massa ijzererts worden verwerkt, waardoor de totale lostijd van een bulkvrachtschip tot een minimum wordt beperkt.

Het gebruik van virtuele prototypes van grijpers (*virtual prototyping*) is een nieuwe simulatiemethode waarmee het ontwerp op een betaalbare manier kan worden geëvalueerd. Cosimulatie van een virtueel prototype van een grijper en de werking op het bulkmateriaal wordt op ware grootte uitgevoerd door twee verschillende oplossers aan elkaar te koppelen: Discrete Element Method (DEM) en MultiBody Dynamics (MBD). Voor de cosimulatie zijn als input vereist een virtuele kraanmachinist, een CAD-model van een grijper die met een kraan is verbonden, en een gekalibreerd DEM-materiaalmodel. In het afgelopen decennium zijn er betrouwbare DEM-kalibratieprocedures ontwikkeld voor het modelleren van vrij stromende vaste bulkstoffen, zoals ijzerertspellets, zand en grind. Als gevolg van het vochtgehalte vertonen de meeste ijzerertsproducten echter gedrag dat afhangt van cohesie en belastingsgeschiedenis; bij de kalibratieprocedure moet daarmee rekening worden gehouden. Bovendien is, gezien de deeltjesgrootte en -vorm van dergelijke fijne ijzerertsproducten, de extreem lange rekentijd van

DEM-simulaties een uitdaging die moet worden opgelost. Verder wordt een grijper vaak gebruikt voor een grote verscheidenheid aan ijzerertsladingen met bijvoorbeeld verschillende vochtgehaltes, schuifsterktes en bulkdichtheden. De variabiliteit van de eigenschappen van de bulkgoederen beïnvloedt het grijpproces aanzienlijk, en daarmee ook de efficiëntie van de grijper.

Het hoofddoel van dit proefschrift is een nauwkeurige cosimulatie van grijper en cohesief ijzererts ontwikkelen en deze gebruiken om virtuele prototypen te optimaliseren. Als de eigenschappen van een ijzerertsproduct in interactie met de apparatuur eenmaal zijn gekarakteriseerd, moeten met behulp van een betrouwbare multivariabele kalibratieprocedure de verschillende invoerparameters van een DEM-materiaalmodel worden vastgesteld, inclusief continue en categorische variabelen. Zodra de juiste schalingsregels op de DEM-simulatie zijn toegepast, kan een modelsimulatie van grijper en materiaal op ware grootte worden geconfigureerd en gevalideerd. Vervolgens moeten de optimale instellingen van de ontwerpvariabelen worden bepaald, zodat het effect van variatie in de bulklading op het rendement van de grijper kan worden geminimaliseerd. Dit is de basisstrategie van robuust grijperontwerp. Exploitanten van bulkterminals hebben graag grijpers die geoptimaliseerd zijn voor meerdere doelstellingen, zoals een maximaal rendement bij een minimale afwijking.

Een *consolidation-penetration*-testmethode is ontwikkeld om te onderzoeken of het belastingsgeschiedenisafhankelijke gedrag van ijzererts belangrijk is voor de werking van de grijper. In deze laboratoriumtest wordt de spanning gerepliceerd die wordt verwacht vóór de zetting (*consolidation*) in een stapel bulkgoed tijdens het grijpen. Vervolgens worden voor de grijper relevante eigenschappen van een reeks ijzerertsproducten gekarakteriseerd met behulp van laboratoriumtestmethoden, zoals *consolidation-penetration*, *ring shear*, *wall friction* en *ledge angle of repose*. Met de verkregen gegevens wordt een realistisch materiaalmodel gekalibreerd. De statische wrijvingscoëfficiënt, de oppervlakte-energie en de schuifmodulus van de deeltjes blijken de meest significante continue variabelen te zijn voor de gesimuleerde processen, en de rolweerstand blijkt een significante categorische variabele. Vervolgens wordt het DEM-materiaalmodel van cohesief ijzererts opgesteld met behulp van een betrouwbare multivariabele kalibratieprocedure met meerdere doelstellingen. De gekalibreerde DEM-parameterset en de ‘definitiviteit’ (*definiteness*) worden geverifieerd aan de hand van 20 verschillende bulkresponswaarden.

Zodra het materiaalmodel is gekalibreerd, worden schalingsregels voor het gekozen contactmodel toegepast om de rekentijd van de cosimulatie te minimaliseren. De schalingsregels

worden geverifieerd voor diverse deeltjesgroottes, geometrische afmetingen, testinrichtingen en cohesiekrachten. De geometrische afmetingen moeten los van de deeltjesgrootte worden geschaald om de bulkmassa en de volumehoeveelheden constant te houden. De cosimulatie van grijper en cohesief ijzererts is geconfigureerd met behulp van opgeschaalde deeltjes met een gemiddelde diameter van 55 mm. De schalingsregels leidden tot een vermindering in rekentijd, van 10^3 uur voor ongeveer 8 miljoen deeltjes tot iets minder dan 4 uur voor ongeveer 600 000 deeltjes.

Het gesimuleerde grijpproces wordt gevalideerd door middel van grijpexperimenten op ware grootte in het vrachtruim. Hierdoor kon het proces onder realistische bedrijfsomstandigheden worden vastgelegd. De cosimulatie wordt gevalideerd door de voorspellingen te vergelijken met experimentele gegevens over diverse aspecten, zoals de kinematische en dynamische eigenschappen van de grijper. De voorspellingen van de cosimulatie kwamen goed overeen met de experimentele gegevens op alle aspecten: de kracht in kabels, het koppelmoment in lieren, de kinematische eigenschappen van de geometrie, het laadvermogen, het verwerkte volume en de gemiddelde porositeit van het bulkgoed. De gevalideerde cosimulatie bewijst dat het belastingsafhankelijke gedrag van cohesieve lading tijdens de interactie met de grijper met succes is gemodelleerd.

Ten slotte is er een optimaliseringskader met meerdere doelstellingen opgesteld om in de ontwerpprocedure rekening te houden met de variatie in de bulklading. In het optimaliseringskader zijn twee doelstellingen opgenomen: een maximale gemiddelde prestatie van de grijper en een minimale afwijking van de gemiddelde prestatie. Om de relaties tussen geometrische ontwerpparameters en de genoemde doelstellingen in kaart te brengen, worden verschillende virtuele prototypen van grijpers gesimuleerd voor een breed scala aan ijzerertsladingen. Vervolgens wordt er een op surrogaatmodellen gebaseerde optimalisatie toegepast en wordt er een optimaal ontwerp van de grijper gemaakt. Het optimale grijperontwerp wordt vervolgens getest met behulp van de cosimulatie, waarbij wordt nagegaan in hoeverre de voorspellingen van het surrogaatmodel overeenkomen met de gesimuleerde respons. Het aldus opgestelde optimaliseringskader voorziet in directe stappen voor het ontwerpen van grijpers voor diverse bulkladingeigenschappen.

De gehele keten van een systeem voor de afhandeling van bulkladingen, vooral voor cohesieve materialen, kan nauwkeurig op ware grootte worden gesimuleerd, zodat de efficiëntie van het gehele systeem kan worden gemaximaliseerd. Hiertoe kan de in dit werk gepresenteerde

methode worden toegepast voor andere vaste bulkgoederen en ook voor andere bulkverwerkingsapparatuur dan grijpers. Bovendien kunnen er op basis van de gevalideerde cosimulatie van grijper en cohesief ijzererts innovatieve ontwerp- en exploitatieconcepten worden bedacht, zodat de tijd en energie die nodig zijn voor het lossen van ijzerertsvrachtschepen verder worden geminimaliseerd.

Publications

Journal papers

1. M. Mohajeri, F.M. Sickler, C. van Rhee, D.L. Schott, “A consolidation-penetration test for wedge-shaped penetration tools”. Journal of FME Transactions, Volume 46, Issue 3, 2018, 392-399. DOI: 10.5937/fmet1803392M.
2. M.J. Mohajeri, M.J. van den Bos, C. van Rhee, D.L. Schott, “Bulk properties variability and interdependency determination for cohesive iron ore”. Journal of Powder Technology, Volume 367, 2020, 539-557. DOI: 10.1016/j.powtec.2020.04.018.
3. M.J. Mohajeri, R.L.J Helmons, C. van Rhee, D.L. Schott, “A hybrid particle-geometric scaling approach for elasto-plastic adhesive DEM contact models”. Journal of Powder Technology, Volume 369, 2020, 72-87. DOI: 10.1016/j.powtec.2020.05.012.
4. M.J. Mohajeri, C. van Rhee, D.L. Schott, “Replicating cohesive and stress-history dependent behavior of bulk solids: feasibility and definiteness in DEM calibration procedure”. Accepted in Journal of Advanced Powder Technology, 2021.
5. M.J. Mohajeri, W. de Kluijver, R.L.J. Helmons C. van Rhee, D.L. Schott, “A validated co-simulation of grab and moist iron ore cargo: replicating the cohesive and stress-history dependent behaviour of bulk solids”. Accepted in Journal of Advanced Powder Technology, 2021.
6. M.J. Mohajeri, A.J. van den Bergh, J. Jovanova, D.L. Schott, “Systematic design optimization of grabs considering bulk cargo variability”. Accepted in Journal of Advanced Powder Technology, 2021.
7. M.J. Mohajeri, H.Q. Do, D.L. Schott, “DEM calibration of cohesive material in the ring shear test by applying a genetic algorithm framework”. Journal of Advanced Powder Technology, Volume 31, Issue 5, 2020, 1838-1850. DOI: 10.1016/j.apt.2020.02.019

8. S.W. Lommen, M.J. Mohajeri, G. Lodewijks, D.L. Schott, “DEM particle upscaling for large-scale bulk handling equipment and material interaction”. Volume 352, 2019, 273-282. DOI: 10.1016/j.powtec.2019.04.034
9. D.L. Schott, M.J. Mohajeri, J. Jovanova, S.W. Lommen, W. de Kluijver, “Design Framework for DEM-supported prototyping of grabs Including full-scale validation”. Under review.

Conference papers

1. M.J. Mohajeri, C. van Rhee, D.L. Schott, “Penetration resistance of cohesive iron ore: a DEM study”. 9th International Conference on Conveying and Handling of Particulate Solids, 2018.
2. M.J. Mohajeri, C. van Rhee, D.L. Schott, “Coarse graining of adhesive elasto-plastic DEM contact models in quasistatic processes”. 13th International Conference on Bulk Materials Storage, Handling and Transportation, 2019.

Supervised student reports

1. F.M. Sickler, “Developing a test method to investigate effect of compaction on penetration resistance of moist iron ore and coal”, Delft University of Technology, 2016.TEL.8083, 2017.
2. L. Wissink, “Optimization techniques for 3D design problems”, Delft University of Technology, 2017.TEL.8135, 2017.
3. M.J. van den Bos, “Investigating the effect of compaction on the penetration resistance of moist iron ore”, Delft University of Technology, 2017.TEL.8180, 2018.
4. A. Karaca, “Increasing grab lifetime through wear management”, Delft University of Technology, 2018.TEL.8285, 2018.
5. N. de Vries, “Simulating the shear cell test for a cohesive iron ore in EDEM 2018”, Delft University of Technology, 2018.TEL.8201, 2018.
6. A. van den Bergh, “Design optimization of grabs using Design of Experiments”, Delft University of Technology, 2018.TEL.8299. 2018.
7. A. van den Bergh, “Systematic design optimization of grabs handling cohesive materials”, Delft University of Technology, 2019.TEL.8363. 2019.
8. K. Lunesu, “Sensitivity of the grabbing process to variation of bulk surface geometry”, Delft University of Technology, 2019.MME.8386. 2020.
9. N. de Vries, “Design of grabs under operational conditions”, Delft University of Technology, 2020.MME.8452, 2020.